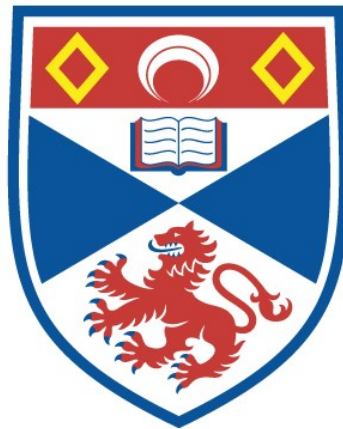


ELECTRICAL TRANSPORT PROPERTIES OF $\text{UR}_{\text{H}}\text{Ge}$ AND BiPd AT VERY LOW TEMPERATURE

Jack Barraclough

A Thesis Submitted for the Degree of PhD
at the
University of St Andrews



2015

Full metadata for this thesis is available in
St Andrews Research Repository
at:

<http://research-repository.st-andrews.ac.uk/>

Please use this identifier to cite or link to this thesis:

<http://hdl.handle.net/10023/6327>

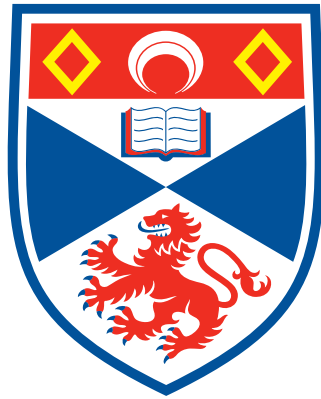
This item is protected by original copyright

This item is licensed under a
Creative Commons Licence

<https://creativecommons.org/licenses/by-nc-nd/4.0/>

Electrical transport properties of URhGe and BiPd at very low temperature

Jack Barraclough



University of
St Andrews

This thesis is submitted in partial fulfilment for the degree of PhD

4th February 2015

Abstract

URhGe has garnered interest recently as one of the few known ferromagnetic superconductors. The superconductivity in this material appears to arise from magnetic fluctuations rather than phonons, and take a triplet form which is remarkably resistant to field. In this thesis, a number of measurements on the material are presented.

Some probe the Fermiology, with strong evidence appearing for a model which has both light open sheets and heavy, small, closed pockets. The open sheets, associated with chains of real-space electron density running along the b axis, dominate the conductivity in most circumstances. Evidence for their existence arises from the general large and non-saturating magnetoresistance, and from the unusual observation of negative temperature coefficient of resistance at high fields. The closed pockets have provided a few Shubnikov-de Haas oscillations, but mostly they remain inferred from the high specific heat γ and their role in the magnetism.

In order to better probe the superconductivity, a high precision low noise DC resistance measurement bridge was built using a SQUID. Along with conventional measurements, this provides evidence that the two pockets of superconductivity on the phase diagram are the same phase. The re-entrance can be understood simply as a result of magnetic field being a tuning parameter, but also suppressing bulk superconductivity through orbital limiting. The SQUID bridge allowed the detection of domain wall superconductivity linking up these two pockets.

The SQUID bridge was also used to study the highly structured superconducting transition in BiPd. This material lacks inversion symmetry in its crystal structure, so is a good candidate for unusual forms of superconductivity. Here again non-bulk superconductivity is considered the most likely cause for the structure. Unusual and distinctive IV curves have been measured, and a simple model of inhomogeneous conductivity channels with different critical currents is proposed as an explanation.

Declarations

Candidate's declarations

I, Jack Barraclough, hereby certify that this thesis, which is approximately 79990 words in length, has been written by me, and that it is the record of work carried out by me, or principally by myself in collaboration with others as acknowledged, and that it has not been submitted in any previous application for a higher degree.

I was admitted as a research student in September 2009 and as a candidate for the degree of Doctor of Philosophy in Physics in September 2009; the higher study for which this is a record was carried out in the University of St Andrews between 2009 and 2014.

Date: Signed: (candidate)

Supervisor's declarations

I hereby certify that the candidate has fulfilled the conditions of the Resolution and Regulations appropriate for the degree of Doctor of Philosophy in Physics in the University of St Andrews and that the candidate is qualified to submit this thesis in application for that degree.

Date: Signed: (supervisor)

Permission for electronic publication

In submitting this thesis to the University of St Andrews I understand that I am giving permission for it to be made available for use in accordance with the regulations of the University Library for the time being in force, subject to any copyright vested in the work not being affected thereby. I also understand that the title and the abstract will be published, and that a copy of the work may be made and supplied to any bona fide library or research worker, that my thesis will be electronically accessible for personal or research use unless exempt by award of an embargo as requested below, and that the library has the right to migrate my thesis into new electronic forms as required to ensure continued access to the thesis. I have obtained any third-party copyright permissions that may be required in order to allow such access and migration, or have requested the appropriate embargo below.

The following is an agreed request by candidate and supervisor regarding the publication of this thesis:

Printed copy: Embargo on all of print copy for a period of 2 years on the following ground: Publication would preclude future publication.

Electronic copy: Embargo on all of electronic copy for a period of 2 years on the following ground: Publication would preclude future publication.

Supporting statement for electronic embargo request: Much of the material in the later chapters could be published as papers, but this has not yet been done. An embargo will greatly increase the number of journals we could consider, as it will allow us to comply with the various publishers' policies on previous publication. This will allow us to publish in higher impact and/or more appropriate journals than would be possible without an embargo.

Date:

Signed:

(candidate)

(supervisor)

Thanks and Acknowledgements

First and foremost I must thank my supervisor, Ed Yelland. He has guided and assisted me in every aspect of my PhD: from the practicalities of handling cryogenics and refrigerators; through the process of analysing and interpreting large data sets; and all the way through to presenting results and preparing this Thesis. Along with Ed, I would also like to thank the others who have worked in the Field Induced Quantum Ordering Laboratory during my PhD, in particular Volodya Khotkevych and Calum Lithgow, for their help in such day-to-day tasks as transferring helium and all the other things necessary in keeping the lab running.

In addition to those named above, I have also had valuable discussions on a variety of physical concepts with Andrew Huxley and Chris Hooley, who have helped guide my understanding of the underlying physics.

No experiment is possible without samples, so my thanks also go to those who have grown or helped to prepare the samples upon which this work is based. Table 3.2 lists samples and growers, but in short I would like to thank Andrew Huxley, Dmitry Sokolov and Bhanu Joshi and his group. Michal Kepa also deserves thanks at this point, as he spent much time taking crystals from a polycrystal growth and preparing them for measurement.

Some of the data presented here was measured at fields over 20 T, this was taken at the European High Magnetic Field laboratory in Grenoble. As with any facility experiment, many hands are indispensable for spreading the load of long night shifts and quick sample changes. For this I thank again Ed Yelland and Michal Kepa, and also our local contact in Grenoble, Ilya Sheikin.

A large part of the work leading to this thesis has been in the building of a sample rotator and a SQUID bridge. Dave Steven and his team in the Physics workshop have been indispensable in turning my designs into the actual parts necessary to build both devices. Also amongst the technical staff at St Andrews I would like to thank Reg Gavine, who's hard work running the liquefier kept a constant supply of liquid helium available for me to run my experiments with.

Finally, I should thank the various bodies which have provided the funding necessary for me to complete my PhD, including the Engineering and Physical Sciences Research Council, the Scottish Universities Physics Alliance, the Condensed Matter Doctoral Training Center and of course the School of Physics.

Contents

1	Introduction and theoretical background	1
1.1	Resistance in zero field	1
1.2	Magnetoresistance	5
1.2.1	Motion of the electron in a lattice	5
1.2.2	The free electron gas	8
1.2.3	Closed Orbits	10
1.2.4	Open orbits	13
1.2.5	Magnetic breakdown	15
1.3	Shubnikov-de Haas oscillations	16
1.3.1	Quantization and extremal areas	16
1.3.2	Amplitude of the Oscillations	19
1.3.3	Classifying orbits	22
1.3.4	Field dependent areas	22
1.4	Unconventional superconductivity	25
1.4.1	Ferromagnetic superconductors	27
1.4.2	Flux Flow Resistance	29
1.4.3	Superconductivity without inversion symmetry	30
2	Introduction to URhGe	34
2.1	Ferromagnetism	34
2.2	Superconductivity	39
2.3	Other relevant measurements and materials	40
3	Methods	43
3.1	Basic resistance measurement techniques	43
3.1.1	Understanding noise and interference	43
3.1.2	Building blocks of a good measurement	46
3.1.3	Typical measurements	52
3.2	Low temperatures and high fields	54
3.2.1	Wiring for very low temperatures	54
3.2.2	Filtering	56
3.2.3	Cryostat used for measurement	56
3.2.4	Thermometry	59
3.3	Sample rotation	61
3.3.1	Design	61
3.3.2	Materials and construction	63
3.3.3	Measurement and control	65
3.3.4	Performance	66
3.4	Use of SQUIDs for resistance measurements	67
3.4.1	DC SQUID and flux locked loop	68
3.4.2	The SQUID null-detector bridge circuit	70
3.4.3	Sensitivity and noise considerations	71
3.4.4	Wiring and shielding	74
3.4.5	Vibration	75

3.4.6	Computer control	77
3.4.7	Performance	78
3.5	Samples	78
3.5.1	Mounting a sample	79
3.6	Treatment of data	81
4	Measurements on URhGe	83
4.1	Zero field resistivity	84
4.2	General Magnetoresistance	90
4.3	Negative temperature coefficient of resistance	98
4.4	Symmetry considerations and calculations	107
4.4.1	Symmetry considerations	107
4.4.2	DFT calculations	111
4.5	Quantum Oscillations	116
4.5.1	Near $B \parallel c$	116
4.5.2	Near $B \parallel b$, below the moment rotation field	119
4.5.3	Near $B \parallel b$, above the moment rotation field	122
4.5.4	Summary	129
4.6	Overview of the Fermiology	131
4.7	Additional Measurements with field near the b -axis	134
4.8	Measurements with the SQUID resistance bridge	144
4.8.1	Measurements in the resistive state	145
4.8.2	Attempts to measure critical current	149
5	Results on BiPd	152
5.1	AC Measurements	152
5.1.1	Angular dependence of critical field	154
5.1.2	Current dependence of critical field	156
5.2	DC Measurements	157
6	Summary and Conclusions	164
A	Circuit symbols	168
A.1	Conductors	168
A.2	Components	169
B	Supplementary Information	170
C	Paper: High-field superconductivity at an electronic topological transition in URhGe	171
	Bibliography	172

List of Figures

1.1	Types of orbit	8
1.2	Calculated magnetoresistance of simple models	11
1.3	Quantum oscillation amplitude reduction factors	19
1.4	Examples of Flux Flow	30
1.5	Fermi surface symmetries	31
2.1	Unit cell of URhGe	35
2.2	Phase diagram of URhGe	36
2.3	Doping URhGe with Cobalt	41
3.1	Balancing transformer for eliminating common mode	49
3.2	A simple measurment circuit	54
3.3	Measurement circuit with transformer	55
3.4	Measurement circuit with multiple samples and transformers	55
3.5	Measurement circuit with low-temperature transformers	55
3.6	Simplified sketch of the rotator design	62
3.7	Rotator performance	67
3.8	Simple flux-locked-loop	68
3.9	Block diagram for Model 5000	69
3.10	SQUID bridge circuit for resistance measurement	71
3.11	Low thermoelectric voltage screw terminals	73
3.12	Photographs of SQUID bridge parts	76
4.1	Zero field resistivity of URhGe	84
4.2	Heat capacity of URhGe	86
4.3	Magnetoresistance in the ab -plane	91
4.4	Magnetoresistance as a function of current direction: low RRR	95
4.5	Magnetoresistance as a function of current direction: medium RRR	96
4.6	Negative temperature coefficient of resistance	98
4.7	Simple model for NCTR	100
4.8	Phase diagram in the ab plane	103
4.9	Temperature dependence in NCTR	105
4.10	Chains in the URhGe structure	106
4.11	Calculated Fermi surfaces for URhGe	114
4.12	Angle dependence of SdH near $B\parallel a$	117
4.13	Temperature dependence of SdH near $B\parallel a$	118
4.14	Angle dependence of SdH in URhGe below moment rotation	120
4.15	Pinching off of SdH in URhGe below moment rotation	121
4.16	Giant SdH near $B\parallel b$	122
4.17	Fitting oscillations at high field	124
4.18	Effective mass from oscillations at high field	125
4.19	Angle dependence of high field oscillations	127
4.20	Angle dependence of giant SdH	127
4.21	Topological changes in Fermi surface due to field	132
4.22	Example temperature sweeps on URhGe bars	135

4.23	Fit parameters for temperature sweeps on URhGe bars	136
4.24	Variation in temperature fit coefficients in URhGe#1	138
4.25	High temperature magnetoresistance of URhGe bars	141
4.26	AC resistivity between superconducting pockets	145
4.27	IV curves of URhGe	146
4.28	DC resistance of URhGe near the superconducting transition	149
4.29	DC resistance of URhGe is consistent with sample heating	150
5.1	Structure and Fermi surfaces of BiPd	153
5.2	Specific heat of BiPd	153
5.3	Structured superconducting transition in BiPd	154
5.4	Current dependent transition in BiPd	156
5.5	BiPd IV curves	157
5.6	Simulated IV curves	158
5.7	Angle dependent critical current vs field in BiPd	159
5.8	Temperature dependent critical current vs field in BiPd	160

Chapter 1

Introduction and theoretical background

1.1 Resistance in zero field

The physics of electrons moving in a lattice under the influence of both electric and magnetic fields is by no means simple. It is useful to begin with simpler models and from them build up an understanding of the more complex systems. Let us begin with the conductivity of a non-interacting free electron gas, then add an arbitrary band structure.

The conductivity of a sample is dictated by the response of the electrons to the applied field. By Newton's law, electrons accelerate $\mathbf{F} = \frac{d\mathbf{p}}{dt} = e\mathbf{E}$, where \mathbf{E} is the applied electric field. For convenience we shall define our axes with \mathbf{E} applied along the x axis and \mathbf{B} , when it is introduced, along z . This acceleration can be thought of in momentum-space as a rigid shift of the whole population of electrons to ever increasing momentum. This shift does not go on indefinitely however, as individual electrons scatter after some characteristic time τ and cease to contribute to the current.

The simplest approach to the problem is the Drude model. Here, one observes that the electron gains on average, in addition to their Fermi momentum, the momentum $\Delta\mathbf{p} = e\mathbf{E}\tau$ before being scattered. For now we shall consider only catastrophic scattering, which we shall define as moving the electron to a completely random point on the Fermi surface (i.e. the momentum change is large and has no preferred direction or magnitude), so we do not need to consider the behaviour of an electron after it is scattered, or its history before the previous scattering event. So on average, the electrons have momentum $\mathbf{p} = e\mathbf{E}\tau$. One can then use $\mathbf{p} = m\mathbf{v}$, $\mathbf{J} = nev$ and $\mathbf{J} = \sigma\mathbf{E}$ to write the Drude conductivity:

$$\sigma = \frac{ne^2\tau}{m} \tag{1.1}$$

Another way to obtain this equation is to consider the behaviour of a bunch of electrons contributing a current. In a steady state, the current, and thus the number and speed of electrons in the bunch, remains the same. This implies the forces on the bunch sum to zero, and we obtain this through a pseudo-force which represents the scattering. As this force destroys the drift velocity \mathbf{v}_d in time τ , it must be $m\frac{\mathbf{v}_d}{\tau}$. Equating this to the force due to field $e\mathbf{E}$, doing the same for the hole and rearranging yields the same as above. Here we have introduced the drift velocity \mathbf{v}_d as the change in velocity due to the applied field. This force-balance method must always produce the same results as considering the shift in the mean velocity, but in some cases is more tractable.

This was originally formulated without recourse to any quantum theory. Quantum mechanics is introduced by the Drude-Sommerfeld model, where the electrons act as free electrons but are subject to the exclusion principle. Since the electrons still have a free electron dispersion, they still respond to forces in the same way as the classical electrons, and the result still holds. Where the classical electrons have random thermal motion in addition to the momentum added by the electric field, the quantum ones have much larger velocity of up to v_F , but like the thermal motion, it sums to zero when all electrons are considered.

Once a realistic band structure is introduced, the situation becomes more complicated. The Fermi velocity, density of states and effective mass can change away from the free electron values and we can no longer write $\mathbf{p} = m\mathbf{v}$. The force due to the electric field still makes a shift in the whole Fermi sea to $\Delta(\hbar\mathbf{k}) = e\mathbf{E}\tau$, but this changes the velocities of all the particles therein in a way which varies throughout the Brillouin zone. So the Drude model breaks down. Fortunately however, because the change in k is small compared to k_F the vast majority of states remain occupied. Only a small number of states at one side of the surface are depopulated, and only a small number at the other side are filled. So we need only consider the mass, velocity and density of states at the Fermi surface. As electrons are indistinguishable, instead of considering a rigid shift of the whole surface, we are free to consider the movement of a small number of electrons from one side to the other. Equivalently, we may create a thin shell of electrons at one side, and a thin shell of holes at the other.

It is useful at this stage to introduce the concept of a “probe electron”. We shall consider the consequences of creating a single electron just above the Fermi surface, then, once its behaviour is understood we can integrate over these shells of electrons and holes to get the collective behaviour. We should also consider the behaviour of a probe hole at the other side, in this case, both the electron and the hole behave quite simply, but the magnetic case discussed in the next section is more complicated. Each probe electron appears as a moving charge of magnitude e and velocity \mathbf{v}_F directed so that $\mathbf{v}_F \cdot \mathbf{E} > 0$. Each hole has charge $-e$ but holes are only created on sections of the Fermi surface where $\mathbf{v}_F \cdot \mathbf{E} < 0$. The two minus signs cancel out, and we may treat both electrons and holes as contributing $\mathbf{v}_F e$ to the integral. We shall for now rely on the symmetry

of the system to prevent any net current in the y and z directions, so simplify this to $v_F^x e$.

The thickness of the shell of electrons can be obtained by thinking of a rigidly shifted Fermi surface. At its thickest point it is given by $\Delta(\hbar\mathbf{k}) = e\tau\boldsymbol{\varepsilon}$, but where the electric field is not normal to the Fermi surface it is thinner. The normal vector to the Fermi surface can be written conveniently as $\mathbf{v}_F/|\mathbf{v}_F|$, so the thickness of the shell at any \mathbf{k} on the Fermi surface can be written as $e\tau\mathbf{v}_F \cdot \boldsymbol{\varepsilon}/|\mathbf{v}_F|\hbar$. We have defined the electric field to be along x so this simplifies $e\tau v_F^x \varepsilon/|\mathbf{v}_F|\hbar$. The conductivity can then be obtained by evaluating the integral over the Fermi surface \mathcal{S}_F :

$$\sigma = \frac{1}{4\pi^3} \frac{e^2\tau}{\hbar} \int \frac{v_F^x(\mathbf{k})^2}{|\mathbf{v}_F(\mathbf{k})|} d\mathcal{S}_F \quad (1.2)$$

And of course substituting in the properties of the free electron model, one can recover the result in equation 1.1.

A more rigorous variant of the derivation above comes from Boltzmann transport theory. The Boltzmann equation is a differential equation formed by considering the time derivative of the density of electrons at a given location which are in a given k -state, denoted $N(\mathbf{r}, \mathbf{k})$. The equation consists of three parts, one each for diffusion, field and scattering. The field (or force) term describes the influence of electric and magnetic fields on the electrons, which cause a change in \mathbf{k} by Newton's law. The diffusion term is something of a misnomer, arising from the use of the equation to model classical statistical problems, but simply states that electrons with Fermi velocity $\mathbf{v}_F(\mathbf{k})$ move around with that velocity, but remain in the same \mathbf{k} state. The scattering (or collision) term, usually simplified to the elastic scattering case, describes the transitions of electrons from one k to another due to scattering. In its full form it depends on the scattering probability $Q(\mathbf{k}, \mathbf{k}')$.

In steady state, all of these must sum to zero. The Boltzmann equation then provides a differential equation which can be solved for N . In practice, it is necessary to further constrain and simplify it before it can be solved. The first step is to assume the steady state N is a small variation from the equilibrium state $\Delta N = N - N_0$, which is given by the band structure and the Fermi distribution function. This results in a powerful formalism for treating a wide range of problems. If one includes a \mathbf{r} -dependent temperature, one can gain information about the thermal conductivity and thermopower, as well as the electrical conductivity. The full form of the scattering term, including $Q(\mathbf{k}, \mathbf{k}')$ can also capture interesting and detailed physics, however since Q is often unknown, we make the relaxation time approximation and write the scattering term as just $-\frac{1}{\tau}\Delta N$. From this point it is possible to recover equation 1.2. The complete derivation, which yields the full form of the conductivity tensor, rather than just σ_{xx} as above, can be found in [1].

At this point it is worth considering the nature of τ . In general, there will be several different scattering times in a material. Examples are scattering from defects in the lattice or scattering

from phonons. But we can nonetheless take a single scattering time for the band. This comes from some simple statistics. If you have random events of several different types happening independently, each at its own characteristic frequency $\frac{1}{\tau_i}$, then the frequency of events is the sum of the individual frequencies: $\frac{1}{\tau} = \sum_i \frac{1}{\tau_i}$. Substituting this into equation 1.2 gives the equation generally known as Matthiessen's rule:

$$\rho = \sum_i \rho_i \quad (1.3)$$

Of course this is only true if all electrons are affected equally by the different scattering sources, a rule to which there are some notable exceptions. The first is the multi-band case, some scattering processes can affect one band more than another. In practice, it is not uncommon for one band to dominate the conductivity, and then only scattering of carriers in that band need be considered. Some scattering processes also have different cross sections for electrons within a band, depending on their k -vector.

Matthiessen's rule is still a very useful result, as many of the sources of scattering present in metals have characteristic temperature dependencies which allow them to be identified. The possible scattering processes depend on the other physics of the material: spin waves appear near ferromagnetism for example. An enumeration of possible scattering processes for URhGe is presented, along with the evidence for them in section 4.7.

One final point is that so far we have considered non-interacting electrons. One way of introducing electron interactions into our model is to make corrections to the band structure. The simplest way of doing that is the Hartree approximation, where the lattice potential is modified to be the potential of the lattice plus the coulomb interaction of the electron being considered with the mean electron density. This makes the problem into a self consistency one, which is solvable directly in a few special cases, but more usually requires an iterative numerical technique. Adding another term to the potential to account for electron exchange further improves the model, at the cost of making analytic solutions intractable in most cases. This is the Hartree-Fock method. For our purposes, both of these can be thought of as an improved method of calculating the band structure and hence the Fermi surface. So the discussions above regarding resistance and those below about magnetoresistance are unaffected. For a more accurate description, particularly in the case of strong interactions, we move on to Fermi liquid theory.

In general, no non-interacting electron band structure will ever fully describe interacting electrons, so the single electron states will not be stationary states. If however the lifetime of those states is longer than the typical scattering lifetime, then they may be good enough to describe the system. To better understand this, we introduce the idea of quasiparticles. The principle is that although the collective ground state cannot be decomposed into a collection of individual electron states, it can be decomposed into some form of collection of quasiparticle

states. Furthermore, these quasiparticle states can be mapped 1:1 to the non-interacting electron states. This latter statement is known as adiabatic continuity, and can be expressed either as the quasiparticle states having a large overlap with the non-interacting states, or the non-interacting states morphing continuously and smoothly into the quasiparticle states if the interaction is “turned on” slowly. Provided that this is true (and it is not always true, a Fermi liquid is just one of many states a material may take at low temperature) then it is possible to prove that the non-interacting electron model is very close to the interacting one at sufficiently low temperatures and for electrons close to the Fermi surface.

The quasiparticles do not behave exactly like the free electrons however. One cannot simply excite a single quasiparticle in the way one can excite a single electron. In general, the energy cost of doing so will be different, as the remaining quasiparticles will change their configuration a little. This means that the dispersion relation $E(\mathbf{k})$ will be modified, just at the Fermi surface. This naturally also changes the Fermi velocity and density of states, but in most cases, it is sufficient to represent this by an increase in the effective mass over that of the free electron. This applies to most measurements of the mass, including the specific heat, the mass in the Drude equation, and the cyclotron mass derived in the next section. Provided one adjusts these parameters appropriately to represent the corrected dispersion relation, the results in these sections also apply to a Fermi liquid.

1.2 Magnetoresistance

When a free electron is in a magnetic field (which, in keeping with [2], we define to be along the z -direction), it experiences a Lorentz force and this results in a helical path with the axis of the helix along z . The rate of direction change is easily derived from the Lorentz force and is given by $\omega_c = \frac{eB}{m}$. This value, compared to the scattering rate τ is what dictates the effect of the magnetoresistance in such a free electron gas. If the product $\omega_c\tau$ is much less than one, the magnetic field would not have any effect, as the electron is scattered before it curves much. If it is large, the electron makes one or more orbits between scattering events and the magnetoresistance may be substantial.

The situation in a metal is much more complicated, and to gain a reasonable understanding of the magnetoresistance this free electron model is not enough. Much more detail is needed.

1.2.1 Motion of the electron in a lattice

An electron in a metal is not free; it is in a periodic crystal lattice, and is a constituent in a Fermi sea. This leads to different equations of motion than the free electron case. As above we need to use the crystal momentum $\mathbf{p} = \hbar\mathbf{k}$ in place of $m\mathbf{v}$, the velocity becomes $\mathbf{v} = \frac{1}{\hbar}\nabla_{\mathbf{k}}E(\mathbf{k})$, and the mass must be corrected to $m^* = \frac{1}{\hbar^2}\nabla^2E(\mathbf{k})$.

Conveniently, the electron's velocity is directed up the gradient of the energy. As Fermi surfaces are sheets of constant energy, the velocity must always be normal to the Fermi surface. If the velocity is normal, the Lorentz force, being perpendicular to both \mathbf{v} and \mathbf{B} , must induce a change of \mathbf{k} which is directed in the plane of the Fermi surface and in a plane perpendicular to \mathbf{B} . This implies the electron moves through a series of states at a series of \mathbf{k} s which proscribe an orbit in k -space. This orbit is the intersection of the Fermi surface with a plane at fixed k_z . At first glance, it appears that this also applies to all electrons below the Fermi surface which would follow the intersection of an equal-energy surface with the constant k_z plane. But one must be careful as interacting electrons far from the Fermi surface are generally poorly described by Fermi liquid theory. In practice the distinction does not matter, as these electrons are inert.

Using point 1 above, and using subscript xy to denote the component of a vector in the x - y or k_x - k_y planes, we can write the Lorentz force as:

$$\mathbf{F} = \hbar \frac{d\mathbf{k}_{xy}}{dt} = e\mathbf{v} \times \mathbf{B} \quad (1.4)$$

As there is no force in the z direction, k_z does not change with time, but this does not mean that v_z does not change. For now however, it is useful to neglect v_z , and consider the motion of the electron projected onto the xy plane. By separating \mathbf{v} into $\mathbf{v}_{xy} + v_z$ we can write equation 1.4 as:

$$\hbar \frac{d\mathbf{k}_{xy}}{dt} = -e\mathbf{B} \times \left(\frac{d\mathbf{r}_{xy}}{dt} + \frac{dr_z}{dt} \right) \quad (1.5)$$

and integrate with respect to time to get

$$\hbar\mathbf{k}_{xy} = -e\mathbf{B} \times \mathbf{r}_{xy} + \mathbf{C} \quad (1.6)$$

Where \mathbf{C} is some constant of integration containing information about the starting position of the electron in the lattice, the neglected v_z term and the location of the orbit in k -space.

The main result here is that the real-space orbit is defined by the Fermi surface. As the electron goes round the Fermi surface, and \mathbf{k}_{xy} changes, \mathbf{r}_{xy} changes such that it is perpendicular to \mathbf{k}_{xy} and proportional to it in magnitude. This makes a real space orbit of the same shape as the k -space orbit, but rotated by 90° . The size of the real-space orbit is proportional to the size of the k -space orbit and inversely proportional to \mathbf{B} . It is often useful to use this to write the relationship between the area of the k -space orbit, denoted \mathcal{A} , and the area of the real space orbit projected on a plane perpendicular to field $\alpha = (\hbar/eB)^2 \mathcal{A}$.

Returning to the question of motion parallel to the field, it too is dictated by the shape of the Fermi surface. As the electron moves around its k -orbit, it passes through different parts of the Fermi surface, each with its own local $v_z = \frac{dE}{dk_z}$. Consequently, as it goes around its real-space orbit, v_z varies and the electron moves in the direction parallel to the field. In general, the

electron will end up displaced from where it started, but if the integral of the velocity around the orbit is zero, it will return to its starting point.

Knowing its k - and real-space paths, it is also possible to work out how long it will take to complete an orbit. We can express the distance s the electron travels in k -space using equation 1.4 and the fact that \mathbf{v}_{xy} is perpendicular to \mathbf{B} as

$$\hbar \frac{ds}{dt} = e |\mathbf{v}_{xy}| |\mathbf{B}| \quad (1.7)$$

If we define the element $d\mathbf{k}_{out}$ such that it lies in the k_x - k_y plane and is directed perpendicular to the orbit and outwards, then $\hbar \mathbf{v}_{xy} = \frac{dE}{d\mathbf{k}_{out}}$ and the above becomes

$$\hbar^2 \frac{ds}{dt} = e \left| \frac{dE}{d\mathbf{k}_{out}} \right| |\mathbf{B}| \quad (1.8)$$

If we now introduce the area inside the orbit \mathcal{A} and the element of that area $d\mathcal{A}$ as an annulus of thickness $d\mathbf{k}_{out}$ on the orbit, then $d\mathcal{A} = d\mathbf{k} \cdot d\mathbf{s}$ and:

$$\frac{1}{dt} = \frac{e |\mathbf{B}|}{\hbar^2} \frac{dE}{d\mathcal{A}} \quad (1.9)$$

Integrating around the whole orbit and defining the time to complete an orbit as $T = \frac{2\pi}{\omega_c}$ yields

$$T = \frac{\hbar^2}{e |\mathbf{B}|} \frac{d\mathcal{A}}{dE} \quad (1.10)$$

$$\omega_c = \frac{2\pi e |\mathbf{B}|}{\hbar^2} \left(\frac{d\mathcal{A}}{dE} \right)^{-1} \quad (1.11)$$

And so we have derived the cyclotron frequency for an electron in a lattice.

If we use a free electron dispersion $E = \frac{\hbar^2 \mathbf{k}^2}{2m}$ then the area of an orbit is $\mathcal{A} = \pi \frac{2mE}{\hbar^2}$ and ω_c becomes the familiar $\frac{e|\mathbf{B}|}{m}$. Comparing this result to the one above, we see that the value $\frac{\hbar^2}{2\pi} \frac{d\mathcal{A}}{dE}$ behaves like a mass. This is known as the cyclotron mass, and is the only correction one needs to make for a great many of the results of the free electron model to be applicable to electrons in a lattice.

Up until this point, we have considered only a simple Fermi surface entirely within the Brillouin zone, where any orbit around it is closed. This is not the only type of orbit possible, consider the Fermi surface shown in figure 1.1. We can define three types of orbits. The closed orbit is type discussed above, where the electron will traverse the orbit and return quickly to its starting position. This does not necessarily imply it stays within the Brillouin zone, just that its enclosed area is less than the Brillouin zone cross section. Consider for example the orbit which would be obtained from the Fermi surface in figure 1.1 by tilting the field to the unique axis of the tetragonal structure, there would be an orbit crossing both necks which would traverse four zones.

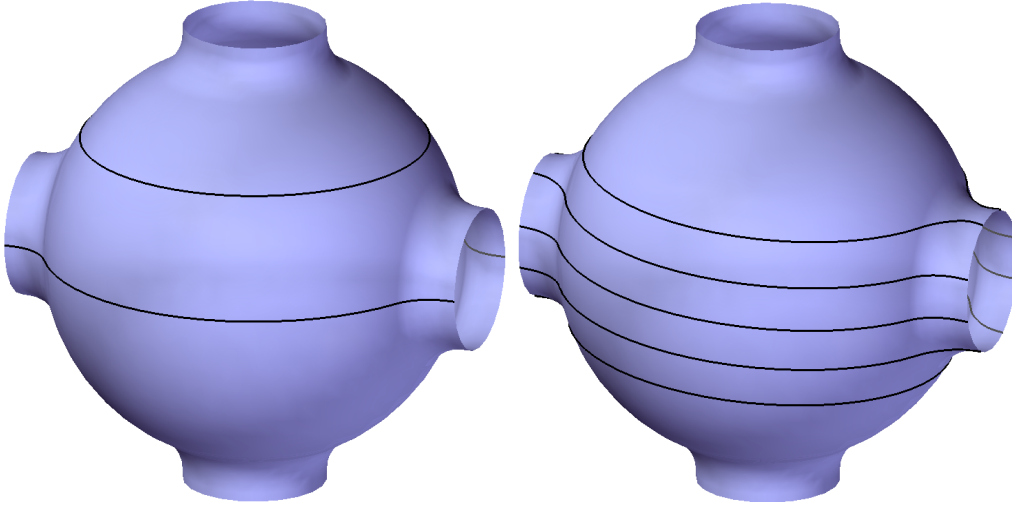


Figure 1.1: A simple Fermi surface, as might be obtained from the Harrison construction in a tetragonal lattice, plus anticrossings at the zone boundary. **Left:** An open orbit and a closed orbit. **Right:** With the field tilted by 5° , the open orbit becomes an extended orbit, where the electron must traverse 5 zones before it returns to its original \mathbf{k} .

The second type of orbit is the open orbit. This is also shown in the left panel of figure 1.1. In this case, when the electron leaves the zone on the left hand side, it reappears on the right hand side and moves along the same path it traversed on its first passage through the zone. In the repeated zone scheme, it runs along an infinite chain of connected spheres without ever coming back. Clearly, the concepts of cyclotron mass and frequency defined above are somewhat meaningless for such an orbit. The consequences of such orbits being present are dealt with in section 1.2.4.

Extended orbits lie somewhere in between the open and closed cases. On these orbits, the electron will eventually return to its original \mathbf{k} and \mathbf{r} , but it may require a long time and may traverse a large number of zones. Extended orbits will behave as either open orbits, if the scattering time is such that electrons cannot complete an orbit, or closed orbits otherwise. For our purposes, it is sufficient to consider only open and closed orbits, but to remember that there may exist orbits that can go from the former to the latter as field or sample quality increases.

One material where many of these effects can be seen is copper. In copper, the Fermi surface is similar to the one drawn in figure 1.1, but has eight necks not four. The additional necks make identifying the various orbit types much more complicated, but the presence of the different orbit types is clearly visible in the magnetoresistance. Pippard[2] provides a good overview.

1.2.2 The free electron gas

As explained in the free electron discussion at the start of this section, the balance between the time taken to complete an orbit and the average time taken to scatter an electron dictates the behaviour of the metal. This is usually discussed in terms of the value $\omega_c \tau$, with large values

indicating the electron completes many orbits before being scattered and values much less than one behaving like the zero field case.

Beginning with a circular orbit, one might assume that as the electron now follows a curved path, but has the same v_F , τ and l that one can calculate the reduction in current simply by calculating the reduction in distance moved in the direction of the electric field. However, in this model there is also a transverse current which increases with \mathbf{B} . In a real measurement, the equilibrium current is forced to be in the same direction all the time. This transverse current will quickly build up a surface charge at the side of the sample. These surface charges will create a field which will act to oppose the Lorentz force and straighten out the path of the electron. As the electron is now back on a straight path, it contributes the same current as the zero field case. The only difference is the appearance of an electric field. Thus the free electron gas has a hall effect, but no magnetoresistance, in this regime at least.

At this stage it is convenient to introduce the conductivity tensor $J_i = \sigma_{ij}\varepsilon_j$, which is in general a 3×3 matrix of non-zero elements, but which can be simplified somewhat:

$$\boldsymbol{\sigma} = \begin{pmatrix} \sigma_{xx} & \sigma_{xy} & \sigma_{xz} \\ \sigma_{yx} & \sigma_{yy} & \sigma_{yz} \\ \sigma_{zx} & \sigma_{zy} & \sigma_{zz} \end{pmatrix} = \underbrace{\begin{pmatrix} \sigma_{xx} & \sigma_{xy} & 0 \\ \sigma_{yx} & \sigma_{yy} & 0 \\ 0 & 0 & \sigma_{zz} \end{pmatrix}}_{\text{for } \mathbf{B} \parallel z} = \underbrace{\begin{pmatrix} \sigma_{xx} & \sigma_{xy} & 0 \\ -\sigma_{xy} & \sigma_{xx} & 0 \\ 0 & 0 & \sigma_{zz} \end{pmatrix}}_{\text{for an isotropic system}} \quad (1.12)$$

Where the first simplification arises from the fact that the motion of an electron in the z direction usually is unaffected by field, and in turn does not affect the Lorentz force. The second simplification arises from the system's rotational symmetry in the xy -plane. From the conductivity tensor we can straightforwardly define the resistivity tensor $\boldsymbol{\rho} = \boldsymbol{\sigma}^{-1}$. The second simplified form of the isotropic conductivity tensor is much easier to invert than the full form, and yields:

$$\begin{aligned} \rho_{xx} &= \sigma_{xx}/(\sigma_{xx}^2 + \sigma_{xy}^2) \\ \rho_{zz} &= 1/\sigma_{zz} \\ \rho_{xy} &= -\sigma_{xy}/(\sigma_{xx}^2 + \sigma_{xy}^2) \\ \rho_{xz} &= \rho_{yz} = \rho_{zx} = \rho_{zy} = 0 \end{aligned} \quad (1.13)$$

Note that if the Hall conductivities σ_{xy} and σ_{yx} are zero, as they are at zero field, the usual result that $\rho_{ii} = 1/\sigma_{ii}$ is regained for all three axes.

We can use this formalism to fully analyse the free electron gas. The force balance on a probe electron is $m(\mathbf{v}/\tau) = -e(\boldsymbol{\varepsilon} + \mathbf{v} \times \mathbf{B})$, where here we have used the combined behaviour of the electron and the hole left behind to write \mathbf{v} as the drift velocity without reference to the Fermi velocity, which is permitted for a free electron gas. Also as per the zero field case, we noted that the destroying an electron of velocity \mathbf{v} after time τ effectively contributes an acceleration \mathbf{v}/τ .

By setting $\mathbf{B} = (0, 0, B)$ and $\boldsymbol{\varepsilon} = (\varepsilon, 0, 0)$ we can separate this into two equations:

$$\begin{aligned} v_x &= \frac{-e\tau}{m}(\varepsilon + Bv_y) \\ v_y &= \frac{-e\tau}{m}(-Bv_x) \end{aligned} \quad (1.14)$$

solving these linear equations for v_x and v_y yields:

$$\begin{aligned} v_x &= \frac{-e\tau}{m}\varepsilon \frac{1}{1 + \omega_c^2\tau^2} \\ v_y &= \frac{-e\tau}{m}\varepsilon \frac{\omega_c\tau}{1 + \omega_c^2\tau^2} \end{aligned} \quad (1.15)$$

and using the definition of $J_i = -nev_i$, the zero field conductivity $\sigma_0 = ne^2\tau/m$ and the definition of the conductivity tensor we may write:

$$\begin{aligned} \sigma_{xx} &= \sigma_0 \frac{1}{1 + \omega_c^2\tau^2} \\ \sigma_{xy} &= \sigma_0 \frac{-\omega_c\tau}{1 + \omega_c^2\tau^2} \end{aligned} \quad (1.16)$$

Which we can then substitute into equations 1.13 to obtain the results:

$$\rho_{xx} = \frac{1}{\sigma_0} \quad \rho_{xy} = \frac{-\omega_c\tau}{\sigma_0} \quad (1.17)$$

Which indicates the free electron gas has no magnetoresistance, but does have Hall. Using the definitions $\sigma_0 = ne^2\tau/m$ and $\omega_c = eB/m$ obtains the familiar hall coefficient $\rho_{xy}/B = -1/ne$.

1.2.3 Closed Orbits

The simplest model which shows a magnetoresistance is a two band model with one hole surface and one electron surface, both of which are free electron-like. We can understand why this system has a magnetoresistance by considering the contributions of the two bands separately. An electron-hole pair on the electron-like surface will act as a pair of electrons with a drift velocity to $+x$, so will curve to $-y$, in accordance with the arguments set out above. The electron-hole pair on the hole-like surface will act like a pair of holes with a drift velocity to $-x$, but because of the opposite charge will also curve to $-y$. This provides a net current in the x direction, but rather less in the y direction, so the hall field does not build up. We can use the same formalism as above to treat this effect in detail. We may simply sum the conductances of the two bands,

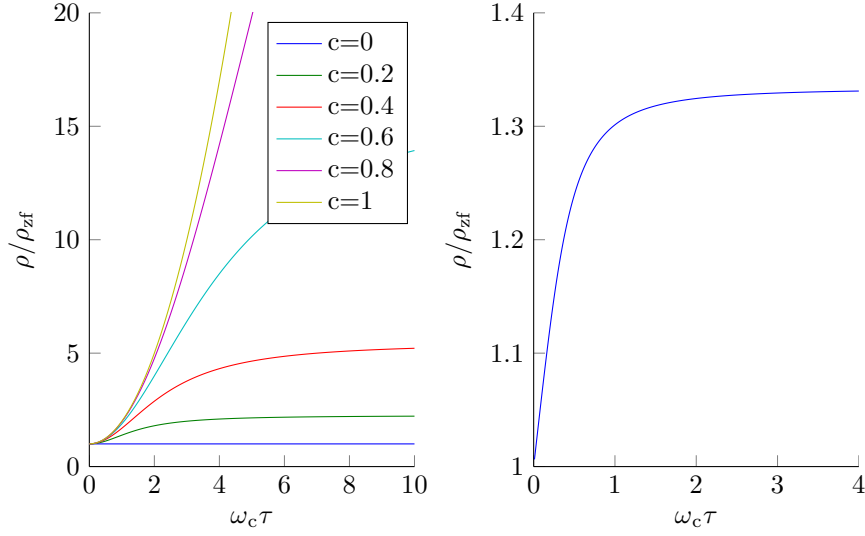


Figure 1.2: Calculated magnetoresistance of some simple models. **Left:** Two free-electron like bands, one electron, one hole. $c = n^+/n^-$. See equation 1.19. **Right:** The square Fermi surface, see equation 1.20.

each of which behaves according to equations 1.16:

$$\begin{aligned}\sigma_{xx} &= (\sigma_0^+ + \sigma_0^-) \frac{1}{1 + \omega_c^2 \tau^2} \\ \sigma_{xy} &= (\sigma_0^+ - \sigma_0^-) \frac{-\omega_c \tau}{1 + \omega_c^2 \tau^2}\end{aligned}\tag{1.18}$$

Where the negative sign in σ_{xy} actually arises from a change in sign of ω_c , as a hole will orbit in the opposite direction from an electron. The process of inverting these to obtain ρ_{xx} is quite laborious, however one can obtain:

$$\rho_{xx} = \frac{1}{\sigma_0} \frac{(1+c)^2 + (1-c)^2 \omega_c^2 \tau^2}{(1+c)^2 + (1-c)^2 \omega_c^2 \tau^2}\tag{1.19}$$

where c has been defined as the ratio n^+/n^- . It is plotted for a few different values of c in figure 1.2. This has a few interesting properties. Firstly, consider the case $c = 1$, the case of a compensated metal. One finds that the magnetoresistance goes as $\Delta\rho \propto B^2$ for all fields. By setting $c = 0$ one can also recover the result of the free electron gas outlined above. For intermediate values of c , it is useful to consider the limits. We can identify two limits: small B case, where $(1+c)^2 \gg (1-c)^2 \omega_c^2 \tau^2$, and $\Delta\rho \propto B^2$; and the large B case where $(1+c)^2 \ll (1-c)^2 \omega_c^2 \tau^2$, and $\Delta\rho$ is constant. This is termed saturation of the magnetoresistance.

Another way to find a magnetoresistance is to have a more complicated but still single band Fermi surface. One where the probe electron may follow a path of length l such that the vector \mathbf{L} joining the ends is shorter than l , but still parallel to the measurement-enforced zero field current.

This is not so strict a requirement as it seems, as the hall voltage will ensure the latter, it is only necessary to find an orbit which has a high sinuosity $S = l/|\mathbf{L}|$ over a section that the electron can traverse within its lifetime. One thing which is obvious from this analysis is that, as \mathbf{L} cannot be longer than l , the magnetoresistance is normally positive. Negative magnetoresistance can only arise if τ or the Fermi surface (and thus the cyclotron mass) are field dependent. This is most commonly seen in ferromagnet, where the scattering from magnetic fluctuations is field dependent.

One model where this effect is visible is the square Fermi surface with \mathbf{J} perpendicular to one of the faces. It is treated in some detail by Pippard[2] who obtains:

$$\rho_{xx} = \frac{1}{\sigma_0} \frac{D(2D \cosh(2D) - \sinh(2D))}{(2D + 1) \cosh(2D) - 2D \sinh(2D) - 1} \quad \text{where } D = \frac{\pi}{4\omega_c \tau} \quad (1.20)$$

This result is also plotted in figure 1.2, and shows some similar properties to the two band model. It too saturates, in fact this is a general result for closed orbits where the Fermi surface is not compensated. In practice, real metals usually show saturation which is not complete, at large fields there remains a slow rise in resistance with field. Several possible explanations for this phenomenon have been put forward, but none are completely satisfactory[2].

One major difference is that the low field dependence is $\rho \propto B$, not B^2 . It should be borne in mind though that the square Fermi surface is a bit unusual in that at an arbitrarily small field, some population of carriers makes it to the corner and is completely lost to the conduction. This is necessary to have $\frac{d\Delta\rho}{dB}$ not equal to zero at the origin. If the Fermi surface is smooth, then for small B the electron cannot move to a substantially different \mathbf{v}_F , and the gradient of $\Delta\rho$ at the origin is zero. Thus a linear magnetoresistance all the way down to zero field is often taken to be evidence of sharp features in the Fermi surface. In a real metal, there are likely to be many smooth orbits in addition to any with sharp features, so linear magnetoresistance from this mechanism is rare, but reductions below B^2 are reasonably common. One such example is aluminium, where the second zone hole surface has sharp edges.

Another observation is that both of the formulae only depend on B and τ through $\omega_c \tau$. This is easily understood by considering the motion of the electron in real space. It prescribes an orbit as per equation 1.6, which is the same shape as the k space orbit but scaled by an amount proportional to ω_c . The physics of the system is defined by the behaviour of the electron as it follows that orbit. If ω_c is increased, and τ reduced to keep their product constant, then this scales the real-space orbit down but keeps the fraction around it that the electron progresses the same. This leads to the expression known as Kohler's rule:

$$\frac{\Delta\rho}{\rho_{zf}} = \mathcal{F}(\omega_c \tau) = \mathcal{F}'(B/\rho_{zf}) \quad (1.21)$$

where \mathcal{F} and \mathcal{F}' are arbitrary functions dependent on the material. Thus, if one can obtain

samples with different scattering rates (different impurity levels for example), the measurements should all lie on the same curve on a graph of $\Delta\rho/\rho_{zf}$ against B/ρ_{zf} . Many materials also obey this rule when the change in τ is caused by heating and introducing more phonons. This form of Kohler's rule is somewhat weaker however, as the change in temperature also changes the frequency distribution of the phonons. This rarely causes gross violations of the rule, but small deviations are common.

1.2.4 Open orbits

The presence of open orbits complicates things, if we naïvely attempt to apply the results derived above, we run into several problems. Firstly, the area inside an open orbit is infinite, and so the cyclotron mass as defined by equation 1.11 is infinite. This causes $\omega_c\tau$ to be zero, as one expects if the electron will never complete an orbit. Like a closed orbit however, there can still be two regimes: that where the electron traverses many Brillouin zones, and that where it traverses much less than one. For easy comparison with the closed orbits, we shall continue to refer to these as the large and small $\omega_c\tau$ limits. This is not a completely facile convention, as now $\frac{2\pi}{\omega_c}$ may be thought of as the time for an electron to reach a part of the orbit which is very similar to where it started — usually one Brillouin zone away, but occasionally a multiple or proper fraction thereof. In real space the electron path will be given by an oscillatory function, and ω_c still has the meaning of an angular frequency when considering the repeat period of this path. By a similar argument a cyclotron mass for the orbit can be defined.

If $\omega_c\tau$ is small, then the electron cannot go all the way across the zone. It does not matter whether it would or would not. So in this limit, the open orbit will behave in a similar manner to the closed one. At large $\omega_c\tau$, the electron crosses the zone many times, and its path in real space is, as per equation 1.6, the same shape as its k -space one but rotated through 90° and scaled. The current contributed by the electron then is perpendicular to the open orbit (plus an arbitrary z component, as always). The magnitude of the current will depend on the sinuosity of the orbit. By considering the behaviour of a pair of straight orbits the normal to which make an angle θ to the electric field, one can write down the components of the conductivity tensor. The electric field creates a population proportional to $\cos\theta$, which then contributes a current with x component proportional to $\cos\theta$ and y component proportional to $\sin\theta$. Requiring the conductivity at $\theta = 0$ be $\sigma_{\theta=0}$ yields:

$$\begin{aligned}\sigma_{xx} &= \sigma_{\theta=0} \cos^2 \theta \\ \sigma_{yy} &= \sigma_{\theta=0} \sin^2 \theta \\ \sigma_{yx} &= \sigma_{yx} = \sigma_{\theta=0} \sin \theta \cos \theta\end{aligned}\tag{1.22}$$

And if we wish to generalise to a non-straight orbit, then in the high field limit we simply need

to reduce each of the conductivities by a factor of the sinuosity S . Inverting these in the usual way produces infinity for both ρ_{xx} and ρ_{yy} for any conditions other than ϵ perpendicular to the orbits. This simply represents the fact that in the high field limit this system cannot carry any current in any direction other than normal to the orbits.

This is not really a very useful result as open orbits rarely occur alone. More insight can be obtained by first adding in a closed orbit, but once again the algebra involved in the inversion becomes quite laborious. It can be made simpler by taking only the high field limit, with a single isotropic closed orbit (i.e. $\sigma_{xx} \approx \sigma_c/\omega_c^2\tau^2$ and $\sigma_{xy} \approx \sigma_c/\omega_c\tau$). Writing $\sigma_{\theta=0}/S$ from the discussion above as σ_o we have:

$$\sigma = \begin{pmatrix} \sigma_o \cos^2 \theta + \sigma_c/\omega_c^2\tau^2 & \sigma_o \sin \theta \cos \theta + \sigma_c/\omega_c\tau \\ \sigma_o \sin \theta \cos \theta - \sigma_c/\omega_c\tau & \sigma_o \sin^2 \theta + \sigma_c/\omega_c^2\tau^2 \end{pmatrix} \quad (1.23)$$

Which can be inverted without too much difficulty to yield

$$\rho_{xx} = \frac{\sigma_o \omega_c^2 \tau^2 \sin^2(\theta) + \sigma_c}{\sigma_o \sigma_c + \sigma_c^2 / \omega_c^2 \tau^2 - \sigma_c^2} \quad (1.24)$$

As we are interested in the high field limit, we may neglect the $\sigma_c^2/\omega_c^2\tau^2$ in the denominator as small compared to the σ_c^2 term. In this case the magnetoresistance clearly has a B^2 form for any θ other than $\theta = 0$, even at high field. In other words, this model does not show saturation. Pippard[2] extends this to the case of an open orbit with several other free-electron like bands of hole and electron nature with the same result, and indeed lack of saturation can be taken to be a universal result of open orbits being present. This can also be understood somewhat more qualitatively by observing that the open orbit, unless $\theta = 0$, always contributes a current in the wrong direction. As B increases, this current remains the same, but the current provided by the closed orbits falls off as B^2 . Thus when you invert the conductivity tensor, the closed orbits are unable to compensate for the open one, and the B^2 form remains.

It is quite possible to extend many of these arguments well beyond the level discussed above. A complete review is found in [3], which also provides alternative derivations for some of the results given in this chapter. There, the distinction is made between electron-like and hole-like Fermi surfaces even if they support open orbits, which can be very useful in calculating the Hall. The special case of orbits around the inside of a torus is also considered. Open orbits are split into periodic and aperiodic, with aperiodic open orbits being obtained with the field aligned at an angle to the crystal axes such that the electron must cross an extremely large number of Brillouin zones before reaching a point that is materially similar to where it started. Tensor inversions for a number of different combinations of the above are presented, which demonstrate the same properties as presented here, but in a more complete way. This more complete survey allows us to state some general rules with confidence.

If only closed orbits are present and the system is not compensated, the field saturates for all field angles. If only closed orbits are present, but the system is compensated, then non-saturation is expected for all angles. If open orbits exist in a single direction in the xy -plane, then non-saturation occurs for all angles except for a narrow range perpendicular to the open orbit. Multiple open orbits in different directions allow saturation.

1.2.5 Magnetic breakdown

We have constructed our theory in a semi-classical way, assuming that the electron moves along the equal energy surfaces. This implies the electron is transitioning through the zero field single electron states, when in reality there will be new eigenstates with the rotation built in. In writing our model this way we are saying that the perturbation caused by field is small, and the new eigenfunctions can only consist of wavefunctions at the equal energy surface it started on. If there is an area where another band lies close to the band the electron is on, the field may be strong enough to mix the states on the two bands. When the electron leaves this area, it may then do so on either of the two bands. It is often convenient to consider magnetic breakdown as the electron hopping between two bands (if they are close in energy at the k -point the electron passes through, they will usually also pass through the Fermi energy at points close together in k -space). It is however the energy gap between the bands, denoted E_g which dictates the hopping probability. A naïve approach would be to compare this to the energy scale of the field, $\hbar\omega_c$, however, this greatly overestimates the field required to start breakdown. Shoenberg[4] provides an argument based on the low-field limit where the field causes the electron to travel on a circular path, modifying the probability of Bragg reflection, and obtains the criterion $\hbar\omega_c \sim E_g^2/E_F$, a result which Pippard[2] also obtains in the high field limit by considering the lattice potential as a small perturbation on the circling electron. A complete treatment is provided by Blount[5], and the criterion given above is known as the Blount criterion.

When considering the consequences of magnetic breakdown for magnetoresistance, it is usual to discuss an electron moving around an orbit in k -space and reaching a point where breakdown is possible. It then continues on its low-field orbit with probability Q , or hops across to the other sheet with probability $P = 1 - Q$, with P increasing with increasing field. This has the effect of creating a number of new orbits, open orbits may appear where there were none before, new closed orbits may appear, and long, complex, self-crossing orbits within the zone can also appear. In general, this can cause a huge variety of different effects. One group of materials where magnetic breakdown is both commonly seen and well understood is the hexagonal transition metals (such as Mg and to a lesser extent Zn, Al and Sn) with the field applied along the hexad axis. These can be understood in terms of the hexagonal network. This model is a network made from Harrison's construction of overlapping circles, with each crossing made into an anticrossing. This makes hexagonal hole surfaces and small triangular electron surfaces, compensated overall. Switching

on a field initially just causes a B^2 magnetoresistance. When breakdown begins, there are a few effects. Firstly, compensation is lost, as electrons on the hexagonal hole surfaces can start making electron-like orbits, and the B^2 magnetoresistance disappears. As the switching probability gets larger, the magnetoresistance then falls and saturates to a new level dependent on the new orbits. Also, large oscillating components of the resistivity appear, for reasons explained at the end of the next section. A good description is given in [2].

1.3 Shubnikov-de Haas oscillations

When $\omega_c\tau$ is much greater than one, the electron completes many orbits before being scattered. In this case the electron can interfere with itself in a manner analogous to the electron in the Bohr atom. This leads to quantized orbits, modifying the density of states to be peaked at these orbits, and zero elsewhere. As the magnetic field changes, the radius of these permitted orbits (in k -space) changes, so the DOS at the Fermi surface oscillates as the permitted orbits pass through. This in turn affects many observables, and oscillations in the resistance are called Shubnikov-de Haas (SdH) oscillations. Oscillations in magnetization are often measured, and are called de Haas-van Alphen (dHvA) and the general phenomenon is called Quantum Oscillations.

1.3.1 Quantization and extremal areas

To begin with, consider an electron in an arbitrarily shaped orbit, without any net velocity in the direction of the field, which as before we label the z -direction. The condition for an orbit to be allowable is that the phase accumulated round the orbit is an integer multiple of 2π . Phase is accumulated from three sources, the motion, the magnetic field and ‘everything else’ where the latter is the same for nearby orbits, and can be expressed as some extra phase γ . Expressed mathematically, this is:

$$\oint_{orbit} \mathbf{k} - \frac{e\mathbf{A}}{\hbar} d\mathbf{r} = (n + \gamma)2\pi \quad (1.25)$$

where \mathbf{A} is the magnetic vector potential. One can solve this by replacing the motion in k -space by the corresponding motion in real space using equation 1.6, and it should be no surprise that one can obtain:

$$\frac{-e}{\hbar c} \Phi = (n + \gamma)2\pi \quad (1.26)$$

Or, using the definition of the flux quantum $\Phi_0 = 2\pi\hbar/e$, it is $\Phi = \Phi_0(n + \gamma)$; the allowed orbits are those where the real-space path encloses an integer multiple of the flux quantum, plus some phase factor. For our purposes it is more useful to express this result in terms of the area enclosed by the k -space orbit. From equation 1.6, we take $\alpha = (\hbar/eB)^2\mathcal{A}$ so our result becomes:

$$\mathcal{A} = 2\pi \frac{e}{\hbar} (n + \gamma) B \quad (1.27)$$

Which is known as the Onsager relation.

So for any orbit the zero temperature density of states as a function of B is an array of delta functions at the fields for which the above relation is true. Whilst so far all of the discussion of orbits has been based on orbits at the Fermi surface, it should be obvious that it can also be applied to any equal-energy surface (or, in a Fermi liquid, any area close enough to the surface that quasiparticles are well defined). So the density of states is also split into discrete levels at all other points in the zone. Joining possible orbits with the same n leads to tubes, known as Landau tubes, and one can visualise these as expanding or contracting as the field changes.

From this we wish to obtain the behaviour of an observable such as the resistance or magnetisation. For most if not all observables, it is the global density of states, summed over all the orbits, which enters. So we shall first calculate this. For now we shall consider the high field low temperature limit with no scattering, unlimited lifetimes and a perfectly sharp Fermi surface. We shall also ignore the effects of spin and Zeeman splitting. Writing $F = \frac{\hbar}{2\pi e} \mathcal{A}$ we might reasonably write the oscillatory part as

$$\tilde{n} = \sum_p a_p \sin\left(\frac{2\pi p F}{B} + \gamma\right) \quad (1.28)$$

Where we have included a sum over harmonics in case the dependence is not sinusoidal.

If we wish to obtain \tilde{n} , we must integrate the density of states over the whole Fermi surface. Whilst all of the surface contributes to the density of states n , if we only care about the oscillatory part \tilde{n} we can think about the phase of the individual oscillating contributions. If the field direction is parallel to a patch of Fermi surface, then all of that patch will have a high density of states at the same time, and will make a non-negligible contribution to \tilde{n} . A patch of Fermi surface which makes even a relatively small angle to the field will not have this phase coherence, so will make a negligible contribution to the oscillatory density of states. Of course the 3D nature of Fermi surfaces makes this argument a little more complicated but it should be clear that only extremal areas make a non negligible contribution to \tilde{n} . A more detailed analysis of the problem, such as that given in [2] or [4] treats the contributions from areas close to an extremal area in more detail, and yields two interesting results. Firstly, the amplitude of the oscillations will depend on the contributions from the surface area of Fermi surface which is close to the extremal orbit, and this leads to the first of our amplitude factors, the curvature factor $A_c = |\mathrm{d}^2 \mathcal{A} / \mathrm{d} k_z^2|^{-1/2}$. Secondly, if these areas can be considered ellipsoidal and there are many Landau tubes within, the oscillations become fully sinusoidal and $a_p = 0$ for $p > 1$ in equation 1.28. In the ellipsoidal case, one can also gain some information about the phase factor γ . If the orbit is a maximum, then γ is reduced by $1/4$, if it is a minimum then it is increased by $1/4$. In theory this can help identify orbits, but in practise γ is rather hard to measure, and one must also be careful to consider other contributions to it.

Included in this analysis is the assumption that there are a great many Landau tubes. This is

known as the large- n approximation, and the alternative case is known as the extreme quantum limit. In this case, the system becomes much more complicated. Firstly, if the Landau tubes are no longer close enough together that the extremal area contains many of them over the scale over which it is curved, then both the curvature factor and the lack of harmonics become unreliable results. Though as we shall see, the higher harmonics are strongly attenuated, so they only appear at very sharp edges or small numbers of Landau tubes. In extreme cases, where the number of Landau tubes in the whole Fermi sea becomes small, the orbits away from the extremal areas can also start to contribute. The best known example of such behaviour is in bismuth.

We now return briefly to γ . One can solve the Schrödinger equation for the free electron case to find $\gamma = \frac{1}{2}$ for isolated orbits, before the addition or subtraction of $\frac{1}{4}$ mentioned above[4]. Moving away from the free electron case, the problem becomes much more complicated. If one wishes to keep the semiclassical image of electrons moving through a series of zero-field stationary states, then one must consider the consequences of adiabatically changing the state of the electron. These changes introduce a Berry phase, which will in general not be a multiple of 2π , so contributes to γ . In many SdH measurements, including those presented in this thesis, it is not practical to measure γ with sufficient precision to draw any conclusions. This is because γ is the phase at infinite field, so one must extrapolate from the highest field one can reach. If there are many oscillations (large- n) between this field and infinity, or if the frequency changes with field, the extrapolation is impractical. In some materials in the extreme quantum limit however it can yield useful information.

We now turn to the SdH effect specifically. Here one could turn to the Drude conductivity formula $\sigma = ne^2\tau/m$, and observe that n enters directly. This does not tell the whole story however, as the varying density of states will also have an effect on τ . The scattering probability for an electron at a scatterer with potential V_s is $\sum_f \langle \psi_i | V_s | \psi_f \rangle$ where ψ_f are the possible final states. If the density of states is oscillating, so is the number of possible final states and thus so is τ . In a multiband model, where interband scattering is permitted (catastrophic scattering from impurities for example), the changes in τ affect every band, even if the band containing the extremal orbit does not make a major contribution to the conductivity.

When considering SdH, one should also consider magnetic interaction. As the density of states oscillates, so does the magnetization. This effect is the dHvA effect, and is often measured in its own right, but here we are only interested in the way it makes B vary from $\mu_0 H$. Whilst \tilde{M} is never going to be large in comparison to $\mu_0 H$, it can be appreciable in comparison to the period of the oscillations (which, from equation 1.28 we may write as $(\mu_0 H)^2/F$). In the case of a single frequency being present, this will obviously modify the waveform and introduce harmonics. In the case of multiple frequencies, the magnetization oscillations will reflect all of them, each observed frequency will be mixed with all the others, to produce a complex array of new frequencies.

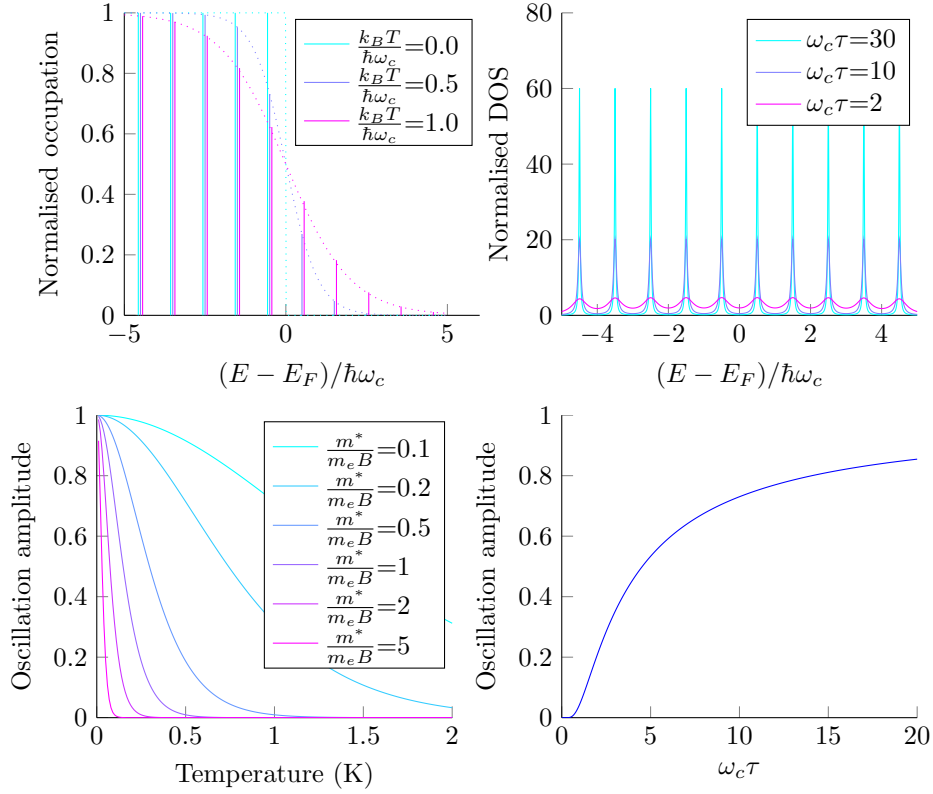


Figure 1.3: The effects of the temperature reduction factor and the dingle factor on quantum oscillations. In the top two graphs we have used the Onsager relation and the definition of the mass to write the energy in terms of the gap between tubes. **Top left:** The changing occupancy of the landau tubes as a result of the broadening of the Fermi distribution with temperature (tubes offset slightly for clarity). **Bottom Left:** The resulting temperature reduction factor, plotted for values of m^* and B typical of heavy fermions, i.e. masses between 1 and $50 m_e$ at 10 T. **Top right:** Broadening of the peaked density of states as a result of scattering. **Bottom Right:** The Dingle factor.

1.3.2 Amplitude of the Oscillations

After the curvature factor, the second factor which may reduce the amplitude of the oscillations is temperature. This can be understood quite simply by observing that the Fermi distribution is broadened. Instead of each landau tube going from full to empty as it crosses the Fermi surface, it instead reduces smoothly — this is shown schematically in figure 1.3. As the broadening happens on an energy scale of $k_B T$, but the gap between tubes is in \mathcal{A} , the gradient $d\mathcal{A}/dE$ will enter into the expression for amplitude. Referring back to equation 1.11, it is this gradient which determines the cyclotron mass, so temperature will damp away orbits with heavier masses faster. This is a very useful phenomenon, as it allows the determination of the cyclotron mass from the observed oscillations, though it can make the observation of heavy orbits difficult. Figure 1.3 also shows the form of the temperature reduction factor for a few masses and fields typical of heavy fermions, and it should be obvious that dilution refrigerator temperatures and/or high fields will be required for masses over about $20 m_e$.

A complete treatment of the effect can be found in the usual textbooks[2, 4], and yields:

$$A_T = \frac{X}{\sinh(X)} \quad X = \frac{2\pi p k_B T}{\hbar \omega_c} \approx 14.69 \frac{pm^*/m_e T}{B} \quad (1.29)$$

Which in addition to the properties mentioned above, contains the harmonic number p . This can be quite useful in identifying harmonics in a measured spectrum. If a frequency is observed at double another, then finding that the apparent mass is also double is a good indicator that it is a harmonic, not an orbit.

Another effect which will reduce the amplitude is if $\omega_c \tau$ is not much greater than one. If a substantial fraction of the carriers do not make it all the way around the orbit, the density of states does not completely assemble into Landau tubes. There are different ways to approach this problem, which can yield slightly different results. Historically, this was found experimentally to appear similar to an additional temperature in the expression above, which was termed the Dingle temperature, and some texts still use that convention. A clearer approach is to consider the high field limit, but to note that the electron has a finite lifetime. The uncertainty principle then implies that the momentum cannot be known exactly, and the electron wavefunction is spread over a small range of momenta. As the electron progresses around the orbit, this spread of momenta implies that the phase gets smeared out, and thus a small distribution of orbits around the infinite lifetime one become possible. The density of states changes from a comb of Dirac functions to an array of Lorentzians, as shown in figure 1.3. These orbits contribute to the oscillating density of states slightly out-of-phase with each other, and so reduce the amplitude of the resultant. A complete treatment along these lines yields the Dingle factor:

$$A_D = e^{\frac{-\pi p}{\omega_c \tau}} = e^{\frac{-\pi p m^*}{e B \tau}} \quad (1.30)$$

which is also plotted in figure 1.3.

One notable property of this formula is that it attenuates higher harmonics very strongly. If harmonics would be expected from the lack of large- n limit, then this term may well attenuate them beyond the point where they can be observed. This is especially true at intermediate temperatures where they are further attenuated by the temperature reduction factor discussed above. One should note however that both of these factors are applied before one should consider magnetic interaction, so they do not prevent the appearance of harmonics from that source.

A second observation is that if m^* , the cyclotron mass, is known from the temperature reduction fit, it is possible to obtain τ directly. Knowing also the frequency, and thus the area of the k -space orbit, one can estimate the perimeter of the real space orbit which the electron traverses in time $\frac{2\pi}{\omega_c}$. Combined with τ , this yields the mean free path l of the electron in the lattice:

$$l = \frac{\hbar \tau}{m^*} \sqrt{\frac{\mathcal{A}}{\pi}} \quad (1.31)$$

There are a couple of other things which can also affect the amplitude. The first of these is the presence of other orbits. Since the total oscillatory part of the resistance is just the sum of all the individual parts, it is subject to all the usual consequences of adding waves of different periods and amplitudes, such as beats between similar frequencies. Generally speaking, one analyses quantum oscillations by taking the Fourier transform of $\tilde{R}(1/B)$, in which case peaks can be resolved only if there is at least one full beat in the field over which the oscillation is visible. One very common case is in a paramagnetic metal, where there will be two almost identical orbits, one on the spin-up and one on the spin-down surface. For reasons discussed in section 1.3.4, they will actually produce the same frequency, but with a different phase, so reducing the amplitude. The details of this effect can provide useful information about a number of properties of the material, not least the Lande g factor of the electrons. However, since this thesis deals with quantum oscillations in ferromagnets, where the spin-up and spin-down orbits are well separated, these effects are not particularly relevant.

Finally, it is worth noting the effects that magnetic breakdown can have on SdH oscillations. The most obvious is that new extremal orbits can appear (and existing ones have their amplitude greatly reduced). The simplest case is a circular orbit which is centred close to and crosses the zone boundary, and so crosses a copy of itself in the next zone. At zero field, the crossings become anticrossings and there are two orbits, one ‘lens’ shaped, the other ‘binocular’ shaped, and at low fields there will be two observed oscillations. At high field P approaches 1 and only the circular orbits appear. At intermediate fields, all three of these orbits may be visible, along with others where the electron makes one or more laps of each orbit before returning to its starting point. The relative amplitudes of these orbits will be governed by the product of the switching probabilities around each one. In a more complicated system, one will often find two or more orbits of different frequency connected by breakdown points, and will observe new orbits at all frequencies that can be constructed as a sum of the original ones. To obtain a form of the amplitude, we need to know the form of the switching probability P and Q ; Blount[5] gives the form of P as $P \propto e^{E_g^2/H}$ provided that the band structure remains unchanged with H . This leads to the same form for the amplitude as the dingle factor.

Another, more subtle effect of magnetic breakdown is in how the density of states couples into the resistance. If a breakdown point lies on an extremal orbit, then the oscillating density of states couples directly to the switching probabilities P and $1 - P$. If one of the resulting orbits contributes much more to the conductivity than the other (perhaps by virtue of one being open and the other closed, or both closed but at different angles), then very large oscillations of the resistance can be seen. This is sometimes referred to as giant SdH, and the best known example is in Zinc[6]. It is also seen in magnesium and a few other metals[4], and is discussed further with reference to URhGe in section 4.5.3.

1.3.3 Classifying orbits

Ideally, with a large set of measurements at a variety of different field angles, it is possible to work out the shapes of the various Fermi surfaces present in the Brillouin zone. Whilst quantum oscillations will rarely give a completely unambiguous determination of the Fermi surfaces (it cannot, for example, tell where in the zone a pocket lies or how many equivalent copies of it there are) it can be a powerful tool for verifying or helping to refine theoretical predictions. In the measurements presented in this thesis however, too few frequencies have been observed to make good direct comparisons. It is nonetheless useful to consider what a frequency's dispersion with angle can tell us. For this purpose we consider a few basic shapes: the cylinder, the spheroid and the neck.

The behaviour of a sphere is obvious, the frequency remains constant. The simplest other shape is the cylinder of radius k' . If the field starts parallel to the axis of the cylinder, and tilts through an angle θ , then the orbit so produced will be an ellipse. The semi-minor axis of the ellipse will remain k' and the semi-major axis will be $k' \cos^{-1} \theta$. So the area, and hence the frequency, will vary as $\cos^{-1} \theta$. A similar process lead to the fact that spheroids which have different cross sectional areas for the new field directions will vary as $\sqrt{(\cos^2(\theta) + a \sin^2(\theta))}$, with a the relative area at 90° .

We can make a more general classification of extremal areas into two groups. Those that disperse slower than the cylinder, which implies they curve inwards, are bulge-like. Spheres and spheroids fall into this category. The other group is neck-like: anything that disperses faster than a cylinder is neck like. For simple Fermi surfaces, one can see that it can only be closed if the number of necks is one less than the number of bulges. This can be useful when considering the shape and topology of such surfaces.

1.3.4 Field dependent areas

A field dependent Fermi surface leads to a field dependent frequency, however the observed frequency is not simply related to the changing Fermi surface size by $F = \frac{\hbar}{2\pi e} \mathcal{A}$. Under these conditions, it is not possible to make a direct measurement of the extremal area causing the oscillation. To understand why this is the case, it is enough to consider a Taylor expansion of the frequency $F(B) = a_0 + a_1 B + a_2 B^2 + \dots$. The oscillatory part of the Lifshitz-Kosevich formula then becomes

$$R \propto \cos \left(\frac{2\pi(a_0 + a_1 B + a_2 B^2 + \dots)}{B} + \gamma \right) \quad (1.32)$$

and it is obvious that a_1 is indistinguishable from the phase γ . A microscopic view of this phenomena can be provided by recalling that the origin of the quantum oscillations is the expansion of Landau tubes through the Fermi surface. The frequency of the oscillations is given by the spacing between the tubes. If the Fermi surface is moving in or out, the oscillating DOS will be

Doppler shifted to a different frequency[7].

The argument of the of the oscillatory part of the Lifshitz-Kosevich formula is still given by:

$$\frac{2\pi F(B)}{B} + \gamma \quad (1.33)$$

Where we are continuing to write the ‘true frequency’ F as a shorthand for $\frac{\hbar}{2\pi e}\mathcal{A}$, which is different the observed frequency F_{obs} . When considering the oscillations as a function of $\frac{1}{B}$, we need to know the rate of change of the above with $\frac{1}{B}$, so:

$$F_{obs} = \frac{d}{d(\frac{1}{B})} \left(\frac{F(B)}{B} + \frac{\gamma}{2\pi} \right) = F(B) - B \frac{dF(B)}{dB} \quad (1.34)$$

Which, if the form of F_{obs} is known, yields a linear ordinary differential equation for F . Note that it is also an equation for a straight line through the point $F(B = B')$ with gradient $\left. \frac{dF(B)}{dB} \right|_{B=B'}$ and intercept F_{obs} . This leads to a common description of F_{obs} as the frequency back-projected to zero field. It is immediately obvious that this differential equation admits a complementary function of the form $F = a_1 B$, for any a_1 , in agreement with the simpler arguments above.

We can proceed no further without knowing the form of F_{obs} . For all measurements presented here, F_{obs} is smooth and slowly varying, so it can be represented as a Maclaurin series of relatively few terms. In order to continue our calculation then we assume a form

$$F_{obs} = \sum_{n=0}^{\infty} \alpha_n B^n$$

To solve equation 1.34 shall begin with the ansatz

$$F(B) = a_0 + a_{log} B \log(B) + \sum_{m=2}^{\infty} a_m B^m$$

Differentiating the latter and substituting both expressions into equation 1.34 yields

$$\sum_{n=0}^{\infty} \alpha_n B^n = \left(a_0 + a_{log} B \log(B) + \sum_{m=2}^{\infty} a_m B^m \right) \quad (1.35)$$

$$\begin{aligned} & - B \left(a_{log} (1 + \log(B)) + \sum_{m=2}^{\infty} a_m m B^{m-1} \right) \\ & = a_0 + a_1 B + \sum_{n=2}^{\infty} a_n (1 - n) B^n \end{aligned} \quad (1.36)$$

Finally we can equate coefficients in the two Maclaurin series, to obtain the result that:

$$\begin{aligned} a_0 &= \alpha_0 \\ a_{log} &= -\alpha_1 \\ a_n &= \frac{\alpha_n}{1-n} \quad n > 1 \end{aligned} \tag{1.37}$$

Which, combined with the complementary function noted above, is used in later chapters to convert observed frequencies into a family of possible real frequencies and thus extremal areas. In reality, we cannot use an infinite series, so must truncate it at some value of n . If we choose n_{max} so that F_{obs} is well-represented, we can have confidence that F is well represented as the final relation in equation 1.37 ensures that large- n terms contribute less to the series for F than F_{obs} .

It is useful to consider how this simplifies in some of the more familiar cases. In the case of a single, constant Fermi surface, the only term in either series is the zeroth term, and $F_{obs} = F$. The other well known case is the paramagnetic case with spin. In this case, the field dependence of the extremal area is very small, and results from Zeeman splitting. It is linear, and depends on the Landé g factor and the effective mass. The linear term is lost into the phase, and $F_{obs} = F(0)$, so no special consideration is required when converting F to \mathcal{A} . There is still a difference between the two orbit's areas, but it changes with field at the same rate as the spacing between Landau tubes changes. This means the phase difference between the two oscillations remains the same, and there is no change in properties with field. The phase difference is non zero though, so the total amplitude is reduced. This is usually represented by a spin reduction factor R_S when analysing quantum oscillations, but in a ferromagnet, where different spin bands are often well separated, it is usually better to treat the bands separately. That is why the spin reduction factor was omitted in the discussions in section 1.3.2.

The ferromagnetic case is different for two reasons. Firstly, in any ferromagnet the magnetization M is no longer small, and may be a strong function of applied field. As the field driving the oscillations is B , not $\mu_0 H$, the changing M makes the splitting, though linear in B , nonlinear in $\mu_0 H$. This is the same effect which leads to magnetic interaction, though that term is normally reserved for things arising from the oscillatory magnetization of the dHvA effect. Two examples of such materials are ZrZn_2 [7] and UPt_3 [8]. In the latter case, it is not strictly a ferromagnet, rather the magnetization increases with B as one would expect from a paramagnet,* then jumps to a higher value. But the same logic applies.

The second effect is in itinerant ferromagnets, and is, where present, much stronger than the first. In this case, the magnetization and some of the Fermi surfaces are strongly coupled. The energy gap between the \uparrow and \downarrow bands can be much more than one would expect from Zeeman

* UPt_3 is discussed in the cited reference as a Pauli paramagnet, but more recent work suggests it is a weak antiferromagnet[9]. In either case, the discussion about field dependent Fermi surfaces remains relevant.

splitting. Also, the bands in question are often heavy, flat bands with substantial f -weight. This means that as the exchange splitting changes the filling of the band, the size and shape can change drastically, leading to strongly field dependent orbits. These bands are also much less likely to be undergoing a rigid shift, rather they will be changing shape and nature too as the magnetization evolves.

In extreme cases, a band may move totally above (or below) the Fermi energy, resulting in an electronic topological transition, as has been suggested to be the case in YbRh_2Si_2 [10]. In other cases, phase transitions can occur, and it may be possible to follow the field dependent Fermi surface up to and even through the transitions, as in the metamagnet $\text{Sr}_3\text{Ru}_2\text{O}_7$ [11].

1.4 Unconventional superconductivity

To discuss unconventional superconductivity, we should first say what we mean by conventional superconductivity, and how and why the theories associated with it are not able to describe the unconventional form. Conventional superconductivity is described by BCS theory, and some of the major parts are as follows.

Firstly, in BCS theory, one chooses to write the waveform of a cooper pair as consisting of two electrons just above the Fermi sea, with zero net momentum i.e. with $k_1 = -k_2$. One can then write the wavefunction as a sum over possible k states which the electrons could occupy:

$$\psi(\mathbf{r}_1, \mathbf{r}_2) = \sum_{\mathbf{k} > \mathbf{k}_F} g_{\mathbf{k}} e^{i\mathbf{k} \cdot \mathbf{r}_1} e^{-i\mathbf{k} \cdot \mathbf{r}_2} = \sum_{\mathbf{k} > \mathbf{k}_F} g_{\mathbf{k}} e^{i\mathbf{k} \cdot (\mathbf{r}_1 - \mathbf{r}_2)} \quad (1.38)$$

multiplied by some spin component. We require the whole thing to be antisymmetric under the exchange of the two electrons. For BCS theory, we choose to write the spin part as antisymmetric, as the spin-singlet ($\uparrow\downarrow - \downarrow\uparrow$). This implies the spatial part is symmetric, requiring $g_{\mathbf{k}} = g_{-\mathbf{k}}$. To obtain unconventional superconductivity, we could instead choose to make the spin part symmetric, with one of ($\uparrow\downarrow + \downarrow\uparrow$), ($\uparrow\uparrow$) or ($\downarrow\downarrow$), and make the spatial part antisymmetric with $g_{\mathbf{k}} = -g_{-\mathbf{k}}$. This gives rise to one of the classifications of unconventional superconductivity. Spin-singlet superconductivity uses the singlet spin part, and may be conventional or unconventional, and spin triplet uses the other part and is unconventional. Note that spin triplet superconductivity does not mean that all three pairing types are present, in a ferromagnet for example the pairing is likely to be pure ($\uparrow\uparrow$) as all the spins are aligned anyway. A third option, mixed parity, is described later in this section.

The second stage where unconventional superconductivity varies from BCS theory is in the form of the attractive potential. In BCS theory, it is assumed that the potential is isotropic in \mathbf{k} and constant out to some cut-off energy $\hbar\omega$ above the Fermi energy. It is generally found that this is a good model for phonon-mediated interactions in an isotropic material, but other forms

are possible. In BCS, this choice of isotropic V results in an isotropic pair wavefunction. This is known as s -wave.

A different form of V may give a different form of pair wavefunction. In an argument broadly similar to that of the Schrödinger model of the atom, the pair wavefunction must have a continuous phase throughout, so must have quantized angular momentum. The spatial part can be written, again like the atomic eigenfunctions, in terms of the spherical harmonics. There are a variety of ways of constructing wavefunctions from these, but the parities are relevant. The $l = 0$ spherical harmonic has even parity and is isotropic, it is the conventional superconductivity case. The $l = 1$ case, known as p -wave, is antisymmetric, so occurs in spin triplet cases. Similarly d -wave is singlet, f -wave, would be triplet and so on. Note that in the $l > 0$ spherical harmonics, there is a zero at the center of the wavefunction, which implies that the electrons in the cooper pair do not overlap as much as in the s -wave case, but are still bound. Thus, these higher l solutions are more likely to be found in cases where the attractive interaction between electrons becomes repulsive again at small distances.

These changes have a variety of effects on the remainder of the BCS theory. The most notable is that the gap, Δ , becomes a function of \mathbf{k} . In a real material, the gap's symmetries are affected by both the symmetries of the lattice and the parity of the pair wavefunction. In the simple s -wave case, the gap may vary from isotropic as a result of lattice anisotropy (such as in Pb or Sn), but this is not considered unconventional and it has no nodes, which are lines or points where the gap is zero. If the pair wavefunction has a higher l , then the gap has the same parity and with it the nodes of the spherical harmonic. The p_z harmonic for example has a line node in the xy -plane, so the corresponding gap will go to zero in a line node around the Fermi surface. The gap function will often have a lower symmetry than lattice, one well known example of this is d -wave pairing in the tetragonal cuprates.

As the gap appears in many of the results derived from BCS theory, its anisotropy carries through to many observables. Critical fields will likely be different along different directions, as the gap enters the expression for the orbital limiting field through the coherence length. Direct probes of the density of states will see either varying gap or some states in the gap, depending on how they average over the Fermi surface. Good theoretical background on the modifications to BCS theory can be found in Mineev's book [12], and a brief survey of some of the methods for probing the gap symmetry are found in [13].

We now turn to possible origins of the pair interaction. As has already been mentioned, the case in conventional superconductivity is phonons. It can be thought of as an electron passing through the ionic lattice pulling the ions in slightly. As the electron moves on the heavy ions take time to return to their original position, and for a brief period the resulting area of positive charge may attract an electron. When considering a ferromagnet, one can, by analogy, see how spin fluctuations could cause an attractive potential. A mobile spin- \uparrow electron will be

screened by \downarrow spins. As it moves on, those spins can attract another spin \uparrow electron, leading to an attractive interaction and a preference for $(\uparrow\uparrow)$ order parameter. A complete approach, and one which might also be useful in antiferromagnets (where the interaction oscillates between attractive and repulsive over a distance of order the lattice parameter), would be to attempt to derive the interaction from the form of the screening potential. This will have different results in, for example, the Kondo and RKKY models, where the response of the spin field to a moving spin is different. In cases where the spin-spin interaction is not much stronger than the charge charge one, then that too should be taken into account. A good overview of the successes of this theory, along with some indicators of what conditions are required to observe superconductivity, is given by Monthoux *et al*[14]. From this explanation, one might imagine that superconductivity might be equally viable in ferromagnetic and antiferromagnetic materials, but in fact there are many more known antiferromagnetic superconductors than ferromagnetic ones. There are a few effects which contribute to this. In a tetragonal antiferromagnet, a d -wave order parameter can be arranged so that the repulsive parts of the potential are aligned with the nodes of the pair wavefunction. Singlet order, which is unlikely in ferromagnets, is generally stronger than triplet order[15]. And of course, as detailed below, ferromagnetism and superconductivity have some fundamental incompatibilities in many cases.

One can however ask what conditions will favour such spin-interaction superconductivity. In BCS theory, a softer material with more mobile ions tends to have a higher T_c . The equivalent in spin-interaction superconductivity would be a material with a high susceptibility. This is often found close to a transition into or out of the magnetic state, or equivalently in a critical ferromagnet. Combined with the usual result that superconductivity happens below some T_c , it should be obvious that this can lead to a superconducting dome on a phase diagram with a quantum critical point underneath. One particular model, that of p -wave pairing in an itinerant ferromagnet has been developed in some detail by Fay and Appel[16]. They predict two domes of superconductivity, one each side of the line where the ferromagnetic T_{Curie} goes to zero. In real materials, the transition tends to be more complicated, and the double dome is not observed.

1.4.1 Ferromagnetic superconductors

Several ferromagnets have been discovered to which the models discussed above may be applicable. The first hint of such a state was the discovery of p -wave spin triplet superconductivity in Sr_2RuO_4 [17], a layered perovskite material. Although it is not magnetic, other closely related materials are[18]. As this material has metal oxide planes like those found in the high temperature superconducting cuprates, this was taken by some as evidence for a completely different form of superconductivity from that described above, the resonating valance bond theory.

Ferromagnetic superconductors without these planes soon followed however. The first was UGe_2 , which has a T_{Curie} of 56 K which can be tuned to zero by the application of pressure. In

this case, superconductivity is seen within the ferromagnetic state, but the picture is complicated somewhat by a transition, the nature of which is not fully understood, which is driven to zero temperature by pressure at the same pressures that superconductivity is observed. Two closely related materials, URhGe and UCoGe were discovered soon after. In both of these ferromagnetism can be destroyed by the application of field, and in the latter case pressure also works. URhGe is discussed in much more detail in chapter 2.

Normally, superconductivity and ferromagnetism are considered antagonistic states, as the magnetic field produced by the ferromagnetism acts to destroy superconductivity. There are two methods by which this happens. The first is known as the paramagnetic limit. If a pair of Fermi surfaces is split into spin-up and spin-down surfaces, then for the usual spin singlet superconductivity, it is no longer possible to pair two electrons of equal but opposite momentum. One can make an estimate of the paramagnetic limiting field by comparing the energy scale of the superconductivity, Δ , with the energy shift of the spin-up and down bands, $g\mu_B H$. This limit of course only applies when one is pairing opposite spins, so to the singlet case and the $(\uparrow\downarrow + \downarrow\uparrow)$ case. If the pairing is $(\uparrow\uparrow)$ and/or $(\downarrow\downarrow)$ then the limit does not apply.

The second limit is the orbital one. The superconductor naturally attempts to expel field through the Meissner effect, but the ferromagnetism requires a field to exist. As in the conventional case, field can penetrate as an array of flux lines provided two conditions are met. Firstly, it must be possible for an isolated vortex and flux line to exist. The key test for this is comparing the penetration depth λ with the coherence length ξ , provided $\sqrt{2}\lambda > \xi$ the material is type II and vortices may exist. Secondly, it must be possible to fit sufficient vortices into the material to make up the required field. If each vortex carries flux Φ_0 then they will be separated by a distance $d \sim \sqrt{\Phi_0/B}$. The size of each vortex is given by the coherence length, and the vortex lattice can no longer be sustained once $d \approx \xi$.

This goes some distance to explaining why ferromagnetic superconductors are relatively rare. In order to be observed as a bulk property the superconducting state must be sufficiently robust to survive the field due to the magnetism. Short coherence lengths are beneficial in both of these limits. As the coherence length depends in turn on the carrier effective mass, it is perhaps not a surprise that ferromagnetic superconductivity is seen in the heavy fermions. Other, less conventional methods for avoiding these limits have also been proposed. If the superfluid is not homogeneous, magnetic flux could thread the gaps. This could arise if the unit cell is large, and the superconductivity is confined to planes (or lines) within the unit cell. It could also happen through the FFLO state, where the cooper pairs are formed with non-zero net momentum. Finally, even if the superconductivity is destroyed by orbital limiting in the bulk, it may continue to exist at surfaces or domain walls. Specific heat measurements are then the best test for bulk or non-bulk superconductivity, and neutron scattering can also help by identifying a flux lattice.

1.4.2 Flux Flow Resistance

In a ferromagnetic superconductor with vortices, the usual results from a type-II superconductor hold. When making resistance measurements, the most notable of these is flux-flow and the associated resistance. Flux flow resistance occurs when the force on the vortices due to the interaction between the field within them and the current makes them move. The manner in which this leads to dissipation is rather complex, with complete explanations involving the back emf from the moving vortices; a relaxation time in the superfluid; and an energy cost of destroying the superfluid at the leading edge of the vortex and recreating it at the other side[13, 19]. However, a simple model where the current density is the same within the vortex cores as without, and the vortex has radius given by the coherence length, yields a result that is usually found to be remarkably accurate. This is the Bardeen Stephen result:

$$\rho_{ff} = \rho_n \frac{B}{B_{c2}} \quad (1.39)$$

where ρ_{ff} and ρ_n are the resistivity in the flux-flow and normal states respectively, and B_{c2} is the orbital limiting field discussed above (which may be larger than the observed critical field, if the material is paramagnetically limited). It is noteworthy that at $B = B_{c2}$ the flux flow resistance is the same as the normal state resistance, and so resistance is not always a good indicator of superconductivity at field.

In the absence of pinning, one might expect the equation above to hold for all currents and all fields between B_{c1} and B_{c2} . Pinning is the tendency for flux lines to get stuck at certain points in the lattice, such as lattice defects. Whilst the force due to the current is small, the flux line will remain at the pinning site, and the resistance will be zero. Because the flux lines are lines, move perpendicular to their length, and have a repulsive interaction, it is not easy to move a single flux line if the others are still pinned. As a single line begins to move, it exerts a force on the pinned lines. This means that when the lines begin to move, they all do so at the same time. One might then expect resistance to show a sharp transition from zero to the value given by the equation above. In reality, this is rarely if ever seen, the dissipative process is rather more complicated, and the motion of the vortices is critical. A good review is given by [19].

In practice, it is usually observed that the voltage remains zero up to the critical current, and then rises linearly with current at the rate one would expect from the Bardeen-Stephen result. A few examples of this behaviour are shown in figure 1.4. Changing the density of pinning centres changes the critical current, but leaves the gradient unchanged. Changing the field changes the gradient, but larger fields also reduce the critical current by introducing more vortices.

These results are for conventional superconductors, so one might ask how unconventional superconductors differ. Unconventional superconductors can vary from the Bardeen-Stephen result that the resistivity goes as B/B_c , the IV curve will still be linear (with perhaps some

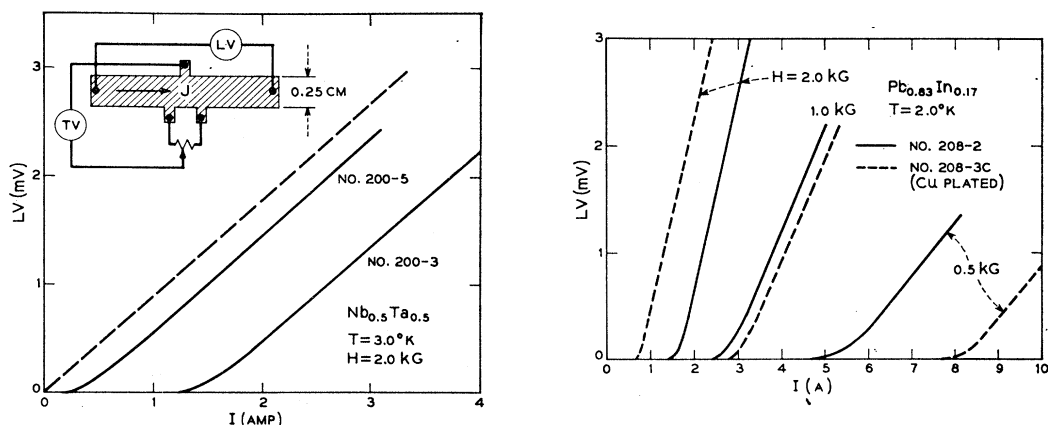


Figure 1.4: Examples of typical flux flow resistivity in conventional superconductors, reprinted with permission from [19], available at [dx.doi.org/10.1103/PhysRev.139.A1163](https://doi.org/10.1103/PhysRev.139.A1163). **Left:** Dashed line shows the Bardeen-Stephen result, solid lines show the IV curve of two samples of niobium-tantalum alloy with different RRR. The density of pinning centres changes the critical current, but both samples have the same gradient as the dashed line. **Right:** Two samples of lead-indium alloy at different fields. One is copper plated, which adds more pinning centres. As in the other panel, this changes the critical current. Here, the changing gradient with field that one expects from the Bardeen-Stephen result is also visible.

rounding as in figure 1.4), but the gradient will no longer be simply related to B . Instead, a graph of gradient against field may be convex. This has been seen in UPt_3 [20].

1.4.3 Superconductivity without inversion symmetry

Finally, it is worth mentioning a different type of unconventional superconductivity. If we refer back to the beginning of this section, we stated that we could write the pair wavefunction as the product of a spin and spatial part. This is not always true, and when it is not, the distinction between singlet and triplet disappears.

To understand how this occurs, we must first consider what various symmetries mean for the lattice and the Fermi surface. We shall consider both inversion and time reversal, as the consequences have some similarities, and the combinations of the two are interesting. The following rules are all that are required to understand the changes to the Fermi surface in both cases.

1. The inversion operator \mathcal{I} changes \mathbf{k} to $-\mathbf{k}$
2. Inversion does not change the spin
3. Time reversal \mathcal{T} also changes \mathbf{k} to $-\mathbf{k}$
4. Time reversal does flip the spin

Thus if we have both symmetries, as in a metal with an inversion center at zero field, then the combination \mathcal{IT} takes a state to the same \mathbf{k} as it started with but flips the spin. If these two states are symmetric, they have the same energy and thus the Fermi surface has a twofold spin degeneracy at all points.

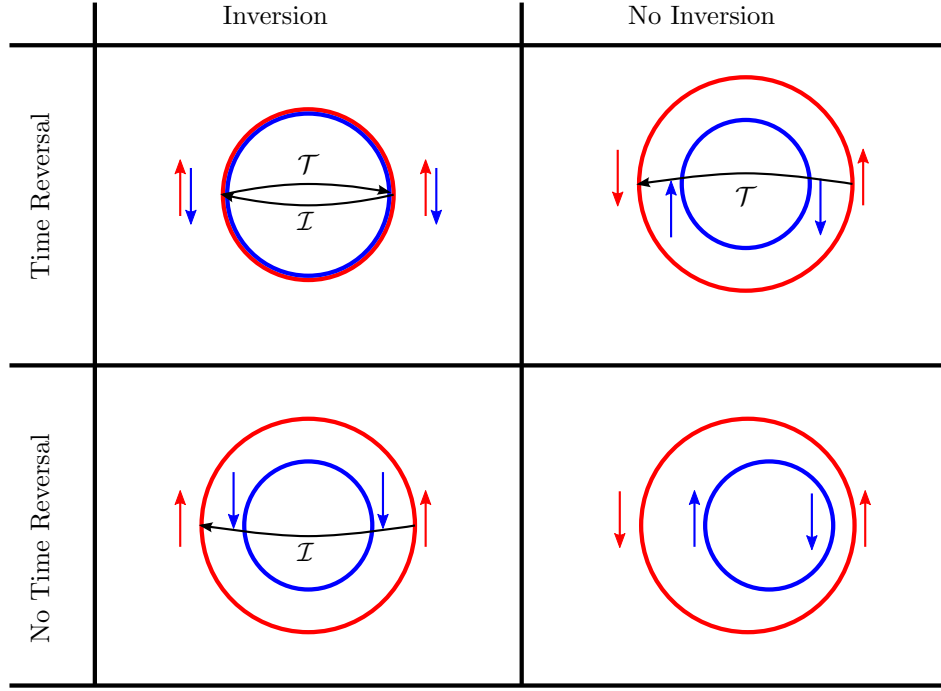


Figure 1.5: Possible distortions of the spherical Fermi surface with different symmetry constraints. With both inversion and time reversal, degeneracy is enforced. With one but not the other, there will be an surface at $-\mathbf{k}$ if there is one at \mathbf{k} , with the symmetry choosing the spin. With neither symmetry, a large variety of shapes are possible, the one drawn is what one might expect if the one above were distorted by a small magnetic field. Note that although the non-inversion surfaces are drawn split into clockwise and anticlockwise sheets, in and out and other more complicated options are also possible. Indeed in and out are perhaps more likely, given that one cannot comb a hairy ball flat.

If time reversal is lost, but inversion is kept, then this degeneracy can be broken. Inversion still requires that there be an equal-energy state at $-\mathbf{k}$, with the same spin, but there is no requirement that the opposite spins share the same energy. This is the situation in a metal with a magnetic field applied. A similar state can be obtained by keeping time reversal but breaking inversion. There is still required to be a state at $-\mathbf{k}$ with the same energy, but now it is required to have the opposite spin. The degeneracy can still be broken, but now the two Fermi surface sheets cannot be classified as spin-up and spin-down, as both spins are present.

Finally, if both symmetries are broken, such as in BiPd with field applied, the Fermi surface is free to take on much more unusual forms. Each of these four cases is sketched for a simple spherical Fermi surface in figure 1.5. To begin with, consider the case of a non-centrosymmetric material in the absence of field. This has time reversal but not inversion, so corresponds to the top right panel of the figure. Time reversal relates the spins at \mathbf{k} with those at $-\mathbf{k}$, as drawn, but does not specify how they change around the Fermi surface. Still, if the spin at one side is required to be opposite to the spin at the other, the spin must change around the surface. This connection of spin and momentum means one cannot write equation 1.38 as the product of separate spin and orbital parts. Instead, one must use a wavefunction which has spin dependent on \mathbf{k} around the Fermi surface.

At this stage it is worth noting that the loss of inversion symmetry allows, but does not require, a distortion of the Fermi surface. For the Fermi surface to split into two bands with spin varying around the surface one requires an interaction which involves both spin and momentum. The obvious choice is spin-orbit. If the energy scale of spin orbit interactions is larger than the energy scale of the gap, then the two bands are well split, and the current discussion applies. If on the other hand the spin-orbit splitting is small, then one may have inter-band pairing and an ordinary form of superconducting order. A similar argument applies to loss of time reversal — small applied fields break time reversal, but only when they become large enough does one see a significant splitting of the Fermi surface.

This is exemplified in $\text{Li}_2(\text{Pd}_{1-x}\text{Pt}_x)_3\text{B}$. Palladium and Platinum are in the same group, the Pt ion is slightly larger but this only changes the lattice parameter by less than 0.1%. The salient difference is the strength of the spin-orbit splitting. With Pd, the antisymmetric band splitting is 30 mV, with Pt it is close to 200 mV. NMR measurements show a complete gap (i.e. *s*-wave order) in $\text{Li}_2\text{Pd}_3\text{B}$, whereas the clear gap is not present in $\text{Li}_2\text{Pt}_3\text{B}$, and evidence of line nodes is seen. Penetration depth measurements also show BCS behaviour in the first case, but non-BCS behaviour in the second. Intermediate dopings show intermediate effects. A good review of this material (and many others) can be found in [21].

When either of both of inversion and time reversal are broken, one degenerate band becomes two distinct bands. Only rarely will either of these move completely above or completely below the Fermi surface, so the material will in general show multi-band physics once the degeneracy

is lifted, even if it did not before. This has various consequences for the superconductivity. The nature of multiband superconductivity varies somewhat depending on the relative interband and intraband interactions. In the absence of interband interactions, superconductivity naturally develops separately on the two bands. The two bands will be different as they are no longer degenerate. In some cases they will show very similar properties to each other, in other cases they may be more different, or superconductivity may not appear at all on one band. As interband interactions appear or strengthen, the properties of the two bands will tend to converge, though two distinct gaps will remain.[\[22\]](#)

Chapter 2

Introduction to URhGe

URhGe was first grown in the 1990s[23, 24], as part of a survey of a number of related uranium containing compounds. It crystallises in the orthorhombic structure shown in figure 2.1 and is ferromagnetic with moments partially localised at the U ions and polarised along the c -axis[25, 26]. It is unusual in that superconductivity coexists with ferromagnetism at low fields, and in that superconductivity re-enters with fields applied along the b -axis. This re-entrant superconductivity is very robust against magnetic fields, and this complex interplay between different orders is what motivates us to study it. The presence of uranium ions also adds to the interest, providing both the possibility of strong spin-orbit effects and the 5- f valence electrons which show rich heavy fermion physics.

2.1 Ferromagnetism

In the absence of applied field, magnetization measurements[26, 25] indicate a low temperature moment of $0.42 \mu_B$ per formula unit (or $\mu_0 M = 0.09$ T, ignoring domains), aligned parallel to the c -axis. The transition temperature is 9.5 K, a value which seems to be independent of sample purity, showing no discernible variation between the Czochralski grown single crystals with single digit RRRs and the quenched melts with RRRs of over 100. Neutron measurements [25] agree on the transition temperature and point to the magnetic moment being located at the uranium sites. They do give a slightly smaller magnetization, but probably still within experimental error. Magnetization measurements at low fields[27] close to and above the Curie temperature indicate the magnetism is slightly anisotropic in the bc -plane, but that the a -axis is much harder. This is borne out by low temperature measurements at higher fields, with fields along the b -axis ultimately causing the moment to align with field, but no such rotation for fields along the a axis.

As the material is metallic at low temperature (i.e. is conductive and has a resistance which usually rises with temperature), the question of localised versus itinerant electron behaviour arises. In a localised ferromagnet, the magnetization arises from electron spins fixed at individual

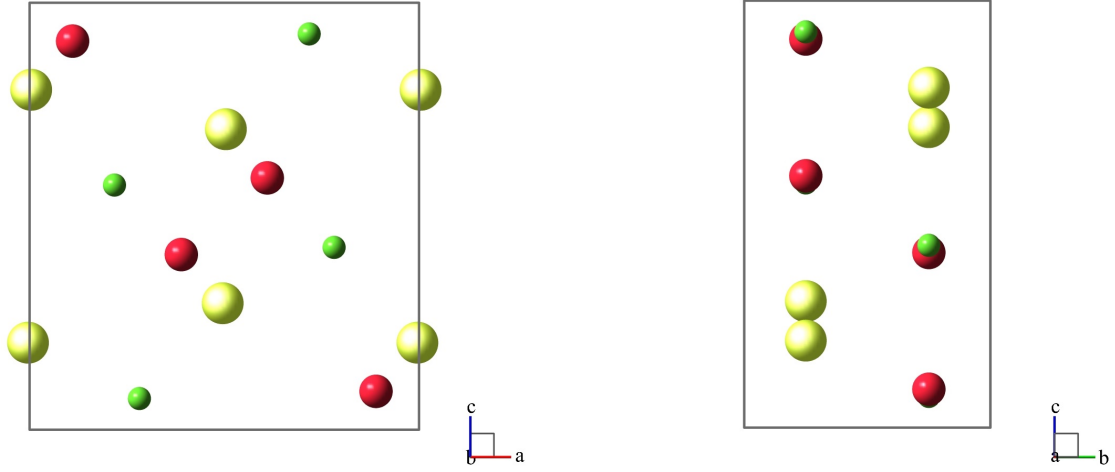


Figure 2.1: The crystal structure of URhGe, yellow is uranium, green is rhodium, red is germanium. The space group is Pnma, and the lattice parameters are $a = 682$ pm, $b = 431$ pm and $c = 748$ pm. Some refs also draw lines connecting the nearby uranium ions along the a -axis, forming zig-zag chains, to indicate the nearest neighbours, however the distance along b is not much longer.

lattice sites, and coupled by some form of interaction. They can be well described by a Heisenberg model, and this model shows such features as a Curie-Weiss susceptibility above T_{Curie} , and of course moments localised at some point in the unit cell. It does not explain how the moment can be non-integer multiples of μ_B . Nor does it explain any particularly strong interactions with the conductivity — the interaction is limited to the appearance of additional scatterers, as the conduction happens in an unrelated electron population. In an itinerant system on the other hand, the electrons contributing to the magnetism are the conduction electrons. This too is fairly well understood, and can be explained simply by the Stoner model. This is a mean field theory, where alignment of spins creates a magnetic field, which in turn aligns the spins. Provided the energy cost of moving the electrons from the spin-down band to the spin-up band is less than the energy gained by aligning the spins with field, then the lowest energy state is polarised. But one cannot easily recover the Curie-Weiss law from this theory, nor the observation that the moment is centred on the lattice sites.

In reality, the classification of itinerant or localised is a false dichotomy. Most real ferromagnetic metals show some aspects of both behaviours. One can see how this develops from a localised picture by considering the consequences of involving the electrons of the conduction band in the interactions between lattice sites, such as in RKKY. This necessarily means mixing localised moment with the conduction electrons states. The conduction states will then take on some of the moment's character. From the itinerant end of the spectrum, one might imagine that the exchange interaction would be strongest in the states which have a large part of the atomic f orbitals mixed in, which will be the ones with a large real space density near the uranium ions. Various theories have been developed to try to unify these two pictures, though a completely

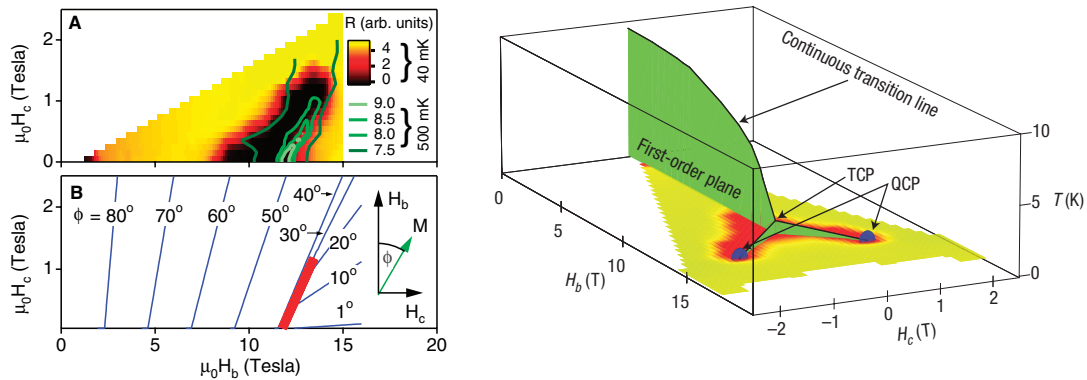


Figure 2.2: Magnetic and superconducting phase diagram of URhGe for applied fields in the bc -plane. **Top Left:** Resistance at low temperature (colour plot, black is superconducting) and at 500 mK (green contours show peak in resistance). **Bottom Left:** Magnetization deduced from neutrons and capacitive torque measurements. The thick red line represents the first order moment rotation transition. The thin blue lines mark contour of equal moment-angle, measured from the b axis. **Right:** Temperature dependence of phase diagram. Green planes mark first order transitions, the large one is the usual transition between ‘up’ and ‘down’ that one expects in any anisotropic ferromagnet, the small ones correspond to the red line in the left panel. Red areas highlight superconductivity as per the black areas in the left panel. Note that this figure was prepared before the field dependence of the continuous transition line was known in detail, it is actually somewhat flatter at low field and drops sharply down to the TCP, the exact temperature of which is not known. These diagrams are taken from papers by Lévy *et al.* Right: reprinted by permission from Macmillan Publishers Ltd: Nature Physics, 3(7):460[30], copyright (2005). Left: From Science 309(5739):1343[29]. Reprinted with permission from AAAS.

successful one is still lacking. A good overview is given by Moriya and Takahashi in [28]. That reference reffers mostly to 3- d metals, but the theories developed have also been applied to 4- and 5-, d and f metals.

URhGe shows a mixture then of itinerant and localised behaviour. In addition to the observation mentioned at the start of this section, a Curie-Weiss susceptibility has been observed above the Curie temperature[25]. The moment appears to be around $1.8 \mu_B$, rather larger than the saturated moment in the ferromagnetic state. That the Curie-Weiss susceptibility exists is evidence of some localised behaviour, but the large moment suggests that the local moments are strongly screened in the ordered state, which is in turn evidence of strong coupling to the conduction band. The quadratic dependence of the squared magnetization on temperature is also taken to indicate predominantly itinerant behaviour[25].

The magnetic structure is affected by field, the phase diagram is shown in figure 2.2. In agreement with the magnetic anisotropy inferred from low field magnetization, fields applied along the a -axis have little or no effect. Fields applied along the c -axis increase the saturation moment slightly. Fields along the b -axis provide a more interesting result, as they can trigger a moment rotation. Small fields along b reduce T_{Curie} very slightly, such that at 8 T it is reduced to about 7 K. It then drops abruptly to zero at 12 T, and at fields above this the moment is

aligned along b . At low temperatures the moment as measured by neutrons[29] increases 10% in magnitude and rotates by about 30° at 10 T, then abruptly rotates at 12 T — the rotation is very visible in both neutrons and magnetization[29]. A field of 1–2 T applied along c can stabilise the moment, and put off the rotation to $\mu_0 H_b = 15$ T. The abruptness of the rotation, combined with a large enhancement in scattering, indicates that for low temperatures, and for $\mu_0 H_c < 1$ –2 T the moment rotation transition is first order. This phase diagram is shown schematically in figure 2.2, along with some of the data which suggests the transitions are first order, and the superconductivity which we shall come to later.

This magnetic phase diagram is by no means unique to URhGe, similar forms are seen in the very similar material UGe₂[31] but also more generally in other ferromagnets[32, 33]. In fact the bifurcation is not a huge surprise, as it can be found quite easily from a Landau expansion of the free energy[29]. Recent theoretical work suggests it might even be universal to ferromagnets[34]. This magnetic phase diagram shows a variety of interesting features. Firstly where the first order planes end as temperature increases, there will be a line at which they become second order. These lines, and to a lesser extent the area around those lines, will show classical critical behaviour. At a magnetic critical line, one expects long correlation lengths, slow fluctuations, and divergent susceptibility. In quantum mechanical terms, this means the existence of soft magnetic modes, and a large population of spin waves and/or magnetic fluctuations. In URhGe, where the magnetic anisotropy is quite strong at zero field, longitudinal fluctuations will probably play a larger part than spin waves, but as the moment rotation field is approached spin waves may well enter too. At the moment rotation point, the system is critical, but can choose between three, not two, ordered states. This is known as a tricritical point, and is expected to show a modified form of critical behaviour. Different scaling laws are expected, but general arguments about fluctuations and soft modes remain. Along the top of the wings, critical behaviour is again expected, but now spin waves are perhaps more likely than longitudinal fluctuations.

When these lines reach zero temperature, a quantum critical point (QCP) is formed. Quantum criticality opens up a huge variety of possible behaviours and new states, the theoretical understanding of which is much less complete than their classical counterparts, a good review is [35]. These points do share some properties with their classical counterparts, but also many differences.

Firstly, scaling laws. Classically, one obtains:

$$\xi \propto \left| \frac{T - T_c}{T_c} \right|^{-\nu} \quad (2.1)$$

$$\tau_c \propto \xi^z \quad (2.2)$$

Where ξ is the correlation length and τ_c is the characteristic time of the fluctuations. Above the scale of the lattice, the coherence length is the only relevant length scale, and the correlation time is the only relevant time-scale. The two critical exponents are known as the correlation

length and dynamical exponents. In a classical system, the statics and dynamics decouple, and z is unrelated to ν and the other critical exponents. Their behaviour is universal; there are a few different classes, but any system with the same order parameter symmetry and dimension has the same critical exponents.

If we wish to introduce quantum mechanics, the first observation is that the fluctuations now have a characteristic energy scale:

$$\hbar\omega \propto \frac{1}{\tau_c} \propto \left| \frac{T - T_c}{T_c} \right|^{\nu z} \quad (2.3)$$

The second change is that the statics and the dynamics are no longer separable. The fluctuations now take place in a space where both are relevant, which has a dimension of $d_{eff} = d + z$. This has a substantial effect on the fluctuations. Firstly, the critical exponents are dimension-dependent, and secondly there is an upper critical dimension beyond which the fluctuations become irrelevant and a mean field theory is sufficient to describe the system. As this upper critical dimension is four, a 3D material with a quantum critical point is usually beyond it.

All this leads to a phase diagram where at one side the system is ordered. At the edge of the order is a region of classical criticality, but as one moves further away from it, quantum fluctuations dominate and a simpler mean-field model is appropriate. Adjusting the tuning parameter of the system away from the ferromagnetic state, the physics of the paramagnetic Fermi liquid state takes over from the quantum fluctuations.

If the order parameter couples to the electronic fluid, as it does in an itinerant ferromagnet, then it leads to changes in the nature of the electronic fluid. Some phenomena are observed in a wide range of quantum critical materials. Firstly, the effective mass of some or all of the carriers diverges. This is a consequence of the strong long-range interactions mediated by the fluctuations in the order parameter. Within the applicability of Fermi liquid theory, the strong interactions lead directly to a larger mass. Ultimately, the interactions lead to a breakdown of Fermi liquid theory entirely, in which case many of the well known properties of a Fermi liquid are lost, including the T^2 resistance. This is observed where the temperature energy scale $k_B T$ exceeds the quantum energy scale, which goes as $|(B - B_c)/B_c|^{\nu z}$. So this behaviour is seen in a wedge at temperatures above the quantum critical point.

Secondly, in many materials a new phase forms in a dome over the critical point. Superconductivity is a common choice, especially where the fluctuations can result in attractive interactions between electrons and this is dealt with in the next section. One way of seeing how these may occur is to observe that if they did not, then the ‘naked’ quantum critical point would have non-zero entropy. This is forbidden by the third law of thermodynamics, but if a different phase forms, then the QCP can never be reached. In URhGe the formation of a superconducting phase is observed, and a divergent effective mass has been proposed as an explanation for its robustness[30].

Deviations from the usual Fermi liquid behaviour are also observed, but both observations can be explained by other means also. It is still not clear whether or not quantum criticality plays a major role in shaping the material's physics.

2.2 Superconductivity

Superconductivity in URhGe was first observed in URhGe in 2001[25]. The cited paper presents evidence of a zero resistance state, large negative susceptibility and specific heat anomaly. Whilst in broad terms, these are what one would expect of a superconductor, all three have oddities which are repeatable insofar as measurements have been made. The resistive transition is reasonably sharp at its foot, but rolls off broadly into the normal state. Given the ferromagnetic nature of URhGe, the transition could be broadened somewhat by inhomogeneous fields due to domains. But the broadening persists at fields above the saturation field, so other explanations are also necessary, some possibilities are discussed in section 4.8. The susceptibility is diamagnetic, as one would expect, but does not reach -1 even when the demagnetization factor is taken into account. This can be explained by the ferromagnetism: the material is always in the vortex state. Finally the specific heat anomaly shows a non-zero C/T at low temperature, instead it is reduced from 160 to approximately $100 \text{ mJmol}^{-1}\text{K}^{-2}$ *. This reduction, along with the diamagnetism, is large enough to imply that the superconductivity is a bulk state, but still well short of complete. The simplest explanation would be some part of the sample remaining normal, due to inhomogeneity for example, but the complete and sharp resistive transition suggests otherwise. It is also possible that some part of the electron population does not take part in superconductivity. Aoki *et al*[25] suggest that it could be the case that the order parameter is pure $\uparrow\uparrow$ and down-spins remain unpaired. An alternative source of residual C/T comes from any order parameter with a line-node, as electrons on or close to this line may not pair. This is generally a somewhat smaller effect[25, 36], but combined with some volume fraction remaining normal due to vortices could be sufficient to explain it.

These measurements, along with detailed measurements of $T_c(B)$ for all three field directions and several different RRRs allowed Hardy and Huxley[37] to classify it as p -wave. The strong dependence of T_c on sample quality (RRR $\gtrsim 10$ is required to observe superconductivity, and T_c improves with RRR) is taken as evidence of unconventional superconductivity. This is because though one might expect scattering to always break pairs and thus reduce T_c in dirty materials, Anderson[38] showed that for non-magnetic scatterers in a conventional superconductor this is not the case. Because the interaction used in BCS theory is isotropic, the scattered electron is still in a state where it may be attracted to its partner. If however the order parameter has a

*This includes specific heat measurements below 50 mK, where they are notoriously difficult. However, even if one discards data below 100 mK and instead extrapolates the linear trend between 100 and 180 mK one obtains a residual γ not less than $60 \text{ mJmol}^{-1}\text{K}^{-2}$

phase change around the Fermi surface, the scattered electron may end up in a state where it cannot remain part of a Cooper pair. Also, the relatively large critical fields along particularly the a and b axis compared to the critical temperature are difficult to reconcile with the paramagnetic limit in opposite-spin pairing. A theoretical model for a p -wave state fits very well however, and by considering the ratios of the critical fields $B_c||a/B_c||b$ (which varies with T) and $B_c||b/B_c||c$ (which does not) the cited authors[37] infer that there is probably a line node in the bc -plane.

The next major observation[29] was that superconductivity re-enters around the magnetic tricritical point described in the previous section. The extent of this superconductivity is shown in figure 2.2, along with the magnetic phase diagram. Further measurements[30, 39] have shown that this high field pocket of superconductivity is remarkably resistant to field applied along the a axis — even up to the limit of practically available fields at 35 T. Similar arguments concerning disorder and robustness against paramagnetic limit apply to this pocket, and imply it is spin-triplet in nature. Whilst it is not proven that the two pockets share the same properties, it is usually assumed that it is the same phase re-entering. If one measures the orbital limiting field by applying a field along the a -axis, in addition to the component along the b -axis required to tune the material to the moment rotation, the orbital limiting field of the two pockets form a smooth curve. The area in between, where superconductivity is absent, is simply the area where this curve drops below the field required to tune to that point. In qualitative terms, the variation in T_c is consistent with this, being higher where the orbital limiting curve most exceeds the applied tuning field.

Two separate suggestions have been made as to why the orbital limiting field diverges in this way as the moment rotation is approached. Levy *et al*[30] suggest the mass may be diverging as the moment rotation is approached, based on arguments concerning quantum criticality. Measurements of the A coefficient of a $\rho = \rho_0 + AT^2$ fit[40] seem to support the divergent mass postulate, though measurements presented later in this thesis suggest that the T^2 fit does not fully capture the temperature dependence of the resistivity. Our paper[39] however finds no evidence for a divergent mass in Shubnikov de-Haas measurements, and suggests instead that the Fermi velocity on a vanishing pocket tends to zero. This is discussed in more detail, with further measurements, in section 4.5.2. One feature of this second model is a Lifshitz transition, where a pocket of the Fermi surface disappears (or a pocket appears, or a neck pinches off) as the minimum of a band (or a maxima or a saddle point) passes through the Fermi level. This is also discussed in more detail, along with the resistance measurements that support it, in section 4.7.

2.3 Other relevant measurements and materials

A pressure study has been completed[41]. It is found that pressure increases T_{Curie} and reduces the superconducting T_c , a result which is consistent with dilatometry[42] at the transition. This

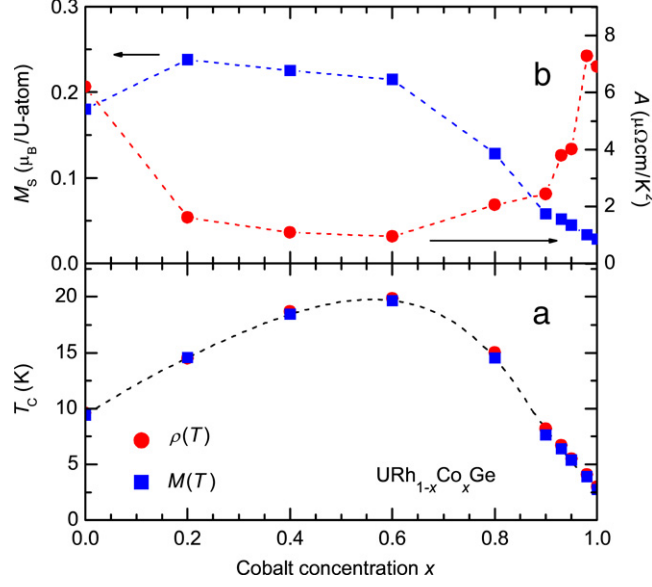


Figure 2.3: Phase diagram for cobalt-doped URhGe. T_{Curie} goes through a maximum at intermediate dopings before dropping back close to zero for UCoGe. The spontaneous magnetization follows a similar form. Also notable is that insofar as the temperature dependence of resistivity is representable as T^2 , the A coefficient is peaked at either side, pointing to increased scattering from magnetic fluctuations. Reprinted from [43] with permission from Elsevier.

provides some further evidence that the low T_{Curie} and associated magnetic fluctuations are closely tied to the superconductivity. Unfortunately however, pressure tunes the system in the wrong direction and cannot help us reach the TCP or QCPs. Whilst negative pressures cannot be achieved, uniaxial tensile strain might be a useful tuning parameter, but no such measurements have been reported, perhaps due to the difficulty in preparing large enough good quality crystals.

Chemical pressure is somewhat more practical, but doping rapidly destroys the superconductivity. By incrementally replacing Rh with Co, which is in the same group but lighter, one reduces the lattice parameters in a similar way to applying pressure. The Curie temperature initially rises to 20 K for 60% cobalt, then falls back to 3 K for UCoGe[43], where a , b and c are reduced by 0.3% 2.8% and 3.7% respectively compared to URhGe. Application of pressure to UCoGe continues the trend, pressure reduces T_{Curie} , and the superconducting T_c is peaked near the point where T_{Curie} is driven to zero[44]. Superconductivity is observed in both URhGe and UCoGe, but not in the intermediate compounds, due, presumably, to disorder but also weaker magnetic fluctuations. Taken together, these measurements are strongly suggestive of a phase diagram consisting of a dome of ferromagnetism, with smaller domes of superconductivity present at either side where T_{Curie} goes to zero.

One can go in the other direction, UIrGe is an antiferromagnet which can be made to magnetise along c with a field of about 14.2 T[45], though intermediate dopings do not seem to have been studied. Alternatively, doping with Ru to reduce the electron density, can tune T_{Curie} to zero

at zero pressure and field[46], but once again no superconductivity is observed. Another similar material is UGe_2 , unlike all the other materials mentioned in this section, it does not crystallise as $Pnma$ but rather $Cmmm$, a supergroup of $Pnma$. It has a Curie temperature of 56 K which can be suppressed to zero by pressure, near which superconductivity is observed. Application of field reveals the tricritical point and wing structures seen in URhGe . The system is slightly complicated however by a second transition (usually denoted T_x) within the ferromagnetic phase, where the total moment changes. Superconductivity is peaked where this transition goes to zero, so possibly magnetic fluctuations associated with it are more important than those associated with T_{Curie} , but otherwise much of the same physics is observed[47, 48, 31].

Chapter 3

Methods

3.1 Basic resistance measurement techniques

Most of the data presented in this document is resistance measurements. Before going into details of how these measurements were taken, it is useful to consider the nature of the problem. The constraints are:

1. The samples have resistances of less than $1\text{ m}\Omega$, typically $50\text{ }\mu\Omega$.
2. The sample contacts have resistances typically $50\text{ m}\Omega$.
3. When in a dilution fridge, the power dissipation must be kept low, preferably less than 10 nW .

Thus the power dissipation in the contact limits the current to about $300\text{ }\mu\text{A}$, and this in turn limits the voltage across the sample to 15 nV . In order to achieve a good signal-to-noise ratio, a voltage-measurement noise of substantially less than 1 nV is desired. It is also essential that the measurement rejects the contact resistance.

3.1.1 Understanding noise and interference

There are many types of noise and interference which can obscure the detail in a measurement. Here I give a brief description of the main types, and some of the basic measures which can reduce or eliminate them. In the remainder of this section I describe more specific techniques.

3.1.1.1 Noise in components

Johnson noise arises from any resistive component at non-zero temperature. It follows a Gaussian distribution, with frequency-independent amplitude up to some very high frequency far above that used in these measurements. It can be modelled as an ideal voltage source in series with the resistor with:

$$\frac{V_{rms}}{\sqrt{\Delta f}} = \sqrt{4k_B T R} \quad (3.1)$$

By simple circuit theorems and Ohm's law, it can also be modelled as an ideal current source in parallel with the resistance, with:

$$\frac{I_{rms}}{\sqrt{\Delta f}} = \sqrt{\frac{4k_B T}{R}} \quad (3.2)$$

It is clear that reducing the temperature will always reduce the noise, but the effect of changing resistance varies according to the measurement being made. If a voltage measurement is made, such as is usual with a lock-in, a low resistance is required. If a current measurement is made, such as with a SQUID-null-detector resistance bridge, a high resistance is preferred.

3.1.1.2 Noise in instruments

Most measurement equipment, such as lock-in amplifiers, have some intrinsic noise. This can come from a number of different sources including Johnson noise, shot noise (which arises from the discrete nature of electrons) *etc.* In almost all cases, it can be adequately modelled as an ideal voltage source in series with the input of the instrument, which is Gaussian and has an rms voltage given in the manual for the instrument. The effect of this noise can only be reduced by careful use of transformers or preamplifiers to increase the signal size before it is exposed to the noise.

Also relevant to the choice of instrument is common mode. Usually one wants to make a differential voltage measurement between two wires, neither of which is at the ground potential. If both of those wires differ substantially from ground in the same direction, that potential may enter into the measurement. Most instrument manuals quote a figure for Common Mode Rejection Ratio (CMRR), that is the attenuation, of the part of the common mode signal entering into the measured signal. Eliminating this source of interference requires selecting an instrument or gain stage with high CMMR, and designing the measurement circuit so that it presents a small common mode signal to the measurement instrument.

The end format of any data taken is digital. This necessitates that at some point an analogue to digital conversion must occur, and at that point the question of bit depth is important. Most instruments, including the lock-in amplifiers used and the SQUID controller use 16-bit ADCs, which provide for 65536 discrete levels. In all cases the ADC is combined with some form of variable-gain preamplifier, so in most cases if the preamplifier is set correctly, the digitisation level is less than the other noise sources in the system. If it is not, then some form of oversampling and averaging can be effective. If pre-ADC noise is much less than ADC resolution, it may be beneficial to introduce some extra noise (called dither) to make the oversampling work well.

3.1.1.3 Noise in wiring and cables

Any loop of wire, including pairs of wire running to the sample, will act as an antenna to pick up noise from the environment. By its very nature this is not white, but instead tends to consist

of specific individual frequencies or narrow bands, and in many cases the corresponding source can be identified. Usually, the strongest source is mains wiring, at 50 Hz and harmonics. Other measurements can also produce interference, particularly where wires run together in a loom inside the cryostat, and interference at many megahertz from radio and TV broadcasts is also often visible. There are three main ways to reduce this interference: to find and remove the source; proper use of cables and shielding; and measuring at a frequency where the effect is minimised.

A particular case of such interference which deserves special mention is pickup by ground loops. Where shielding is used, it is essential that all parts of the shield have a low-resistance path to ground. If they have more than one path to ground, a ground loop is created. Being of very low resistance these loops pick up substantial circulating currents, which then couple into the circuit they are supposed to shield. This is eliminated by ensuring that all shields, (including instrument chassis) have exactly one connection to ground, and that connection is low resistance.

Another case worth treating specially is interference from the measurement itself. If a pair of wires carrying the measurement current run alongside the pair carrying the voltage signal, inductive coupling will create a spurious signal in the latter. As the field produced by the current wires goes as I but the emf in the voltage wires goes as $\frac{dB}{dt}$ this is generally only a problem for A.C. signals, where it appears out-of-phase with the desired signal. Proper use of twisted pair wiring will normally solve this problem.

Closely related to coherent interference is transient interference. This enters the measurement system by the same methods, but takes the form of a brief broad spectrum pulse. Typical sources are arcing in faulty or dirty switches, inrush current when a pump motor starts, the igniters on florescent lamps and many more. The effects can be reduced by the same measures as described above, but in some cases it is still necessary to remove one or two data points after the data is taken, see Section 3.6 for details.

As well as pickup from free space, interference can enter through the mains and communications cables. Such noise is often present due to switch-mode power supplies in most modern electrical appliances, including computers. In the case of communication cables, very effective isolators are available for GPIB and USB which also help deal with ground loops, for most measurements an NI GPIB120A was used. For mains, a power conditioning transformer and/or clean ground can be used, see section 3.1.2.6.

The triboelectric effect can also introduce noise, mostly when cables are touched or moved, but also to a lesser extent due to acoustic vibrations (this is also known as microphonic noise). Overcoming this is very simple: use good quality cables and avoid disturbing them.

The thermoelectric effect is another source of noise. Where the circuit contains dissimilar materials, or even copper wire with different impurities, emfs are created. If all junctions are the same temperature, the emfs cancel out, if not they enter the measurement. As the temperatures change slowly, the voltages also change slowly, so this tends only to be a problem with D.C.

measurements. The best way to avoid this type of noise is to use the same material throughout the circuit. Long copper wires with no solder joints or other junctions are excellent for D.C. measurements, but not always practical in a dilution refrigerator. Superconductors, with their zero Seebeck coefficient, are also useful, but again are restricted in the temperature and field ranges over which they are effective. Where a mix of different materials is necessary, one may be able design the circuit to be insensitive to the emfs created, and tie junctions to each other with a strong thermal link to minimise temperature differences.

3.1.1.4 Noise in a magnetic field

As the emf produced in a wire moving through a field is proportional to the cross product of the wire velocity and the field, a loop of wire moving in a uniform field will not produce any noise. However, if the loop is not well glued down and different parts move differently, or if the field is slightly different at different points around the loop, or if the vibration rotates the loop rather than translating it then an emf will be generated. In all cases, the amplitude of the noise will scale with field (assuming inhomogeneity scales with field, which is likely). The spectrum of the noise is broad, but may have extra weight at frequencies corresponding to mechanical vibration modes in the structure supporting the loop.

This type of noise is quite recognisable, as the amplitude scales linearly with field. The most effective way of reducing it (other than buying a high-homogeneity magnet) is to minimise the area of any wire loops. Using twisted pair is very effective, but where the wires meet the sample they must spread out to reach the contacts. With most samples a solder join between the cryostat wiring and the gold sample wiring is necessary too, but even then it is usually possible to keep the loop area down to a few square millimetres.

If wires are stuck to each other in a bundle, but not to a solid object, then the current flowing in the current wires will make the bundle move, and the voltage wires will pick an emf. As the force on the wire scales with field, and the pickup also scales with field inhomogeneity, the total effect scales with the square of field, and appears in Y on a lock-in. The solution is to use twisted pair and make sure it's well glued down.

3.1.2 Building blocks of a good measurement

3.1.2.1 Four terminal measurement

This is a simple and easy way to reject contact resistance from the measurement. Instead of connecting two contacts to the sample, and using them to both pass the current and measure the voltage, one should connect four contacts and use two for current and two for voltage. An extension of this technique is to attach six or more contacts, two for current and the rest as voltage pairs. This is useful as it provides a cross check on the voltage measurement, yielding

information on sample homogeneity for example.

3.1.2.2 Lock-in amplifier

Thermoelectric voltages in the circuit are likely to be much larger than the voltage to be measured, and will vary with time. A lock-in amplifier solves this problem by making a measurement with AC; in these measurements usually a frequency between 25 and 120 Hz. A lock-in works by multiplying the amplified input signal with a reference signal which is phase-locked to the excitation current. Given the trigonometric identities:

$$\sin(A) \sin(B) = \cos(A - B) - \cos(A) \cos(B) \quad (3.3)$$

$$\sin(A) \cos(B) = \sin(A - B) + \cos(A) \sin(B) \quad (3.4)$$

it is clear that only when $A = B$ and the two signals are in phase will a DC level be generated. By passing the output through a low pass filter, a DC level proportional to the signal is produced.

Modern lock-ins have an analogue gain stage then digitise the signal and do the multiplication and filtering digitally. The models used here* also simultaneously demodulate with respect to a 90° phase-shifted reference, the in-phase component is referred to as X, the out-of-phase component as Y. The Y component does not normally contain any information about the sample (for an exception see 3.1.2.3) but can be useful in diagnosing problems with the measurement.

The noise rejection of a lock-in is quite complicated. Firstly, white noise sources will have some density near the measurement frequency, which will be down-mixed to produce low frequencies in with the DC after the demodulator. The time constant of the filter controls how much of these make it through, essentially controlling the bandwidth of the measurement. Secondly weight at frequencies away from the measurement frequency can cause problems with setting up the input amplifier. The amplifier must not clip, as that would distort the desired signal, but if the gain is too low, the desired signal will be lost in the intrinsic noise of components further down the signal chain. This gives a maximum ratio between the desired signal and the largest noise signal, analogous to a dynamic range. Finally the input amplifier has limited CMRR, typically about 100 dB and the common mode which is not rejected enters without a phase shift so is hard to identify and remove.

Provided a lock-in is configured correctly, and has a suitably high input gain, it should have an equivalent input noise of less than $10 \text{ nV} \sqrt{\text{Hz}}^{-1}$. This is a good start, but it is not good enough for the signal levels described above.

*Signal Recovery model 7265, Signal Recovery model 7230 and Stanford Research model SR830

3.1.2.3 Using a Transformer or Preamplifier

The $< 10 \text{ nV}\sqrt{\text{Hz}}^{-1}$ noise level given above is a consequence of the input amplifier used in the lock-in. This is a high-quality instrumentation amplifier, and preamplifiers will not generally do much better. They were used on a few occasions where the lock-in had to be positioned some distance from the cryostat, but a preamplifier could be placed much closer, thus avoiding long cables carrying small signals.

Transformers on the other hand can be very useful. A transformer essentially trades some of the lock-in's high input impedance for low-noise gain. Starting from the ideal transformer equation one can derive equations for the gain, and for the impedance presented at both windings:

$$G = \frac{N_s}{N_p} \quad (3.5)$$

$$Z_s = G^2 Z_{Source} \quad (3.6)$$

$$Z_p = \frac{1}{G^2} Z_{Load} \quad (3.7)$$

Though it is important to note that these equations only hold while the transformer is acting as an ideal transformer. One of the prerequisites for this is that only a very small current flows in the secondary winding, which is equivalent to saying $Z_s \ll Z_{Load}$. It is this which ultimately limits the gain which can be provided by a transformer. If this limit is exceeded, the gain starts to reduce, and the signal undergoes a frequency-dependent phase shift. As long as the gain is still greater than unity, the transformer may still be useful, but the analysis is complicated by the uncertain gain and the need to apply a rotation of the from

$$X' = X \cos(\theta) - Y \sin(\theta) \quad (3.8)$$

$$Y' = X \sin(\theta) + Y \cos(\theta) \quad (3.9)$$

to the signal detected by the lock-in. θ , like the gain, is usually unknown, but it is normally sufficient to choose it such that features which are known to be present in the resistance appear in X and not Y .

There are two places a transformer can be placed, either inside the cryostat or outside. Room temperature transformers typically have a gain of 100*. Given that most lock-ins have an input impedance of around $10 \text{ M}\Omega$ the equations above hold provided the sample and cryostat wiring present a source impedance of less than around 10Ω . In this case the noise is dominated by Johnson noise in the primary winding and (if fitted) filterbox, and should be around $0.3 \text{ nV}\sqrt{\text{Hz}}^{-1}$.

A transformer can also be placed within the cryostat. This has the advantage that the primary winding is cold, so has less Johnson noise. As the transformer is placed before any filterbox, its

*For most measurements, a Stanford Research Systems SR554, which has a $\times 100$ transformer and a $\times 5$ preamplifier/buffer (which is usually bypassed)

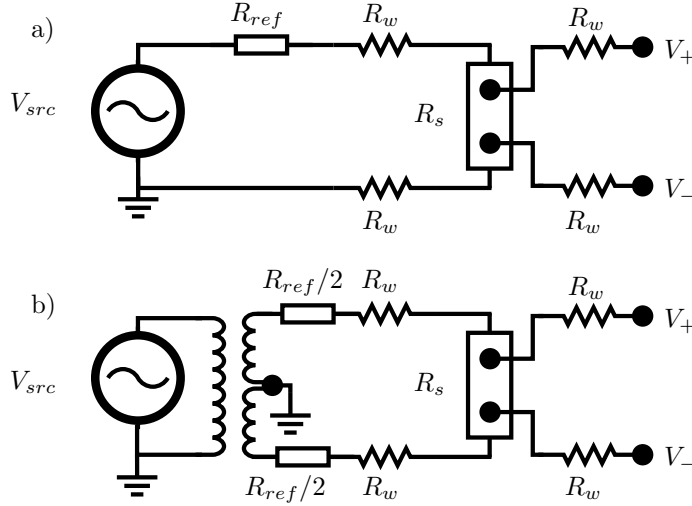


Figure 3.1: Circuit diagrams showing the use of a balancing transformer for eliminating common mode in the presence of resistive wires. **Top:** A voltage source provides a measurement current through a resistor. **Bottom:** A balancing transformer reduces common mode.

Johnson noise is applied to the amplified signal, and its impedance is not transformed. This means larger gains can be used, typically up to 300*. Under ideal circumstances, noise levels of $10 \text{ pV} \sqrt{\text{Hz}}^{-1}$ can be achieved, but at the cost of making measurement problems somewhat harder to diagnose.

Another way in which transformers are superior to preamplifiers or going directly to a lock-in amplifier is in their response to common mode signals. The SR554 transformer has a CMRR of up to 160 dB compared to the SR830 lock-in at 100 dB. The common mode signal also enters with a 90° phase shift, as it is due to capacitive coupling between the primary and secondary winding[50], which makes it easier to identify and subtract.

3.1.2.4 Balancing transformers and common mode

In addition to providing gain, transformers can be used to move or remove the ground point on an A.C. signal. To see how this is useful, consider figure 3.1a which shows a sample connected for four-point measurement using a lock-in. The lock-in output is a ground-referenced voltage source, so a resistor R_{ref} much larger than other resistances in the circuit is used to regulate the current. In this case, the wires leading to the sample have a substantial resistance R_w , such that $R_{ref} \gg R_w \gg R_s$. From this we state that the current in the circuit $I = V_{src} R_{ref}$ and the voltage at the terminals is:

$$V_+ = IR_w + IR_s \quad (3.10)$$

$$V_- = IR_w \quad (3.11)$$

*The CMR LTT-m model was used, which has selectable gain of 30, 100, 300 or 1000

This has a common mode component $V_{CM} = IR_w$, and a differential component $V_s = IR_s$. Given typical values for a URhGe sample on manganin wires of $R_w = 200\ \Omega$ and $R_s = 20\ \mu\Omega$ the common mode component is 10^7 or 140 dB larger than the signal. This is rather larger than the CMRR for a lock-in, and, depending on frequency, uncomfortably close to the CMRR of a room temperature transformer.

Consider the circuit in figure 3.1b). A 2:1+1 transformer is added, and R_{ref} is split between the two outputs. Where in circuit a) the current wires carried a signal consisting of a ground and a signal, known as an unbalanced signal, the wires here carry a signal which is symmetric about ground, or balanced. As the remainder of the circuit is also symmetrical, the voltages presented at the terminals are $V_+ = IR_s/2$ and $V_- = IR_s/2$, and the common mode signal is zero.

In a real circuit, the resistance $R_{ref} + R_w$ on the I^+ and the corresponding one on I^- may not be identical. If they vary by 0.1 %, the common mode is reduced by a factor of 60dB compared to circuit a). This brings the common mode signal within the CMRR of most measurement instruments. For the measurements presented here, Sowter Type 8920 audio transformers with 1:1+1 winding were used where necessary.

3.1.2.5 Cables for small signals

Good cables form an important part of any measurement. For large signals, the common 50 Ω BNC cables are adequate, but for very small signals, something better is required. The best design of cable for small DC or audio frequency AC is shielded twisted pair (STP). The signal is carried on a pair of identical wires which are twisted around each other and enclosed in a braided or foil shield, which is held at ground potential.

The purpose of the twisting is mostly to reduce pickup of interference from the environment. Assuming the two wires are essentially joined together at the end (by a low resistance sample for example) they form a loop. The area of the loop dictates the level of interference picked up, and a twisted pair presents only very small loop area, and what there is faces opposite directions with every twist, so the induced voltages mostly cancel out. This is of course most effective when the twist length is short compared to the distance over which the interfering fields vary, so for low frequencies. Using two identical wires twisted together, as opposed to coax, helps keep balanced signals correctly balanced too.

By virtue of being a hollow conductor, the shield is very effective at blocking high frequencies where skin depth is comparable to or less than the thickness of the shield. To be effective though, very complete coverage is needed, many commercially available STP cables have only 65 % coverage, 95 % or more is much better. The shield also acts to prevent capacitive coupling from nearby objects into the wires. To do this it needs to be connected to ground by a very low resistance path.

There are two more requirements for wiring which is to be used outside the cryostat. First,

it must be non-microphonic. This is achieved by using combinations of materials with low triboelectric effect, and by constructing the cable to avoid internal friction. Second, it must be flexible and durable. In particular, this normally means multi-strand conductors and a braided rather than foil shield. XKE classic made by Van Damme was used for most measurements, along with LEMO B series two-pin connectors. Where I needed a higher density of connector or cable was needed, Klotz Multicore PolyFLEX (which contains 12 separately shielded twisted pairs) and Fischer 24-pin connectors were used.

Within the cryostat, the shield can often be dispensed with, as the cryostat itself is more than adequate. In this case enamelled wire, usually in diameters between 50 and 150 μm was used. This was twisted to about 5 twists per millimetre, and often several such pairs are stuck together with GE varnish* to make a loom. The material used for the wires varies depending on the purpose and where in the cryostat they are to go, and may be Manganin, copper, or NbTi.

For particularly sensitive measurements, such as with a SQUID, a shield is still needed within the cryostat. Superconducting niobium capillary is the best shield, but for areas where that is not possible copper and CuNi were used, see section 3.4.4.

3.1.2.6 Using a clean ground and isolating transformer

In theory a wall socket has neutral and earth pins at ground potential, and a 230 V sine on the live pin. In practice any or all pins may carry other frequencies picked up from a wide variety of sources, mostly the same as those interfering directly with the measurement. In addition, in many cases neutral and earth are joined where the supply enters the building, so as large currents flow in neutral, the ground voltage moves away from true ground.

Of these, the most problematic is noise of the ground pin. It travels via instrument chassis onto the shields and the cryostat and from there into the sensitive measurements, particularly SQUID-based measurements. An isolation transformer is needed to provide clean power. The primary is connected to the supply live and neutral, the case is connected to supply ground. The secondary provides clean live and neutral, and clean ground is provided by a dedicated grounding rod. For measurements made in St Andrews, an AGT 450 Constant Voltage Transformer was used, which has the added advantage of stabilizing the line voltage and reducing harmonic content.

This scheme of course can be compromised to some extent by connecting ‘dirty’ instruments or appliances to the clean supply. The experiment control computer was left on the building (henceforth referred to as dirty) power supply and used a GPIB optical isolator to connect it to the instruments. Once this system is set up it is important not to connect the clean ground to the dirty ground. As the paths to ground are separate, and the dirty ground may be carrying currents from other users, the potential of the grounds can differ. Connecting them would allow a ground current to flow, which would almost certainly interfere with the measurement.

*Also known as IMI 7031, GE 7031 or VGE 7031

3.1.3 Typical measurements

From the building blocks described above, there are several circuits which were used regularly. Their advantages and disadvantages are summarised in table [3.1](#), which also contains numbers for the associated figures.

Fig.	Description	Typ. Noise	Advantages	Disadvantages	Comments
3.2	Direct lock-in	$6 \text{ nV}/\sqrt{\text{Hz}}$	Simple, easy to debug, decent CMRR.	Poor noise	Used where noise is not a big problem: for quick test measurements, large resistances and/or where large currents can be used.
3.3	Transformer outside cryostat	$0.3 \text{ nV}/\sqrt{\text{Hz}}$	Simple to debug as transformer is outside cryostat. Very good CMRR.	Noise still not great, needs low source resistance including cryostat wires and filterbox for best results.	Generally used when a LTT is not available.
3.3	Transformer and preamplifier	$1 \text{ nV}/\sqrt{\text{Hz}}$	As above.	As above.	Essentially the same as above, but used at the LNCMI where the lock-ins must be placed about 6m from the cryostat. The preamplifier avoids sending small signals over that distance.
3.4	Several samples share current	$0.5 \text{ nV}/\sqrt{\text{Hz}}$	As above, and uses less wires per sample	As above, but also one failed sample may prevent measuring the others	Used where the experiment is only really worthwhile if all samples are measured (such as in section 4.2) and there is a shortage of suitable wires in the cryostat.
3.5	Transformer placed at low temperature	$50 \text{ pV}/\sqrt{\text{Hz}}$	Best possible noise for a lock-in measurement.	Hard to debug failures within the cryostat. LTT not always available, if the field is too strong for example.	This is the circuit used for most of the measurements made.

Table 3.1: Comparison of the measurement circuits used for most of the measurements.

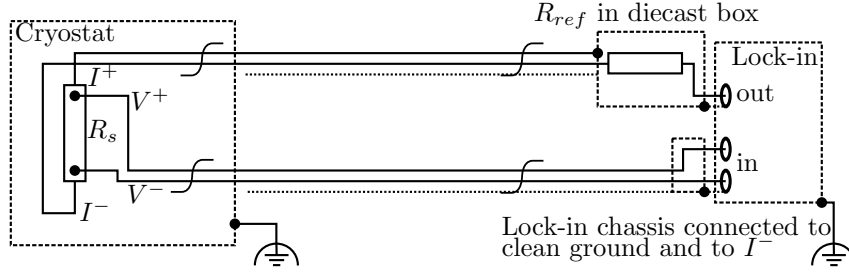


Figure 3.2: Simple measurement circuit, for an explanation of symbols see appendix A.2. This is just about the simplest circuit possible for measuring resistance with a lock-in, if the cryostat is a dilution refrigerator one should add filters just outside the cryostat as described in section 3.2.2. A typical value of R_{ref} would be $10\text{ K}\Omega$, which, combined with a output voltage of 1 V yields a $100\text{ }\mu\text{A}$ measurement current

3.2 Low temperatures and high fields

3.2.1 Wiring for very low temperatures

There are no special requirements for wiring at temperatures $> 1\text{ K}$ or so, it is sufficient to use reasonably thin copper wire. In the millikelvin regime however the cooling powers available are much smaller, so copper wire is unsuitable. Assuming the Wiedemann-Franz law, and a constant residual resistance, the heat flow \dot{Q} is given by:

$$\dot{Q} = \frac{A\sigma}{L} \times 2.44 \times 10^{-8} \times \frac{1}{2}(T_1^2 - T_2^2) \quad (3.12)$$

where A is the cross sectional area, L is the length, σ is the low temperature electrical conductivity and T_1 and T_2 are the temperatures joined by the wire. A 1 m length of $100\text{ }\mu\text{m}$ copper wire between 1 K and 50 mK would introduce a heat load of about $4\text{ }\mu\text{W}$, which is obviously unacceptably large. Even if it is fully heatsunk at every intermediate plate, it still introduces 29 nW per wire - acceptable for one or two wires, but not for a large number.

Note that in equation 3.12 the inverse of the $\frac{A\sigma}{L}$ term is the resistance of the wire. For any metal wire, the heat load depends directly on the resistance (which is about $7\text{ m}\Omega$ in the above case), so using a resistive wire with a higher resistance reduces the heat load. A manganin wire with resistance $100\text{ }\Omega$ introduces less than 2 pW , which is not a problem.

Such resistive wires do present a problem with some measurements, particularly transformers as described in 3.1.2.3. Transformers need a low source impedance to function correctly at high gain. Passing large measurement currents through resistive wire can also cause unacceptable heating. The only way to escape the relationship between electrical resistance and thermal conductivity is to use a material which does not obey the Wiedemann-Franz law. A superconductor is an ideal choice: zero electrical resistivity and very low thermal conductivity. There are several problems with superconducting wire however: it only works at low temperature and it only works at reasonably low ($< 15\text{ T}$) fields.

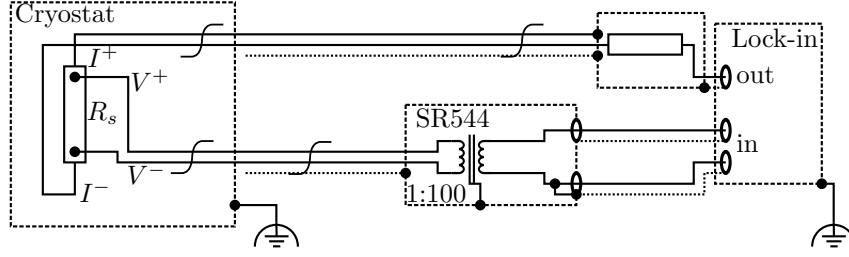


Figure 3.3: Measurement circuit using a transformer for gain. Variations on this circuit are to use a pre-amplifier to increase the signal size after the transformer if the lock-in is a more than a meter or two away. If the cryostat wires are resistive, using a balancing transformer on the current wires as per section 3.1 helps to reduce common mode. Note the grounding arrangements on both the primary and secondary and associated shields.

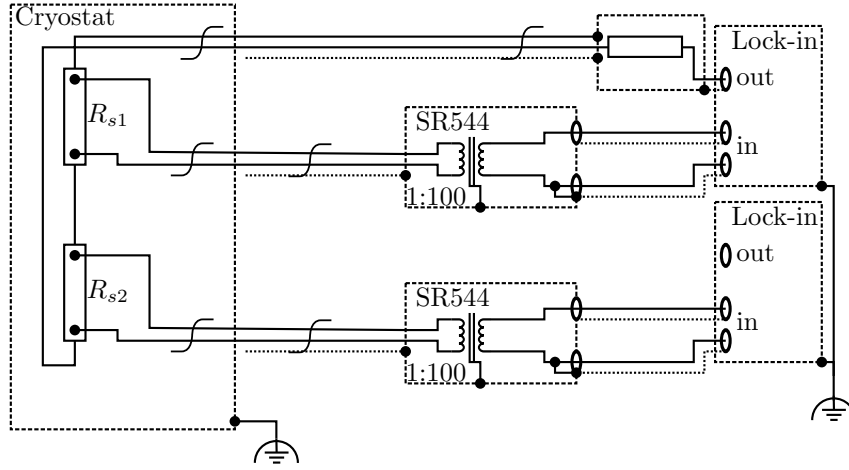


Figure 3.4: Measurement circuit for measuring several samples at once when there are not enough wires for separate measurements. The top lock-in drives the current and provides a phase reference for the other lock-ins to use, one is drawn but more are possible. As is the case with a single measurement, a balancing transformer can reduce noise.

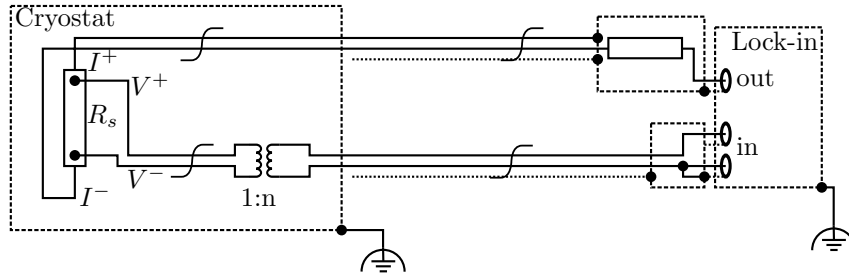


Figure 3.5: The best AC measurements made for this thesis use a transformer within the cryostat. The transformer is usually mounted on the 1K plate in a dilution refrigerator. Note the grounding arrangement on the transformer secondary, this is necessary to avoid sudden steps in signal as static builds up and discharges.

3.2.2 Filtering

Another problem that can arise with very low temperatures and low cooling powers is heating of samples and thermometers by noise. Wiring outside the cryostat picks up high frequencies. The high frequency voltages result in power being dissipated in the resistive samples and thermometers on the end of the wires. The way to prevent this is the inclusion of passive filters in the wires close to the top of the cryostat. In order to be effective at cutting out very and ultra high frequencies, feed-through capacitors mounted on aluminium plates inside a diecast box were used. The feedthrough capacitors have very low series resistance and inductance, which essentially makes them good capacitors up to high frequencies. The aluminium plates prevent the high frequencies from coupling past the filters. In addition to capacitors, either inductors or resistors are necessary, and inductors are usually the better choice as they yield a faster roll-off for the same number of components; have less Johnson noise; and present a lower source impedance to room temperature transformers. One exception to this is when the filterbox is to be used with a Keithley model 6221 current source which cannot reliably drive inductive loads, it leads to oscillation in the output circuits and lots of high-frequency noise. When a filterbox was used with a 6221, it was of an RC design with extra poles to make up the poorer roll-off.

3.2.3 Cryostat used for measurement

3.2.3.1 Dipper

The simplest cryostat is the dipper. The dipper is a length of 11mm diameter steel tube, which fits into the neck of a helium transport dewar. At the bottom end is a sample plate to which samples can be glued, the top end is sealed with epoxy. There are 6 pairs of copper wire terminated with solder pads at the bottom and BNC connectors in a diecast box at the top. There is no thermometry, and no magnet.

The dipper is useful for rapidly measuring RRRs, for materials which reach their residual resistance at reasonably high temperatures. This ratio provides a good measure of the quality of most samples, and is useful for deciding which samples to do further measurements on. It is also good for measuring the low-temperature resistance of metals to estimate their thermal conductivity.

3.2.3.2 Resistivity Rig

The simplest controllable cryostat is the resistivity rig. The resistivity rig is a continuous flow cryostat which draws helium directly from a transport dewar using a transfer tube, and pumps it through the cryostat with a diaphragm pump. The cold gas flows up the cryostat through an annular space, with the sample space inside the annulus. The sample space is filled with low-pressure helium to act as an exchange gas.

The impedance is fixed, and some limited temperature control can be achieved with a valve on the pumping line which can regulate the helium flow between zero and $2 L_L/\text{Hr}$. The sample is mounted on a copper plate along with a diode thermometer and a heater, which is controlled by a PID controller. The resistivity rig as designed has a temperature range of about 3-300 K.

3.2.3.3 Kraken

Kraken is a cryogen-free system built by Cryogenic Ltd and installed in Edinburgh. It uses a pulse-tube cooler to cool a 9T NbTi magnet and to condense helium from a room-temperature storage vessel. The condensed helium provides cooling to a 50mm variable temperature insert (VTI) via an needle valve and heat exchanger, with the sample exposed directly to the cold gas. The top of the VTI is equipped with an airlock, allowing samples to be changed without warming the whole cryostat. The minimum achievable temperature is 1.8 K, but for reliable, continuous running, 2.5 K is the practical minimum and the maximum is around 300 K.

There are several different probes which will fit the system, for my measurements I usually used a simple one provided by Cryogenic and designed for resistance measurement. I first mount my sample on a 'puck' which is a small circle of PCB material with 6 gold-plated contacts on top and 6 pins extending from the back. The probe has space for two such pucks, 1 horizontal and one vertical, along with a thermometer and heater. All 12 puck-pins are connected to copper twisted pair leading up to room temperature. The whole assembly is covered by an anodized aluminium shield which is intended to help keep everything at the same temperature.

As the gas flows directly over the sample and the thermometer is some distance away next to the heater, establishing good temperature control can be problematic. The best way is to use the heater at the base of the VTI to heat the stream of helium gas to about 0.5 K below the desired temperature and make up the difference with the probe heater. It is still necessary to ramp temperature slowly to keep the sample at equilibrium with the probe.

3.2.3.4 Green Fridge

The green fridge is a conventional wet system made by Cryogenic and installed in St Andrews. It has a 75 mm, 9/11 T NbTi magnet. The insert that was made in St Andrews, it consists of a pot which is filled from the main helium reservoir via a needle valve and pumped by a $12 \text{ m}^3/\text{Hr}$ rotary pump. With this arrangement the base temperature is about 1.4 K. The variable temperature plate is stood off from this plate with glass fibre rods, so it can be heated smoothly above the temperature of the pot plate. This is necessary as it is difficult to heat a helium pot smoothly through 4 K due to the latent heat of the helium in the pot. The maximum temperature on this system is limited by concerns over radiative heat transfer to the IVC walls to about 150 K. At 150 K the heater runs at about 5 W and boiloff in the main reservoir is substantially increased.

The magnet was not used for most of the measurements in this cryostat, so in these cases the

sample was mounted directly on the variable temperature plate (in vacuum). For the occasional measurement using the magnet, the sample was mounted on a brass plate in the field centre, connected to the variable temperature plate by a copper rod. Wiring is copper, with 18 twisted pairs in place.

3.2.3.5 Blue Fridge

The blue fridge is the cryostat that was used for most of the measurements. It is an Oxford Instruments Kelvinox 400 wet dilution refrigerator with 15 T superconducting magnet. The field centre is 400 mm below the mixing chamber and is in vacuum.

The magnet is a 15 T NbSn design with compensation coil which reduces the field at the refrigerator mixing chamber to below 0.1 T when at full field. The magnet also has a lambda point refrigerator, which allows fields of 17 T. The magnet is large and has a high heat capacity, so the lambda fridge takes 3 hours to cool the magnet, and consumes helium rapidly. This ultimately limits time above 15 T to about 12 hours.

Within the magnet is a set of 4 coils which can be used to generate an arbitrary combination of field and gradient up to 20 mT and 1 T/m both of which can be modulated at frequencies of up to 100 Hz (though frequencies over about 5 Hz cause unacceptable eddy current heating of the dilution fridge). To separately control the modulation and gradient fields, two power supplies are needed, suitable for AC and DC operation up to 8 amps, Labworks model pa-138 power amplifiers were used.

The fridge provides a little over 400 μ W at 100 mK, dropping to zero at a base temperature of about 14 mK with wiring installed but no measurements running. For operation below 300 mK it uses a roots booster to increase the circulation of helium-3 above that which the 3-stage rotary pump can achieve. This can cause some problems as the large induction motor on the roots booster causes a lot of EM interference when it starts, as well as a sudden change in cooling power which causes a temperature excursion. For many measurements this was avoided by running it continuously, including at higher temperatures.

The fridge has three line-of-sight ports of 37 mm diameter which allow access for services from room temperature. None of these in the centre of the fridge though, so there is no line-of-sight access to the field centre. There are also a couple of small diameter ports used for wiring.

The fridge was supplied with 12 pairs of Cu/NbTi wiring, and an additional 24 pairs of resistive (mostly Manganin) wires had been installed. Special shielded wires for the SQUID bridge system, which are described in section 3.4.4, were added. The resistive wires use Manganin or Constantan all the way from room temperature to the mixing chamber, and limit their heat load by virtue of having a resistance of about 150 Ω each. The Cu/NbTi wires are copper from room temperature to the 1K plate, where heat loads are not a big problem, then phosphor bronze-coated NbTi from there to the mixing chamber. New connectors were fitted to all the wires to facilitate easy

changes of probe and samples* The fridge also has 4 stainless steel and 4 superconducting coaxes, but these were not used.

Four pairs of Cu/NbTi wire are broken at the 1K plate to include low-temperature transformers as described section 3.1.2.3. These are covered by lead shields, which protect against the stray field which was measured to be 30 mT.

Below the mixing chamber the sample space has a diameter within the radiation shield of 50 mm, or without radiation shield of 66 mm, and the field centre is 400 mm below the mixing chamber plate. As the sample is in vacuum, the only way for heat created by the measurement to leave is by conduction, the problem of effectively thermalising the sample platform is described in section 3.3.2.

3.2.3.6 M9 at CNRS Grenoble

Some measurements were also made at the Laboratoire National des Champs Magnétiques Intenses (LNCMI) in Grenoble. The LNCMI is a facility with several resistive magnets which it makes available to researchers from across Europe. The magnet used was M9, which is of a copper, water cooled, 24 MW design. The maximum field varied between experiments, but was 32–34 T.

The strong field and lack of compensation coils means that superconducting wires are impractical, so the probe is wired with 12 pairs of Manganin wires, each with a resistance of about $40\,\Omega$. The high field and limited space in the top-loading probe also precludes the use of low temperature transformers. Room temperature transformers were used, placed inside a mu-metal can to shield them.

The refrigerator is a Kelvinox 400TLM, which provides about $350\,\mu\text{W}$ at 100 mK and has a base temperature of 12 mK indicated (though the thermometry is only accurately calibrated to 50 mK). This design has the sample immersed in mixture, so cooling is somewhat easier, but the bore is also much smaller. A Swedish rotator provided by the LNCMI was used, it allowed rotation of about 100° but had a sample space of only $9 \times 8 \times 7\text{ mm}$.

3.2.4 Thermometry

For most of the cryostats listed, calibrated resistance thermometers from Lakeshore Cryotronics Inc were used. For temperatures above $\sim 1\text{ K}$ Cernox thermometers were used, as thermal conductivities are quite high at these temperatures, it is workable to just keep these sensors outside the magnetic field. At the LNCMI the thermometers provided by the lab were used, which did not have magnetoresistance calibrations. For the blue fridge, field calibrated ROX

*LEMO 14-pin contact blocks, part numbers FGG.1B.314.ZLA and EGG.1B.314.ZLL for male and female respectively. Using the contact block but not the rest of the connector provides a high density and avoids large metallic parts. The disadvantage is that it is quite easy to break wires at the back of the block when mating them, to prevent this they were encapsulated in Stycast 2850

thermometers were made.

The blue fridge has a Lakeshore ROX-102B calibrated thermometer on the mixing chamber. Whilst it can be relied upon to give an accurate temperature for the mixing chamber, the reduced thermal conduction of all metals and high boundary resistances of joints below about 100 mK, mean the samples can be somewhat hotter. A ROX thermometer placed near the sample will be in the magnetic field, and ROX chips tend to have significant magnetoresistance, so it was necessary to calibrate some thermometers in magnetic field.

The raw materials were some ROX-102B from Lakeshore and some commercial 1 K Ω ROX resistors. The Lakeshore chips were provided glued onto copper bobbins, but there is not enough space in the field centre for them, they were moved to smaller copper bobbins made in house. The bobbins have space for the chip at the top, then a few millimetres of copper which the thermometer leads wrap around to help thermalise them. There is also a lid to reduce radiative heat transfer and protect the chip from anything which might introduce mechanical stresses. The bobbins were gold plated with an electrodeless solution to improve thermal contact with the sample plates.

There are essentially two options for securing the chip to the bobbin: glue it with stycast 2850, or leave it free and held in place by its wires. The former will give better thermalisation, the latter reduces the risk of the resistance changing with thermal cycling. Several of each type were prepared, and the stycasted ones found to have no noticeable drift and be better thermalised at low temperature and high field.

Before calibrating the thermometers they were cycled many times from < 10 K to room temperature. This cycling is necessary to relax any internal stresses in the chip which build up as a result of differential thermal expansion. It was achieved using a platform stood off from the blue fridge 4K plate, which was cycled at about 1 hr^{-1} for several weeks after which additional cycling did not change the resistance at 10 K.

For calibration a U shaped probe attached to the mixing chamber plate was used. This has one leg made of copper and the other copper up to just below the mixing chamber but with a thin plastic spacer. A thermometer is mounted just below the plastic spacer, within the field-compensated region around the mixing chamber. For heat to flow out of the probe at low temperature, it must go through the copper leg. Heat enters the probe by eddy current heating, and a small amount through the temperature measurement, both near the bottom of the U shape. As the end of the U with the plastic spacer is a thermal dead end, very little heat flows along it, and it quickly thermalises to the bottom of the U. Thus by waiting for the thermometer on this leg to stop drifting, one can be fairly sure the whole assembly, including thermometers, is at the mixing chamber temperature.

A calibration function was constructed from these measurements, which is believed to be accurate to 2 % or 2 mK, whichever is smaller, across the full range of field and temperature

accessible by the fridge.

3.3 Sample rotation

For measuring quantum oscillations, it is very useful to be able to rotate the sample between measurements. A low temperature sample rotator was built to achieve this. The literature has a number of different designs for rotators[51, 52, 53, 54, 55], each with their own advantages and disadvantages; the design built is a relatively simple one driven by a drive shaft that comes out of the cryostat.

3.3.1 Design

The first decision is the source of motive power for the rotator. This can be generated outside the cryostat; in the field compensated region; or in the field centre. The only type of motor commercially available that can run in a high magnetic field is a stick-slip piezoelectric one, Attocube make a variety of such motors and some research groups have also made their own[56]. The problem with these motors is the reliance on friction, which means they generate a lot of heat when operating. They were also found to have very limited torque and poor reliability. If the motor is placed in the compensated region, conventional magnetic motors can be used, either as-is or re-wound with superconducting wire. Due to space constraints in the blue fridge, any such motor would have to go above the mixing chamber in the bottom of one of the line-of-sight ports. As the fridge is well-provided with line-of-sight ports, it made sense to instead put the motor on the top of such a port at room temperature where maintenance is easy and heat dissipation irrelevant.

Putting the motor outside the cryostat means finding a way to transmit the motion to the field centre. The options were either a drive shaft, or some form of drive belt after the form of Palm and Murphy[53]. The drive shaft and gears were chosen as being less susceptible to thermal contraction, and not susceptible to slipping. As the line of sight port is not in-line with the magnet bore, it was necessary to move the line of the drive shaft across at the mixing chamber. Spur gears are easy to make with small teeth so this type of gear runs smoothly with little backlash, so a simple two-gear arrangement was used.

At the field centre the vertical drive shaft has to drive the horizontal rotation of the sample platform. The commonest solution is the Swedish rotator design, which uses a spiral plate on the end of the drive shaft to turn a large spur gear on the platform. The problem with this, and with a worm gear, is that it is designed with sliding surfaces, so will generate a fair amount of heat. Bevel gears on the other hand have entirely rolling contact, so produce much less heat. The disadvantage of bevel gears is that it is difficult to cut small teeth with the correct form, so gears with a mod of 1 and less are hard to source. A 4:1 bevel gear set made from phosphor bronze by

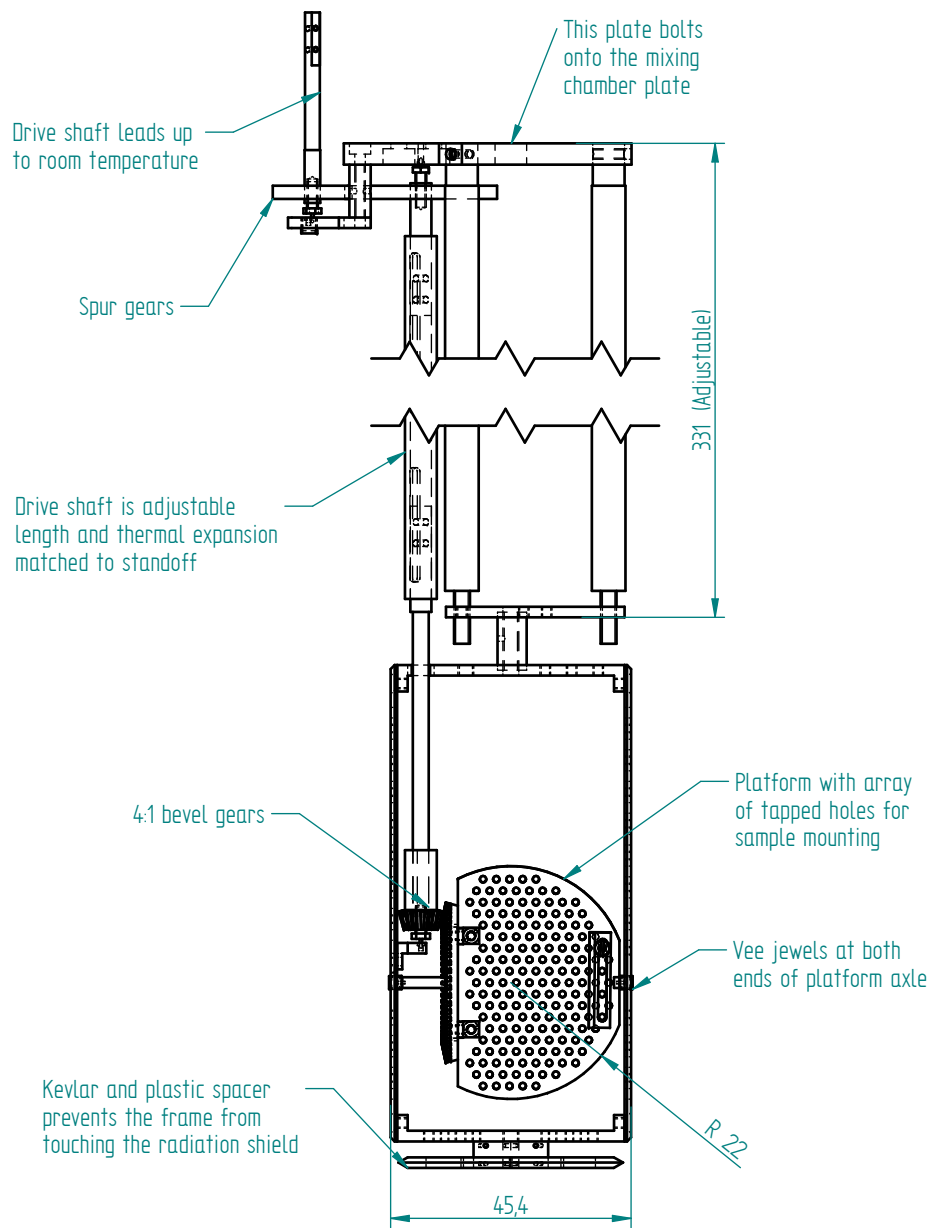


Figure 3.6: Simplified sketch of the rotator design

HPC Gears Ltd was used, milled down to reduce the heat capacity.

A sketch of the design in in figure 3.6.

3.3.2 Materials and construction

The drive shaft has the same limitations with regard to heat load as the wiring described in section 3.2.1. Thin-walled stainless steel tube was used to make the drive shaft, broken by short lengths of G10 (a type of glass-fibre reinforced resin) at low temperature to keep heat flow low. Short lengths of silver wire join the drive shaft to the refrigerator plates to intercept as much of the heat load as possible. The end result was that fitting the drive shaft made no detectable difference to the base temperature of the refrigerator.

For the feed-through at the top-plate of the fridge, a very low leak rate even whilst rotating is necessary as the fridge usually stays cold for a several months with the rotator being run regularly. This was achieved with a magnetic coupled feedthrough consisting of a steel “top hat” shape, the brim of which forms a KF40 vacuum seal. Within the top hat is a brass drive shaft, with magnets around its circumference, and outside the top hat is a brass carrier with more magnets which is driven by the motor.

One key aspect of the design that is essential for precise running is adjustability. No part will ever be made exactly as drawn, rather it will be within some tolerance of what was intended. Most of the rotator is not really a precision device, the frame and standoff need only be accurate to a millimetre or so, but the gears are rather more important. The problem varies slightly between spur and bevel gears, but in essence if the gears are too close they will run rough and jump, if they are too far apart there will be backlash. For the spur gears, one axis of adjustment is enough – the distance between rotation centres. Bevel gears are more complicated, and four axes of adjustment are allowed for: both gears can move along their axes of rotation; and the wheel* can be rotated about either axis perpendicular to the rotation axis using shims. Correct setting of all these adjustments is necessary to gain a backlash of less than 0.2° . Whilst less essential the standoff can also be adjusted, to get the exact length to the field centre correct and to keep it from touching the radiation shield, from which it has only 0.75 mm clearance. In practice, preventing contact by adjusting it is awkward and not all that reliable, so a spacer which will hold the rotator away from the wall was also built. This uses a web of kevlar thread to support a tufset triangle, providing mechanical stiffness with a very low heat flow.

Having chosen a design with minimal friction in the drive mechanism, it makes sense to also minimise the friction in the bearings, and for this two types of jewel bearings were used. For the platform itself, which rotates about a horizontal axis with minimal thrust load V-jewels and non-magnetic steel pivots were used. For the vertical sections of the drive shaft olive ring jewels

*With bevel gears, the large gear is known as the wheel and the small one as the pinion. In most cases the pinion drives the wheel.

to constrain the bearing radially and flat end-stones to take any thrust load were used.

The rotator platform and frame are made from Phosphor Bronze, as a compromise of strength, stiffness, low electrical conductivity (to avoid eddy current heating), no superconductivity (which would damage thermal conductivity) and good machineability. In theory the lack of magnetic solutes also avoids magnetocaloric effects, but in practice the material used may contain more solutes than desired. The standoff between the mixing chamber and the rotator frame initially used 316LN steel, which should be free of magnetism[51], but this was found to have a large increase in specific heat at low temperatures, so was replaced with OFHC copper.

A major challenge was thermalising the platform to keep it cold even in the presence of heat from measurements and eddy currents as the magnetic field changes. At 200 mK this is easy enough, using a few strands of silver or copper wire, but as the thermal conductivity of a metal scales with T by the Weidman Franz law* it becomes increasingly difficult at low temperatures. As well as needing very conductive wires to carry the heat, it was necessary to make sure the ends of these wires made good thermal contact with the rotator platform and mixing chamber. The heat flow through a junction depends on the force with which it is clamped, not the area[57]. This requires bolting the wires down firmly, and using bolts with thermal expansion coefficients that would tighten, not loosen, as the system cooled.

The best choice for thermalising things is silver wire. It has a high thermal conductivity and is readily available quite pure with good RRR. It is better than copper in that it has a small, saturating magnetoresistance, so retains its high thermal conductivity in a strong field. Wire is better than rod of the same cross section as it will heat less by eddy currents, and of course is flexible. A good starting material is 99.99% purity silver wire from Advent Research Metals, which was measured to have an RRR of 79. The residual resistance is dominated by electron scattering from impurities, and Advent indicate 100 ppm copper, and 10 ppm each of iron and a number of other metals. The iron is of particular interest as it can form magnetic scattering centres with much higher cross section than the others. A similar thing happens in copper, and the solution is to anneal in an oxygen atmosphere[52] which clusters the iron into non-magnetic Fe_3O_4 centres. Though much less common, this also works with silver[58], so some wires were treated in a similar way. Some lengths of 0.37 mm wire were annealed at 750°C for 20 hours with a pressure of about 5×10^{-4} mbar of flowing oxygen, then cooled to room temperature under vacuum over two hours. This resulted in visible grains of over 1 mm in size, and an RRR, provided the wires are handled carefully, of over 1500. Mechanical stresses reduce the RRR very quickly, winding the wire into a 4 mm diameter bobbin and unwinding it stiffens it and reduces the RRR to 250. One can assume therefore the low temperature scattering is dominated by crystalline defects after work hardening. The wires installed on the rotator will maintain an high RRR over most of their length, but will have a moderate RRR where they bend to come onto

*Assuming the resistivity is saturated at the residual value, which is true for most metals at dilution refrigerator temperatures

the rotator platform, but even with this reduction they are at least 5 times as conductive as the untreated wire.

With the very low friction jewel bearings, the main resistance to rotating the platform comes from the wires. It makes sense therefore to try to minimise the the force, which was achieved by winding the wires around the axle of the sample platform inside the bevel wheel. Thin $25\text{ }\mu\text{m}$ wire for the twisted pairs was used to reduce their stiffness. The winding also increases the distance the rotator can turn before the wires pull tight: with just the silver thermalising wires and the 18 twisted pairs on the primary solder-board, the platform can rotate through slightly more than 360° . On some cooldowns more than 18 pairs were required, and/or some coaxes for my colleague's measurements. The coaxes, though flexible at room temperature, are not very flexible when cold. The coaxes used* consist of a stranded copper core, a thin Teflon dielectric, woven copper braid and fluorinated ethylene propylene (FEP) outer insulator. The inner three layers are fairly flexible, but the FEP insulation freezes and cracks off when the cable is bent at low temperature. This problem was solved by cutting the insulation into rings with a scalpel, with cuts separated by about one cable diameter, then removing about one ring in ten. With the remaining rings of FEP spread out, they have a gap about equal to the half their thickness between each ring, which allows the cable to bend with a radius of about 2 cm whilst maintaining the insulation of the braid from the frame of the rotator. This radius is still too wide to wind the coaxes in with the other wires, so they go directly to the platform, limiting the angle through which the platform can rotate to a little over 180° . Also added were an extra 12 pairs on a secondary solder-board which can be used when more than 18 are needed, with similar constraints on rotation angle.

3.3.3 Measurement and control

While the rotator position rarely deviates more than two degrees from the position one would expect from turning the drive shaft, a higher precision was needed, and it is also useful to have a clear indicator that the platform is turning in case of problems. To achieve this modulation coils fitted to the magnet were used, along with pick-up coils on the sample platform to measure the platform angle.

The modulation coils are part of the blue fridge magnet assembly, and are described in section 3.2.3.5. Two pick-up coils consisting of 750 turns of $25\text{ }\mu\text{m}$ with an inner diameter of 2 mm were built, and mounted perpendicular to each other on the rotator platform. To minimise the effect of eddy currents in the phosphor bronze platform on the angle measurement, these are mounted on a 1 cm tufset post. Eddy currents will effect the homogeneity of the modulation field, and if the field varies between the two coils this will result in an incorrect angle measurement. By making the coils small and close compared to the distance to the nearest metal abject, this problem is avoided.

*Lakeshore Cryotronics ultraminiature coax type SC

To actually make the measurement, two lock-in amplifiers are required, one to measure each coil. One lock-in also drives the modulation coil amplifiers, and provides a phase reference to the other. There is a slight complication in that the lock-ins are connected to the coils in the cryostat, which is on the clean ground, and to the modulation coils, which are powered from the dirty ground. The two grounds are separated at the power amplifiers which drive the modulation coils.

With a stepper motor to drive the rotator and these pick-up coils to measure the angle of the platform, closed-loop control is possible. A software routine on the experiment control computer implements P-control with a fairly high gain. As there is nothing driving an error, this settles without droop. Also due to the nature of P control it tends to make large movements first and small movements as it approaches the set point, which is good from a heating standpoint.

3.3.4 Performance

With the closed loop control in place, the rotator can reach a set position with 0.05° precision. If the rotator has moved a long way ($> 10^\circ$) to reach a new position, there can be a small amount of drift. If, after an hour or so, the position is set again, the drift is much less, and the ultimately achievable precision is better than 0.01° . This is better than any of those reported in the literature except the one by Ohmichi et al[56] which has comparable precision, but is limited to 20° range. The angle sensors do have a very slight field dependence, so for best possible precision the angle should be set at zero field.

The base temperature of the rotator platform, with the mixing chamber at 20 mK and at zero field is just under 25 mK. The heat link from the sample platform to the mixing chamber was measured to be approximately $40 \mu\text{W/K}$ at 100 mK and reducing linearly with temperature. This is broadly what one would expect from the measured resistance of the annealed silver wire and the Weidemann Franz law, allowing a little extra resistance for junctions. It is also insensitive to field, which is as expected given silver's low magnetoresistance. At zero field the heat capacity of the rotator platform is such that the time constant at 100 mK is 5 seconds, increasing to a minute below 30 mK. The time constant increases drastically with field however, to 30 minutes at 100 mK and 15 T, and well over an hour at 70 mK. There is also a substantial magnetocaloric effect, which increases the base temperature on field-increasing ramps and reduces it when the field is decreasing. This is likely due to enhanced heat capacity of the phosphor bronze due either to magnetic impurities or the nuclear moments in the copper. Ideally, the platform should probably be made from silver to avoid this.

Rotating causes some heating, how much depends on speed, a typical rotation is shown in figure 3.7. The closed loop controller rotates at $5.6^\circ/\text{min}$, and this produces a constant temperature increase of about 100 mK from base temperature. Given the heat link described above, this corresponds to $4 \mu\text{W}$ heating. A small proportion of this comes from eddy current heating when

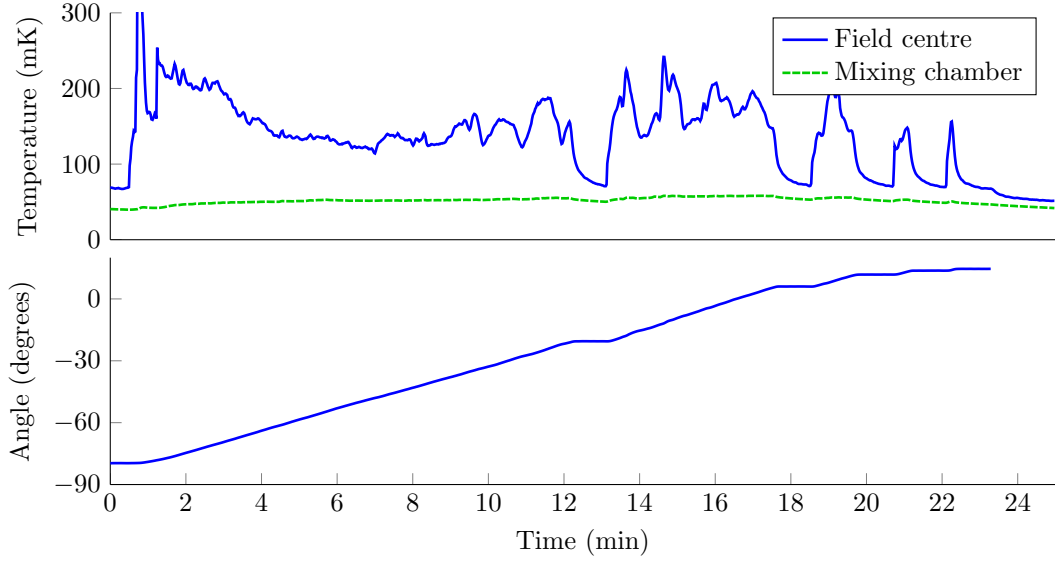


Figure 3.7: An example rotation. The rotator is initially at -80° , and is instructed to go to 14.5° with 0.1° accuracy. During the rotation, the temperature is typically increased from the setpoint of 70 mK by about 100 mK. Deep troughs in the temperature, combined with flat sections on the angle plot, mark points where the control routine is measuring the angle and deciding how far to rotate in the next step. After 23 minutes the platform is at 14.56° and the modulation coils switch off (note the kink in the temperature curve).

the modulation coils and angle sensors are operating, the majority from internal friction as the wires and coaxes bend, and from friction due to imperfections in the bevel gears.

3.4 Use of SQUIDs for resistance measurements

A SQUID based resistance bridge has two main advantages over an AC measurement using a lock-in. The first is potentially better signal to noise, if the system is set up well. The second is that it is a DC measurement. DC measurements are of course possible with precision DC voltmeters placed outside the cryostat, but Johnson noise in the room temperature wiring and voltmeter makes sub-nanovolt noise levels very hard to achieve. Unless continuous copper wires are used all the way from sample to voltmeter (which is difficult given the heat load constraints of a dilution fridge) then random changes in thermoelectric voltages can easily swamp the measurement. A SQUID bridge avoids both these problems, as explained below.

The scientific motivation for doing a DC measurement comes mostly from the possibility of observing non-linear IV curves. An AC measurement does contain some information about non-linear IV curves, especially if a large number of harmonics can be measured, but a direct measurement yields much more information. In particular they allow detailed measurements near the critical current in a superconductor.

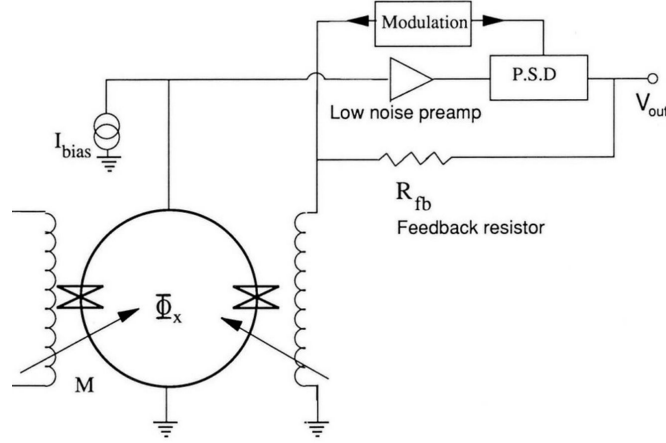


Figure 3.8: Simple flux locked loop circuit. The input signal (DC) comes from the coil on the left, and the feedback loop causes a DC current in the coil on the right to keep Φ_x close to zero. An AC modulation applied through the coil on the right, combined with a phase sensitive detector, helps in getting a precise measure of the voltage across the SQUID itself. Figure adapted from Gallop[59] and published with the permission of CRC publishing.

3.4.1 DC SQUID and flux locked loop

The DC SQUID is quite a complicated object; when biased with a current above the critical current, an extremely high frequency circulating current flows in the loop. For my purposes however, it is enough to consider the time averaged response, by which I mean the response to signals below about 10 MHz. The SQUID will have a voltage drop across it given by:

$$V = V_0 \sin \left(\frac{2\pi\phi}{\phi_0} \right) \quad (3.13)$$

Where V_0 is a constant which depends on the characteristics of the junctions and the bias current, ϕ is the flux passing through the ring and ϕ_0 is the flux quantum.

This can be used to measure an external current by using a coil to convert the current to flux in the loop. The problem is that the above voltage characteristic is periodic in ϕ so if the voltage is to yield a unique current measurement, the current has to be kept small enough that $-\frac{\phi_0}{4} < \phi < \frac{\phi_0}{4}$. In order to make the SQUID into a useful current sensor, feedback is needed. By using the voltage across the SQUID to drive a feedback coil, which couples flux through the SQUID in the opposite direction from the input coil, the range can be increased to hundreds of flux quanta. The dynamic range can be further improved by also injecting a modulation into the feedback coil and demodulating the voltage with respect to this modulation, as is shown in figure 3.8.

To build the SQUID bridge, a commercially available SQUID and control circuit built by Quantum Design was used. The SQUID is their standard Laboratory Squid and the controller is their Model 5000. A simplified block diagram of the SQUID and control circuit is shown in

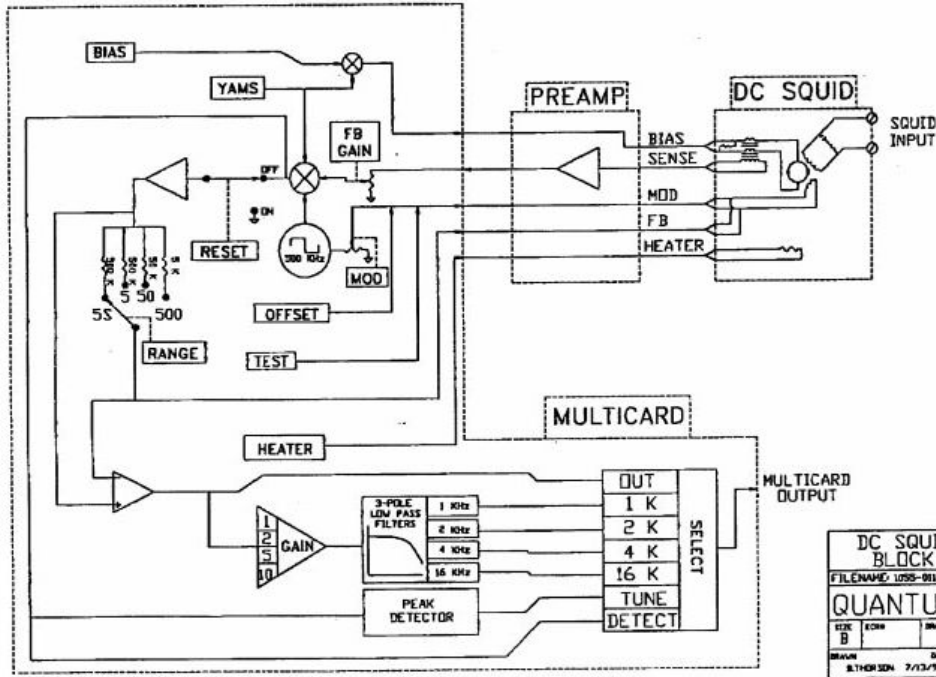


Figure 3.9: Block diagram for the input stage of the Model 5000, including SQUID sensor and micropreamp. This invaluable diagram is not in the manual, but is reproduced here with the permission of Quantum Design. It is © 2014 Quantum Design Inc.

figure 3.9. It is essentially the same as the circuit shown in figure 3.8 with a few improvements. Firstly, there is a filter fitted across the SQUID input coil to suppress oscillations and attenuate high frequencies which would otherwise interfere with the SQUID. Secondly the voltage sense is separated from the bias current at low temperature, and amplified by a $\times 400$ preamplifier mounted just outside the cryostat. Thirdly, the feedback resistor is selectable to allow different full scale ranges. Fourthly, there is some additional signal conditioning in the lower section of the diagram, which can be used to clean up the signal before digitizing. The Model 5000 also includes a 16-bit 48 KHz ADC to digitize the signal. Also included are a heater, for driving the SQUID briefly normal to clear trapped flux from the junctions. The offset DAC can be used to add an arbitrary DC level to the feedback coil, so allowing the operator to choose where their zero position is — which is absolutely necessary to make full use of the dynamic range.

When working correctly, the SQUID and Model 5000 together can be thought of as a very low noise precision current meter. The manual indicates that the noise level should be $4 \mu\phi_0/\sqrt{\text{Hz}}$, which corresponds to $0.8 \text{ pA}/\sqrt{\text{Hz}}$ with the built-in input coil. In addition to the low noise, the SQUID has the advantage of being fully superconducting and of working at low temperature.

The main disadvantages of the DC SQUID as an ammeter are with respect to its response to noise, and its absolute accuracy which is much poorer than its precision. The poor accuracy arises

from two sources, firstly the uncertain sensitivity of the input coil. This varies by more than 10 % from sensor to sensor, and also varies by a few percent as a function of temperature. The second comes from the nature of the feedback circuit: as it is essentially a proportional controller, it exhibits droop. The droop depends on the value of the feedback resistor (called the range in the Model 5000 documentation).

There are two distinct problems with noise. The first is the SQUID's response to broad-band noise, especially at high frequencies. If high frequency noise reaches the SQUID sensor itself, it interferes with the microwave frequency circulating currents, and the sensor simply stops acting according to equation 3.13. This is recognisable as the output of the model 5000 slewing to full range and staying there. The second problem is the response to transients of more than one flux quantum in amplitude, if the signal slews too fast for the model 5000 to follow, then once the transient has passed and the control loop has stabilised, there is no guarantee that it will be locked onto the same period in equation 3.13, it might be an integer number of flux quanta away from where it should be. This is called a flux jump, and cannot be detected immediately at the Model 5000. To avoid flux jumps, one can increase the bandwidth (by adjusting the range or the pot labeled *FB gain* in diagram 3.9) so the system can slew fast enough to follow the whole transient. This only works if the transient is small enough not to rail the feedback amplifier. The opposite approach is to reduce the bandwidth so much that the transient is over before the system has time to slew more than half a flux quanta, so it will settle back on the correct flux. In practice, as transients come from different sources and have different time-scales, this kind of adjustment is very difficult, and it is better to try and prevent the transients from reaching the SQUID sensor at all.

3.4.2 The SQUID null-detector bridge circuit

Bearing in mind the performance described above and the requirements for the measurement, there are several possible approaches to build a resistance measurement system. The simplest is to pass current through the sample in the usual way, then use the SQUID in series with a resistor to measure the voltage. Provided the resistor is substantially more than the resistance of the sample, contacts and wires, it works to convert the SQUID from an ammeter to a voltmeter. This is the approach used by Walker[55].

There are several problems with this approach for measuring materials like URhGe. Given that contact resistances are typically tens to hundreds of milliohms and temperature dependent, the resistor would need to be at least 10 Ohms to properly reject the contacts. Taking the SQUID noise level of $0.8 \text{ pA}/\sqrt{\text{Hz}}$ given in the previous section this would yield an effective voltage noise of $8 \text{ pV}/\sqrt{\text{Hz}}$. This is comparable to the best possible AC measurements described in section 3.1, but as described below, better is possible. The second problem is in unreliable contacts. In some cases, particularly when silver paint is used, contact resistances may drift up to many ohms, and

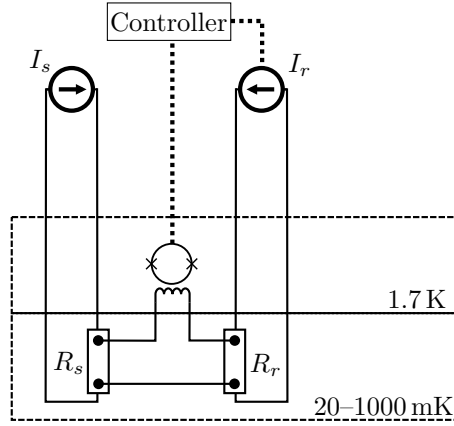


Figure 3.10: SQUID bridge circuit for resistance measurement

return to normal on warming up. This simple circuit has no way of identifying such a failure; it would be possible to measure predominantly a contact and, until the measurement turned out to be not repeatable, be none the wiser. Finally the accuracy of the measurement depends on the accuracy of the SQUID as an ammeter, which as explained above is not as good as its precision.

A better circuit is shown on figure 3.10. Here one current supply passes the current I_s through the sample, and the other passes a current I_r through a known reference resistor R_r . The SQUID measures the circulating current between the two resistors, which will be exactly zero when the voltage drop across both resistors is the same. This leads to the condition:

$$V_s = I_s R_s = V_r = I_r R_r \quad (3.14)$$

$$R_s = R_r \frac{I_r}{I_s} \quad (3.15)$$

This has the advantage that the SQUID is being used as a null detector, so any non-linearity or inaccuracy is irrelevant. The zero current position can be identified easily, by turning off the supplies then resetting the SQUID, so the relevant properties of the SQUID are noise, sensitivity and drift of the zero position, all of which are very good.

3.4.3 Sensitivity and noise considerations

The sensitivity and noise of the circuit described above depend on the choice of reference resistor and the properties of the sample and contacts. First let us consider Johnson noise. Assuming superconducting or very low resistance wires — which is easy enough to achieve in a dilution refrigerator if all component are kept cold — the resistance around the loop is $R_s + 2R_c + R_r$ where R_c is the contact resistance of the sample. As the reference resistor can be made of copper, and the four contacts made with solder, the contact resistance at that side of the circuit

is negligible. As the SQUID is a current sensor, the Johnson noise it will see will be:

$$\frac{I_{rms}}{\sqrt{f}} = \sqrt{\frac{4k_B T}{R_s + 2R_c + R_r}} \quad (3.16)$$

However, to compare this measurement with an AC one it is helpful to calculate an equivalent voltage noise. If the controller is perfect, the noise on I_r will be exactly that which is required to cancel out the noise current in the loop. Noise on I_r can be converted to equivalent voltage noise by first converting to a resistance noise with 3.15 then dividing by sample current, which yields:

$$\frac{V_{rms}}{\sqrt{f}} = \sqrt{\frac{4k_B T R_r^2}{R_s + 2R_c + R_r}} \quad (3.17)$$

Which always reduces as R_r reduces. Given typical values of $T = 100 \text{ mK}$, $R_c = 100 \text{ m}\Omega$ and $R_r = 10 \text{ m}\Omega$ this gives a Johnson noise of about $100 \text{ fV}/\sqrt{\text{Hz}}$.

The other main source of noise in the circuit is the intrinsic noise of the SQUID, which is about $0.8 \text{ pA}/\sqrt{\text{Hz}}$. This too can be converted to an equivalent voltage noise and works out as $0.8 \times R_r \text{ pV}/\sqrt{\text{Hz}}$ or $8 \text{ fV}/\sqrt{\text{Hz}}$.

The sensitivity of the bridge, that is its ability to remain fully balanced, depends on the current resulting from being a small distance off-balance. Being off balance means $V_s \neq V_r$, and the current driven by this voltage will be $V_s - V_r / R_s + 2R_c + R_r$. This is another incentive to reduce R_r , albeit with diminishing returns once $R_r < R_s + 2R_c$.

Small reference resistors are not completely without drawbacks however. Small resistors lead to larger power dissipation in the resistor ($P = \frac{V^2}{R}$), which is a problem as the resistor is inside the niobium casing on the mixing chamber. As superconducting niobium has a very low thermal conductivity, all heat has to conduct out to the mixing chamber plate via a silver wire. Small resistors are also harder to make accurately, and very small resistors must be wide compared to their length, which can lead to problems with non-linear IV curves as the current spreads out through the sample. To avoid these problems while still getting low noise and good sensitivity, a reference resistance small compared to the contact resistances at $10 \text{ m}\Omega$ was chosen. The resistor was made from copper wire, as it has very low temperature dependence at low temperature and high conductivity, which allows long, thin, easy-to-make resistors. 39 mm of $25 \text{ }\mu\text{m}$ wire with an RRR of 124 were used.

A harder to quantify source of noise is thermoelectric voltages. These can be separated into two groups: those that act to drive currents round the low-temperature loop, and those which act in the wires leading up to room temperature. In the latter, temperature differences can be quite big, as absolute temperatures are large, so microvolt scale thermoelectric voltages are not unexpected. Fortunately these wires are used to carry a current, and the current supply will adjust the voltage it puts out to always give the correct current. A perfect current supply

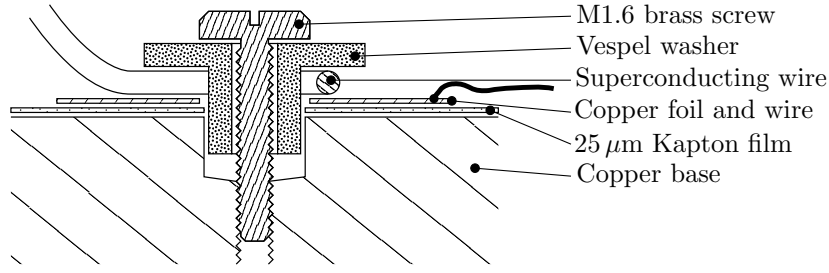


Figure 3.11: Screw terminals for connecting NbTi wire with minimal thermoelectric voltages. Not to scale: the thickness of the Kapton film is greatly exaggerated. The Kapton film and copper foil are stuck to the copper base with Stycast 2850, then the screw is tightened to clamp the superconducting wire on top. Several such terminals share the same copper base, which limits temperature differences and thus thermoelectric voltages.

would completely counter the thermoelectric voltages, an imperfect supply has some internal resistance. For the Keithley 6221 the specification sheet indicates it should be $100\text{ T}\Omega$, which means a $1\text{ }\mu\text{V}$ thermoelectric voltage would introduce a $0.01\text{ }\mu\text{A}$ current. In reality, the effective source impedance is probably somewhat less, the insulation resistance of the wiring is probably less than $1\text{ T}\Omega$ for example, but the effect is still negligible.

Thermoelectric voltages in the low-temperature loop on the other hand, are much more of a problem. The round loop resistance $R_s + 2R_c + R_r$ is less than an Ohm, so any thermoelectric voltage will cause large circulating currents. Here the careful use of superconductors can be very effective. The SQUID is mounted on the 1K plate, as it dissipates too much heat in operation for the mixing chamber. The input coil is superconducting, probably Niobium, and superconducting NbTi wire was used to link it to the mixing chamber. As superconductors have zero Seebeck coefficient, this wiring will not generate any thermoelectric voltages. The wiring in the field centre is copper, as is the reference resistor, and the sample has short gold wires to make contacts (see section 3.5). As there is no readily available superconducting wire with a critical field of over 15 T , superconductors cannot be used here, and instead one must aim to minimise temperature differences between junctions. Junctions on and near the sample are small and close together, so naturally thermalise quite well and in any event, the fragility and value of good samples makes one reluctant to try and re-mount them. For junctions on the mixing chamber, where the copper part of the circuit meets the superconducting part, screw terminals based on one in Ekin[51] but more compact were used, see figure 3.11 for details.

The selection of current supply also has a bearing on the achievable noise. It is obvious from figure 3.4.2 that the supply must be able to provide a completely floating current. That is to say, that neither end of the current supply should be tied to ground, and the current sourced on the positive terminal must be identical to the current sunk on the negative terminal. This requirement cuts out a surprisingly large number of commercial current supplies, and the common trick of using a good voltage source and a resistor to simulate a current supply. The supply must also have a large effective internal resistance for reasons given above. Other authors [60] have

used MacMartin-Kusters direct current comparators to drive both halves of the bridge, and whilst these are now commercially available* they are designed to work with much larger currents than required here. Two Keithley model 6221s were used in this bridge.

Both the Model 5000 and the Keithley 6221s are 16-bit instruments, so support 65536 discrete analogue levels. In both cases, there are different ranges, so the available levels can be scaled to make best use of them, but there can still be problems with digitization. In the case of the Model 5000, the full range of the analogue electronics is needed to keep the system locked as the sample current changes, and in the case of the reference 6221 the noise on the controller output is less than the digitization level. In both cases, this problem is avoided by oversampling. The Model 5000 DAC runs at 12 KHz and averages the data for 20ms to get a single number. As the noise at that bandwidth is larger than the digitization level, the average represents the true level and has greater resolution than the DAC. For the 6221 the controller updates the supply at 50 Hz and if the required output is between two digitization levels, it makes the source jump back and forth between them so the average over one second is the correct value.

In practice the dominating noise is the Johnson noise, at about $50\text{-}500\text{ fV}/\sqrt{\text{Hz}}$ depending on temperature. This could be improved slightly by using a smaller reference resistor.

3.4.4 Wiring and shielding

As mentioned in section 3.4.1, the SQUID can have strange behaviour or stop functioning when exposed to noise. Combined with the very low voltage noise described above, this necessitates very good shielding to prevent noise reaching the sensor. The wiring also has to comply with the strict limits for heat load at the mixing chamber in a dilution fridge, and needs to be made with a minimum of joints to keep thermal emfs to a minimum. Normally, wire is heat-sunk at every plate in a dilution fridge by winding onto a copper post, but this is not as easy if a complete superconducting shield is to be maintained.

NbTi has a very low thermal conductivity in its superconducting state, somewhat variable from sample to sample but less than $0.03 \times T^2 \text{ W/m/K}$ [61, 62]. A single $125\text{ }\mu\text{m}$ wire from the 1K plate to the mixing chamber will introduce a heat load of only around 2 nW, so thermalising the wire at intermediate plates is less important. For shielding these wires niobium capillary of 1 mm ID \times 0.125 mm wall was used, with Teflon tube inside to protect the wires. This has a much larger cross section than the wire, and a thermal conductivity of up to $6T^{2.5} \text{ W/m/K}$ [63], so if run directly from the 1K plate to the mixing chamber plate would introduce $15\text{ }\mu\text{W}$ per capillary. This is unacceptable, but by thermally anchoring at the still and 100 mK plates, this was reduced to slightly less than 1 nW per capillary at the mixing chamber, and 700 nW at the 100 mK plate. Thermal anchoring was achieved by clamping about 15 mm of tube between two copper plates which were bolted to the fridge plates. The other potential problem with niobium

*Example: Guildline 6622 Direct current comparator

capillary is a smaller thermal expansion coefficient than the steel of the fridge, so some $\sim 30^\circ$ bends were added to allow the capillary to stretch to match the fridge.

Niobium is the preferred material for shielding as in addition to the low thermal conductivity the superconducting material provides a very good shield at all frequencies. Low frequencies are blocked by the Meissner effect, and high frequencies by the perfect conductivity. Niobium is type II, but the field at which vortices start to enter — which is over 1 T at 1 K[64], for pure bulk samples — is still higher than any type I superconductor. As well as the capillaries Nb shields were used to protect the connection boxes on the mixing chamber plate, and the SQUID sensors themselves are provided with Nb shields.

Niobium cannot be used for the length between the field centre and the mixing chamber as the field is too strong. Fortunately thermal conductivity here is not a concern here, so copper capillary with a fairly thick wall was used, and OFHC copper boxes protect the samples. The run of wiring from the 1K plate to the top of the cryostat is less susceptible to noise as the round loop resistance is much higher, but shielding was still used. The temperature is too high for superconducting shields, and copper shields would introduce too much heat load, so CuNi capillary was used.

Wires outside the cryostat will inevitably pick up some noise, and the current supplies also produce a reasonable amount of high frequency noise, so a filterbox just outside the cryostat was used. The Keithley 6221s do not work well when driving an inductive load, so RC filters were preferred over LC filters. The box was constructed as per section 3.2.2 with filter topology $10\text{ K}\Omega - 100\text{ pF} - 10\text{ K}\Omega - 100\text{ pF} - 10\text{ K}\Omega$, which has a roll-off near 150 KHz and attenuates at 40 dB/decade. Also included in the filterbox are switches which tie any or all of the wires to ground, in order to protect the SQUID from static or transients as the current supplies are connected and disconnected.

All wires outside the cryostat are shielded twisted pair, except for a short length connecting to the supply which is triax, as the supplies use a triax connector. To avoid EHF noise, the shields of the cables, particularly the shields of the short cables between the cryostat and filterbox, must be tied to ground with a very low ($< 10\text{ m}\Omega$) resistance, and the best place to ground them is the feedthrough on the cryostat.

3.4.5 Vibration

With the samples in the field centre, vibration leads to noise. This noise tends to be a mix of low ($< 10\text{ KHz}$) frequencies and large transients, and appears as both a worsened noise level in the measurement and an increase in flux jumps. With the cryostat set up as normal, the largest field practical was about 2 T before flux jumps overwhelmed the measurement.

The vibration comes from a variety of sources, each needing to be eliminated to get a good measurement. The easiest to deal with was cryogenic noise, the helium bath on the blue fridge



Figure 3.12: Photographs of SQUID bridge parts. **Top Left** Close up of screw terminals, one with screw and washer removed. The copper foil should thermalise well with the bulk without being electrically connected to it. **Top Right** Fully shielded thermalising posts on the 1K plate. This is also where the wire changes from CuNi shielded Cu to Nb shielded NbTi. **Bottom Left:** Wiring between 1K plate and mixing chamber, note copper clamp to thermalise and support capillary, and bends to relieve stress. **Bottom Right:** Mixing chamber junction boxes. Three pairs of superconducting wire enter at the top and come to screw terminals, two pairs from room temperature current supplies and one from the SQUID sensor. Copper wires leave from the contacts at the bottom to go to the sample (not connected). There is a section in the middle where all wires are glued together and wrapped around a copper post to keep them thermalised to each other and the post, which is in turn connected to the mixing chamber by the silver wires visible mid-right. The grey metal is the niobium shield, a second similar part completes the assembly. A second assembly is visible in the background.

normally evaporates with little or no bubbling, but the inside of the sliding seal was not properly vented, so gas generated inside would bubble out underneath. By connecting a vent at the top of the sliding seal to the recovery line, this was stopped completely.

Ground-borne vibrations were the biggest problem. The compressors used by the department's helium recovery system are the largest source, but large vehicles passing near the lab and a host of other unidentified sources were also problematic. The cryostat rests on a concrete pad which is supposed to be isolated from the surrounding foundations by rubber foam, but it is not very effective. A rubber crumb mat (of the type used in children's playgrounds), was enough to allow measurements up to about 5 T without excessive vibrational noise. The best solution, and the only way of measuring up to 15 T, was to hang the entire cryostat from the roof of the lab. The horizontal resonant mode is pendular, with a frequency of 0.2 Hz and the vertical resonant mode is spring-and-mass, with a frequency of about 1 Hz*. Frequencies above these resonant frequencies are blocked very efficiently.

Even with the cryostat suspended, ground-borne vibrations still entered through the pumping lines. The pumping lines come from the pumps several meters unsupported to a concrete block, then to the cryostat. The concrete block is supposed to sit on the lab's foundations, and so be fairly free of vibrations. It was also touching the lab's floor, so picking up vibrations as people moved about the lab. Once that was rectified the dominant vibration source is acoustic, which could be reduced with anechoic tiles on the cryostat, but this is not necessary provided ambient noise levels in the lab are kept low.

3.4.6 Computer control

A computer was used to read the Model 5000 and control the reference current supply. As explained above, rapid measurements are necessary to get the best possible signal to noise. The control loop runs at about 50 Hz, with each measurement of the SQUID taking exactly 20 ms as this rejects line noise very effectively. The controller is implemented as a PID controller, but I only usually provides good performance.

The computer also handles several other housekeeping tasks, including controlling the sample current; re-ranging both sample and reference sources as necessary; heuristic detection of flux jumps; zeroing and resetting the bridge as necessary to clear flux jumps; aggregating and averaging data for the main experiment computer; and displaying some indicators as to the general health of the bridge.

The program is designed so that all calculations and communication with the current supplies happens while the Model 5000 is acquiring data, this is essential to keep the noise level as small as possible. The combination of all these tasks and the requirement for speed mean a

*This was achieved by using rope designed for climbing, which is both quite stretchy and strong enough to support the ~ 300 Kg cryostat and magnet

dedicated PC is required. The system is designed so that the PC, its own GPIB bus, the two current supplies, model 5000 and all the cryogenic wiring act like a single instrument which the experiment computer controls and queries over UDP using SCPI-like commands.

3.4.7 Performance

The theoretical Johnson noise limit described above (of $50\text{-}500\text{ fV}/\sqrt{\text{Hz}}$ depending on temperature) is realised in practice, provided the cryostat is sufficiently isolated from vibration for the magnetic field being used. This could perhaps be improved by as much as a factor of 10 by using a smaller reference resistor, then the SQUID’s intrinsic noise will dominate.

The controller is usually able to keep the bridge balanced. If the sample voltage changes too fast, then the bridge may not keep up, in which case it will return a reference current of “NaN” when queried. This can be dealt with by re-tuning the PID controller to be faster and more responsive, but at the risk of increasing noise or even causing oscillations.

The thermoelectric voltage induced errors in the circuit are of order 0.1 % of a typical measurement, but that is still much larger than other measurement errors. Where practical one can take two measurements, with currents in opposite directions, to eliminate thermoelectric offsets.

The bridge cannot be used while sweeping the field. It seems to cause a flux jump every 2 mT or so, this may be because the NbSn magnet does not increase field smoothly but in small jumps, as newly created flux jumps through the innermost coils into the bore. Similar problems are reported by Walker[55], and he solved the problem by fitting a single crystal aluminium tube with RRR 2000 over the sample, to act as a low pass filter for magnetic field by virtue of eddy currents. Whilst that would probably also be effective here, it would prevent the sweeping of the field whilst maintaining the very low temperatures needed.

The biggest limitation is the same as for many of the AC measurements: heating of the sample by the contacts. Whilst the bridge is capable of running with currents up to 1.5 mA*, the samples heat up substantially above the temperature of the fridge if currents over 100–300 μA are used.

3.5 Samples

Several different materials were measured, but the techniques for handling and mounting them are the same. Samples varied in size from a hundred microns up to several millimetres, and were grown using a variety of different methods. I did not grow any samples myself, but am including a brief description of the methods as it has a direct bearing on the samples available. Table 3.2 includes details on the method and grower for each sample.

URhGe is grown from a melt using one of two methods. The first is known as quench, the melt is cooled very fast and small crystals form in a polycrystalline ingot. The crystals all have

*Limited by the voltage of the current sources and the resistance of the filterbox

the stoichiometry of the melt and generally have a high RRR. Crystals taken from such an ingot tend to be at most $400\text{ }\mu\text{m}$ across, and the best ones are usually smaller, less than $200\text{ }\mu\text{m}$ across. The other method is to dip a tungsten needle into the melt, and draw out a column of material which solidifies as it is drawn. Known as the Czochralski process, this yields large single crystal. The crystal ends up being slightly off stoichiometric, and thus has a poor RRR. Certain annealing processes can improve the RRR, but not to the level of the single crystals from polycrystal growths. When discussing this material polycrystal growths will be referred to as high-RRR, the annealed Czochralski growths as medium-RRR and the unannealed Czochralski growths as low-RRR.

The BiPd samples used were grown using the Bridgmann technique, which involves cooling the melt very slowly in an alumina crucible under vacuum.

3.5.1 Mounting a sample

The first step is to verify that the sample is a single crystal. Czochralski crystals sometimes have two closely-aligned crystals, and samples from a polycrystal can easily contain two crystals. This is done by taking Laue back-scatter photographs. As the crystal structure is known, it is relatively easy to match the pattern to a simulated one and identify the orientation of the crystal. If all parts of the sample have the same orientation, it is a single crystal. Uranium containing samples tend to have a large diffuse reflection, as well as weak reflections from the lattice planes. Some software post-processing is very helpful in picking out the reflections.

Once aligned large samples are into bars, with flat faces aligned with crystalline axes, so they are easy to orient when mounting and have well-defined geometry for calculating resistivity from resistance. For cutting URhGe a spark eroder is used, and I did not need to cut any other materials but for BiPd a wire saw is best.

For a resistance measurement, at least four wires must be attached to the sample, which is done with a micro spot welder. The spot welder is a machine capable of producing a large current at a user selected voltage, typically around 8 V , for a user selected time, usually less than $100\text{ }\mu\text{s}$. with one contact connected to the gold wire to be welded and the other to the sample, the discharge melts the two together. It is essential that every part of the circuit except the joint to be welded has a low resistance, so the power is dissipated where it should be. Where possible sample was stuck to a large metal plate with silver paint*, and a thick tungsten pin pressed onto the wire just above the weld makes the other contact. Another requirement for getting a good weld is that the voltage and time be adjusted correctly, too little and the bond is weak, too much the discharge melts the wire or makes a crater in the sample. A good weld has a resistance at room temperature of $100\text{--}200\text{ m}\Omega$ and is strong enough to that a small sample can be lifted by the wire and a large one moved across a smooth flat surface by it. To aid in designing the SQUID

*Dupont 4929N silver epoxy, which cures at room temperature and is reasonably easy to remove with acetone

URhGe (Pnma)					
ID	Growth Type	Grower	RRR	Current	Comment
#1	Quench	A. Huxley	120	Mostly c	$T_C = 275$ mK
MK3	Quench	A. Huxley	~ 80	Mostly a	Mounted by M Kepa
barA1	Czochralski	D. Sokolov	4.5	a	
barB1	Czochralski	D. Sokolov	3.2	b	
barC1	Czochralski	D. Sokolov	2.6	c	
barA2	Annealed	A. Huxley	24	a	
barB2	Annealed	A. Huxley	18	b	
barC2	Annealed	A. Huxley	10	c	
BiPd (P2 ₁)					
ID	Growth Type	Grower	RRR	Current	Comment
#1	Bridgeman	B. Joshi[65]	180	In-plane	
#2	Bridgeman	B. Joshi[65]	120	In-plane	

Table 3.2: List of samples. Samples grown by the ‘Quench’ method are single crystals separated from the polycrystal growth. RRRs are for the single crystals once separated and mounted for measurement. Growth methods are described further in text and in the cited works, grower affiliations are as follows.

A. Huxley and D. Sokolov: School of Physics and Astronomy and Centre for Science at Extreme Conditions, University of Edinburgh, UK.

B. Joshi: Department of Condensed Matter Physics and Materials Science, Tata Institute of Fundamental Research, Mumbai, India

bridge the temperature dependence of a few such contacts was measured on the resistivity rig. They were found to be very like URhGe in form, with a resistance maximum near 9 K, and an RRR of much less than the bulk sample. One can assume therefore that the contact resistance is dominated by the sample near the contact, which has a very small area.

Once the sample is wired, it must be aligned and glued to a suitable platform. Large samples which are cut into bars are easy to align, high-RRR small samples were aligned with the Laue camera, then carefully glued down. The purpose of the platform is to support the sample with its thin gold wires and some contact pads for larger wire, and to provide clearly defined square edges for aligning the sample on a sample platform. BeCu foil was usually used, as it is stiff, reasonably thermally conductive but not so conductive as to suffer from excessive eddy current heating. For samples to be measured in the high field resistive magnet at LNCMI plastic was used to avoid eddy currents completely. The metal platform was covered with a 25 μ m Kapton film to insulate it then the sample was glued on with GE varnish. With bar samples this usually gets an alignment of 1° or so, but small samples tend to move slightly as the glue dries, so 5–10° errors are not unusual. In both cases, but particularly the latter, metal or plastic wedges were cut to bring the alignment within the tolerance needed for the measurement.

Table 3.2 lists the samples which yielded the data in this thesis.

3.6 Treatment of data

There are some simple manipulations which have been applied to most of the data reported in this document. These are described here, and should be assumed to have been applied unless indicated otherwise.

Both AC and DC measurements are susceptible to transient interference. This can arise from a number of sources, which are discussed earlier in this chapter. In theory, a transient results in a single data point being corrupted and this point should be discarded before continuing with any analysis. In practice, both the AC and DC SQUID methods have a characteristic time constant built into their measurements. In the AC case, it is the time constant of the lock-in, in the DC case the response time of the PID controller. If the system is disturbed by a transient, it will return to the correct measurement value after the time constant. If the control computer reads data from the measurement system within this time, two points may be corrupted. It should however never be more than two if the system is correctly configured. These transients can be effectively automatically removed by comparison with their neighbours. The function used is called `despike` and is included in the supplementary information. It compares every point to not its nearest neighbours, as these may be part of the transient, but to its next nearest neighbours. If any point is more than a set multiple of the spread of these points from their median, it is discarded. This is effective at removing most transients from the data.

It is often also desirable to reduce the number of data points and in doing so reduce noise. This is done using a function called `qbin`, which takes a set of (x, y) co-ordinates and places them into bins according to the x value. The y values in each bin are then averaged to give a new y value, which is placed at the centre of the bin in x . If the noise on the measurement is approximately Gaussian, and the measured value is changing slowly relative to the variable x , this yields the same results as changing the averaging time on the measurement system and making an equivalent change in the rate at which the control computer queries the system for a measurement. Of course it is not always possible to know *a priori* how fast y will vary with x , so in practice it is usually best to run the data collection as quickly as practical and use binning after the measurement. The function `qbin` also has the ability to discard any data points which lie far from the mean of the points in the bin, which is sometimes used to remove any transients which have slipped past the `despike` function.

In addition to these general functions, there is a specific correction that is required when using transformers on an AC measurement. If the transformer is operating near to its limits, that is if $Z_{in}G^2 \ll Z_{out}$ is no longer true, it will apply a phase delay to the AC waveform it is amplifying. This can be corrected by applying a rotation as described in section 3.1.2.3.

Finally, when making any magnetoresistance measurement it is easy to contaminate the measurement with a Hall component. This is especially a risk with the small single crystal samples where it is difficult to attach contacts in a straight line. Whenever this was considered to be a

non-negligible risk, measurements were taken with the magnet polarity reversed, and compared to the normal polarity. If necessary the mean of these two measurements would be an accurate magnetoresistance, but in practice, no major problems were ever found.

Any other treatment of the data presented in the following chapters will be described in the text. If a more detailed description of the treatment is required, it can be found by reading the scripts used to generate the figures, which are provided, along with the raw data, in the supplementary information.

Chapter 4

Measurements on URhGe

A number of measurements have been made which probe the Fermi surface of URhGe. The direct probes of the Fermi surface that prove so useful in many other materials are rather less effective in URhGe than we would like. The most direct probe is ARPES, but ARPES requires very flat surfaces which are hard to obtain on URhGe. It averages over a range of k_{\perp} , which is not ideal in a 3D material. This means that ARPES measurements are difficult; they have only recently been attempted, and have met with limited success. These results are discussed at the end of this chapter.

The other first class probe of the Fermi surface is quantum oscillations. This too has some limitations, firstly, it is insensitive to sheets which do not support closed orbits. Secondly, URhGe is known from specific heat measurements to be a heavy fermion material. For reasons explained in section 1.3, this makes very low temperatures and large fields a necessity for effective measurement. Nevertheless, some quantum oscillations have been observed, indicating small pockets with a mass enhancement of between 8 and 90. These results are presented in section 4.5. These pockets are not large enough to account for the specific heat γ , so there must be other sheets present but not seen in the SdH.

Magnetoresistance measurements can also probe the Fermi surface, but somewhat less directly. Their sensitivity to open orbits makes them a good complement to quantum oscillation measurements. In the first two sections of this chapter, results are presented which provide strong evidence for open Fermi surface sheets. Firstly, the large non-saturating magnetoresistance indicates either open sheets or compensation. Secondly, an unusual negative $d\rho/dT$ appears at high field. This is interpreted in terms of a dimensional crossover between a fully 3D metal and a reduced dimensionality as a result of weakly warped flat Fermi surface sheets. The geometry of the measurements indicates the sheets are open in the directions perpendicular to k_b .

In addition to the fermiology, measurements have also been made probing other aspects of the material physics. Measurements of the temperature dependent resistivity are useful in estimating

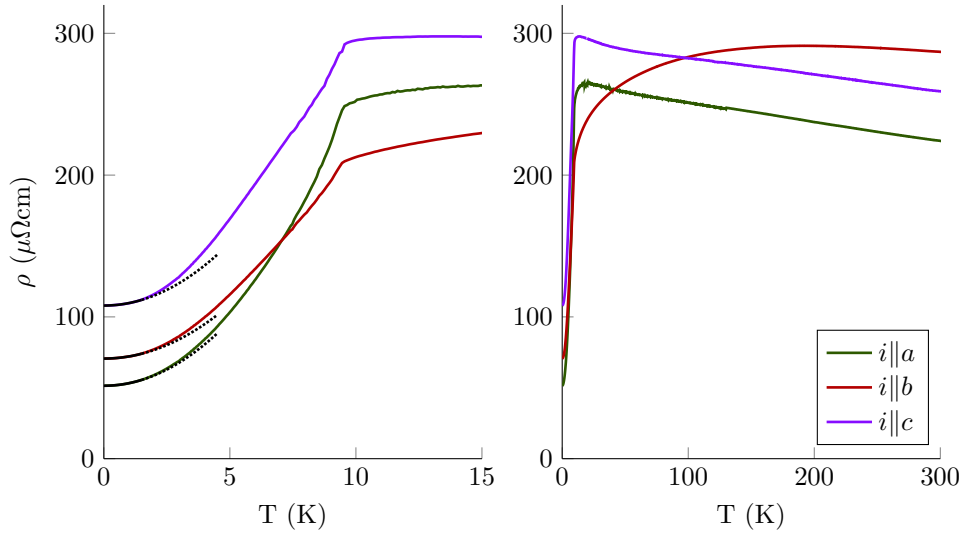


Figure 4.1: Zero field resistivity of URhGe samples barA1 barB1 and barC1, with current along a , b and c respectively. Data taken on Kraken and the blue fridge combined to give resistivity over the full temperature range. Black lines are $\rho_0 + AT^2$ fits, and dotted black lines are extrapolations of those fits.

the true residual resistivity, which shows a strong anisotropy in current and in some directions large changes at the moment rotation transition. For currents along the crystal b direction, there are few features, as one might expect if conductivity is dominated by the aforementioned open sheets. Changes for currents in the other directions suggest some rearrangement is occurring. The temperature dependencies also poorly fitted by a T^2 law, suggesting some more unusual physics. Over some ranges, they are consistent with scattering near an electronic topological transition, which is consistent with the observed field dependence of some of the quantum oscillations.

This electronic topological transition has been proposed[39] to be the driver of superconductivity. Measurements with the SQUID resistance bridge show slight deviations from linear IV curves in the area between the two superconducting pockets. This phenomenon, believed to be superconductivity at domain walls, links together the two superconducting pockets and provides evidence that they are the same nature, exiting and entering solely because the orbital limiting field drops below then returns above the field required to act as a tuning parameter.

4.1 Zero field resistivity

Figure 4.1 shows the resistivity of URhGe low-quality single crystals with the current applied along each of the crystal axes. These samples all come from the same Czochralski grown crystal, so should have similar quality. It is immediately obvious that the resistivity is strongly anisotropic with respect to current direction, and that this results in different RRRs along different current directions — in this case differing by a factor of nearly 2. The variation in RRR between annealed bar samples (see table 3.2), with $I||c$ much lower than the others, follows a similar pattern. Many

authors[37] use RRR as an indicator of sample quality, but it is clear that if current direction is not considered, it is a fairly crude indicator.

Insofar as the usual considerations for the RRR of a metal can be applied to a material which appears non-metallic in the high temperature range, anisotropic RRR has implications for the scattering. The dominant scattering process at high temperature (the Debye temperature is reported to be 213 K from specific heat[27]) would normally be phonons. With phonons at all \mathbf{k} present there are no restrictions on initial state for scattering and τ would be expected to be isotropic. The density of states contributing to transport along each direction, and the effective mass m^* can be anisotropic, but in the absence of large temperature induced changes in the band structure should have the same anisotropy at high and low temperature. The band structure can change at T_{Curie} , due to exchange splitting, but for reasons explained below and in section 4.3 it is considered that the changes to the band which contributes the most to the conductivity is small. That essentially leaves only τ to have temperature dependent anisotropy, and if it is isotropic at high temperature, it must be anisotropic at low temperature. Though an indicator of possible anisotropic scattering at low temperature, this result should be viewed with some suspicion given the lack of evidence for metallic transport at high temperatures.

At this stage it is worth noting that this measurement has been made before, at least for temperatures above 4 K[27]. The c -axis data is similar, but the reported a axis data is like my b axis data, and the reported b axis data looks like something in-between my b axis data and my a and c axis data. The former could be explained by a mistake in handling and identifying samples. The latter is consistent with the reported b axis data actually being taken with the current misaligned 60° towards c , which, due to some coincidences of the lattice parameters, produces a very similar Laue pattern to the correct alignment. This error actually led to an erratum against the paper[26], though the resistivity result was not listed as affected. With the benefit of knowing my results are different, I have checked my methods and satisfied myself that I am correct. A third measurement, using the Montgomery method, also agrees with my results[66]. So I will proceed on the basis that the data shown in figure 4.1 is correct.

The three curves were taken on three different samples, and two different measurement systems. The data taken on the blue fridge extends up to 7 K, the data from Kraken extends down to 2 K. After rescaling slightly, the data agree very well. The rescaling is necessary as a broken and repaired contact slightly changed the geometric factor, and because the room temperature transformer gain can change by a percent or two between measurement systems. Consequently each resistance curve is internally consistent and accurate. When calculating the resistivity, uncertainties in the geometric factor and current distribution are much larger than errors on the resistance measurement, so the absolute resistivity values have an uncertainty of about 10%. Rescaling to account for such uncertainties cannot however make any of the curves lie on top of each other, so the conductivity is fully (i.e. 3D) anisotropic both above and below T_{Curie}

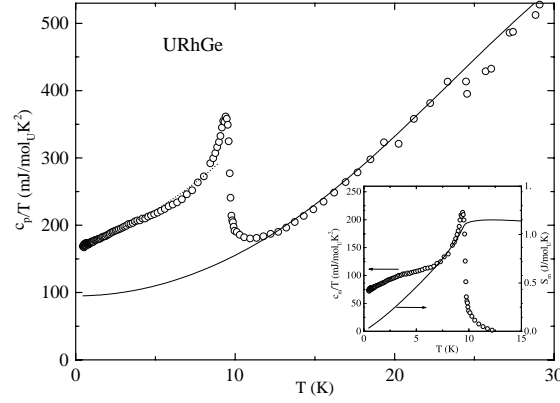


Figure 4.2: Heat capacity of URhGe measured by Prokeš *et al.* Reprinted from [27] with permission from Elsevier. **Main figure** Heat capacity c/T of a URhGe single crystal. Solid line: $c/T = \gamma + aT^2$ fit above 15 K with $\gamma = 95 \text{ mJ/mol}_U\text{K}$ and $\Theta_D = 213 \text{ K}$. Dashed line: $c/T = \gamma + bT^{0.5} + aT^2$ fit with $\gamma = 155 \text{ mJ/mol}_U\text{K}$ and $\Theta_D = 195 \text{ K}$. **Inset:** Magnetic heat capacity, calculated by subtracting the solid line from the data in the main panel. Solid line: Integral of data, compare with resistivity in figure 4.1

Considering the data below T_{Curie} , the resistance appears metallic along all three axes. The curvature in all three cases is less than the T^2 expected of a low temperature nonmagnetic metal, but gets closer to it as temperature is reduced. A fit of $\rho_0 + AT^2$ to the lowest temperatures is at best reasonable, and quickly diverges from the data (red lines in figure 4.1). A better fit is obtained with $\rho_0 + AT^n$, yielding $n = 1.8$, but it is unlikely that there is a single scattering process which scales this way. More likely is a combination of T^2 electron-electron scattering and some other process or processes. This is discussed together with the field dependence of the fit in section 4.7.

At T_{Curie} there is a sharp downward kink in the resistivity. One possible reason for this is the ordering of spins which are partly localised at lattice sites, reducing their ability to scatter. It is commonly observed that this leads to the specific heat contribution from these spins being related to resistivity by $c_{mag} \propto \frac{d\rho}{dT}$. This is known as the Fisher-Langer relation after the researchers who provided a theoretical explanation[67]. The specific heat at zero field was measured by Prokeš *et al.*, and their measurement is included in figure 4.2. They fit $c/T = \gamma + aT^2$ to identify electronic and lattice specific heat, and attribute the remainder to magnetic. This, along with its integral is shown in the inset. As expected, the form of the integral is very similar to the resistivity.

Some caution must be applied to this result, for several reasons. Firstly, the Fisher-Langer relation was strictly only derived for local moments, but URhGe is believed to be fairly itinerant. In practice however, the Fisher-Langer relation has been observed in a wide variety of different materials with different levels of itinerant and localised behaviour[68, 69]. Secondly, the magnetic specific heat in figure 4.2 does not approach $c/T = 0$ at low temperature. This indicates there may well be some electronic component involved, and the c being integrated is not solely c_{mag} .

Ultimately, this does not affect the result near T_{Curie} , as the shape of the integral there is dominated by the peak in c_m . The possibility of an electronic component being included therefore does not upset the qualitative result, but would affect any attempt at a quantitative comparison.

The specific heat data at this point warrants some further discussion. In a localised magnet, the magnetic part of the specific heat usually approaches zero temperature as $T^{3/2}$, as the dominant excitation is spin waves. The fact that c_{mag} does not have a zero intercept on the c/T graph can be explained by the fact that URhGe is not a local moment ferromagnet. In an itinerant ferromagnet, the electronic specific heat γ is expected to change at T_{Curie} simply because the electronic structure must change to give unequal occupancy of spin bands. The specific heat data then suggests that URhGe is at least partly itinerant, as inferred from the magnetization measurements[25]. Above T_{Curie} , γ is about 95 mJ/mol_UK, and below it is near 155 mJ/mol_UK.

Let us assume that in the paramagnetic state the uranium 5*f*-electrons have little influence on the conductivity of the material, either as they are fully localised or simply not at the Fermi level. The physics is dominated by *s*, *p* and *d* bands which are generally light. Below T_{Curie} , the *f*-bands hybridise with the conduction bands. This may result in a change in the electronic density of states which would change γ . If the main effect was to introduce some new small heavy pockets, the change in γ would not be accompanied by a large change in transport properties. If, for reasons outlined in section 4.3 we assume the conductivity is dominated by open Fermi surface sheets which see no major changes across T_{Curie} , then the non-conductivity-dominating bands increase their contribution by 60 mJ/mol_UK. This would be consistent with small, heavy pockets, which do not contribute much to the conductivity because of their high mass.

Above T_{Curie} , the behaviour for currents along the *b* axis is of a different form from that along the other axes. *a* and *c* axis conductivities are similar, but not identical in shape. The latter remain metallic up to a peak at 13–20 K, then show linear drop to the highest temperatures measured. ρ_b remains metallic to a peak at 190 K, and also shows a linear drop above about 250 K. In both cases this is strongly suggestive of a crossover to incoherent transport, and the shape of the curves is very reminiscent of the *c*-axis conductivity in layered materials like strontium ruthenate[17].

In strontium ruthenate this is understood to be the result of two parallel channels for conduction along the *c* axis[70]. One channel can be thought of as metallic, with resistance rising with temperature. The other is an incoherent process, with resistance falling with rising temperature. At low temperatures the metallic channel dominates completely, and the conductivity looks metallic. At high temperatures the incoherent channel dominates, and at intermediate temperatures, the resistivity follows $1/\rho_{total} = 1/\rho_1 + 1/\rho_2$. For a similar model to apply to URhGe would imply a similar set of parallel channels. This is consistent with the magnetoresistance measurements detailed in section 4.2, where the application of field at low temperature also causes a crossover from metallic to incoherent transport.

An alternative model for crossover to incoherent transport as a function of temperature is the Mott-Ioffe-Regel (MIR) limit (also known as the Ioffe-Regel limit). In its simplest form, this theory states that when the mean free path l becomes shorter than a lattice parameter a , the electron is no longer extended over several unit cells and Bloch wavefunctions are no longer appropriate as a description. The limit is variously given as $l \approx a$ or $k_F l \approx 2\pi$. The latter being more accurate, as it considers the wavelength of the Bloch waves at the Fermi level, rather than the unit cell size, it also usually leads to a shorter permissible l . Unfortunately without an estimate of the mean free path and Fermi wavevector, it is hard to say whether URhGe is near the limit in absolute terms. Most metals reach the MIR limit somewhere around 100–400 $\mu\Omega\text{cm}$, so the resistivity of URhGe puts it in the right area. One reasonable estimate of the mean free path is from the Dingle factor of quantum oscillation measurements on URhGe#1[39]*, and gives 55 nm. That sample has an RRR of 120, which, assuming the path on the observed orbit is representative of the rest of the Fermi surface, yields a mean free path at saturation of 460 pm; very similar to the lattice constants. Indeed, this is substantially less than the a or c lattice parameter, suggesting that URhGe should reach the MIR limit at a lower resistance. A better estimate, using k_F , would almost certainly increase the resistance at which the MIR limit is expected. It is also not uncommon for strongly correlated systems to saturate well above the MIR limit predicted from simple calculations such as these, the cuprates being the best known example[71].

It is also noteworthy that the a and c lattice parameters are similar, at 683 and 748 pm respectively, which is consistent with the peak in ρ_a being at slightly higher temperature than the peak in ρ_c . The peak in ρ_b however is at ten times the temperature, yet the lattice parameter is only one third less at 431 pm, which requires that either the mean free path is very anisotropic, or the scattering rate is rising much faster at ~ 20 K than it is above.

An experimental observation is that the resistivity in the MIR limit follows the same parallel resistor formula given for the parallel channel case above in a wide range of materials[72]. The details of the method remain unclear[71], not least because by definition at the MIR limit semi-classical transport theories used to derive it break down. The observation of resistance falling with temperature after saturation is also common[73]. All in all, the data is consistent with URhGe being in the MIR limit.

The behaviour described here is in no way unique to URhGe. Many other materials of the form UTX (T is a transition metal, X is Ge or Si) show similar properties[74]. Two of the most similar metals to URhGe are UCoGe and UGe₂. The former is isostructural to URhGe, the latter crystallises as $Cmmm$ which is a supergroup of $Pnma$. Both materials show the downward kink in resistivity at the Curie temperature, and both have much reduced $d\rho/dT$ at higher temperat-

*With the caveat that the area of the orbit is needed to get the correct l , but frequency alone does not give it uniquely in a material where it is field dependent. Thus the estimate of the mean free path in the cited paper is not as reliable would be usual for such a result. But in the absence of a better estimate it will suffice for this calculation.

ure, with UGe_2 nearly flat at 300 K and UCoGe negative. No comprehensive measurements of resistance anisotropy have been performed on these materials, so it is not obvious which current direction in URhGe should be compared to the reported resistivity, but UCoGe at least seems to match very closely the a and c data on URhGe .

The kink at the curie temperature is also observed in a wide variety of other materials as diverse as SrRuO_3 [69] and $\text{La}_{0.7}\text{Ca}_{0.3}\text{MnO}_3$ [68] and is really just a result of the Fisher-Langer relation.

The broad peak and crossover to incoherent transport is also observed in a fairly wide variety of materials. It is commonly seen in the “bad metals” such as La, Ti or the transition metal A15 compounds*, where it is understood to be due to the MIR limit. Hussey *et al*[75] provide an overview of materials which do and do not saturate as expected from the MIR limit, and include heavy fermions as a class of materials which usually do. In particular UPt_3 saturates and is anisotropic, but does not turn over to $d\rho/dT < 0$ over the temperatures measured (up to 300 K)[76]. The tetragonal heavy fermion antiferromagnet URu_2Si_2 shows both anisotropy and complete saturation[77], but the saturation temperature is the same along different axes. In short, whilst saturation is reasonably common in heavy fermions, and MIR is a commonly advanced theory as to why, it is not totally clear it applies universally, and the strongly anisotropic saturation in URhGe is clearly not common.

To summarise then the high-temperature resistance of URhGe saturates, and this is reasonably consistent with the MIR limit, but also consistent with a model of parallel channels, one metallic and the other incoherent. Fitting the parallel resistor formula to the data is impractical because the form of the metallic part is not known in detail so close to the Curie temperature, but both models predict the same form so it would not discriminate between them. That both of these models predict similar behaviour is not entirely coincidental. In both cases the metallic channel is lost, and the transport above a critical temperature is incoherent. The parallel channel model explicitly includes an incoherent channel, but it would not be unreasonable to assume that in the MIR limit any remaining conductivity would be incoherent. The real difference between the models is why the metallic channel ceases to dominate. In the MIR model, it is because it has effectively ceased to exist, at least insofar as it cannot be described as a metal in terms of Bloch wavefunctions and Fermi surfaces. In the parallel channel model, two distinct processes are involved, and the metallic channel ceases to dominate simply because it has become more resistive than the incoherent one.

*Here A15 refers to compounds with formula A_3B , with A a transition metal, these are often superconductors. The A15 space group is also known as Pm-3n. Example: Nb_3Sn .

4.2 General Magnetoresistance

Figure 4.3 shows the magnetoresistance of a URhGe sample as it is rotated with the field in the ab plane. In this plane, the b component of the field acts as a tuning parameter, but the a component does not. As such, the observed effects can be split into two groups, those which are a result of the tuning, such as superconductivity, always occur at the same B_b , and are most obvious in the right panel of the figure. Those which depend only on B , such as the magnetoresistance, are clearer in the left panel.

Leaving aside for now the re-entrance of superconductivity and magnetoresistance in the moment-rotated state, the most striking feature is the large magnetoresistance and lack of saturation. The magnetoresistance is very large in absolute terms, $\Delta\rho/\rho_{zf}$ at 30T is over 250. This can be explained by reference to equation 1.24, which is the conductivity of an open sheet and a closed one in the high field limit. Taking the resistance at zero field to be $\rho_{zf} = 1/(\sigma_o + \sigma_c)$ and taking the limit $\sigma_o \gg \sigma_c$, it can be rewritten as:

$$\frac{\Delta\rho}{\rho_{zf}} = \frac{\sigma_o}{\sigma_c} \omega_c^2 \tau^2 \sin^2 \theta \quad (4.1)$$

Where, as the current direction in this sample is believed to be predominantly along c^* , and the open sheets normal to k_b , the $\sin \theta$ part is a constant approximately one. Since equation 1.24 was obtained for a free-electron like closed orbit, the expression above goes as B^2 , however it should be clear that if the closed orbit alone deviates from B^2 then so will the combination of open and closed. Such deviations are discussed in detail in section 1.2.3, but generally arise from orbits with sharp features. Taking $\omega_c \tau \sim 1$ at 14T would suggest $\frac{\sigma_o}{\sigma_c} \sim 7$, which is well within the realm of possibility if the closed orbits lie on small pockets. The data is also consistent with this simplified model in that the magnetoresistance does not depend on the angle at which the field is applied, at least up until the moment rotation.

The second interesting observation is non-saturation. As explained in section 1.2.4, non-saturation is commonly seen when open orbits exist on the Fermi surface, which is likely the case here. Before stating that open orbits are the cause, it is prudent to consider other possibilities. Saturation occurs when: $\omega_c \tau \gtrsim 1$; the scattering is catastrophic[†]; and the material is neither compensated nor able to support open orbits.

One of the fundamental requirements for quantum oscillations is that $\omega_c \tau \sim 1$, so that at least some of the electrons complete a full orbit, and interference can occur. Any event which changes the phase of the electron will prevent interference. Oscillations have been observed in this sample of URhGe at fields as low as 8T[39], so at least some orbits of the Fermi surface do not have

*The current direction is not known precisely, due to the small size and irregular shape. It is inferred to be along c by comparison with samples where the current direction is known.

[†]Catastrophic here having the meaning defined in section 1.1: large angle and to a completely random point on the Fermi surface. When considering the path of a probe electron created by the electric field just above the Fermi surface, catastrophic scattering destroys the probe electron.

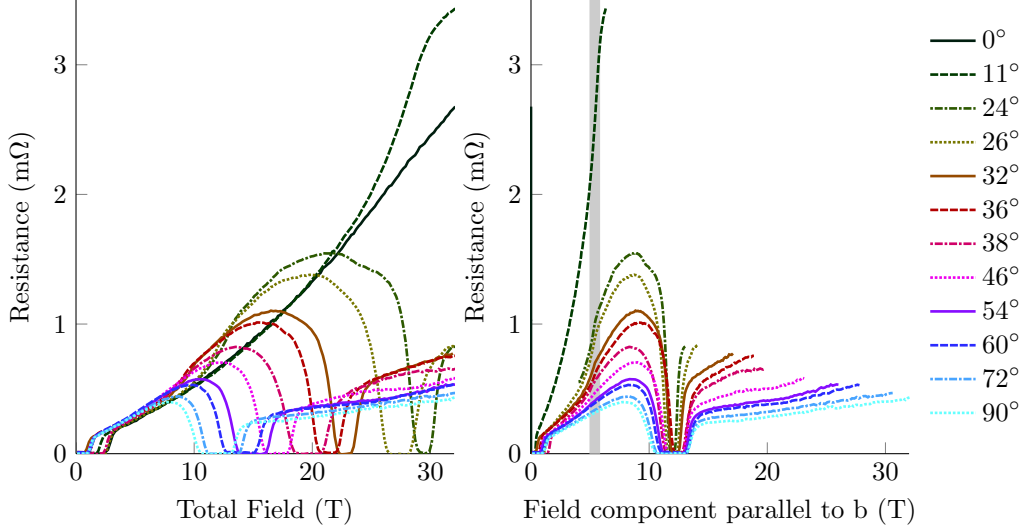


Figure 4.3: Low temperature (30-50mK) magnetoresistance of URhGe#1 (with current mostly along c) measured with the field in the ab -plane, angles measured from the a -axis. **Left:** Resistance plotted against field applied. Note that the magnetoresistance is large and, until the kink, similar at all angles. **Right** Resistance plotted against the component of field projected along the b -axis. Note that the kink (marked by the thick grey line) and the superconductivity now all fall at constant field.

$\omega_c \tau \ll 1$. Where it is practical to fit a dingle factor to these oscillations, it implies $\omega_c \tau \sim 1$ at 14 T. Whilst it is possible for scattering rates to vary around the Fermi surface, oscillations have been seen at several different field directions and substantially different frequencies (see Section 4.5), so it is hard to believe that there are sufficient high-scattering points on the Fermi surface to prevent saturation whilst still allowing the range of quantum oscillations observed.

The τ which is relevant for assessing when saturation will occur is the transport lifetime, labelled τ_{tr} . This is the time-scale over which an electron leaves the excited state it has entered as a result of the applied electric field, and returns to the equilibrium Fermi surface. If the scattering is catastrophic, then by definition a single scattering event will do, and τ_{tr} is the lifetime between scattering events. Small angle scattering does not randomise the direction of the electron wavevector, but rather changes it only slightly, so the electron will continue to contribute a current. The position of the electron on the Fermi surface can be thought of as a combination of the magnetic field-induced motion along its orbit combined with a random walk caused by small-angle scattering. It will only cease to contribute a current when the random walk has taken it far from its original orbit. The number of scattering events necessary to do this will depend on the detailed nature of the scattering, but will be much more than one, so in the small angle scattering case the transport lifetime will be longer than the scattering time. Saturation will still occur, but the effective τ_{tr} which determines when $\omega_c \tau \gtrsim 1$ is much longer, and so saturation can be put off to much higher fields[2].

With the exception of the area of negative temperature coefficient described in section 4.3, and

areas where the low temperature resistance is obscured by superconductivity, the resistivity has settled close to a residual value at low temperature. This indicates that the dominant scattering is not phonon scattering, which is a common type of small angle scattering (when $T \ll \Theta_D$ and only low \mathbf{k} phonons are excited). That which remains is usually impurity scattering, and small, local impurities are normally catastrophic scattering centres. One exception to this is in high-RRR oxygen annealed copper, where the low temperature scattering process is small angle. This is believed to be the result of magnetic impurities clustering together during the annealing process to form large, non-magnetic scattering centres[78, 2]. A similar thing could happen in URhGe if the impurities formed small inclusions rather than simply appearing as interstitials, vacancies or atomic substitutions.

Of course small angle scattering also affects the appearance (or otherwise) of quantum oscillations in a sample. The relevant τ is the coherence lifetime, which will always be equal to or shorter than the transport lifetime. If small angle scattering were the dominant mechanism, quantum oscillations would be suppressed until fields substantially above the saturation field. Thus small angle scattering is also considered very unlikely.

Let us now consider compensation. Compensation is actually quite common in metals containing an even number of electrons per unit cell, and URhGe has four formula units in each unit cell. Assuming for now that different spins are degenerate, most of the electrons will be in filled bands far below the Fermi surface, with two electrons per Brillouin zone in each band. This will leave an even number of electrons in the partially filled bands too. If the bands are fairly far apart compared to the band width, then there will be two electrons left, occupying a small number of bands. If they occupied one band then that band would be exactly full and the material would be a band insulator, which we know is not the case. If they spill over into a higher band, then the volume unfilled in the lower band (hole pockets) would be equal to the volume filled in the upper band (electron pockets) and the material would be compensated. Less commonly, the volume remaining in the lower band may be small enough that it forms an electron pocket, in which case the metal is not compensated and will appear to have 2 electrons per unit cell. This argument can easily be extended to the case where the bands are close in energy compared to their width, and the number of electrons in partly filled bands increases. The number of electrons in those bands will be an even integer $2n$, and the Hall measurement will indicate an even number of electrons in the range $\pm 2n$.

Fawcett and Reed[79] provide a rigorous derivation of this result, and also extend it to the ferromagnetic case. Unsurprisingly, with the spin degeneracy broken, the number of electrons vying for space in partly filled bands can be any integer (not just an even integer) and the Hall measurement, ignoring the practicalities of separating the normal and anomalous Hall and assuming free electron-like bands will also indicate integer n . Inherent in this calculation however is the assumption that the contents of every band can be characterised as hole or electron, and

this is certainly true of any simple pocket. It is also true of some multiply connected pockets, provided open orbits do not exist. When open orbits exist, it is possible however to have a band with occupancy neither hole-like nor electron-like, such as a pair of flat sheets which completely cross the zone in two directions. In this case, the Hall measurement is free to vary from integer electron number and the very concept of compensation or otherwise becomes rather ill-defined.

The best way to identify whether or not URhGe is compensated would be a measurement of the normal Hall coefficient. In a simple metal we can get $n = n^- - n^+$ from the Hall, and by referring to figure 1.2 we can see that no saturation at the fields reached implies $c = |n^- - n^+| > 0.5$. With both of these figures, we could see if there are any integers satisfying the relations. Unfortunately the literature does not seem to contain a Hall study. Some preliminary results[80] indicate that the normal Hall is small but non-zero well below the Curie temperature. Even if such a study were made, it would be difficult to draw clear conclusions about compensation. This is in part due to the difficulties in separating normal and anomalous hall but also because the simple result of $R_H = 1/ne$ is only valid in the free electron case. If there are two bands with different masses, then one cannot simply compare the volumes of the two Fermi surfaces to find n . If we wish to rule out compensation as the reason for non-saturating magnetoresistance, we must look elsewhere.

Another way to tell if URhGe is compensated is to consider direction. Compensation prevents saturation for all current direction and all field directions. Unfortunately there is not clear and unarguable evidence of saturation anywhere in the magnetoresistance data presented here, but there are some possibilities, in particular in the data taken on bars with well defined current direction. In this case we can also compare samples of differing RRR, and so differing fields at which $\omega_c\tau$ becomes 1. By comparing these samples we can also identify the other effects which are present in the magnetoresistance, and thus isolate the effects which can help identify features of the Fermi surface.

Let us begin with figure 4.4, which shows magnetoresistance measurements of low-RRR samples for all combinations of field and current direction. In these nine graphs, a much reduced magnetoresistance is expected *a priori* in the diagonal panels. This is simply because with the field and current aligned (known as the longitudinal geometry), the electrons are following orbits in a plane perpendicular to the electric and magnetic fields and their travel along the direction of the field is often unaffected. Magnetoresistance will only arise where the electron is swept into an area where it contributes less current than where it was excited, and where no other electrons were excited to be swept into the higher current area. For any given field and current direction, this results in a constant (not \mathbf{B} dependent) magnetoresistance which is normally small if it appears at all[2]. Thus it would be reasonable to assume that the magnetoresistance shown in these three panels is mostly due to changes in scattering induced by the field, rather than magnetoresistance in the orbital sense. Our understanding of the magnetic structure*, based on

*It is worth noting that some early papers report a different magnetic structure[23, 27], which might be expected to have a high susceptibility along a but this has been identified as erroneous[26].

various measurements of magnetization[29] and neutrons[25, 26, 29], is that field component applied along the a -axis has little or no effect, whereas fields along the b - and c - axes cause a slight increase in total moment, and field components along b also cause the moment to rotate. This is borne out in the diagonal panels of figure 4.4: applying a field along a causes negligible change; applying a field along b causes a complex magnetoresistance strongly peaked at the moment rotation; and applying a field along c causes a slight negative magnetoresistance. The latter has been observed before and observed to be stronger at temperatures nearer the Curie temperature[81]. The cited author ascribes the effect to scattering from “magnetic polaron” excitations which are reduced by field, though other excitations are perhaps more likely and are enumerated in section 4.7. Magnetic breakdown can also cause negative magnetoresistance in any measurement geometry, by opening up more efficient paths for the electrons to contribute to the conductivity. Of particular note in the $\mathbf{B} \parallel \mathbf{i} \parallel b$ case is that the magnetoresistance seems to rise superlinearly then saturate, but this is *not* the expected behaviour of orbital magnetoresistance in the longitudinal measurement geometry, so is probably due to a different process.

Comparing then the diagonal and off-diagonal panels, there is little difference on the top and bottom rows. In these cases it is fair to say that the magnetoresistance is due only to a change in scattering, and that we do not see any magnetoresistance in the orbital sense. In the $\mathbf{B} \parallel a$ case the field has little effect, any orbital magnetoresistance is too small to detect. In the $\mathbf{B} \parallel c$ case the field causes a change in scattering that effects all current directions equally; the resistivities are still different (see section 4.1), but their changes are similar. In the middle row, the three graphs are rather different, however the usual signs of orbital magnetoresistance are still absent. This field direction is rather special as it causes a moment rotation, and with that moment rotation may come substantial changes in energies and hence Fermi surface. The large reduction in resistance measured along the c -axis is very likely the result of such changes. The peak seen in the other two panels is due to increased scattering from domains near the first order transition at the moment rotation. The peak is not visible in the former, but as it is smaller than the change in resistance it has quite probably been subsumed into the transition. Below the transition however, the three panels are still not the same, with $\mathbf{i} \parallel a$ following more-or-less the form of the longitudinal geometry case, but $\mathbf{i} \parallel c$ being rather higher. To understand whether this can be attributed to orbital magnetoresistance we can look at higher quality samples.

Figure 4.5 shows equivalent measurements performed on samples with RRR between 10 and 30, or about 4 to 9 times that of those in figure 4.4. An improvement in RRR should imply an improvement in scattering lifetime and a commensurate reduction in the field at which $\omega_c \tau$ becomes 1. As (bar superconductivity) the general form of the $\mathbf{B} \parallel b$ panels is the same as in the low RRR case, we can safely conclude that saturation is not happening in those measurements, and the orbital magnetoresistance is too small to detect. This is not a surprise, as based on the result mentioned above that $\omega_c \tau = 1$ in the high quality sample URhGe #1 at 14 T, and the

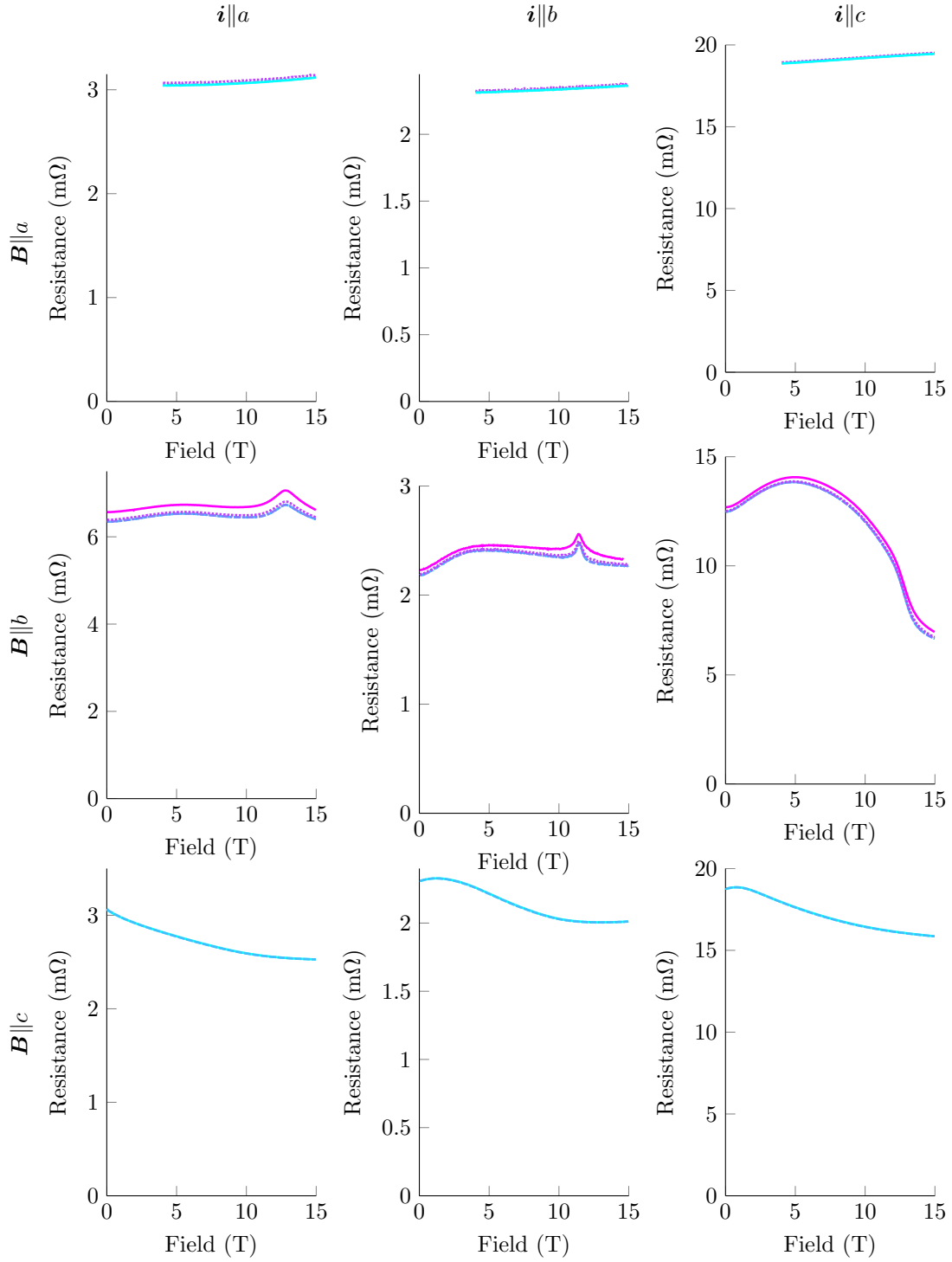


Figure 4.4: Magnetoresistance of low-RRR URhGe samples with the field along each of the crystal axes. Left to right: Current along a , b and c (samples barA1, barB1 and barC1 respectively). Top to bottom : Field along a , b and c . Colours denote temperature, pale blue being 50 mK and pink 1 K, though the temperature coefficient of resistivity is everywhere small. The zero field resistance of the middle row is different from the others as some of the sample contacts broke and were repaired. The peak in the $B \parallel b$, $i \parallel a$ graph is at slightly higher field than one might expect as the sample is misaligned by about 2° .

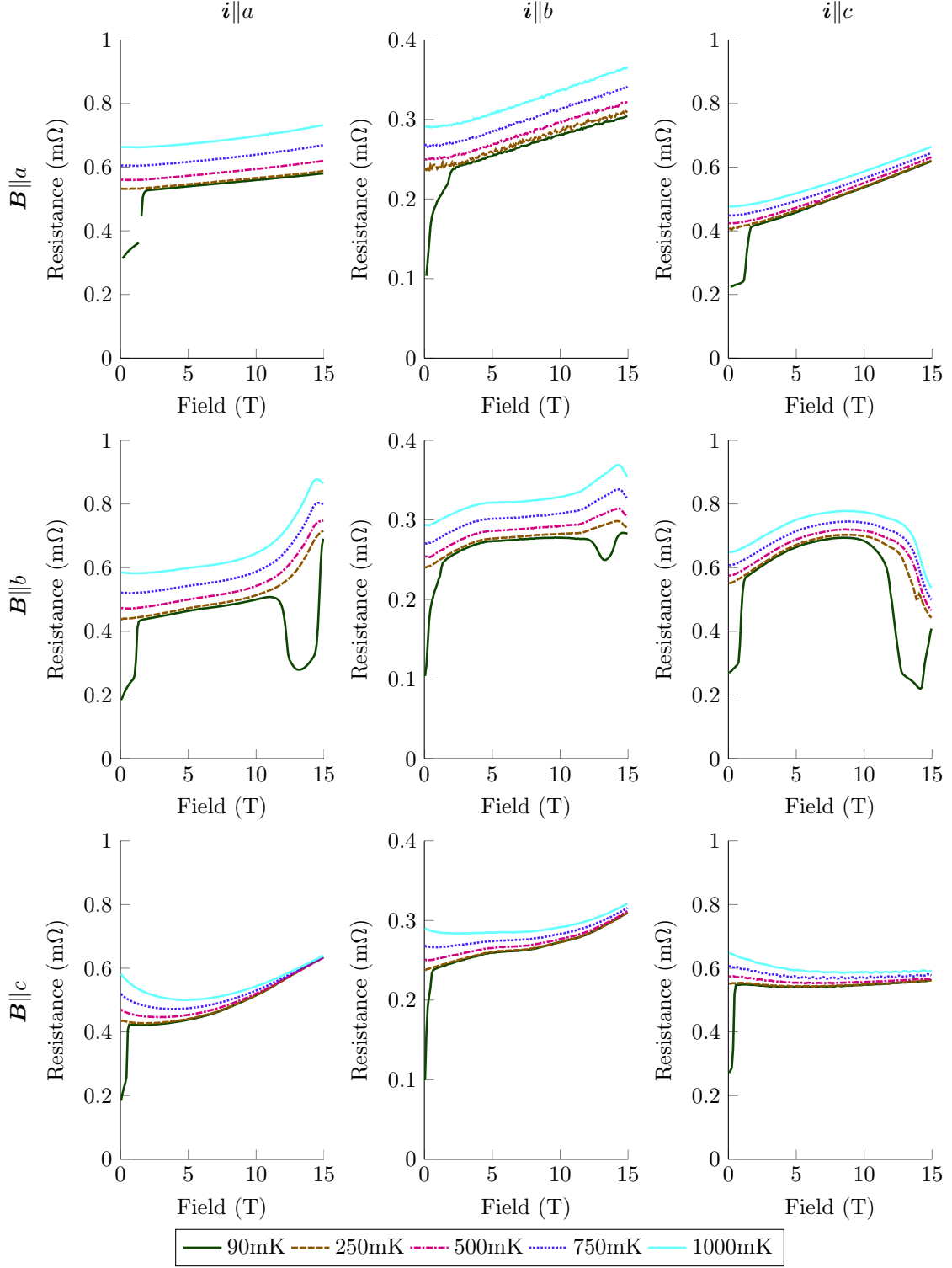


Figure 4.5: Magnetoresistance of medium-RRR URhGe samples with the field along each of the crystal axes. Left to right: Current along a , b and c (samples barA2, barB2 and barC2 respectively). Top to bottom : Field along a , b and c . Again, the moment rotation transition appears displaced on the $B \parallel b$ data due to small misalignments, but this does not materially affect the result. For a closer examination of the angle dependence near b see section 4.7

relative difference in RRR, saturation is not expected until much higher than 15 T.

Comparing the $\mathbf{B}\parallel\mathbf{i}\parallel c$ (bottom right) panels of these two figures, the negative magnetoresistance is gone. It is not clear why the higher quality should suppress it, but it would seem to indicate that the scattering process which leads to the negative magnetoresistance is probably the main one which dictates the RRR in this quality range. Assuming the low temperature resistance is due to two separate scattering processes, one of which is the usual field-independent catastrophic scattering from small impurities and the other is the field-dependent scattering from an unknown scattering centre then the change in RRR has greatly reduced the latter. It is also worth bearing in mind that as $\omega_c\tau$ increases the potential for current jetting to spoil the longitudinal measurement increases[2], especially as the samples are more ‘brick’ than ‘matchstick’ in shape. The usual sign of current jetting is a bizarre, heavily featured, unrepeatable and/or strongly negative magnetoresistance in the longitudinal geometry, but there is no sign of that here.

Moving on to the transverse geometry in the $\mathbf{B}\parallel a$ case, magnetoresistance is almost linear. Most discussion of linear magnetoresistance refers to a slow rise after saturation[2], especially regarding potassium. In this case, the linear magnetoresistance is present from about 2 T; far below the point where $\omega_c\tau$ is expected to approach one. This behaviour has been seen in other heavy fermions at low temperature, in particular CeCu₆[82]. In this case it can be understood, via the work of Mahan[83], as replacing the usual B^2 due to strong electron-electron interactions. It could also result from sharp features on the orbit, such as in the square Fermi surface model discussed in section 1.2.3, but to reduce the magnetoresistance all the way to linear by this method would require a very angular Fermi surface.

It is a similar case for the $\mathbf{B}\parallel c$ measurements, both now show a positive superlinear magnetoresistance which is not present in the longitudinal measurement. In neither case is it quite the B^2 predicted by conventional orbital magnetoresistance nor the B described above, it is a strong sign that orbital magnetoresistance is happening. The initial negative magnetoresistance at higher temperatures could be interpreted as being from the same source as that in the lower quality bars, but in this case it is only visible at finite temperature, and then only at low fields.

Lack of saturation for both these directions is not a surprise, as the quality of these samples, though better than those in figure 4.4, is still rather less than the sample in which quantum oscillations yield a $\omega_c\tau = 1$ at 14 T. The $\mathbf{B}\parallel b$ data taken alone again shows no clear evidence of the presence or absence of orbital magnetoresistance. This is due to the complex other features which, other than the superconductivity, are discussed above.

To summarise, only measurements on high quality single crystals at high fields are certain to reach $\omega_c\tau > 1$, and saturation is not seen at any field angle. Non-saturation on the other hand is only conclusively present for $\mathbf{B}\parallel a$, but the data is suggestive of it along the other directions too. In the absence of clear evidence of saturation for any direction, the observations are consistent

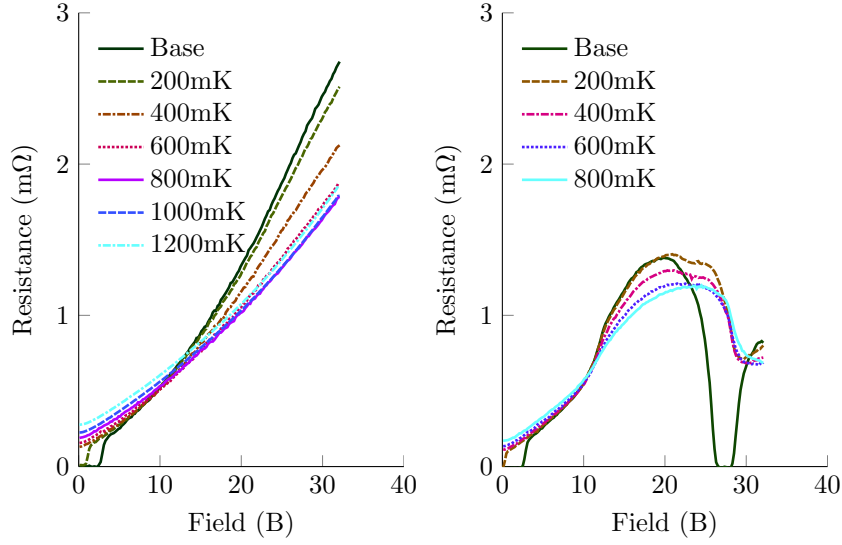


Figure 4.6: Measurements of URhGe#1 (with current mostly along c) at high fields applied close to the a axis show a crossover to a negative temperature coefficient of magnetoresistance. **Left:** Field applied along the a direction. **Right:** Field applied 26° from a towards b .

with compensation. A pair of open orbits, one along the c -direction and one along the a -direction also explain the gross shape of the magnetoresistance in each measurement, and the lack of clearly observed saturation. The presence of open orbits is deemed the more likely explanation, especially in light of the results in section 4.3. In addition to the orbital magnetoresistance, with its implications for the Fermiology, the measurements on a few samples of different RRR allow the identification of several other features related to the moment rotation. These are discussed, with more detailed data, in section 4.7.

4.3 Negative temperature coefficient of resistance

Figure 4.6 shows the temperature dependence of magnetoresistance of a sample of URhGe with the current close to c and the field at two angles near a in the ab -plane. At low field, the resistance increases with temperature, as one would expect, but at high fields the low temperature resistance is nearly 50% more than the resistance at 800 mK, where it goes through a minimum. This sample has been fairly extensively measured, and no such negative temperature coefficient of resistance (NTCR) has been seen with the field applied near the other crystal axes, even at fields of over 30 T. When the field is applied near the b -axis, the temperature coefficient is everywhere positive. When the field is near the c -axis, it is very small but not negative at fields above about 5 T, and positive below that field.

The only other possible occurrence of NTCR observed is shown in the lower left panel of 4.5 where the curves at different temperatures come together just below 15 T. This measurement was taken with $\mathbf{B} \parallel c$ and $\mathbf{i} \parallel a$ – the inverse of the measurement in figure 4.6. In this case, the

temperature coefficient does cross over to be negative, and shows broadly similar features to the first case. But as the measurement was done on a 15 T magnet and the crossover is at higher fields than the first case, the window in which it is observed is very small. Consequently this analysis concentrates on the first case, but bearing in mind the same effect is observed with the field and current directions swapped.

The proposed model for the NTCR is one of dimensional crossover, in a similar manner to that observed in $\text{YBa}_2\text{Cu}_4\text{O}_8$ [84]. The basic premise is that there exist chains of real-space electron density running through the material, which dominate the conductivity under the conditions of the measurement. When a field is applied perpendicular to the chains, the size of the chains perpendicular to the field is set by the amplitude of the electron's real-space orbit. As the field is increased, the chains become narrower and more localised. If a current is being passed perpendicular to both the chains and the field, it relies on the overlap between adjoining chains to progress through the metal. As that overlap reduces, the transport changes from coherent (with positive temperature coefficient) to incoherent (with negative temperature coefficient).

To more fully understand this model, let us consider a simple system with a single chain of electron density running through the centre of the unit cell, with identical chains one lattice constant d away. We define the z axis to be the field direction, the chains to be along y and the current is being passed along x . As we are saying that the electrons are nearly confined to the chains, then for the directions perpendicular to them, the tight binding model seems appropriate. We can assume a dispersion in k_x to be sinusoidal, and choose: $E = -2t_\perp \cos(k_x * d) + f(k_y, k_z)$. Here $f(k_y, k_z)$ is an arbitrary function of k_y and k_z chosen to give two weakly warped Fermi surface sheets open along k_x and k_z . A simple example would be just $f = \hbar^2 k_y^2 / 2m$. This model is sketched in figure 4.7. Given the lattice parameters of URhGe, where b is rather less than a or c , the Fermi surface drawn in the figure should not be considered particularly unlikely or contrived. Indeed it would arise for relatively small changes from the free electron gas, if the filling is chosen so the diameter of the free electron sphere is larger than $2\pi/a$ or $2\pi/c$, but less than $2\pi/b$.

An electron on the Fermi surface will experience a Lorentz force in the usual way. As we have chosen to make the Fermi surface weakly warped, the dominant component of \mathbf{v}_F is directed along y . Thus we can reasonably write the Lorentz force as just $F_{\text{Lorentz}} = \hbar \frac{dk_x}{dt} = ev_{F_y} |\mathbf{B}|$. Integrating with respect to time tells us the position within the Brillouin zone of the electron at time t is $K_x = \frac{e}{\hbar} v_{F_y} |\mathbf{B}| t$, with K_y constrained to keep it on the Fermi surface and no net motion in the k_z direction. To estimate the overlap between adjoining chains, we want to know the amplitude of the real-space periodic motion in the x direction. We can calculate this from the Fermi velocity: $v_{F_x} = \frac{1}{\hbar} \frac{dE}{dk_x} = \frac{2t_\perp d}{\hbar} \sin(k_x d)$. Integrating to give the position yields a semiclassical

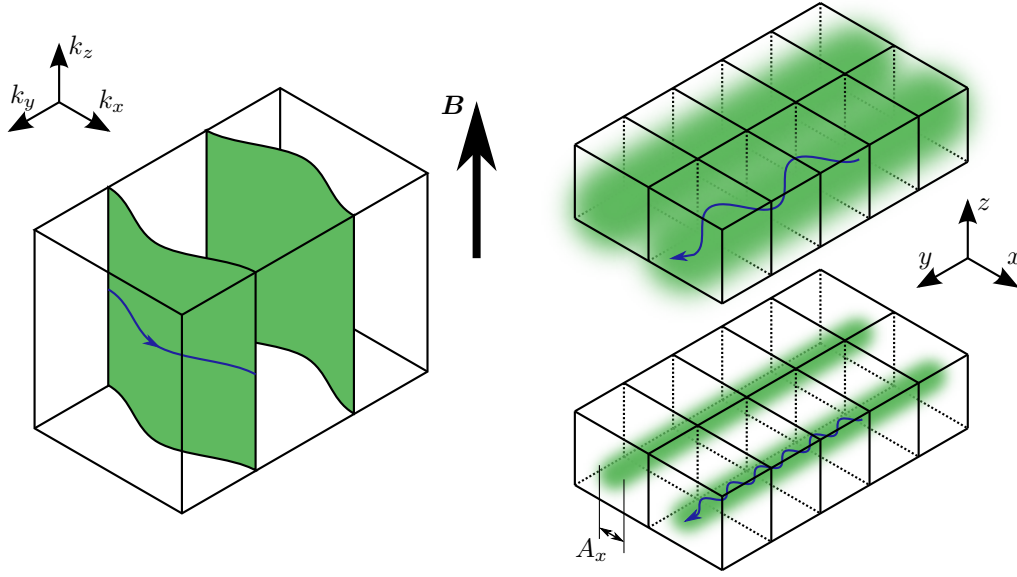


Figure 4.7: Simplified model for NCTR. **left:** Brillouin zone; **top right:** Real-space low field coherent state; **bottom right:** Real-space high field incoherent state. The green areas represent the whole population of electrons contributing to the effect, the blue lines show the path of a single ‘probe’ electron created just above the Fermi surface.

real-space sinusoidal motion with amplitude:

$$A_x = \frac{2t_{\perp}}{ev_{F_y}|B|} \quad (4.2)$$

Broadly speaking, we would expect coherent transport when $A_x > d$ and incoherent transport when $A_x < d$. In the latter case the lack of spatial overlap of the wavefunctions associated with adjacent chains removes their ability to hybridise.

One interesting result here is that A_x does not depend on τ . Of course implicit in the calculation is the assumption that the electron lives long enough to make a periodic motion, so $\omega_c\tau$ must not be much less than one. This is consistent with the observation of quantum oscillations above 8 T in the high quality sample. It can also explain why NTCR is not seen in the top right panel of figure 4.5, which has the same measurement geometry as the high quality sample. The RRR of URhGe.barC2 is a factor of 12 less than that of URhGe#1. These RRRs should be comparable, as the current direction is the same, barA2, which shows possible NCTR in the lower left panel has an RRR in between, but the different current direction makes quantitative comparison less reliable.

A second important note is that although we chose a dispersion based on the tight binding model, where t_{\perp} would be meaningful in terms of the single atom (or chain in this case) orbital overlap, the model still works if it is simply used as a measure of the band width measured along the path of the electron across the sheet. Similarly although the choice of the sinusoidal dispersion is useful in illustrating the model and deriving the results, any dispersion will do, provided the

resulting Fermi surface remains weakly warped.

It is well worth considering the ways in which this model can be extended and made more general, in order to better gauge the applicability to URhGe. The first question that arises is that of open sheets. The discussion above assumes open sheets as that seems the logical consequence of chains of electron density. But there is no explicit requirement for the sheet to be open in the k_z direction. However, for the sheet to be closed, it must curve over to meet itself, and this necessarily dictates that the Fermi velocity on that part of the sheet have a substantial z component. In writing the Lorentz force as we did, we assumed \mathbf{v}_F was directed predominantly along y , but a velocity parallel to the field does not change the Lorentz force, so this is not a problem. A non-oscillatory component of \mathbf{v}_F along z is of course at odds with the statement that electrons are confined to chains. It should be clear that in this case the electrons would be confined instead to planes normal to the x direction, but the result still stands. Obviously in this case the only geometry leading to NTCR is the one described. To also observe NTCR with the field and current swapped, as in URhGe would require a second set of planes perpendicular to the first and second Fermi surface tube, also perpendicular to the first. This is only possible if the planes are interpenetrating, yet somehow protected from hybridization. Alternatively, a change in topology of the Fermi surface due to field may be possible in URhGe due to field changing behaviour of the bands at the zone face. This in turn could change the topology of the Fermi surface, a possibility which is discussed further in section 4.4.

It is also useful to consider the consequences of applying the field or current away from the crystalline axes. If the field is rotated away from z towards x , this will affect the model only insofar as the Lorentz force now drives the electrons along the k_z direction. If the Fermi sheet is open in the k_z direction, this makes little difference, the excited electrons still maintain a velocity which is predominantly along y and the only effect is to reduce the $|\mathbf{B}|$ which enters into the expression for A_x to the component of field projected along the z -axis, denoted B_z . If the sheet is closed in the k_z direction, and forms a tube, the electron would be driven in a spiral along the tube. The model remains valid only if the tube is near-cylindrical, with only weak warping along the open direction. If the field is rotated away from z towards y , this will again only enter through the Lorentz force. As the electron velocity is predominantly along y , there is no new component to the force, only a reduction in amplitude. As above, the only change is to replace $|\mathbf{B}|$ with B_z throughout.

If the current is passed other than straight along x , the result depends on the other conductivity channels present. If the chain bands remain the dominant conductor, then the transport can be thought of a coherent transport along chains and/or between them in the z direction, and coherent-becoming-incoherent transport in the other direction. The coherent-to-incoherent crossover will happen at the same point, but there will be some extra coherent transport in series.

So to summarise, this model indicates that if: i) There exist chains of electron density in the

material and ii) The current is measured perpendicular to the chains and iii) The field is applied with a component perpendicular to both the current and the chains and iv) The chains correspond to a Fermi surface sheet which supports open orbits in the current measurement direction; then the conductivity can cross over to incoherent when the field causes $A_x < d$. To apply this to URhGe we note the two conditions where NTCR is observed, as detailed at the start of this section, namely $\mathbf{B} \parallel a, \mathbf{i} \parallel c$ and $\mathbf{B} \parallel c, \mathbf{i} \parallel a$. Thus we can apply the model in two ways, either $x \rightarrow c, y \rightarrow b, z \rightarrow a$ or $x \rightarrow a, y \rightarrow b, z \rightarrow c$. Both of these are consistent with there being chains of electron density along the b axis of the material. It would require that the associated sheet is open along the k_a and k_c directions, at least under the conditions of the measurements. The possibility remains that the orbits are only open along k_a and k_c when the model requires it, but could be closed otherwise, if the field changes the Fermi surface topology.

The coherent-to-incoherent crossover should happen at a single, well defined field. One would expect all the resistance curves to cross through a single point at this field, as seen in $\text{YBa}_2\text{Cu}_4\text{O}_8$ [84], but they do not. One possible reason for this is the presence of another component to the resistance in series with the component that is crossing over, such as those described above. This is especially likely as the current in URhGe#1 is unlikely to be perfectly along c . In barA2 the current is directed along a , and the spread in crossing points is still present, but a smaller fraction of the crossover \mathbf{B} . If the chain band is strongest, but does not dominate, other bands could also contribute in parallel. If that other band has a more usual temperature dependence, that could cause the crossing points to spread out slightly.

Figure 4.8 shows the locations in the ab plane where NTCR is observed. This graph was made by taking field ramps at several temperature between the base temperature of the refrigerator (about 50 mK) and 1 K, at each of 8 different angles in the ab plane. For each angle, every ramp is compared to the ones adjacent in temperature, and if the lower temperature one shows a higher resistance, a green line is drawn on the graph. The brightness of the green line indicates the average temperature of the ramps being compared. Thus the the data in the left panel in 4.6 is the source of the green lines along the y-axis, and the right panel the green lines crossing the graph at 26 degrees from the y-axis. Also shown on the graph are the extent of the superconductivity at zero field (taken from Levy *et al* [30]) and the high field superconductivity. The latter is taken in the same way as as the NTCR data, but uses only the lowest temperature ramp, and includes a few extra angles where only the base temperature was measured. It is the same data in figure 4.3. That the superconductivity persists up to the limit of the magnet at over 30 T, even though the maximum T_c is less than half a Kelvin, is quite remarkable — see section 4.7 for discussion.

There can obviously be no NTCR when the sample is superconducting. Also, in this sample, and indeed in all URhGe samples, the onset of superconductivity is not particularly sharp as a function of field, temperature or angle. It is therefore expected that NCTR is suppressed both in and around superconductivity. The peak represented by the grey line also affects the appearance

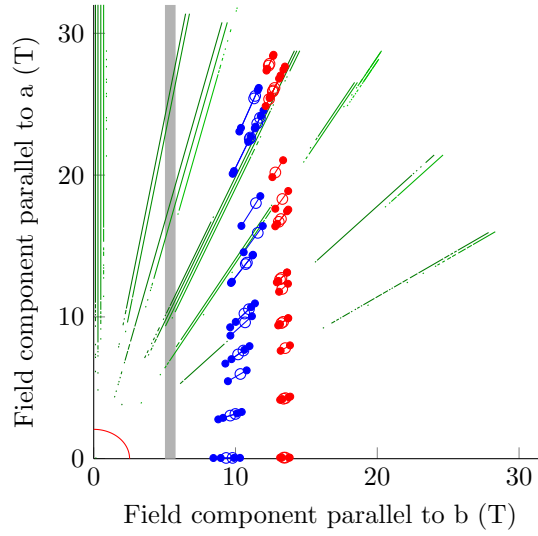


Figure 4.8: Phase diagram showing the observations of superconductivity and NTCR as the field is rotated through the ab plane in URhGe#1 (which has current mostly along c), constructed from field sweeps at various angles. Red line near the origin: superconductivity at low temperature. Red and blue circles: the upper and lower edge of superconductivity at low temperature and high field. Small filled circles show the 10%–90% transition width. Green lines show areas where at some temperature $\frac{d\rho}{dT}$ is negative, paler green lines indicate higher temperatures. The vertical thick grey line has the same meaning as in figure 4.3; it marks the position of a small peak in $\frac{d\rho}{dB}$ which always occurs at constant B_b and broadens slightly with temperature.

of NTCR. The origin of this peak is not known, and is not seen in other samples, so is ascribed to some oddity of contact positioning or inhomogeneity. In practice it is a slight increase in the resistance above the smooth background, which is easiest to detect as a peak in $\frac{d\rho}{dB}$. This peak broadens out as temperature increases, which has the effect of locally reducing $\frac{d\rho}{dT}$ just above it in field and locally increasing $\frac{d\rho}{dT}$ just below. Thus in the area of $B_b = 5$ T, $B_a = 7$ T the weak NTCR is lost, and near $B_b = 9$ T, $B_a = 5$ NTCR may be observed where it should not be.

Taking these other features into account, it is clear that NTCR is observed for all fields where $B_a \gtrsim 6$ T. The way in which NTCR is lost as the field is rotated towards the b axis is also informative. As well as the crossover field moving out to higher field as the tangent of angle from a , the magnitude of the NTCR is reduced. This is also to be expected if the effect depends solely on B_a , and matches the predictions of the model given above, for open sheets. This is further evidence that the sheets are open all the time, not only when the field is applied along certain directions.

What is a bit more surprising is that NTCR is seen equally on the left and right sides of the graph. There have been no direct measurements of magnetic moment with a strong field applied at angles between the a - and b -axes, not least because the area of interest rapidly moves beyond the range of superconducting magnets. It is believed though that the superconductivity and moment rotation transition are closely linked, and the latter occurs at constant B_b , where the former is observed. This is reinforced by the observation of a major change in resistance crossing

$B_b = 12T$ in our data (visible in figure 4.6, right panel) where the current is along c . A peak in resistivity when the current is passed along b [30] also supports this theory. These two observations are wholly consistent with the observations regarding the current-direction dependent changes in resistance at the moment rotation transition in section 4.2.

The major changes in conductivity along c suggest a change in Fermi surface, which is quite possible given the change in magnetization and hence in (\mathbf{k} -dependent) spin-splitting. The continued observation of NTCR implies it is robust against such changes, and that the Fermi surface sheet responsible keeps most of its nature as the spin-splitting changes, and remains the dominant band. This observation is not necessarily at odds with the observation that the resistance changes by a factor of nearly two across the transition. For the onset and strength of the NCTR to remain the same requires that the key values in equation 4.2 must remain the same. This does not require that the Fermi surface sheet remain at exactly the same position in the Brillouin zone, just that its dispersion along k_x remains approximately the same. Nor does it require that the density of states remain exactly the same, or the scattering rate. Changes to these can affect the overall conductivity of the system without invalidating the model. The lack of coupling to the magnetic moment change could also indicate that the relevant band is predominantly of s , p or d nature, as the magnetic changes mostly involve hybridised f -electron bands.

This in turn implies that it is worthwhile to consider the zero field behaviour of URhGe at temperatures above the Curie temperature. The relevant data is considered in more detail in section 4.1. If the physics underlying the NTCR is robust against the change in spin-splitting at the moment rotation transition, it may also be reasonably robust against the changes at T_{Curie} . Above the Curie temperature the resistance shows a substantially different temperature dependence for currents along b than for currents along either a or c , with the latter showing evidence of incoherent transport. This strongly supports the idea of chains along the b axis. The zero-field temperature induced crossover from coherent to incoherent type behaviour can also give us an indicator of t_{\perp} . One would expect the crossover at around $k_B T = 4t_{\perp}$ [84], so the resistivity peak at 15 K would imply $t_{\perp} \approx 0.4$ meV. This of course assumes that t_{\perp} is the same above and below T_{Curie} , which is considered likely but far from certain. The fact that the maxima are at the same temperature for both current directions indicates that t_{\perp} is the same in both directions; this is consistent with both geometries where NTCR is observed being due to the same warped sheet.

Figure 4.9 shows the actual temperature dependence at different fields. In the simple model where there exists only one band, which undergoes the coherent-to-incoherent crossover, the resistivity would be expected to diverge at low temperature at fields above the crossover field. The data appears to show the resistivity saturating rather than continuing to diverge. One possible reason for this is an erroneous thermometer reading at low temperature: moving all the low temperature points to the right would restore the divergence. This is particularly a risk

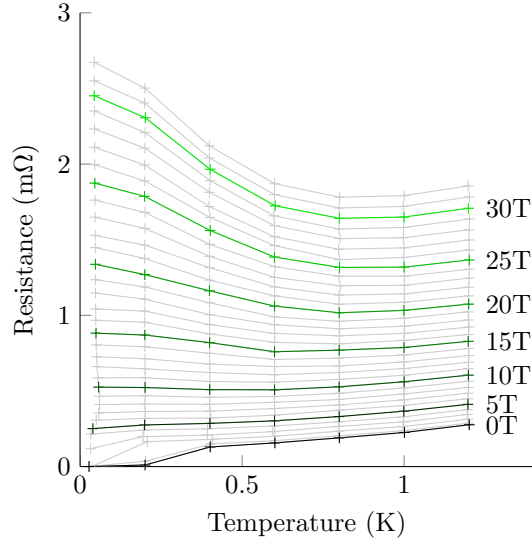


Figure 4.9: Temperature dependence of resistance of URhGe#1 (which has current mostly along c) with $\mathbf{B} \parallel a$, extracted from the field sweeps in figure 4.6.

on high field measurements where the thermometer is some distance from the sample (albeit immersed in mixture with it) and lacking a full field calibration. An error of around 100% would be needed to restore the divergence though, and this seems excessive. The observation of quantum oscillations at high field also suggest this is not the case. Another more likely explanation is a second band providing a parallel conduction channel, with its own magnetoresistance. If at any given field this band alone is capable of providing a conductivity of less than the chain band in its coherent state, then it will have only minor influence on the measured resistivity at all but the lowest temperatures. As the conductivity of the chain band drops off, the conductivity of this other band dominates, and the resistivity saturates near the value given by the second band alone.

It seems most likely then that there are chains of electron density running along the b direction, which correspond to a pair of Fermi surface sheets which are open in both k_a and k_c directions. We can then use equation 4.2 to make some rough qualitative statements about the sheets in question. If we assume that there is one chain per unit cell, then d is 748 pm when measured along c and 682 pm when measured along a . There is no obvious location for the chains based in the crystal structure*, so we must also consider that there may be multiple chains. Based on the high-temperature data, we assume that t_{\perp} is the same for both measured geometries. We can also assume that v_{F_b} is not hugely different, as the same sheet gives rise to the effect in both geometries – the only potential variation is due to different averaging by different electron paths across the sheet. Referring to figures 4.6 and 4.5, we see that the crossover field is not particularly

*Many authors draw the crystal structure with lines joining nearest-neighbour U atoms, and talk about these as chains. They are along the a axis, which precludes them from being the origin of the effect reported here. The next nearest neighbour is along the b axis, and is only slightly longer

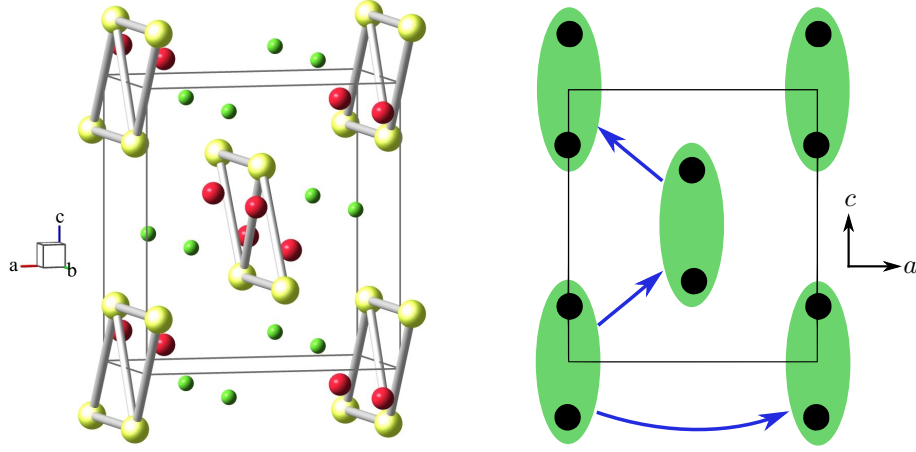


Figure 4.10: **Left:** Possible location of chains of electron density in the URhGe structure, with two chains per unit cell. The bonds are drawn linking uranium atoms into chains. The shortest distance between uranium ions is actually along the a axis, at 349 pm. But the next shortest is only a little longer at 374 pm, these are the zig-zag elements of the chains as drawn. The bonds along the edge of the chains are the third shortest distance at 432 pm. **Right:** Unit cell showing only uranium ions. Electrons hopping along the a direction see one chain per unit cell, whereas those moving along the c direction see two.

clear, probably due to other bands as described above, but in the $\mathbf{i} \parallel a$ case it is about 8 T and in the $\mathbf{i} \parallel c$ case it is nearer 15 T. Given that t_{\perp} is similar in both geometries and v_{F_b} is similar in both geometries, this suggests that the difference is in d , despite the similarity of the lattice parameters. This is possible if each unit cell has two chains running through it, positioned so that current flowing along c passes through both, but current along a passes through only one. The position of the chains would be constrained by the symmetry of the crystal, but there are several possible such positions. One obvious choice is the uranium atoms, as shown in figure 4.10. These chains are not nearest neighbours, but their spacing is only slightly more than the nearest neighbour distance, and they are arranged so that electrons moving along c are more likely to visit both chains. It should be borne in mind however that this ignores the possibility that the crossover field in the $\mathbf{i} \parallel a$ case could be artificially moved up to a higher field by low $\omega_c \tau$, in which case one chain per cell would be a reasonable conclusion.

Using the values for d this yields, combined with the estimate for t_{\perp} from the high temperature data and the observed fields given above, $v_{F_b} = v_{F_y}$ is required by equation 4.2 to be around 2×10^5 m/s. Using the same values in the expression for $v_{F_x} = v_{F_a}$ or v_{F_c} in the simple model used at the beginning of this section yields around 1×10^4 m/s. This implies the gradient of E along k_b is more than ten times the gradient in the perpendicular direction, which is consistent with the model requiring the sheet be weakly warped.

It is possible to estimate a contribution to the specific heat from this sheet. We may write the density of states as $g(E_F) = \frac{A}{\hbar v_F (2\pi)^3}$ where A is the area of the Fermi surface sheet, and the specific heat γ as $\frac{\pi^3}{3} k_B^2 g(E_F)$. Assuming there are two non-degenerate sheets which completely

cross the Brillouin zone perpendicular to k_b , this gives $\gamma_{open} = 0.6 \text{ mJmol}^{-1}\text{K}^{-2}$. So these sheets, being light, make a negligible contribution to the measured γ of $160 \text{ mJmol}^{-1}\text{K}^{-2}$.

Given this value of v_F and the mean free path from Shubnikov-de Haas measurements[39], the scattering time should be $\tau \sim 2 \times 10^{-13} \text{ s}$. Entering these values into equation 1.2 and setting $|\mathbf{v}_F| = v_F^x$ yields $0.1 \mu\Omega\text{cm}$. The low temperature resistivity of the sample in which that mean free path was measured is $\sim 2 \mu\Omega\text{cm}$, but it was measured with the current along the c axis. Low temperature resistivity along c is typically larger than along b , so these values agree within roughly an order of magnitude. Given the very approximate nature of the calculation and the assumptions regarding t_\perp , this level of agreement is acceptable. This further supports the accuracy of the model where these sheets dominate the conductivity.

In summary, the observed NTCR with $\mathbf{B} \parallel a$, $\mathbf{i} \parallel c$ and *vice-versa* is completely consistent with a model of chains of electron density running along the b -axis, and a corresponding pair of weakly warped sheets which are open in the k_a and k_c directions. The latter observation is also consistent with general magnetoresistance measurements set out in section 4.2. It is deemed likely that there are two chains per unit cell, positioned so that current travelling along a passes through both, but current travelling along c passes through only one. One chain per cell is also possible. These Fermi surfaces are robust against the changes in spin-splitting which occur at the moment rotation transition, and probably also the changes at T_{Curie} . If the latter is true, the band width measured along a line perpendicular to k_b , is of order $t_\perp = 0.4 \text{ meV}$ and the Fermi velocity directed along the chains is of order $2 \times 10^5 \text{ m/s}$.

4.4 Symmetry considerations and calculations

4.4.1 Symmetry considerations

Before discussing the calculations which have been made by various authors on URhGe, it is pertinent to discuss the symmetry constraints of the material. Let us begin with the crystal structure, ignoring for now any considerations related to spin-orbit coupling, magnetic field or magnetism. The group Pnma has eight symmetry operations (in addition to the translation operations of the lattice), given in table 4.1. Of particular interest are numbers 2, 3 and 4: the twofold screw symmetries.

Twofold screw symmetries have some important consequences for the band structure at the zone faces. For the sake of argument, let us consider the face perpendicular to k_z , containing the points Z, U, T and R (see figure 4.11 for the position of these points on an orthorhombic zone). At all points on this plane there are two equivalent crystal momenta, $(k_x, k_y, \frac{\pi}{c})$ and $(k_x, k_y, -\frac{\pi}{c})$. As the crystal has spatial inversion symmetry one expects the energy of an $k_z = \pi/c$ electron to be the same as a $k_z = -\pi/c$ one and $E(k_x, k_y, k_z) = E(k_x, k_y, -k_z)$. At the zone face, both these momenta are the same, and the states would be degenerate. In general however, there is

No.	Notation	Description
1	1	The identity.
2	2 ($\mathbf{0}, \mathbf{0}, \frac{1}{2}$) $\frac{1}{4}, \mathbf{0}, z$	Screw, rotate 180° about the line $\frac{1}{4}, 0, z$ then translate along c by half a unit cell.
3	2 ($\mathbf{0}, \frac{1}{2}, \mathbf{0}$) $\mathbf{0}, y, \mathbf{0}$	Screw, rotate 180° about the line $0, y, 0$ then translate along b by half a unit cell.
4	2 ($\frac{1}{2}, \mathbf{0}, \mathbf{0}$) $x, \frac{1}{4}, \frac{1}{4}$	Screw, rotate 180° about the line $x, \frac{1}{4}, \frac{1}{4}$ then translate along a by half a unit cell.
5	$\bar{1}$ ($\mathbf{0}, \mathbf{0}, \mathbf{0}$)	Inversion, about the origin.
6	a ($\frac{1}{2}\mathbf{0}, \mathbf{0}$) $x, y, \frac{1}{4}$	Glide, mirror about the $c = \frac{1}{4}$ plane, then translate half a unit cell in the a direction
7	m $x, \frac{1}{4}, z$	Mirror about the $b = \frac{1}{4}$ plane
8	n ($\mathbf{0}, \frac{1}{2}, \frac{1}{2}$) $\frac{1}{4}, y, z$	Diagonal glide, mirror about the $a = \frac{1}{4}$ plane, then translate by $(0, \frac{1}{2}, \frac{1}{2})$.

Table 4.1: Symmetries of the Pnma space group, as listed in the interational tables[89]. These apply to the ion locations in URhGe, and thus the lattice potential. Not listed are the implicit primitive translations $\mathbf{t}(\mathbf{1}, \mathbf{0}, \mathbf{0})$, $\mathbf{t}(\mathbf{0}, \mathbf{1}, \mathbf{0})$ and $\mathbf{t}(\mathbf{0}, \mathbf{0}, \mathbf{1})$. Of course as the lattice is static it also has the time reversal symmetry operation \mathbf{T}

some part of the lattice potential which will mix them to provide two new states slightly split; the band crossing becomes an anticrossing.

In the absence of spin or magnetism, the Hamiltonian obeys the space group symmetry. With this, Herring[90] uses group theory considerations to demonstrate that in the presence of a twofold screw symmetry, this mixing does not take place, and the bands remain degenerate. The crux of the argument is that the screw symmetry operation, followed by the time reversal operation, maps the wavefunction of the state at $(k_x, k_y, \frac{\pi}{c})$ to the one at $(k_x, k_y, -\frac{\pi}{c})$. If the electron fluid does not break these symmetries, the energy of the two states must remain the same. Most of the discussion at the time focused on the hexagonal close packed metals, but the argument applies to any material with both time reversal and a twofold screw. It enforces a degeneracy on the two zone faces perpendicular to the axis of the screw. For URhGe in the paramagnetic state there is a screw along each axis, and time reversal symmetry, so all faces of the BZ are ‘screw degenerate’. This is in addition to the spin-degeneracy which occurs everywhere in the zone in the non-magnetic case.

In the presence of a magnetic field, the Hamiltonian is more complicated because the time reversal symmetry is lost. However, Herring’s argument still applies if the combined operation of screw and time reversal still stands, even if the individual operations do not. By considering the effect of the symmetry operations on spinning spheres* with the rotation axis aligned with field,

*Spinning spheres are the simplest object which breaks time reversal symmetry, they are also a good model for orbital magnetism, but a poor one for electron spins, which are more complicated. Here we only care about a symmetry breaking object.

the following symmetry rules are self evident:

1. A twofold rotation with axis parallel to $\mu_0\mathbf{H}$ preserves the sense of the rotating sphere, so the symmetry operation is preserved.
2. A twofold rotation with axis perpendicular to $\mu_0\mathbf{H}$ reverses the direction of a spinning sphere, so this symmetry operation is lost. The combination of the rotation and a time reversal however preserve the spinning sphere, so this new operation of ‘time reversal rotation’ joins the symmetry group instead.
3. A mirror about a plane which contains $\mu_0\mathbf{H}$ preserves the spinning sphere, so preserves the symmetry operation.
4. A mirror about a plane perpendicular to $\mu_0\mathbf{H}$ reverses the rotation direction, so the new operation is the combination of the mirror and time reversal.

And it should be noted that any rule which applies to a rotation also applies to a screw, and any rule that applies to a mirror, also applies to a glide. This is simply because we can separate the space and time parts, and is equivalent to saying the eigenstates are a Bloch wave consisting of the product of an $e^{-i\mathbf{k}\cdot\mathbf{r}}$ part, a part with the lattice periodicity and a spin part.

By applying the rules above to the space group operations in table 4.1, we can obtain a new set of symmetry operations for the magnetic material. This new group is referred to as the magnetic double group of the Pnma space group. Let us take the example of the zero field magnetization below the curie temperature, where the spontaneous field lies along c . Operations 1 and 5, (inversion and identity), and the primitive translations are unaffected, whilst time reversal is lost. Operation 2 is preserved, operations 3 and 4 are replaced with a time reversal screw. Operation 6 is preserved and operations 7 and 8 become time reversal glides/mirrors. If time reversal were not included, the preserved symmetries would be 1, 5, 2 and 6, which form a subgroup of the Pnma group, as they should. If the rules above are applied correctly, the preserved operations must always form a subgroup.

Straight away then, we can see that some of the results from Herring’s work still stand in the magnetic case. In his work he applies the screw and time reversal separately, but both are required and the time reversal no longer exists on its own. Thus the degeneracy is preserved on the BZ faces which lie perpendicular to a time reversal screw. For URhGe, this implies a degeneracy on the BZ faces which are not perpendicular to the field. Whilst the absence of a time reversal screw implies the degeneracy can be lifted on the remaining face, it may still be enforced on some high-symmetry lines. Removing a symmetry enforcement on the degeneracy does not mean the degeneracy is lifted, just that it can be lifted. In practice it normally is, and if it is not there is probably another symmetry enforcing it which has not been considered.

It is also worth considering a case where the field is not aligned with a crystal axis. In this case, the field can be perpendicular to one screw (if it is directed in a plane containing two crystal axes) or perpendicular to none. In the former case that screw is replaced by a time reversal screw, as

above. For screw axes that are neither parallel nor perpendicular, the screw-transformed spinning sphere cannot be transformed back to its original form by a time reversal. In this case, neither the screw nor the time reversal screw enter the double group. For our purposes, only time reversal screws are relevant, so the degeneracy is only preserved if the field is perpendicular to the screw controlling it. Equivalently, the degeneracy is lifted on all faces which have some perpendicular component of magnetic field.

Whilst field can remove the enforced degeneracy, it is not correct to say that a gap will necessarily open up. For a gap to appear, one requires an interaction which splits the energy of the two states. One common choice is spin-orbit interaction (SOI). SOI alone breaks neither the symmetry of the lattice nor time reversal, so cannot lift the screw degeneracy. Rather it enters into the manner in which the degeneracy is lifted by field. In a ferromagnet like URhGe, where the spin-splitting can be assumed to be much larger than the energy scale of SOI, the spin quantization axis is chosen by the ferromagnetic moment. The ferromagnetism also breaks the spin degeneracy on a scale of the exchange energy which is much larger than that of SOI, so we can consider now a single band which is degenerate with itself only at the zone boundary. The SOI is then free to lift that degeneracy. The energy scale of spin orbit is often sufficient to provide a gap between the two bands of order tens to hundreds of millielectronvolts. At low fields, this makes a distinct gap, and an electron driven along the Fermi surface by the field will always reappear on the same band when it crosses the Brillouin zone boundary. This energy gap is still small enough though that at higher fields magnetic breakdown effects are to be expected.

One well-known example of SOI causing unusual changes in the Fermi surface of a ferromagnet is in nickel, where small ellipsoidal pockets at the X points show substantial changes in their size as a function of field direction[91]. Another well-known example where some of these effects can be seen is in the divalent hexagonal metals. These crystallise in a hcp lattice which has a screw symmetry perpendicular to the hexagonal face of the zone. None of them are magnetic, so SOI is only able to open a gap with symmetry broken by the application of field. In the light metals, spin orbit is small and the effect is often lost to magnetic breakdown before it is observed at high field. In the heavy metals it is stronger[92]. Elliot[93] calculated the double group for hcp and various other lattices, and Cohen and Falicov[94] used these, together with their own calculations to make predictions about the connectivity of the Fermi surfaces, in particular of Mg. Finally, Joseph *et al*[95] observed the splitting in Zn and Cd directly via quantum oscillations.

We now turn to the practical consequences for URhGe. In the absence of any field or SOI, paramagnetic URhGe would have a fourfold degeneracy on every BZ face. Twofold due to spin, and twofold due to the screw axes. Away from the zone faces, the twofold spin degeneracy would remain, but the screw degeneracy is not enforced. This implies that the bands cross at the BZ face, rather than the more usual anticrossing. When considering the path of a probe electron driven around a Fermi surface sheet by field, the behaviour at the zone edge is different. If there

is an anticrossing, the electron reappears at the other side of the zone on the same sheet it was on when it left. If the degeneracy is not lifted, it will reappear on the other sheet in the degenerate pair. One result of this is that when the Fermi surface reaches the BZ face, the usual extremal neck orbit will not be present.

When splitting is introduced, which can only happen on zone faces with a component of field perpendicular, the crossing changes into an anticrossing. The energy gap between the two bands is limited to the energy scale of the interaction causing the splitting. Whilst atomic spin-orbit interaction can be large, the splitting of bands is usually observed to be very small, this results in a very narrow gap between the bands. There will usually be an extremal orbit on the BZ face, but these small gaps imply it will readily undergo magnetic breakdown. Similarly, the splitting can change the topology of any orbits which cross a zone face, but the original topology can be restored by magnetic breakdown.

4.4.2 DFT calculations

There have been various attempts to calculate some of the electronic properties of URhGe using density functional theory (DFT), in particular under the local spin density approximation (LSDA). In order to understand and analyse the calculations presented in the literature, a simple understanding of DFT is required, and the following introduction is based on the work of Cottenier[96].

DFT is based on the observation by Hohenberg and Kohn[97] that the energy of the system:

$$\langle \Phi | \hat{H} | \Phi \rangle = \langle \Phi | \hat{T} + \hat{V}_{int} + \hat{V}_{ext} | \Phi \rangle \quad (4.3)$$

where \hat{T} is the kinetic energy, \hat{V}_{ext} the potential energy of interactions with the lattice and \hat{V}_{int} the potential energy due to electron electron interactions; can be re-written as:

$$\langle \Phi | \hat{H} | \Phi \rangle = E[n(\mathbf{r})] = F_{HK}[n(\mathbf{r})] + \int n(\mathbf{r}) V_{ext} d\mathbf{r} \quad (4.4)$$

Here, everything is expressed in terms of functionals of the electron density $n(\mathbf{r})$. Critically, the lattice, and hence the specific details of any particular problem only enter through the second term. The problem of minimising the energy of interacting electrons in a lattice is then simplified to minimising the combined energy of the non-interacting electrons in a lattice and the functional $F_{HK}[n(\mathbf{r})]$ which is independent of the problem considered. Kohn and Sham[98] then went on to show that $F_{HK}[n(\mathbf{r})]$ could be written as:

$$F_{HK}[n(\mathbf{r})] = T_0[n(\mathbf{r})] + V_H[n(\mathbf{r})] + V_{xc}[n(\mathbf{r})] \quad (4.5)$$

where $T_0[n(\mathbf{r})]$ is the functional for the kinetic energy of a non-interacting electron gas; $V_H[n(\mathbf{r})]$ is

the Hartree term for electron-electron coulomb repulsion, and $V_{xc}[n(\mathbf{r})]$ includes the complicated exchange and correlation parts. One can then use this to construct a Hamiltonian, known as the Kohn-Sham Hamiltonian, for a system of a non-interacting electron gas in an effective potential which consists of a lattice part and an exchange-correlation part. It is this equation that is solved to obtain a set of eigenstates, and thus the electron density.

This becomes a self consistency problem: The density depends on the eigenstates, the eigenstates on the parameters of the equation and the parameters of the equation on the density. To find the ground state density, one must begin with a guess of the electron density, construct the potentials and thus the Kohn-Sham equation, solve it to get the eigenstates, and construct from them a new density. The process is repeated until the density converges between iterations, at which point the ground state is known.

Practical DFT calculations can be thought of as consisting of three parts. Firstly, one must formulate the problem. Whilst this can in theory be exact, it usually involves approximations when constructing the exchange-correlation term. The simplest class, known as local density approximation (LDA), uses $V_{XC}(n) = \int \epsilon_{XC}[n(\mathbf{r})]n(\mathbf{r})d^3\mathbf{r}$, but these cannot represent any spin-physics. The local spin density (LSDA) is the next class, where $V_{XC}(n^\uparrow, n^\downarrow) = \int \epsilon_{XC}[n^\uparrow(\mathbf{r}), n^\downarrow(\mathbf{r})]n(\mathbf{r})d^3\mathbf{r}$ and other more complex approximations also exist. These might include ∇n terms (GGA), or additional on-site repulsion (U). Another decision which must be made at this stage is the equation to solve: Schrödinger's equation, Dirac's equation, or an approximation in-between. This has implications for the accuracy at which spin-orbit enters (if at all).

Once the free energy functional has been constructed, it must be solved. In this stage, a suitable basis set is selected, and the density $n(\mathbf{r})$ constructed from it. In theory, any complete basis set allows the correct density to be found, but in practice, choosing a good basis set is necessary to make the solver converge quickly, or even at all. One logical basis set is the augmented plane wave (APW) set, this uses atomic orbitals within a sphere centred on each ion, and plane waves in the gaps in-between. In practice this set is very slow to work with, and a linearised set is used instead (LAPW). Core electrons for the ions in the lattice can be included in the basis set, at the cost of increased complexity (LAPW+LO), or in the lattice potential around each ion. There are also several variations on this, including RLAPW, where the full relativistic orbitals are used.

Finally, the results can be interpreted. The electron density is exact, insofar as the approximations made in constructing the functionals are correct. The eigenstates on the other hand are strictly the eigenstates of the Kohn-Sham equation, not the original system. In practice however, they are usually adequate, and are presented as the band structure of the material, including interactions. This practice is equivalent to saying that the Kohn-Sham effective potential is a good mean-field approximation to the interacting problem, which it usually is. Calculating such properties as the density of states from the resulting band structure is usually quite reliable and

straightforward. Features like Fermi surface topologies can be harder, as they can depend crucially on the shape of the band and the precise Fermi energy. In particular, when flat bands such as those found in *f*-electron materials are present, a tiny rigid shift of a band relative to the others, or a small error on the Fermi energy, can hugely change the shape and size of the resulting Fermi surface pockets.

Early calculations then focused on the simpler properties. The first calculations appeared in 2002[99, 100], using LSDA and LAPW. At this time there was still some uncertainty about the magnetic structure[27, 26], but the calculations agree with the structure which is now known to be correct for single crystals. Both of these calculations show that the electron states near the Fermi surface have a substantial $U5f$ weight, with $Rh4d$ also contributing slightly at the Fermi level, and more substantially 2–5 eV below. Both calculations also obtain roughly correct magnetization ($0.31 \mu_B$ [99] and $0.25 \mu_B$ [100], compared to experimental values of 0.37 – $0.42 \mu_B$ [25, 29]). Both papers also note that this arises as a result of larger spin and orbital moments which are directed in opposite directions, with orbital component being slightly larger than spin. Shick[100] also completes the calculation with a Hubbard U term (LSDA+ U), which would be appropriate if the $U5f$ electrons had some localised character, but finds the model without U to be more accurate. This is further evidence of URhGe’s itinerant nature. These calculations predict different magnetic anisotropy energies for the *a*- and *b*-directions, which qualitatively agree with the observation that the magnetization can be rotated abruptly towards *b* with a field $B_b \approx 12$ T, but the material has very little response to fields in the *a* direction. Finally, the calculated DOS can be compared with valence band photoemission studies[101], which show general agreement. Between calculations, and compared to the photoemission data, the agreement is generally qualitative, but differences in detail, and in the position of the Fermi level relative to the spectra, remain.

Another more recent paper[102] repeats the calculation, again using LSDA and LAPW, with similar results. They also consider the consequences of changing the unit cell size, through pressure, and its effect on the spin and orbit parts of the magnetization. Their prediction is that at a pressure near 50 GPa they should become equal, leading to a zero moment ferromagnet. Pressure measurements on URhGe extend up to 13 GPa[41], and include resistivity and heat capacity, but not magnetization which would be a useful test of these predictions.

Very recently, two attempts have been made to obtain band structures and Fermi surfaces for URhGe. One is published as part of a paper on ARPES[104]. The other is recently completed by Ed Yelland[103]. Fermi surfaces from these two calculations are presented side by side in figure 4.11. Unfortunately the calculated surfaces are quite different. [104] also includes band structure plots for the SY, X Γ and UZ high symmetry lines, which can be compared to the band structures from [103]. Whilst it is in some places possible to identify bands from one calculation with those from the other, even these also show qualitative disagreements in shape. The two calculations are

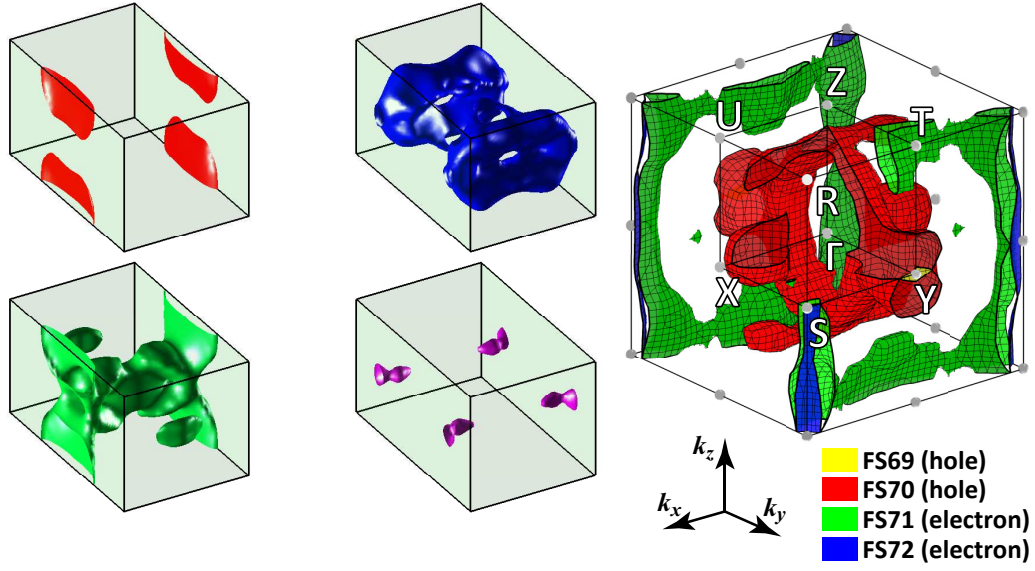


Figure 4.11: Calculated Fermi surfaces for URhGe. **Left:** Calculation from [103], using LAPW and LSDA. It is polarised $M \parallel c$ and the bands are mixed spin due to SOI, which is included at the scalar relativistic level. **Right:** Calculation from [104], using RLAPW and LDA, for the paramagnetic state. Both calculations treat all U-5*f* electrons as itinerant. Both calculated structures are oriented the same way, but the right panel is scaled into a cube. The bands which can be degenerate at the zone faces are one above the other in the left panel, the degeneracies appear to be absent in the right panel.

in different regimes, [104] is calculated for the paramagnetic case, using LDA, whereas [103] uses LSDA to calculate both the zero field $M\parallel c$ case (shown in figure 4.11) and the $M\parallel b$ case present above the moment rotation transition. However, given the broadly similar properties (especially those detailed in section 4.3) above and below the transition it seems unlikely that the Fermi surface undergoes such a large reconstruction. The similarity of ARPES spectra at the Γ point and ΓX line above and below T_{Curie} also suggest that the band structure is not undergoing huge changes[104].

The ARPES data in [104] is also, in theory, a good direct probe of the band structure. In practice however, the large number of flat bands near to the Fermi level can easily blur together given the limited experimental resolution. As the electron leaves the material it can also lose some momentum in the direction perpendicular to the surface. This results in a further blurring of the experimental resolution in this direction — not a problem for a two dimensional material, but URhGe is believed to be fully 3D. This problem is compounded if, as in URhGe, the material is difficult to cleave. A rough surface has many different perpendiculars in different places, so the blurring happens across a range of directions in k -space, not just the one perpendicular to the face. These issues notwithstanding, the ARPES data does show some structure, though the bands themselves, and the points where they cross E_F remain unclear. As when comparing the calculations, there is some qualitative agreement between the ARPES bands and both of the calculations, but also some substantial qualitative differences. The ARPES is comparatively close to both of the calculations along the YS line, passable along the UZ line but poor along the ΓX line.

We can also attempt to identify some of the observations with features in the calculated Fermi surfaces. Given the highly complex shapes in both calculated surfaces, and the expectation that neither is exactly correct, it would be possible to find an orbit of more or less any frequency somewhere within one of the models. We shall then not attempt to identify orbits with such detail but rather look for more general characteristics.

The open orbits postulated in sections 4.2 and 4.3 are easily found on the band 71 (green) surface in the calculation from [104]. This calculation does not conform to the expectation of degeneracies outlined in the previous section, though around most of the zone faces there are two bands coming quite close together. Some of the lack of degeneracy could be ascribed to numerical issues when interpolating the band structure across the zone boundary. In particular, the band structures given in the paper do have the expected degeneracies, and these are probably calculated in more detail. In the calculation from [103], the green surface also supports open orbits in k_a and k_c directions provided the green sheet connects to itself (degeneracy lifted). But it does not if the degeneracy remains, when the electron changes between green and red sheets every time it crosses a zone boundary.

The magnetic breakdown detailed in section 4.5.3 could occur at several different points, but

the band 69 surface (yellow, at the Y point) in the calculation from [104] is a good candidate. The gap between it and the band 70 (red) surface is due to spin orbit splitting lifting the degeneracy, so will have a small energy gap and magnetic breakdown will be easy.

To conclude then, there are a number of calculations and measurements which further support the established view that URhGe is an itinerant ferromagnet with $U5f$ weight contributing to flat bands near the Fermi surface. The detail of the calculations, including the band structure on the other hand must be considered less reliable, as the calculations differ from each other and the limited experimental data.

4.5 Quantum Oscillations

In addition to the magnetoresistance described in previous sections, a small oscillatory part is also present in the high quality sample URhGe#1. Unfortunately a combination of high masses and generally small amplitude of Shubnikov-de Haas oscillations severely limits the angle range and fields over which oscillations are visible, and the signal to noise when they are. The observations can be split into three groups: one close to $B\parallel c$, one close $B\parallel b$ below the moment rotation and one close to $B\parallel b$ above the moment rotation.

4.5.1 Near $B\parallel c$

This set of oscillations was observed using magnet M9 at LNCMI Grenoble. Given the very large stray fields present at this type of magnet, low temperature transformers are not available. Similarly superconducting wire cannot be used to limit the heat load on the refrigerator, and resistive wire is used instead. Of the methods described in section 3.1, the one shown in figure 3.3 is most suitable, and the best achievable noise is $\sim 0.2 \text{ nV}/\sqrt{\text{Hz}}$. With the magnet running, vibration causes further deterioration of the signal to noise. With the resultant signal to noise ratio near one, it is not possible to analyse the oscillations to the level of extracting a mean free path, but it is still possible to observe the dispersion with angle and estimate the cyclotron mass.

Figure 4.12 shows the resistance measurements at base temperature for angles of up to 16° from the c axis, and their Fourier transforms. There is a single peak at 1120 T, which has no significant angle dependence. Whilst 16° is not enough to make a definitive statement, the lack of dispersion over this range points to a closed, spheroidal pocket. Using $F = \frac{\hbar}{2\pi e} \mathcal{A}$, 1130 T corresponds to a enclosed k-space area of 10.8 nm^{-2} , compared to a Brillouin zone cross section for $B\parallel c$ of 132 nm^{-2} . Thus, despite being the largest frequency observed, it is still only a small pocket. If spherical, it contains $n_p \frac{4}{3\sqrt{\pi}} \mathcal{A}^{\frac{3}{2}} / V_{BZ} = 2.40 \times 10^{-2} n_p$ carriers per unit cell, where n_p is the number of pockets in the zone and $V_{BZ} = \frac{(2\pi)^3}{abc} = 1112 \text{ nm}^{-3}$ is the volume of the Brillouin zone. As URhGe is a ferromagnet, n_p is not required to be even by spin degeneracy.

Given the signal to noise, extracting a reliable mass is not trivial. There are two uncertainties

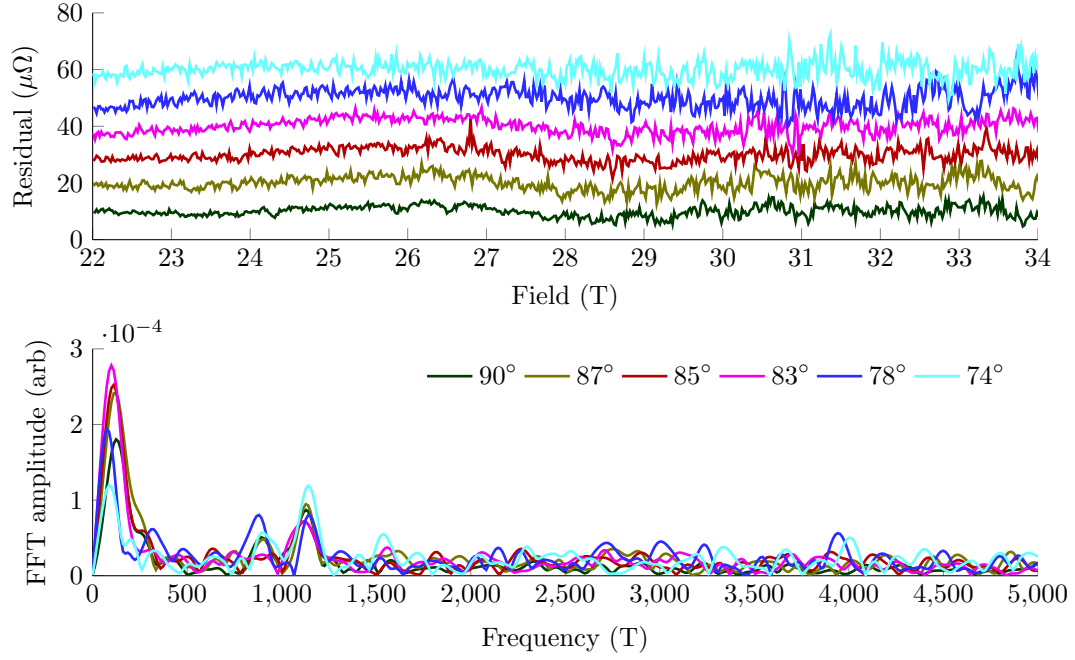


Figure 4.12: Angle dependence of SdH oscillations measured on URhGe#1 near $B\parallel a$. **Top:** Raw data, treated as per section 3.6, and after subtraction of a quadratic background. **Bottom:** Fourier transforms, showing a peak at ~ 1120 T. Angles measured from the b axis in the bc plane.

associated with each data point which must be taken into account when fitting the temperature reduction factor. The first is the uncertainty of the amplitude: as visible in figure 4.12, there is broad-band noise present in the FFT, up to some frequency dictated by sampling rate. The median amplitude of the FFT is a fairly good estimator of the noise, and unlike the mean is not skewed by the presence of peaks. The other uncertainty is in the temperature of each field sweep. There is no magnetoresistance calibration for the thermometer at M9, and the refrigerator is not able to maintain precise temperature control when ramping the magnet. Fortunately in the higher field range (> 20 T) used here these problems are less than at lower fields. The standard deviation in temperature during the run is used as an estimator of temperature uncertainty, for lack of anything better. The amplitudes and temperatures so derived are plotted in figure 4.13. Different currents are used, and sample heating is a risk, but by comparing runs at the same temperature and different currents, it is possible to identify when the current starts to heat the sample. Runs where such heating is evident are omitted from the figure.

From these points, we wish to obtain a mass by fitting the temperature reduction factor described in section 1.3. Calculating uncertainties on coefficients of fit R_0 and m^* algebraically would be difficult and error prone. Transforming the data to allow linear weighted least squares regression, and so obtaining an estimate for the mass and uncertainty, is troublesome here. Weighted least squares regression assumes that each point can be represented by a random variable which is normally distributed around the true value. If the data has been transformed,

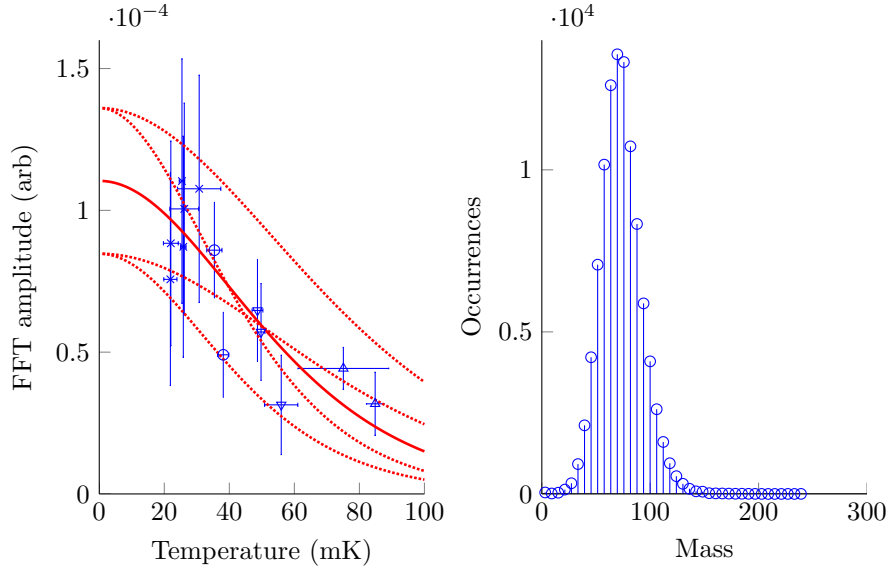


Figure 4.13: Temperature dependence of SdH oscillations measured on URhGe#1 near $B\parallel a$. **Left:** Temperature dependence of peak FFT amplitude. Horizontal error bars indicate standard deviation in measured temperature, vertical error bars indicate median FFT amplitude. Symbols indicate different measurement currents, $500\ \mu\text{A}$ (cross), $750\ \mu\text{A}$ (Circle), $1\ \text{mA}$ (downward triangle) and $2\ \text{mA}$ (upward triangle). Red lines indicate possible fits, solid red line is most likely and dashed red lines indicate uncertainties. **Right** Distribution of possible masses obtained by sampling with a Gaussian distribution around the measured temperature and amplitude, see text for details on method.

the distribution is no longer normal. For data where the uncertainty is small, the transformation looks affine over the size of the normal distribution, so linearisation works well, but here the uncertainty in amplitude is a substantial fraction of the amplitude. The solution is to move to either a nonlinear regression, or a sampling method, and the latter was used here to avoid any concerns about convergence to local minima which can appear with nonlinear regression. The method is detailed in algorithm 1, but in short it consists of fitting many times, and for each fit every point is ‘dithered’ by moving it within its uncertainties. The resulting masses are collated and plotted in the right panel of figure 4.13. The mean and standard deviation are used to give a mass estimate of $75 \pm 20\ m_e$. Finally, the mean values of m^* and R_0 , along with their errors, are used to plot the red lines in the left panel.

There is also a second orbit visible near 900 T. This orbit is even closer to the noise level, and it is not practical to calculate a mass from it. This leaves open the question of whether it is part of the same surface or a second one. If the former, it implies the pocket cannot be spheroidal. The second frequency could then be a neck in a dumbbell shaped pocket, or another bulge in a more complex geometry. If it is a neck, then it would be expected to disperse as $\cos^{-1}(\theta)$ or faster, which equates to no less than 4% over the measured angle range. There is no visible dispersion, but 4% is just within the uncertainty in peak position. On balance, it is unlikely to be a neck. If it is another bulge in the same pocket, then the pocket must be significantly larger than the

Algorithm 1 Fitting and obtaining uncertainties with the sampling method

Let the data points be denoted by the co-ordinates (x, y) with uncertainties $(\Delta x, \Delta y)$
for $n = 1$ **to** 10^5 **do**
 for all data points **do**
 get a random number from a normal distribution with width Δx .
 add this random number to x to get a dithered point
 do the same for y with Δy
 end for
 fit the temperature reduction factor to the dithered points with linearised least squares and
 obtain m_n^* and $R_{0,n}$
end for
plot the distribution of m_n^* and $R_{0,n}$ to check they have a single peak
take the mean and standard deviation of m_n^* and $R_{0,n}$.
use these as the values of m^* and R_0 and their uncertainties.

spheroidal case described above, but the absence of observed neck orbits is quite strange. Overall, it seems more likely that this is a second pocket.

A third orbit is possibly visible, at a very low frequency near 110 T. Because the period of this frequency is so long at high field, and the signal to noise is quite poor, it is difficult to do an FFT analysis. However, it is visible in the residual as slight maxima at 26 and 31 T and minimum at 29 T. It does become slightly weaker with temperature, suggesting that it is a genuine quantum oscillation, but the signal to noise is too poor to get a reliable temperature reduction factor fit. Similarly, it is not practical to see how it disperses with angle, and thus classify it as neck- or bulge-like.

For both clear orbits, the obvious next step would be to fit a Dingle factor, as this would identify whether the orbits are conventional or due to magnetic breakdown. If the former, it would allow an estimate of mean free path. Unfortunately, signal to noise is too poor to get any meaningful conclusions from such analysis.

4.5.2 Near $B \parallel b$, below the moment rotation field

One set of SdH oscillations has been reported before, in our paper from 2011[39]. Whilst these oscillations are small, no more than $2 \mu\Omega$ in amplitude, they are somewhat easier to observe than those in section 4.5.1. This is because they occur at lower fields and can be measured with the much better noise levels practical on the blue fridge.

These oscillations were observed with applied field 7–12° from b in the bc -plane, for fields just below the moment rotation transition. Some of the raw data, along with Fourier transforms, is shown in figure 4.14. In this area, the nearby superconductivity strongly influences the shape of the non-oscillatory part of the resistance: the zero resistance state extends to 5.5°, and the resistance is reduced out to 8°. The resistance reaches a maximum at 10°, which is also where the SdH has the largest amplitude, at about $2 \mu\Omega$. For this reason, the 10° curve was selected for further analysis below. Looking at the right panel of figure 4.14 it is clear that the frequency

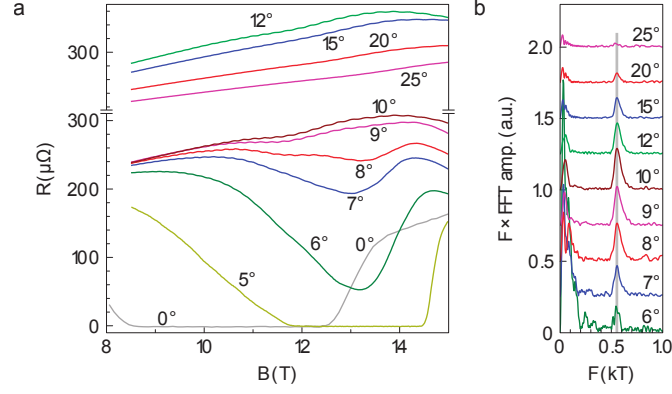


Figure 4.14: **Left:** Raw resistance curves showing weak SdH oscillations. Superconductivity is present at low angle, and continues to reduce the resistance out to 8°. 12–25° curves offset for clarity. **Right:** Fourier transforms of the data in the left pane, after subtracting a linear background. Both panels from our paper[39]

changes very little between 6° and 25°, suggesting that this is a bulge or spheroidal pocket.

Electron masses were obtained in the usual way using a temperature reduction factor linearised least squares fit (the uncertainties being much smaller than those in the previous section), and found to steadily reduce from around 22 m_e at 8 T to 12 m_e where the oscillations disappear. This is close to the moment rotation transition, which has moved out to just over 15 T at this 10°. This observation is in contrast to previous predictions of enhanced mass at the moment rotation based on the coefficients of a T^2 fit to the resistance[30]. Of course the mass on this orbit sheet may not be representative of the rest of the Fermi surface.

The observed frequency varies with field. The variation is small, so it is necessary to consider \mathbf{B} , not \mathbf{H} . The correction was made using separate measurements of \mathbf{M} , and changes the observed frequency by < 15 T. It was then possible to fit a Lifschitz-Kosevitch model with the frequency represented by a Taylor series. This gives the field dependent frequency in the top right panel of figure 4.15. For reasons explained in section 1.3.4 this yields a family of possible extremal areas, some of which are plotted in the lower right panel of the figure.

The pinching off of the amplitude at the moment rotation transition is unusual. Two possible explanations are magnetic breakdown and extra scattering. Extra scattering would be expected if the moment rotation were first order, and domains were present, but at the angle of the measurements it is believed[29] to be a crossover. A Dingle reduction factor fit to the amplitude of the oscillations at fields well below the point where they pinch off (8–11 T) yields a mean free path of $l = 55$ nm. To bring the amplitude back below the noise level at 17 T would mean reducing $B \cdot l$ back to its level when the oscillations first appear at 8 T. A twofold reduction in mean free path would be surprising, certainly there is no commensurate increase in ρ_0 , so extra scattering is considered an unlikely cause of the loss of amplitude. Magnetic breakdown could only destroy the oscillations if it changes the electron's path at the breakdown point almost completely from the low field case, where it is a closed orbit, to a different one over just 4 T. Combined with

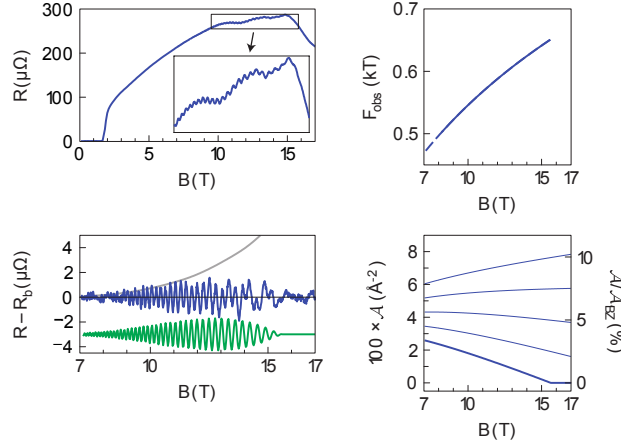


Figure 4.15: **Top Left:** Raw resistance curve at 10° , with magnified oscillations inset. **Bottom Left:** Residuals after the subtraction of a smooth background. Blue is data taken at 20mK, green is the model (offset for clarity) The grey curve is a Dingle factor amplitude envelope. **Top Right:** Frequency obtained by fitting to the raw data. **Bottom Right:** Possible extremal areas consistent with the top right panel. The bold line is the one used in the model yielding the green curve in the bottom left figure. All panels from our paper[39]

the lack of any new breakdown-induced orbits appearing over the given field range, this too is considered unlikely.

The proposed method for pinching off the amplitude is an electronic topological transition (ETT). Either the orbit is around a pocket which no longer exists, or a neck which has become two separate pockets. The small angular dispersion is more consistent with the former. One can put these assumptions into the Lifshitz-Kosevitch equation, including the Dingle and Curvature factors, and get an expression for the residual including both the amplitude and the frequency of the oscillations. If the bold curve in the bottom right panel of figure 4.15 is used, then the green line in the bottom left panel is obtained. This is an excellent fit for the observed oscillation. Thus we conclude that the ETT is the likely cause.

The ETT has interesting consequences for the superconductivity in URhGe. In section 4.7, the argument is made that the unusual high critical field could be explained by a vanishing coherence length. As the coherence length is $\xi = \frac{\hbar v_F}{\pi \Delta}$ and $v_F = \frac{1}{\hbar} \frac{dE}{dk}$ must go to zero at an ETT, this can provide an explanation for the high critical field. Indeed, by taking $k_F \propto \sqrt{A}$ one can obtain a form of the upper critical field very similar to that obtained by measurements in figure 4.3 and in ref. [30], where it was first observed that both low and high field pockets lay on a single smooth critical field curve.

Further information is available in our paper, which is included as an appendix in some versions of this thesis.

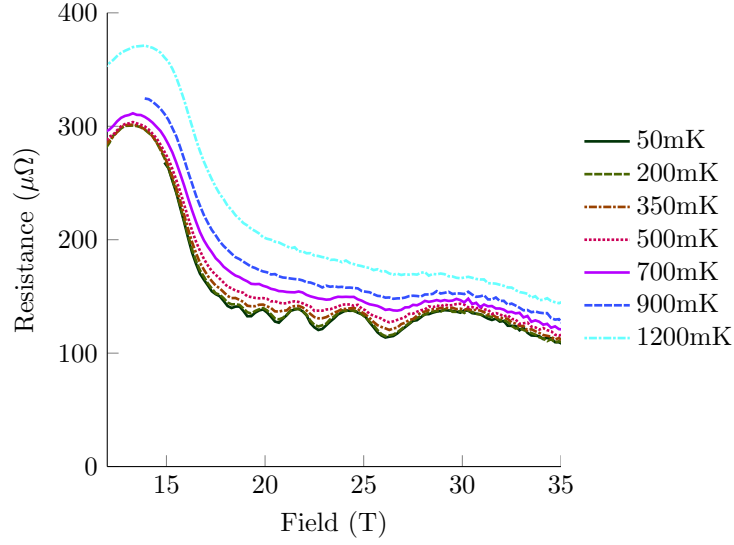


Figure 4.16: Giant SdH observed on URhGe #1 (which has current mostly along c) with B 10° from b in the bc -plane. The peak and steep drop in R near 12–17 T is associated with to the moment rotation transition.

4.5.3 Near $B \parallel b$, above the moment rotation field

With field applied near $B \parallel b$, but with a small c component, giant Shubnikov-de Haas oscillations have been seen. These are present at fields above the moment rotation transition, and have a low frequency. Figure 4.16 shows an example of these oscillations. These have also been observed using M9, so are subject to the same discussions regarding noise and temperature control described above. In this case though, the amplitude is much larger, and the mass much lighter, so the resulting uncertainties matter less.

The size of these oscillations would be quite unusual if they are conventional SdH. Pippard[2] and Shoenberg[4] both outline similar explanations of why SdH oscillations are usually small. The oscillations enter into the resistivity through the influence of the density of states $g(E_F)$ on the scattering rate τ . The probability of an electron being scattered is dependent on the matrix element (which is not oscillatory) and the number of possible final states (which is). For catastrophic scattering, the final states can be anywhere on any Fermi surface sheet. But the vast majority of those sheets will not be an extremal area, so will not have an oscillatory density of states. Precise upper limits depend on the detailed geometry of the Fermi surface, but both authors cited above give less than 1% as a rule of thumb.

To exceed this requires that contributions to the density of states other than that from the extremal orbit be eliminated. This can be observed in the extreme quantum limit provided there is only one pocket (or several identical pockets). One such example is bismuth[2]. The low frequency and high fields do make the extreme quantum limit a possibility. But given the various evidence for different frequencies, and for open sheets described in section 4.3, this explanation for a high amplitude can be excluded for URhGe. Another way to eliminate the other contributions

to the density of states is to have a surface which is all extremal, i.e. a cylinder. This can also be thought of as having a very large amplitude through the curvature factor. Such surfaces are however usually associated with two-dimensional materials, where URhGe seems to exhibit one- and three-dimensional physics.

In both of the above cases, the key to a giant SdH oscillation is that the extremal orbit is on a band which contributes most of the conductivity. This is at odds with the conclusions in section 4.3. One other case where SdH amplitude is routinely seen to exceed the limits described above is in magnetic breakdown. For the purposes of understanding why this is the case, it is enough to consider magnetic breakdown as a point on the Fermi surface where an electron may carry on along its low-field orbit with probability $1 - P$ or hop across to a different surface with probability P . If the original path of the electron would have contributed to the overall conductivity, then a large P reduces it. If on the other hand the new path is better for the conductivity, it could increase. And if there are many breakdown points and many possible paths, the effect can be much more complex. At the breakdown point, the probability P depends on both the matrix element for transition, and the number of states it can transition into. The former is zero in zero field and tends to increase slowly and monotonically with B . If the sheet it is switching to supports closed orbits, then the density of states into which the electron can switch can oscillate, and this will cause P to oscillate. Thus, by mediating magnetic breakdown on the conductivity-dominant band, quantum oscillations can have a large effect on total conductivity.

The obvious first step is to extract the frequency, and from that discuss the size of the pocket. Given that the field component B_b also acts as a tuning parameter, it is not unexpected that the Fermi surface is changing. Indeed, such changes have been observed[39] and are discussed in Section 4.5.2. The consequences for the observed frequency are not completely obvious, and are discussed in some detail in section 1.3.4.

The usual method of doing FFTs over short windows to track the evolution of the frequency is not effective here, because of the low frequency. The windows would contain one or two periods at most. There are two other possible ways to analyse the oscillations. First, to fit a function to the whole data set (after subtracting a suitable background). This has the advantage of making good use of all the data, and is excellent for verifying a prediction. But in the absence of an obvious choice of fit function, is less ideal. If a fit function with few free parameters is chosen, it is difficult to avoid forcing the assumptions used in building the function onto the data. Fit functions with many free parameters tend to be hard to interpret and run into problems getting the fit algorithm to reliably converge to the global minimum. An alternate approach is to measure each individual oscillation to obtain both a frequency and amplitude. This technique is more robust, but necessarily discards some data from the ends of the set. We shall use the latter, in order to have the best possible confidence in the results.

Figure 4.17 shows a data set acquired at low temperature with B rotated 10° from b towards

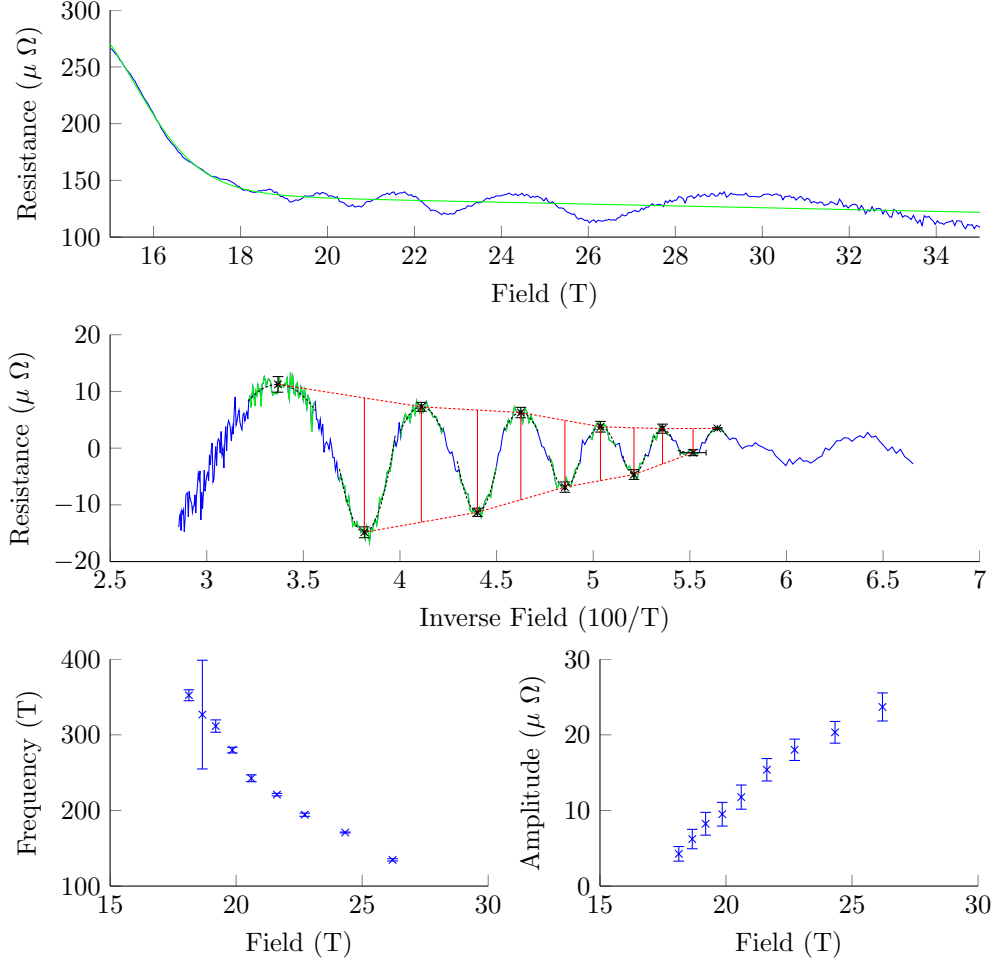


Figure 4.17: Method of extracting frequency and amplitudes from quantum oscillations at high field with \mathbf{B} 10° from b towards c . **Top:** Raw data (blue) and background fit (green) consisting of a linear part and a Fermi function. **Middle:** Residuals from background fit plotted against inverse field (blue). Green sections are fitted by parabolas (black dashed) to obtain peak and trough positions (black crosses). Baselines (red dashed) between peaks are used to measure peak amplitudes (red solid lines). **Lower left:** Period between peaks is used to obtain a frequency at the associated trough, and *vice versa*. This is the observed frequency F_{obs} , the frequency obtained from $F = \frac{\hbar}{2\pi e} \mathcal{A}$ may differ (see text). **Lower Right:** Measured amplitudes as a function of field.

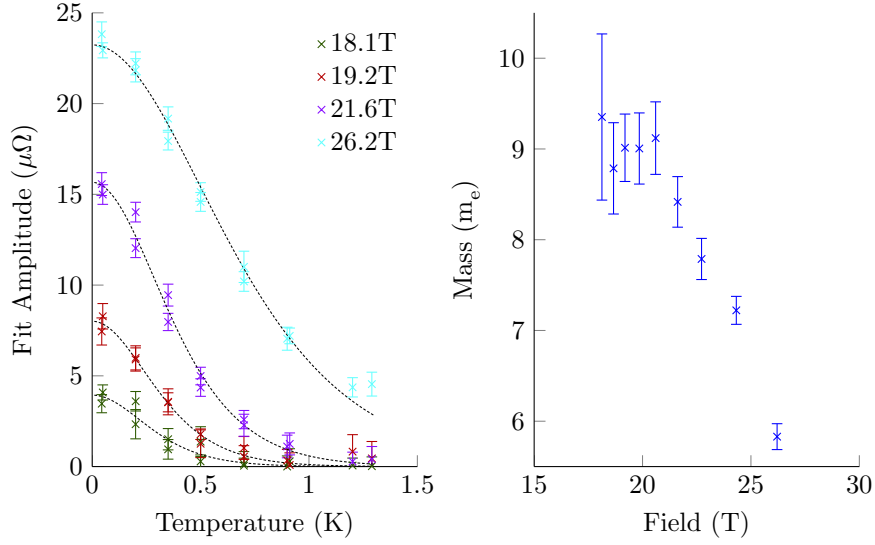


Figure 4.18: Mass plots of oscillations with B 10° from b towards c . **Left:** Selected mass plots, with temperature reduction factor fits. **Right:** Mass extracted from temperature reduction factor fits at each peak and trough position.

c. The first step in the analysis is to subtract a background, and linear or quadratic functions are usually chosen. Here, the low field end of the data encroaches into the moment rotation transition, which is poorly approximated by a low-order polynomial. Instead a combination of linear and Fermi functions are used:

$$R_{BG} = a_1 + a_2 B + \frac{a_3}{1 + e^{\frac{a_4 - B}{a_5}}} \quad (4.6)$$

This is represented by the green line in the uppermost panel. The residual after subtracting this background fit is shown in the middle panel, plotted against $\frac{1}{B}$. Rough peak and trough positions are selected manually, then refined by fitting a quadratic over a small range near the peak/trough. The fit parameters and the covariance matrix of the fit are used to provide both the resistance and field of each peak/trough, along with uncertainties (marked in black). Finally by joining adjacent peaks to provide a baseline (red dotted line) the amplitude (red line) of each peak is measured directly. The amplitudes and frequencies extracted this way are plotted in the lower two panels.

With the peaks located, it is now possible to compare this data set with the others at higher temperature. The method for identifying the amplitudes in the other data sets is essentially the same as for the first one, but instead of fitting a parabola, the mean residual in the area around the known peak position is used. To avoid a potential systematic error, the averaging method is used on the first data set too, but the change in measured amplitudes is negligible. These amplitudes are plotted in figure 4.18, the error bars are the standard error on the mean. Note that there are two data sets at each field, one from a field ramp with B increasing, one reducing.

They do not agree within the error bars, which implies that the curve is not repeatable within the noise level. The most likely cause of this is slight temperature variations between ramps. The data points are not so scattered as to harm the quality of the fit however, so we can proceed to extract masses. The good fit is also an indicator that in this area of the phase diagram at least, Fermi liquid theory still holds. That quantum oscillations exist at all implies that there is still a Fermi surface, but that is also present, if not distinct, in the marginal Fermi liquid. In the marginal Fermi liquid, the usual form of the temperature reduction factor is lost, and a more complex form appears, with the different behaviour normally represented by a temperature and field dependent effective mass[85, 86]. The best known example is Mercury[87], where strong electron-phonon interactions are present. None of these effects are seen here.

The masses from the temperature reduction factor fits are shown in the right panel, with errors estimated from the variance of parameters of the temperature reduction factor fit. The mass clearly reduces, by a factor of 30%, over the range plotted. One must always be a little careful when plotting a field dependent mass, for reasons explained in detail by Mercure *et al*[11]. In short, as amplitude generally grows with field, so does signal to noise. With the traditional FFT analysis, that noise tends to give minimum amplitude, which is most notable on high temperature data points. The noise essentially lifts the tail of the $\sinh(X)/X$ fit, giving an erroneously light mass. As this is more problematic at low fields, where the noise level is a larger fraction of the oscillation amplitude, this can lead to an unwarranted conclusion that the mass is increasing with field. We can be confident that that is not a problem here for two reasons: Firstly, the observed mass is decreasing, not increasing. Secondly, the problem arises because of the minimum amplitude of the FFT, where the noise is folded to positive amplitudes. The technique used here allows for a negative amplitude to be measured, so no such folding occurs.

Figure 4.19 shows how these large oscillations change as a function of field angle. Time limitations on the experiment prevented the measurement of angles between 18° and 26° , but by 26° (not shown) the moment rotation transition has broadened and moved out, and there is no identifiable oscillation. So it remains unclear how in detail the oscillations die away. To low angles, it appears that the amplitude of the oscillations dies away very quickly close to $\mathbf{B} \parallel \mathbf{b}$. The frequency is also a function of angle, with higher frequencies at larger angles. To analyse these observations in detail, the same technique as above, including the manual peak selection and automatic refinement, is used. The resulting frequency and amplitude curves are shown in figure 4.20.

The predicted behaviour for the field dependence of the amplitude is the given by the dingle factor:

$$R_D = e^{\frac{-\pi m}{e} \frac{1}{\tau} \frac{1}{B}} \quad (4.7)$$

with which a passable fit to the 5° data can be obtained. It yields a scattering lifetime of 10^{-12} s, or, using $\frac{\hbar}{2\pi e} \mathcal{A} = 250$ T, a mean free path of 200 nm, rather shorter than expected. It would also

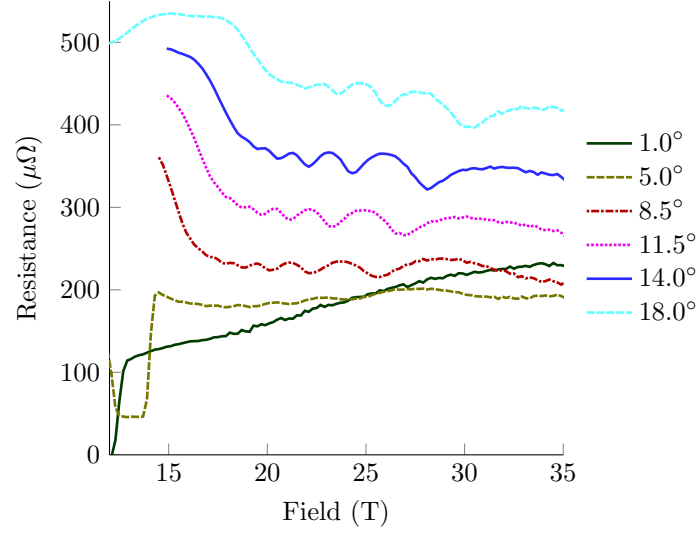


Figure 4.19: Angle dependence of high field oscillations in URhGe #1. Curves offset for clarity ($50 \mu\Omega$ per line). Angles measured from b towards c . Temperature is base temperature of the refrigerator, varying between 40 and 80 mK

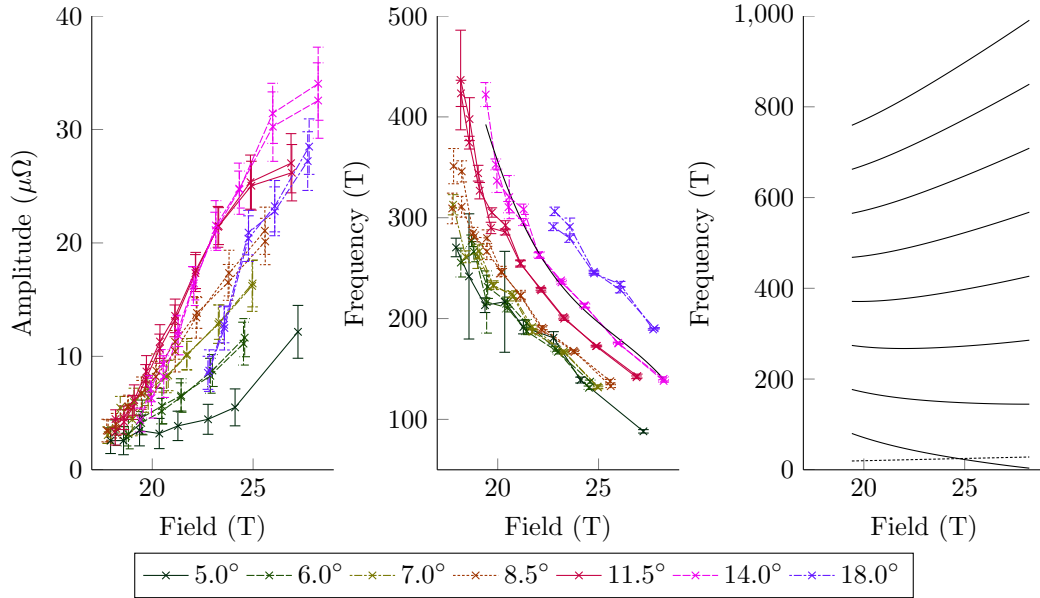


Figure 4.20: Angle dependence of giant SdH measured on URhGe #1. **Left:** Field dependent amplitude. **Centre:** Field dependent frequency. Black line is an analytic approximation to the 14° data. **Right:** Possible real frequencies (i.e. those related to the extremal area by $F = \frac{\hbar}{2\pi e} \mathcal{A}$) consistent with the observed frequency given by the black line in the centre panel. Where a solid line crosses the dashed line, it would enter the extreme quantum limit.

be consistent with magnetic breakdown in an unchanging band structure, which also has a Dingle form. However, given the relatively narrow field window and the poor fit on the other angles, this should be treated with caution. At larger angles the fit is very poor. There are at least two possible reasons for a non-Dingle form. Firstly, magnetic breakdown where E_g is a function of field, which agrees with the arguments for large amplitude given above. An alternative explanation is a field dependent scattering rate, a higher scattering rate at low field (caused perhaps by proximity to the moment rotation transition) would cause a non-Dingle amplitude. This is considered less likely than magnetic breakdown in a field dependent band structure for two reasons, firstly, the prior evidence of magnetic breakdown. Secondly, the increased scattering rate is only expected close to the transition, but the larger angle data remains non-Dingle up to quite high fields.

The field dependent frequency was analysed by first converting to a Taylor expansion, shown by the black line in the middle panel of figure 4.20. This is not strictly a polynomial fit, as such fits with few points have a tendency to oscillate near the ends of the data. Instead it is just a line which adequately represents the data and can be treated according to equations 1.37. This treatment yields a family of possible extremal areas which are shown in the right panel of figure 4.20. The true area must be larger than the lowermost drawn, as that possible area crosses the dashed line. On crossing the dashed line, the surface enters the extreme quantum limit, where the final Landau tube passes through the Fermi surface, and the density of state loses its oscillatory character. The upper limit of possible extremal areas is not immediately clear, it would not fill the zone until over 8000 T, and an extended or breakdown orbit could well be larger than that. Very large orbits are however very field dependent. There are likely other surfaces in the zone which are not changing as quickly if at all, and this surface cannot pass through them. This orbit is believed to be a breakdown orbit, which requires that it pass close to another surface and remain there if breakdown is to continue. These two things, combined with the extremely strong exchange interaction and/or very flat band required, make the larger possible extremal areas unlikely.

We can also gain some insight by looking at the cyclotron mass obtained from figure 4.18. The cyclotron mass is given by $m^* \propto \frac{dA}{dE}$ and is observed to be reducing with field. This implies the band is getting steeper as field increases, which would be consistent with a reduced rate of change of true frequency as B increases. This assumes that the band undergoes a more-or-less rigid shift, if it changes shape then this argument becomes meaningless. It is then a weak argument for choosing a possible true frequency such as the second one from the bottom drawn in figure 4.20. Another weak argument in favour of choosing one of the lower frequencies is that it has a higher rate of change nearer the moment rotation transition, where the magnetization is known to be changing fastest. As URhGe is an itinerant ferromagnet, a change in magnetization is closely tied to a change in Fermi surface.

Possible extremal areas for the other angles are not shown. Within the constraints of the

uncertainties in figure 4.20, the only significant difference is a vertical offset. This corresponds to a change only in $a_0 = \alpha_0$ in the expansion of the observed and true frequencies. The other angles would therefore be the same as the ones drawn in the rightmost panel, but with a small offset. In order to determine whether the angular dispersion is neck-like or bulge-like, we should compare the value of the true frequency with its rate of change with angle. Without knowing which of the possible curves in the right panel is real, we cannot directly make this comparison. However the difference between 5° and 18° is a little over 100 T. Over this range, deviation of 3% or more would indicate a neck. Given that total areas of over 3000 T are considered very unlikely, it seems that this is a neck. This also provides a mechanism for the loss of signal at large angles, if the orbit is no longer closed around the neck, the frequency will disappear or have a discontinuous jump to a much larger value, depending on the nature of the new orbit. A similar argument applies to an orbit on the inside of a toroid, but in this case, no new orbit is seen.

This does not explain why the orbit disappears for angles less than 5° . The amplitude reduces, but whilst the frequency continues to change, it does not show any indications of why the amplitude is reduced. As the frequency of the smaller angles is smaller, they could reach the extreme quantum limit before the others. In the extreme quantum limit, the oscillatory density of states can be lost. However, by comparing the 5° and 8.5° curves in figure it is clear that if the 5° curve reaches the final Landau tube, it does it above 33 T. The amplitude below this point is much less than the 8.5° curve, so extreme quantum limit is not the cause. That leaves three options, increased scattering, increased curvature or loss of magnetic breakdown mediated conductivity effects. It is difficult to imagine either a \mathbf{k} -dependent scattering capable of causing a tenfold reduction in dingle factor over only a few degrees, or a substantial extra scattering caused by having \mathbf{B} exactly on the b -axis. The $\mathbf{B} \parallel b$ axis is not a first order transition line above the moment rotation, so there is no extra scattering from domains.

A neck geometry with much stronger curvature at its narrowest point is possible, consider for example a toroid with a sharp cusp running round the inside. The dispersion with angle would identify such a feature, but here again we run into problems because we do not know the absolute value. The final option, changes in the magnetic breakdown, is also quite possible. The large effect of magnetic breakdown on conductivity is a result of the electron population which contributes most to the conductivity being swept through an area of the Fermi surface at which magnetic breakdown occurs. Changing field direction changes these paths (which are not necessarily extremal orbits, recall the oscillatory part can be on the other sheet involved in the breakdown) and the important excited electrons never reach the breakdown point.

4.5.4 Summary

There are several different field orientations at which Shubnikov-de Haas oscillations can be seen. Near the moment rotation transition, the extremal area associated with the only observable fre-

quencies is field dependent, indicating that the bands being probed are involved in the magnetism.

Given the relatively few frequencies observed, the limited angle ranges, and the undetermined linear part of the field dependent frequencies, it is difficult to draw any robust conclusions about the shape and size of the Fermi surface pockets which contribute the observed frequencies. As noted in section 4.5.1, two frequencies are field independent by virtue of being observed well away from the moment rotation transition. The observations are consistent with spherical pockets, oblate or prolate spheroids or, less likely, more complex geometries. The two frequencies are probably from different pockets, and, if spherical would enclose 1.7% and 2.4% of the Brillouin zone volume. Of course symmetry allows there to be several copies of each pocket in the zone, so integer multiples of these values are also possible. The mass of one pocket has been observed to be $75 \pm 20 m_e$, the other has too poor signal to noise to estimate a mass. The former then, if spherical, contributes $\gamma_{pocket} = \frac{k_F^2}{6\hbar^2} m^* \sqrt{A/\pi}$ per unit volume, or $12 \text{ mJmol}^{-1}\text{K}^{-2}$, to the specific heat γ . This value is again multiplied by the number of pockets in the zone. For $\mathbf{B}\parallel b$, the mass is known, but the exact area is not. Assuming 200 T and $m^* = 8m_e$ for the high-field pocket, it encloses less than 0.2% of the zone and contributes an almost negligible $0.5 \text{ mJmol}^{-1}\text{K}^{-2}$ to γ .

The measured zero field gamma is $160 \text{ mJmol}^{-1}\text{K}^{-2}$ [27, 25]. The only high field measurements are those reported by Prokés [27], which has an erratum [26] reporting some of the samples were misaligned. The erratum does not indicate that the specific heat results were affected, but the resistivity results were also not listed as affected by the erratum, but are different resistivity from those measured here. Nevertheless, they show γ is field independent for $\mathbf{B}\parallel a$, and drops quickly before saturating at about $130 \text{ mJmol}^{-1}\text{K}^{-2}$ for both of the other field directions. Magnetization measurements in the same paper and elsewhere [29] indicate that the response to field along a is much less than the other two, possibly even zero within experimental error. As magnetization is closely tied to Fermi surface shape and size in an itinerant ferromagnet, this is consistent with the change in γ being due to changes in Fermi surface. The fact that γ saturates could be indicative of an ETT, especially as the saturation field is close to the moment rotation transition and possible ETT described in 4.5.2. But it could also be due to the changing surfaces ceasing to contribute through other means, such as filling level changing the effective mass.

There are then two possible opportunities to match up the observed frequencies to the specific heat. First at zero field along b , and secondly the changes between there and high field along b . At zero field along b , we have the pockets measured with $\mathbf{B}\parallel c$, both of which seem to be field independent, so can be assumed to be the same size at zero field. The larger contributes $12 \text{ mJmol}^{-1}\text{K}^{-2}$ per pocket in the zone, the smaller might add another $10 \text{ mJmol}^{-1}\text{K}^{-2}$ if it is the same mass. Both could be larger or smaller if the pockets are not spherical. Allowing then 8 copies of each pocket in the zone, these alone can make up the entire γ . Alternatively, and perhaps more likely, they could fall far short, and there are other bands not observed due to their mass or simply because they are open.

When considering the changes with field, there are two relevant observations, those in sections 4.5.2 and 4.5.3. These could be the same orbit, if the low field one does not disappear at an ETT, or could be different ones. One small surface cannot exist in isolation, as the changing population of the bands associated with the changing magnetization must have another band or bands to transfer to. This does not necessarily imply a second rapidly changing band though, as the population can move to a band with a large density of states at the Fermi level without major effect. To avoid concluding that other bands exist would require that the population is transferring from one of these to the other, and as one grows and the other shrinks, they account for the change in γ . The larger of these bands is estimated to contribute about $2 \text{ mJmol}^{-1} \text{ K}^{-2}$ at 10 T, though with the unknown linear term, possible non-spherical nature, and multiple copies per zone, could be more. It seems unlikely that it could account for the observed reduction in γ of $30 \text{ mJmol}^{-1} \text{ K}^{-2}$. So we reach the unsurprising conclusion that there are other bands present with changing occupation levels, even if they themselves are not strongly field dependent.

Another observation is that all the bands where a mass has been obtained are heavy, ranging from 8 to $75 m_e$. Generally speaking, if light orbits were present, one would expect them to be observed. Various measurements have been taken at higher temperatures where larger currents are possible and signal to noise is improved. Whilst it is possible that the curvature factor on these bands is responsible for their non-appearance, it is also possible that they are not observed as they are open sheets, in keeping with the conclusions from previous sections.

Overall it must be concluded that with the presently available sample quality, SdH is not a good probe of Fermi surfaces. It remains however one of the best available to us. Attempts to measure de Haas-van Alphen via torque are complicated by the large ferromagnetic moment and have thus far proven unsuccessful[88], even in samples where SdH can be observed. Susceptibility measurements have not yet been attempted, and could prove more successful. The other main direct probe of a Fermi surface is ARPES, but the results from an ARPES measurement are (in the section 4.4 are also rather inconclusive.

4.6 Overview of the Fermiology

We can now attempt to draw everything together to gain as much understanding of the Fermi surface of URhGe as is possible. There is a relatively simple model which can explain many of the observations reported in this chapter. It relies on the unusual symmetry constraints discussed in the last section, which can change the topology as a function of field. The key observation is that states on the Brillouin zone boundary are required to be degenerate, unless there is some component of \mathbf{B} perpendicular to that face. This field can arise from $\mu_0 \mathbf{H}$ or from \mathbf{M} . When the bands are degenerate, they form a crossing, otherwise they form an anticrossing, and the gap will be controlled by the strength of the field and the strength of the spin-orbit coupling for that

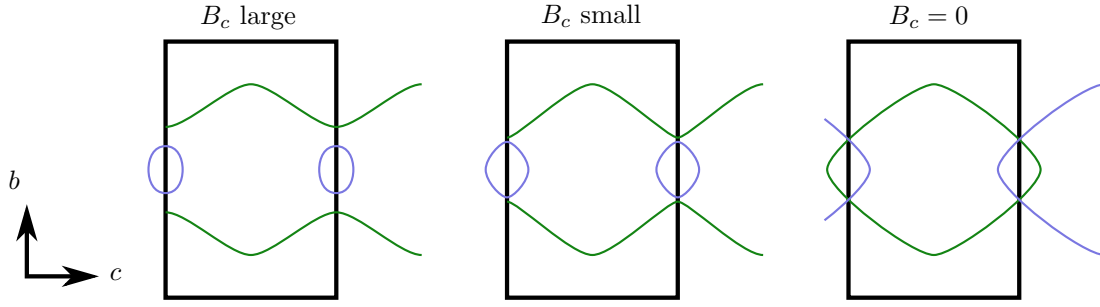


Figure 4.21: A sketch of the proposed model for spin-orbit driven topological change in the Fermi surface of URhGe.

k -state. This has implications for the Fermi surface where it crosses the zone boundary. If there is no field component perpendicular to the zone boundary, then the degeneracy means the Fermi surface can ‘spill over’ into the next zone, overlapping with a copy of itself centred in that zone. If there is a field component perpendicular to the zone boundary then like the case where there is no screw symmetry the Fermi surface reconstructs to form an extended surface, and a separate pocket.

One specific example of this is drawn in figure 4.21. Here a Fermi surface crosses the $k_c = \pm\pi/c$ zone face, but not the $k_b = \pm\pi/b$ one. If there is no field component along the c axis, it forms a single, large pocket which overlaps with the copy of itself in the next zone. When a large B_c is applied, it separates into a pair of open sheets and a pair of small pockets on the zone boundary. Since the gap at the zone boundary depends on B_c , for some intermediate B_c the sheets are separate but the gap is very small, and magnetic breakdown is possible. Since URhGe is a ferromagnet with spontaneous moment along c it is usually in the gapped state. The only condition under which the degeneracy is enforced is with $H\parallel b$ above the moment rotation transition, at all other fields the model behaves as open sheets. The a direction is not drawn in the sketch, and the sheets could be open or closed along that direction, provided they fill a non-negligible part of the zone the discussions here remain relevant. Given the observations in section 4.3, it seems likely that the sheets are open in the a direction, but other topologies are possible.

This model directly accounts for the observations in sections 4.2 and 4.3 of open orbits perpendicular to b , as all of these observations are either at fields below the moment rotation or at large fields where even 0.5° misalignment would bring back the 0.1 T along c that is present at low field. Indeed, given the symmetry considerations, this is one of few models which can support open orbits in that direction. It could also account for some of the Quantum oscillation measurements, in particular those other than for fields near b and above the moment rotation transition. These could be around the pocket formed when $B_c \neq 0$. There are very likely to be more sheets present elsewhere in the zone. This is expected as estimates of γ from the sheets seen so far come well short of the γ measured in specific heat.

It is interesting to consider an oscillation driven by an orbit which passes through these points on the zone faces where the Fermi surface topology changes. At these points, there may be no extremal orbit for $B_c = 0$, but closed orbits appear once the degeneracy is broken. An orbit passing through the degeneracy point (or, in 3D, degeneracy line) may for intermediate fields along c see a very small energy gap to the other band, and thus have a propensity to magnetic breakdown. As B_c continues to increase, the gap opens and magnetic breakdown stops. This magnetic breakdown, joining open and closed sheets, is similar to what has been observed in other materials to lead to giant SdH oscillations such as those discussed in section 4.5.3. It could also qualitatively explain the variation in amplitude with angle, as the component B_c tunes the magnetic breakdown probability. Unfortunately this model does not work in detail however, as symmetry requires that the only extremal orbit passing through the degeneracy points be the one in the $k_a k_b$ plane, driven by field along c . Whilst the gap only ever completely closes, to give a degeneracy, on the zone boundary, it is still possible that there are other gaps which are small and field dependent a short distance within the zone, it is perhaps one of these which controls the giant SdH.

These open sheets are sufficient to explain the majority of the resistance and magnetoresistance measurements. The models presented in section 4.3 assume they dominate the conductivity, even for currents not along b , and rough calculations based on estimated Fermi velocity place the conductivity from these sheets in the same general area as the total conductivity. They cannot however be the only sheets in the Brillouin zone, for several reasons. Firstly, they do not contribute very much to the specific heat γ . Secondly, they show little change across the moment rotation transition and therefore do not seem to play a major part in the itinerant magnetism. Thirdly, there are the quantum oscillation measurements, which imply the existence of other sheets.

It is not clear which quantum oscillation measurements come from the same sheet and which come from different ones. It is possible that all three groups of oscillations come from the same sheet, which changes size significantly crossing the moment rotation transition. This is deemed unlikely however as the measurements are also consistent with this pocket disappearing at the moment rotation, and this in turn is supported by the dramatic increase in coherence length of the superconducting phase also present. If these two groups of oscillations are different (above and below the moment rotation) then the group of oscillations for B near c may be from one of them, or from a third pocket. Given that these have much higher mass, a third pocket is perhaps more likely. Little information is available about these pockets, and any others that may exist, but some reasonable assumptions can be made. These pockets are probably heavy, and contain substantial f -weight. It is these pockets which are taking part in the magnetism, and which are contributing to the very large specific heat. Their number, shape and position in the Brillouin zone remain unknown.

4.7 Additional Measurements with field near the b -axis

Whilst the data in figure 4.5 is sufficient for comparing the magnetoresistance along different crystal axes, there is more to be learned by looking at the behaviour near $\mathbf{B} \parallel b$ in detail. Figure 4.22 shows a few selected temperature ramps at different fields. The behaviour is clearly different for current along each of the crystal axes. It is interesting here to compare the curves at zero field and 12 T, which is near the centre of the high-field superconducting pocket. In the case of barB2 (centre panel) both curves reach the zero resistance state, though T_c is higher at 12 T. This is not a new result, it was originally reported in 2005[29], and has been seen in all other samples measured since. What is new is the observations in samples barA2 and barC2 (left and right panels respectively) that at low temperature, the high field superconducting state is closer to zero resistivity.

Partial superconductivity is observed in these samples, no superconductivity is observed in low-quality samples and full superconductivity is observed in the high quality quenched samples. It seems reasonable to assume that disorder prevents superconductivity, and these samples are somewhat inhomogeneous. In that case the observed partial superconductivity is the result of some superconducting and some normal areas effectively measured in series. This hypothesis is further supported by measurements using eight contacts on two of these samples. Each sample is brick shaped, and one long face is glued to a Kapton-insulated copper sheet. Current contacts were attached to the ends of the brick, and a pair of voltage leads attached to each remaining face. The resistance was measured at room temperature, and again at 2 K, and the ratios compared. The ratios varied by up to 48% between contacts on the same sample. Thus we can conclude that more of these samples is superconducting at 12 T than at zero field. That implies the high-field pocket is more resistant to disorder than the low field pocket.

The argument given above is described in terms of a simple type I superconductor, where it is either superconducting or not. In URhGe, more complex flux-flow effects may be present. One could consider flux flow as an alternative explanation to inhomogeneity for a resistance between zero and that of the normal state. This is believed not to be the case for two reasons, firstly, the inhomogeneous RRR mentioned above. Secondly, the zero resistance state in high quality crystals. If flux flow were the origin of the resistance measured, it would imply weaker pinning in these samples than in the high RRR samples, which seems unlikely.

As mentioned above, the high field pocket also persists to higher temperature than the low field pocket. The effect of magnetic field is also interesting; in URhGe magnetic field along b is a tuning parameter as it causes the moment rotation, and the re-entrance of superconductivity. Similarly, with $B_b \sim 12T$ (necessary to see the re-entrant superconductivity) field along c tends to rotate the moment back towards c , and rapidly affect the associated superconductivity. It too then should be considered a tuning parameter rather than providing us with meaningful critical field data in the usual sense. Fields applied along a however do not seem to affect the magnetic moment, they

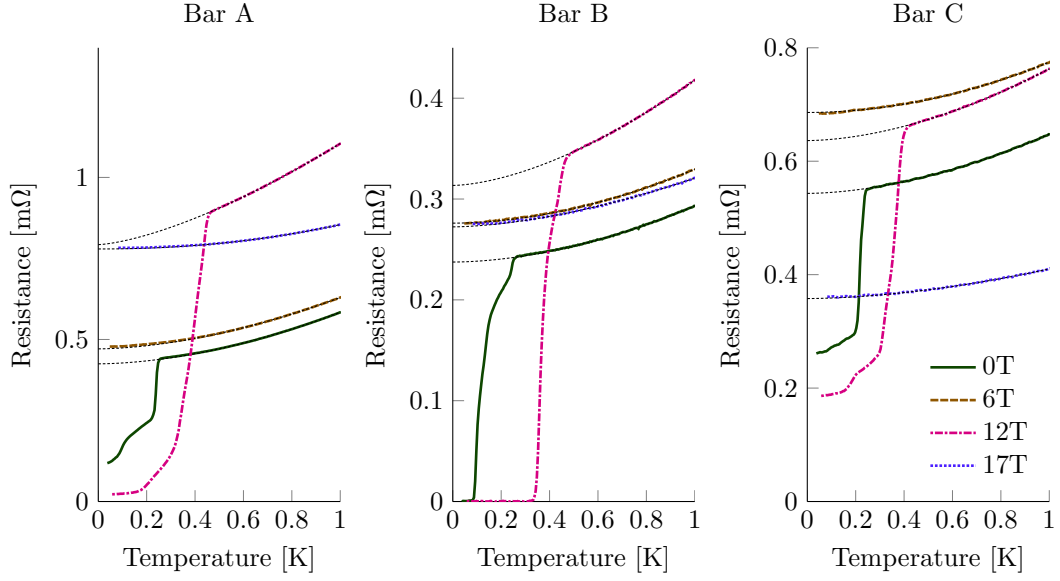


Figure 4.22: Selected temperature sweeps on URhGe samples barA2 barB2 and barC2. Black dashed lines are fits of the form $\rho_0 + AT^n$.

do not move the normal state resistance peak, nor do they move the superconducting pocket. It is probably safe to assume that such fields affect the superconductivity directly via orbital limiting, rather than as a tuning parameter. This being the case, the critical field in excess of 30 T visible in figure 4.8 is extraordinary, especially considering the highest observed T_c (which occurs at $\mathbf{B} = B_b \approx 12$ T) is only 475 mK. Some analysis of this data has been reported[39, 30], but to summarise it is likely that the superconductivity is spin-triplet. At high fields, it contains $\uparrow\uparrow$ and/or $\downarrow\downarrow$ pairing components which are exempt from the paramagnetic limit. It also has either a high electron mass or very small k_F resulting in a large orbital limiting field:

$$B_c^{orb} = \frac{\Phi_0}{2\pi\xi^2} \quad (4.8)$$

Of course, as observed by Hardy *et al*[37], that the superconductivity is dependent on (non-magnetic) disorder at all, is evidence that it is not conventional s -wave BCS. In an unconventional superconductor, superconductivity is expected to vanish when the mean free path l is reduced to of order the coherence length ξ [37]. For all three current directions, the 12 T curve has a higher resistance in the normal state than the zero field curve. This is to be expected, as there is more scattering from domain walls close to the first order moment rotation transition. More scattering would normally mean a shorter l , yet more of the sample is superconducting. This is further evidence for the reduction of ξ in the high-field superconducting pocket compared to the low field pocket. As ξ is a function of both k_F and effective mass, this observation does not help distinguish between a change in k_F or one in m^* driving the change in B_c^{orb} . SdH measurements in section 4.5 suggest it is k_F rather than m^* that drives it.

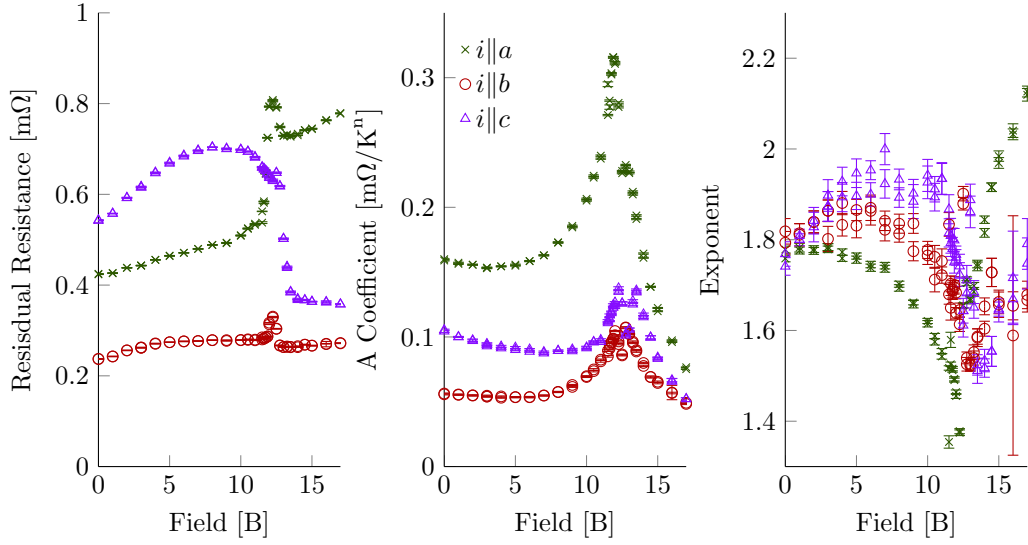


Figure 4.23: Fit parameters for $\rho_0 + AT^n$ fits on URhGe samples barA2 barB2 and barC2 (which have currents directed along a , b and c respectively) at various fields applied along the b -axis. Fits are over the temperature range 500–1000 mK, so omitting any superconductivity.

These conclusions are based on the assumption that the superconductivity is a bulk effect. If it is instead restricted to domain walls (which are present as a result of the moment rotation transition) then the equation for orbital limiting field above is not accurate. That the superconductivity is observed to fields rather lower than the first evidence of reducing magnetization[29] makes this seem less likely. Also, specific heat measurements[25] indicate that at least $\frac{1}{2}$ of the volume of the sample is superconducting at low field, which suggests superconductivity is not confined to particularly thin regions such as domain walls or surfaces.

It is useful to fit to the data in figure 4.22, in order to extract information about ρ_0 and hence the scattering rate. The first problem with this is the presence of superconductivity; there are two possible strategies for dealing with this. Firstly, fitting all of the data other than the superconducting areas. This has the disadvantage that the fits at different fields will not be directly comparable; if there is a feature at low T which affects the fit, it will only affect those without superconductivity. The other option is to only fit data above the maxima of T_c , which has the obvious disadvantage of discarding some data. The latter option was selected as it cannot introduce a systematic error near the areas of interest. The second problem is the choice of fit function. The usual $\rho_0 + AT^2$ is a poor fit right across the range, and especially near the moment rotation; indeed it is obvious in figure 4.22 that the curvature is less near 12 T than below or above. A variety of other fit functions, constructed as a sum of different scattering power laws, were considered and mostly gave acceptable fits to the data. But in all cases the coefficients of fit varied similarly as a function of field, which would suggest they were not independent variables and the data did not support separating out the scattering processes in this way. The same is true of the chosen fit, $\rho_0 + AT^n$, where A and n are strongly correlated, but this was selected as

it provides a good agreement between the extrapolated fit and the data below 400 mK.

The ρ_0 given by the fit is probably reliable even if the functional form of the fit is not correct. This is simply because $\Delta\rho$ between 0 and 1 K is relatively small compared to ρ_0 . ρ_0 is different along all three current directions, but all three show a sharp, < 1 T wide spike at the moment rotation transition. This is very likely a reduced τ from domain wall scattering. The moment rotation is first order for fields along the b direction with $B_c \lesssim 1T$, so domains of mostly c -polarized and mostly b polarized material are expected. For current along b there is no major change in low temperature resistance either side of the transition — the reduction of about 5% is small enough that it could be due to a small c component mixed in. ρ_0 measured along a on the other hand shows a substantial increase across the transition, and measured along c a decrease of over 40%. This could be interpreted as a change in anisotropic scattering, but more likely it represents a change in the underlying Fermi surface.

In section 4.3 conductivity in the a and c directions was identified as dominated by weakly warped Fermi surfaces corresponding to chains of electron density along the b direction. Furthermore, the dimensional crossover physics seemed unaffected by the moment rotation, leading to the conclusion that the warping did not change much, and the bands remain dominant. This is borne out in the lack of changes for the bar with current along the b direction. The only feature is a peak at the moment rotation, attributable to a reduced τ . The other two current directions see a change though; a substantial increase in conductivity for current along c , and a reduction for current along a . To see if this can be reconciled with the model, we have to consider what happens if no one band is completely dominant. Neglecting for now the complexities of hall and inverting the resistivity tensor, the two bands will contribute in parallel. If one band has a negative temperature coefficient of resistance, and the other a very small temperature coefficient, then the total may be negative overall. The existence of such a second band is hinted at in figure 4.9 where it cuts off the divergent resistance predicted by the model. So a change in size, shape or topology of a non-dominant but still substantially contributing band can explain the change in ρ_0 without conflicting with our model.

There are two possible origins of such changes. Firstly, URhGe is an itinerant ferromagnet. As the moment changes, so must the Fermi surface. This could be the case here, but it is also possible that contributions to the conductivity arising from these pockets, which are expected to be very heavy, are too small to see. An alternative is given by the sketch model in figure 4.21, where there is a change in topology at the Brillouin zone boundary as a result of field breaking symmetry. Depending on the details of the Fermi surface close to the zone boundary, the new pockets formed may have areas with more Fermi velocity directed along some crystal axes than others. Since these pockets are formed from the same band as the open sheets, which are believed to be quite light, they too might be light enough to show up in the resistivity measurements. Since so little is known about these pockets, and the distinction between them is not necessarily

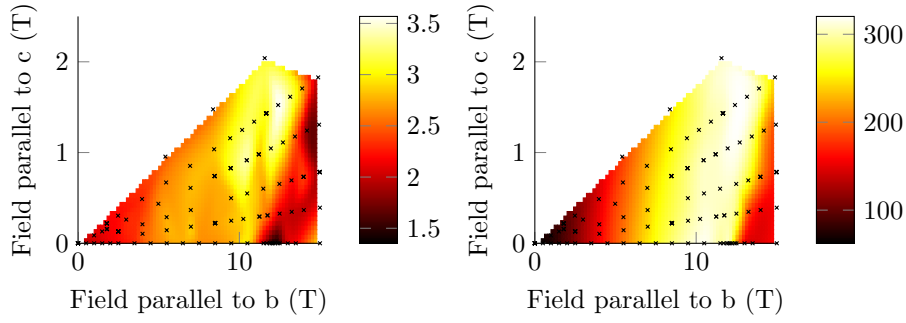


Figure 4.24: Coefficients of $R_0 + AT^n$ fit to resistivity over 500 mK of URhGe#1 for fields near the b -axis in the bc -plane. Black crosses show data points used in constructing the colorplot. **left:** n , **right** R_0 , in $\mu\Omega$

that clear anyway, it is not particularly productive to speculate which is the source of the changes in conductivity. But that it is some change in Fermi surface other than the open sheets seems very likely.

That the conductivity measured along c drops abruptly at the transition is also visible in URhGe#1, and indeed is the main reason for identifying that sample as having current predominantly along c . The right panel of figure 4.24 shows how the residual resistance changes with field and angle in the bc plane. The sample is superconducting, but the fitting technique described above allows us to obtain R_0 with a reasonable level of certainty nonetheless. The figure clearly shows the slow ramp up between zero field and the transition, and the abrupt drop at the transition, which moves to higher field with small fields applied along c . Interestingly, the sharp drop does not broaden out to the highest angle measured. This is in contrast to the torque data presented in [29], which broadens quite quickly with angle. This broadening is taken as evidence of the rotation transition becoming a crossover beyond $B_c \sim 1$ T. That is not apparent from this data. Either the transition remains first order out to $B_c \sim 2$ T in this sample or, perhaps more likely, the resistivity measured along c is a poor probe of the transition. Similar measurements with a sample with current along a different direction might be better, as then the peak, which is attributed directly to domain wall scattering, would be visible.

Previous results[39] identify an increase in n above 2 near the transition, apparently at odds with the result in figure 4.24, however, this data was taken with the field rotated 10° towards c from b . Measurements on the high-quality single crystal URhGe#1 in figure 4.24 show that this is the cause of the discrepancy. For fields applied along b , n rises somewhat above its zero field value, then drops close to 1.5 at the transition, as in the medium-quality bars. The detail is different however, with slightly higher values of n on the high quality sample. The A value is also a little lower, it probably indicates that although the same scattering processes are involved, the balance between them is slightly different. This further reinforces the conclusion that the AT^n fit is not physically significant, but it is still useful to discuss the implications for scattering

processes that could be present.

To analyse the dependence of the scattering rate on temperature, we can use the Born approximation. This is that the fields present at a scatterer are the incident field and the field scattered from the scatterer being considered. Equivalently, the scattering events are sufficiently separated in time and space that they do not interact. The scattering rate is then dictated by the product of several factors:

1. The possible states it can scatter to. This is given by an integral over the density of states $\int g(E)dE$ for states between the Fermi level and the energy of the electron being scattered. It is generally not temperature dependent, but is included here because it can be singular, rendering this simplified model inadequate.
2. The matrix element for scattering from any given scatterer. Usually this is constant with temperature, though if the nature of the scatterers change as a function of temperature then the matrix element can change. Usually the only change is the accessible final states due to conservation laws, but this is dealt with separately in point 4. Again, it is included here mostly because it can be singular.
3. The number of scatterers available. This is usually calculated from the energy spectrum for the specific type of scatterer.
4. A correction factor if the scattering does not destroy the current (for τ_{tr} only, if calculating τ_{QO} it will always be 1 as any scattering causes a loss of phase information)

To illustrate this, consider scattering from point crystal defects such as vacancies. The nature of the scattering is temperature independent, the number of scattering points is fixed and the scattering is catastrophic, so there is no temperature dependence at all. In the case of extended defects, such as larger voids, inclusions or dislocations, there is an additional factor due to point 4, but as it is not temperature dependent either, the overall rate remains temperature independent.

A more complicated example is phonons. For high temperature ($T \gg \Theta_{Debye}$) phonons the population scales as T , and scattering is catastrophic, so the resistivity scales as T . For low temperature phonons, the population scales as T^3 . But in this case the scattering is not catastrophic, but rather limited to small angle by the low momenta of the phonons and conservation of momentum. This small angle scattering means that several scattering events are required to destroy the current, and the distance around the Fermi surface each scattering event moves the electron is important. For phonons, this adds an extra factor of T^2 to the scattering rate, giving a total of $\rho \sim T^5$ [92]. For URhGe the Debye temperature is believed to be of order 200 K[27], so one would expect T^5 .

Another very common form, T^2 , arises from electron-electron (e-e) scattering in a Fermi liquid. While the whole Fermi sea contains electrons, only those within $\sim k_B T$ of the surface are available for scattering, so the population of scatterers scales as T . Unlike most other scattering processes described here, both the scatterer and the probe electron are conserved, and must end

up within $\sim k_B T$ of the Fermi surface. Requiring that the probe electron does so gives a further factor of T — a rare case of point 2 above being relevant without it being singular. For a given initial state of the probe electron, its final state and the initial state of the scatterer are the only free choices*. Conservation of momentum and energy choose the final state of the scatterer. As the scatterer can move from any point on the Fermi Surface to any other, so can the scattered electron, so there are no restrictions relevant to point 4. Collecting factors, the total resistivity scales as T^2 [92].

The T^2 resistivity from e-e scattering is expected anywhere that Fermi liquid theory holds. Ultimately, strong e-e scattering causes Fermi liquid theory to break down. Fermi liquid theory is based on the principle of adiabatic continuity, put simply, the interacting electron eigenstates can be mapped 1:1 to the non-interacting ones. The overlap between the interacting and non-interacting states must be large for this to be true. In this case the non-interacting eigenstates (i.e. the calculated band structure) are a reasonable description of the system, but there will be a tendency for electrons to change between those states because in reality they are not orthogonal. From a transport point of view, this looks like scattering, but with a very low rate in a good Fermi liquid. One way to quantify the scattering rate is to consider the width in energy that the electron actually covers when it is treated as though it is in a given eigenstate. That energy spread (known as the spectral function) dictates the states into which the electron can transition. The arguments governing the scattering rate are exactly the same as those outlined above for scattering due to temperature, so if the spectral function has width ϵ then resistance scales as ϵ^2 . Both these processes allow the electron to transition between states in the same way, so whichever is larger will dominate the resistance. If $k_B T \gg \epsilon$ the Fermi liquid is robust, and $\rho \sim T^2$. If $k_B T \ll \epsilon$ then the T^2 dependence is lost[105]. The fact that this transition-scattering process is large enough to be observed, implies that the intrinsic lifetime of the quasiparticle is comparable to the quasiparticle scattering rate. It is an indicator that Fermi liquid theory is very near, or possibly even past the bounds of its applicability, and the results one can gain from it should be treated with caution. In addition to the loss of T^2 scattering, there are several other indicators that Fermi liquid theory is beginning to break down. Fermi liquid theory provides corrections to the free electron results for such properties as the specific heat, resistivity and susceptibility through the effective mass and Landau parameters. If these corrections become large, it is a crude indicator that interactions are strong and the theory is nearing the limit. URhGe is considered a heavy fermion material, with its specific heat $\gamma \approx 160 \text{ mJ/mol}_U \text{K}^2$ indicating a substantial mass enhancement.

It is worth noting however that the more general result $\sigma = ne^2\tau/m^*$ is not necessarily lost with the Fermi liquid. Provided the new state still supports the concept of carriers with a definable

*Strictly speaking it should be borne in mind that the two electrons are indistinguishable, so it is incorrect to talk about the final state of the probe electron and the final state of the scatterer. There are simply two initial states and two final states. But this does not affect the phase space available and the resistivity still scales as T^2 .

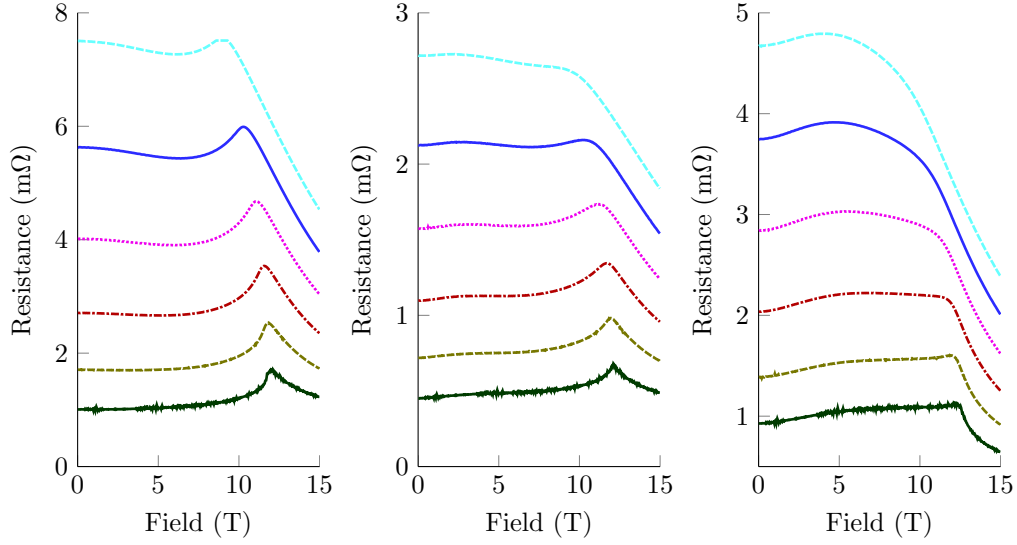


Figure 4.25: High temperature magnetoresistance of URhGe medium-RRR bar samples barA2, (left to right) barB2 and barC2 (left to right). Data at 1 K intervals between 2 K (dark green, lowermost) and 7 K (cyan, uppermost). Note the curie moment rotation transition, indicated by the peak or cusp, moving to lower field only very slowly.

population, mass, charge and scattering rate then the above equation still holds. With it comes Matthiessen's rule and it is still meaningful to consider possible contributions to the scattering rate and their temperature dependences. In the examples above, Fermi liquid theory was not used to derive the ρ_0 of impurity scattering, so that will persist in the non-fermi-liquid. In calculating $\rho_{Ph} \sim T^5$ however we used the concept of small angle scattering on the Fermi surface, so that result may not be valid once the Fermi liquid breaks down. Even then, the fact that conventional Fermi liquid theory breaks down (i.e. interacting-electron eigenstates no longer have a large overlap and adiabatic continuity with the non-interacting eigenstates) does not necessarily imply that the concepts of a Fermi sea and a defined Fermi surface must be lost. It is quite possible, even probable that some models based on a sharp Fermi surface remain applicable, and such systems are described as marginal Fermi liquids.

To return then to the possible scattering processes in URhGe, let us consider spin-waves and magnetic fluctuations. Both of these are changes in the magnetization, but they have slightly different physics. A spin wave is a change in the direction, a longitudinal magnetic fluctuation is a change in the strength. In general, in a ferromagnet one would expect both of these close to T_{Curie} . At temperatures much higher, the electron spins are completely uncorrelated and any collective excitations are suppressed. At temperatures much lower, well within the strong ferromagnetic state, all spins are aligned and there are no degrees of freedom for either excitation to form. Longitudinal fluctuations are suppressed by a strong magnetic moment, spin waves are suppressed by a large magnetic anisotropy. In the context of URhGe however it is not clear that the former is ever true. Various magnetisation measurements[27, 25] show that the magnetization

is slow to saturate with reducing temperature, and even then applying a field can increase the magnetization[27, 29], implying the capacity to support fluctuations in magnetization. In other words, URhGe at low temperature is always close to the critical temperature. Similarly, with a field applied along b of 9–12 T, T_{Curie} reduces very quickly from 6 K to zero (see figure 4.25) and the moment rotates, implying a low magnetic anisotropy*. With field applied, the system comes very close indeed to the critical temperature even at very low T , and both longitudinal fluctuations and spin waves could be present. When $T_{Curie} = 0$ the system is at a quantum critical point (QCP), and the kind of scattering discussed below is often described as being due to proximity to a QCP. Ultimately a system with a Curie point at low temperature is a system near a QCP. All that is required to make the former into the latter is to find an appropriate tuning parameter to drive T_{Curie} the rest of the way to zero. So the physics of a low T critical point and the physics of a system in proximity to a QCP are the same. Whilst the tuning parameter B_b does not cause $T_{Curie} = 0$ in URhGe, a combination of B_b and B_c does.

Mathon[106] discusses the scattering processes for a weak itinerant ferromagnet within the applicability of Fermi liquid theory, and arrives at a result that $\rho \sim T^{\frac{5}{3}}$. Other authors note that the long-range fluctuations involved would lead to a breakdown of the Fermi liquid[105] and treat the problem in terms of a marginal Fermi liquid with the same results. Both assume the interactions are singular, if they are nonsingular, the normal Fermi-liquid T^2 is recovered. Singular interactions are interactions where the matrix element for scattering diverges or is otherwise ill-defined, which happens if the interaction is long-range, as is the case for critical fluctuations. Either way, the $T^{\frac{5}{3}}$ dependence has been experimentally observed where a ferromagnetic transition is suppressed near zero temperature. The two best known examples being MnSi[107] and ZrZn₂[108, 109]. It should be noted however that the dimension of the problem enters into the result. $\rho \sim T^{\frac{5}{3}}$ is the case for $d = 3$; $d = 2$ yields $T^{\frac{4}{3}}$ [107] (and in $d = 1$ long range order is suppressed anyway). For URhGe the dimension might be expected to be 3, but we must take some care as in section 4.3 evidence for reduced dimensionality is presented. In that section, the pertinent physics is the dimensionality of the Fermi surface sheet and associated electron population which dominates conductivity. In this case, the relevant physics is of the population which provides scatterers. This can in general be a different band, indeed, in 4.3 it was observed that the dominant band was s , p or d in nature. This leaves open the question of where the f -weight has gone, and a fully 3D, high-mass, high exchange-splitting band seems a likely candidate. In short then, fluctuations in a ferromagnet near a critical point are a possibility in URhGe, and should yield $T^{\frac{5}{3}}$, or possibly but much less likely $T^{\frac{4}{3}}$.

Similar arguments can be made for critical fluctuations near antiferromagnetism also. In this case the excitation spectrum, and thus the population of excitations is different, and a different temperature scaling appears. $T^{\frac{3}{2}}$ is both calculated and observed[110]. At first it would seem

*Low in the bc plane, the magnetic anisotropy with respect to the a direction remains very high

that this is unlikely in URhGe as it is a ferromagnet not an antiferromagnet. However, as observed by Mineev[111], the Pnma space group has some unusual symmetry properties once ferromagnetism exists along the c axis. These allow an antiferromagnetic moment along the a axis without any further loss of symmetry. Indeed, an antiferromagnetic moment of $0.26 \mu_B$ has been claimed by some authors[23], (compared to a ferromagnetic component of $0.43 \mu_B$) but others[25] report only a ferromagnetic component of $0.37 \mu_B$. The latter give an upper limit of any antiferromagnetic component of $0.06 \mu_B$, and their result is now generally accepted to be correct. On balance then, this scattering process is considered possible but unlikely.

Quantum oscillation results (see section 4.5 and ref[39]) are suggestive of an electronic topological transition (ETT). Also known as a Lifshitz transition, this is where a Fermi surface is changing as the result of some tuning parameter, in this case field, and undergoes a topological change. Examples would be a small pocket disappearing or appearing; a neck pinching off to turn one pocket into two; or a toroidal pocket closing up to make a biconcave disk. The curvature of the underlying band structure defines which of these will occur, the different types being associated with minima, maxima, or saddle points. Such transitions do not give rise to a new form of scattering, but do modify the existing ones. In all these cases the density of states will have a singularity, and large changes in the band mass are also possible. Referring back to the list of influences on scattering, a singular density of states in point 1 leads to a singular scattering rate, implying a breakdown of Fermi Liquid theory. The essential energy scale for such a transition is the difference between the Fermi energy E_F and the energy of the point at which the DOS diverges, E_c . If $|E_F - E_c| < k_B T$, the DOS divergence plays no real role and the usual Fermi liquid $\rho \sim T^2$ form is recovered. If $|E_F - E_c| > k_B T$ then the quasiparticles have access to the infinite density of states at E_c and the scattering rate calculated is singular. This model is addressed fully by Blanter *et al*[112] for non-interacting electrons. For interacting electrons a more complex approach, utilising Green functions is necessary and is presented in reference [113], but yields broadly similar results. In either model, it is possible to derive a temperature dependence of resistivity $\rho \sim T^{\frac{5}{2}}$ or $T^{\frac{7}{2}}$ [113]. One material where an ETT has possibly been observed is YbRh₂Si₂. Whilst the physics in this material is usually viewed as Kondo breakdown, Hackl and Vojta[114] argue that it can be explained by an ETT.

One more scattering rate commonly seen in at finite temperature directly above a QCP is $\rho \sim T$. It is often observed that one of the scattering processes described above is present at low temperature (if not obscured by a new state), followed by a linear regime and finally saturation for reasons described in section 4.1. The origin of this linear regime is not well understood, but a recent paper[115] notes that for a very wide variety of different materials, the relationship $\tau^{-1} \approx \frac{k_B}{\hbar} T$ holds. For URhGe, at the temperatures considered, n is everywhere greater than one, so linear ρ is not observed. This type of scattering then is only relevant insofar as the temperature range studied is quite narrow. If URhGe is crossing over to linear ρ near the top of the range,

it might distort the fit and yield slightly lower n than would be accurate for the main scattering process.

To summarise then, we have identified possible processes for $\rho \sim T^n$ power laws with $n \in \{0, 1, \frac{3}{2}, \frac{5}{3}, 2, \frac{5}{2}, \frac{7}{2}, 5\}$. In URhGe n appears to vary continuously between approximately 1.5 and 3.5 (figure 4.24). Presumably this is the result of several of these power laws being present. Some can be eliminated as unlikely though. There is no evidence for structural changes from dilatometry[42], or under hydrostatic[116] or chemical pressure[43], the sudden appearance of a soft phonon mode causing a large T^5 component seems very unlikely. For the $n > 2$ region then, an ETT seems the likely candidate. This then begs the question of why it is not also visible at small angles from $B||b$. A topological transition, by its nature, separates two areas of the phase diagram with different topology and it is not possible to go from one to the other without a transition. Critical fluctuations destroying the Fermi liquid would render the concepts used to derive the ETT scattering laws somewhat meaningless, and also provide the $n < 2$ scattering seen at low angles. This in turn might not be seen at high angles as the critical point is driven down from the TCP to the QCP and the associated resistivity features disappear into the superconductivity. Whilst the observed n in this regime is closer to the antiferromagnetic $\frac{3}{2}$ than the $\frac{5}{3}$ expected for a critical ferromagnet, the relatively narrow range of temperatures used in the fit make it impossible to state definitively that it is the former not the latter. Antiferromagnetic fluctuations are allowed by symmetry, but ferromagnetic fluctuation still seem to be a more likely case. Finally, the above mentioned power laws are expected to cross over to a Fermi Liquid $n = 2$ away from the transitions and moment rotations, which explains the $n = 1.8$ observed in zero field data in section 4.1 and this section.

Overall then the observed power laws are consistent with a weak, near-critical ferromagnet, provided an ETT accompanies the moment rotation. The reason that these occur close together or simultaneously is not immediately clear, but it is possible to postulate a model where the ETT is a disappearing pocket with a strong f -nature which plays a major role in the magnetism. As this pocket depopulates, the magnetism becomes weaker (in terms of magnetic anisotropy), allowing the moment to rotate to align with the field. This is consistent with a model of large s -, p - and d -like surfaces dominating the conduction, and small, heavy, f -pockets the magnetism. Such a model is also supported by the data in the previous sections.

4.8 Measurements with the SQUID resistance bridge

The DC measurements presented in this section were made using the SQUID DC resistance bridge described in Section 3.4. As a matter of nomenclature, “AC resistance” is used in this section to refer to measurements made with a lock-in and low temperature transformers, at frequencies between 20 and 150 Hz. This is not to be confused with its common usage referring

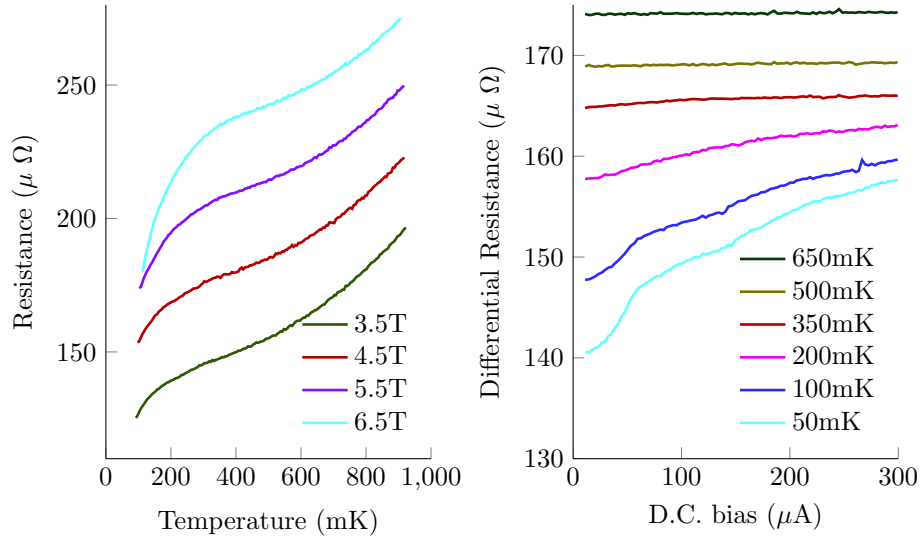


Figure 4.26: AC resistance of URhGe measured between the two superconducting pockets. **Left:** Resistivity as a function of temperature, at several different fields. Note substantial downturn at low temperature. **Right:** Differential resistance measured with an AC method at 6 T

to measurements in the high kilohertz to low gigahertz which probe dynamic effects such as skin depth.

4.8.1 Measurements in the resistive state

AC measurements on URhGe#1 at fields large enough to destroy superconductivity, but smaller than the field at which it re-enters yield intriguing results. At high (>600 mK) temperatures the resistivity fits a power law as described in section 4.7. At low temperatures, the resistivity drops substantially below the power law fit. The left panel of figure 4.26 shows several such measurements, similar features have also been observed on other samples[88]. It has been suggested that this might be evidence of some superconductivity surviving outside the bulk superconducting state*

It is possible to make differential resistance measurements with AC, and the result of such measurements are shown in the right panel of figure 4.26. These measurements were made by passing a direct current through the sample (plotted on the horizontal axis) and a small AC ripple superimposed on top. When this is demodulated in the usual way the DC component disappears and the AC component measures the differential resistance of the sample over the current range of the ripple. For an ohmic sample, this should be completely constant. For a non-ohmic sample, it can change. Thus the data in figure 4.26 is evidence of non-linear IV curves below 500mK, and increasing non-linearities at lower temperatures. Note that as this is the derivative any deviation from constant is evidence of non-linear IV curve. So non-linearity is seen in all curves below

*The low field state is known to be a bulk state from specific heat measurements[25], the high field pocket is believed to be bulk too, but this is not proven.

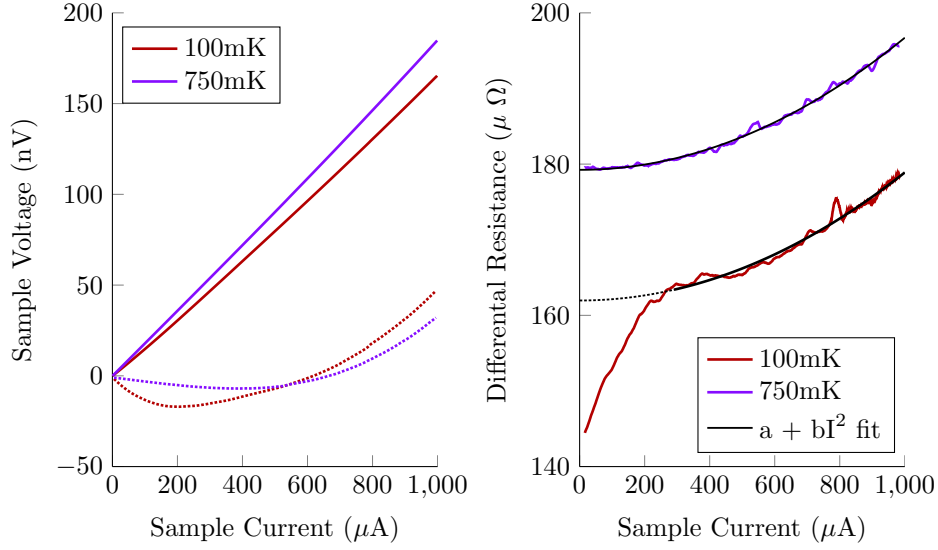


Figure 4.27: Directly measured IV curves of URhGe #1 in the area between the superconducting pockets. Magnetic field is 4.5 T. **Left:** Raw IV curves (solid lines) and the deviation from linear magnified $\times 10$ (dotted lines). **Right:** Derivative of the IV curves in the left panel. Solid black lines are fits, the dashed black line is an extrapolation of the fit.

500 mK. The additional feature at about $50 \mu\text{A}$ is also interesting, but that it occurs exactly when the AC ripple is equal to the direct current is a suspicious coincidence, and there is no equivalent feature in the DC measurements.

This AC technique is not ideal however. Whilst in theory one could regain the IV curve by integrating, there are several possible pitfalls. Firstly, the differential resistance is inevitably averaged over the size of the ripple voltage — in this case $50 \mu\text{A}_{\text{rms}}$. Secondly, it is difficult to be sure the result is not due to some form of relaxation in the sample on time constants similar to the measurement frequency, as might arise from a flux lattice. The SQUID bridge also offers excellent signal to noise characteristics.

In order to further investigate this effect, IV curves were measured using the SQUID resistance bridge detailed in section 3.4. In all cases, the deviation from linearity is very small, never exceeding 5 nV. It is nonetheless present; IV curves are shown in figure 4.27.

The IV curves were measured by sweeping the current continuously from 0 to 1 mA at $1 \mu\text{A/s}$. Each curve was measured for positive and negative currents, to eliminate thermoelectric contributions due to sample heating. Such contributions are two orders of magnitude smaller than the observed nonlinearity, never exceeding 50 pV. Finally, a small correction is made to reflect that the bridge has a response time of about 1 s (due to the PID controller settings), so with a continuous sweeping sample current the observed voltage, calculated from the reference current, is always slightly behind. For a ramp rate of $1 \mu\text{A/s}$, an offset of $1 \mu\text{A}$ would be expected, and an adjustment of $1.05 \mu\text{A}$ was found to make the IV curve smooth and continuous at the origin. This again is much smaller than the scale of the features observed.

To better understand the features, the differential resistance $\frac{dV}{dI}$ is plotted in the right panel of figure 4.27. This is calculated by fitting a straight line over a sliding $30\text{ }\mu\text{A}$ window. The 750 mK data, assumed to be at a temperature well above any superconducting effects, is not the flat line one would expect for a normal metal. This can be understood as the result of heating. One might reasonably assume that for small temperature changes, $R = R_0 + \left.\frac{dR}{dT}\right|_{T_0} (T - T_0)$ and, as the temperature change is due to heating, $T = T_0 + K \cdot I^2 R_{cts}$ where R_{cts} is the series resistance of the two current contacts. This leads to a resistance of $R = R_0 + \left.\frac{dR}{dT}\right|_{T_0} K \cdot I^2 R_{cts}$. Finally we can also write $\frac{dV}{dI} = \frac{d}{dI} IR = R_0 + \frac{1}{3} \left.\frac{dR}{dT}\right|_{T_0} K \cdot I^2 R_{cts}$. This then is the motivation for the black line fit in figure 4.27. We can estimate R_{cts} as $100\text{ m}\Omega$ from direct measurements of a small number of similar spot welds at 2 K , and $\left.\frac{dR}{dT}\right|_{750\text{ mK}}$ as $80\text{ n}\Omega/\text{mK}$ from the left panel of figure 4.26*. This allows us to calculate the strength of the thermal link as $1.4\text{ }\mu\text{W/K}$, a value which is eight times that which one would expect from the Wiedmann-Franz law if heat flow is via the contacts, but which seems reasonable given that the contacts do not lead directly to the bath. The non-linearity of the 750 mK IV curve can then be entirely explained by heating. It should be noted that at 1 mA the sample would be heated by 74 mK , which is 10% of the absolute temperature, but as the temperature dependent resistivity is fairly smooth, our linearisation of $R(T)$ is still valid.

A similar analysis is possible on the 100 mK curve, fitting only to the data above $290\text{ }\mu\text{A}$. The gradient $\left.\frac{dR}{dT}\right|_{100\text{ mK}}$ is larger at $142\text{ n}\Omega/\text{mK}$, which yields $K = 2.5\text{ }\mu\text{W/K}$. This is a little larger than above, which is surprising given the lower temperature. This suggests that heating is not the cause, and it is in fact a property of the normal state resistivity. One possible cause of this arises from the small and irregularly shaped sample, and the presence of field. If the carriers entering the sample spread out from the contacts, their paths are constrained by their orbital motion in the field. This effect is known as current jetting, and can be very complicated and unpredictable in non bar-shaped samples. It is also not proven that the SQUID bridge is perfectly linear in current. The deviation is well outside the specified linearity of the current supplies, and non-linearity of the SQUID should not enter as it is used as a null detector. Ultimately however, whatever the source of the non-linearity it is very similar in both curves so can be identified as some feature of the normal state resistance.

The sharp downturn below $200\text{ }\mu\text{A}$ is however a clear and distinctive feature. If we discount the curvature mentioned above, then what remains is a differential resistance curve which rises approximately linearly (with non-zero intercept) at low currents, then is flat above $250\text{ }\mu\text{A}$. The corresponding IV curve is linear at high I , but curves upwards slightly at low I . A reduced voltage at low current is possibly an indicator that there is some form of superconductivity and a critical current. This is broadly in keeping with the expected form discussed in section 1.4.2 if the critical current is so small that the rounding off of the transition extends all the way to zero,

*A rescaling of 10% is necessary to make the AC measurement match the gradient of the IV curve. This is due to the uncalibrated reference resistor

and if the superconducting material does not form a complete path through the sample.

When considering the possible form of any superconductivity in this region, it is prudent to start with the nature of the low-field pocket. In the limit of weak pinning, one can see a transition from a zero resistance state to one with resistance at H_{c1} , as flux enters the sample. This cannot be the case in URhGe, as its ferromagnetic nature ensures that B is always large enough to have flux in the sample. This is confirmed by torque magnetization measurements on superconducting single crystals[88] which show no evidence for a Meissner state. That leaves two options for the transition, either it is H_{c2} , and the bulk superconducting state is destroyed, or it is a transition from a pinned flux lattice to flux flow.

The former can explain why the deviation from linearity is small. Any remaining superconductivity would be confined to surfaces, defects or domain wall boundaries *etc.* If these filaments do not join up, the majority of the current path is normal. Many small filaments is also a possible explanation for the lack of clear single critical current. If the filaments are randomly distributed through the material, they will experience different current densities and thus transition at different times. If they are associated with different forms of lattice defect (for example) they may also have different critical currents. This then provides a method by which the observations could be due to some form of superconductivity, but it is far from conclusive evidence of such.

Another option that should be considered is superconducting fluctuations near the superconducting state. If small droplets of superfluid can appear and disappear, without being able to nucleate a complete transition to superconductivity, then they can reduce the overall resistance. Tinkham[13] gives a rough estimate of the increase in conductivity from such fluctuations as:

$$\sigma = \frac{1}{32} \frac{e^2}{\hbar \xi(0)} \left(\frac{T}{T - T_c} \right)^{1/2} \quad (4.9)$$

Where $\xi(0)$, the coherence length at zero temperature, is possibly very small in URhGe (see the arguments in section 4.5.2). However, if one estimates a coherence length of 10^{-9} m from the orbital limiting field in [39], this still only contributes a conductivity that is less than one part in 10^4 of the measured conductivity. So it is considered that any contribution from superconducting fluctuations should be negligible.

In conclusion, the small deviation from the normal resistance; the previous measurements that show the transition from the zero resistance state is of the form expected for H_{c2} ; and the low critical currents strongly suggest that these new observations are of a non-bulk state. Several forms of non-bulk superconductivity are possible, but domain-wall superconductivity is an excellent fit for the other known properties of the material. For field applied close to the b axis direction, and below the moment rotation transition, the material is ferromagnetic with domains where the moment is aligned in the $\pm c$ direction. Superconductivity is believed to be destroyed by orbital limiting in URhGe, and there will be some domain walls where the field lies in the

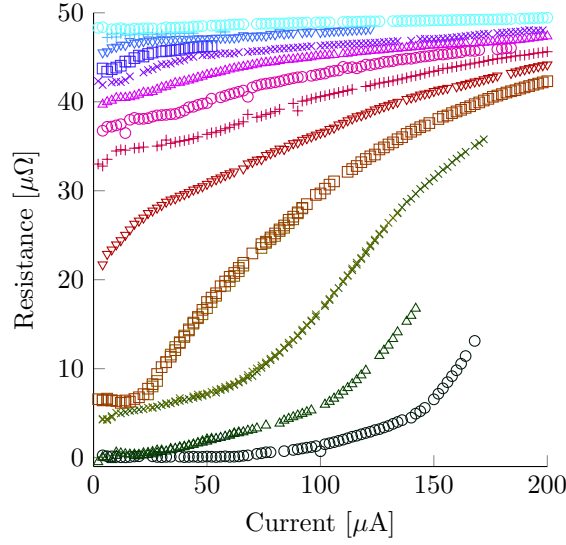


Figure 4.28: DC resistance of URhGe sample MK3 measured at zero field close to the superconducting transition. Curves at 5 mK intervals from 235 mK (bottom, black circles) to 295 mK (top, cyan circles).

plane of the domain wall. These will continue to superconduct at temperatures up to the T_c arising from the effect of field as a tuning parameter. As such, it is considered highly likely that these observations are of domain wall superconductivity. The T_c at which these effects disappear could be useful in identifying what the bulk T_c would be if B were simply a tuning parameter rather than also acting through orbital limiting.

4.8.2 Attempts to measure critical current

Measurements were attempted on sample URG.MK3, with the intent of measuring the bulk critical current. However, the SQUID bridge is not designed for passing large currents, and in any event large currents cause substantial sample heating. Currents of 200 μA are relatively simple to measure, and currents of up to 2 mA can be measured with care. The sample in question is an irregular crystal separated from a polycrystalline growth, which means the geometry is not ideal. The cross sectional area is estimated to be $2 \times 10^{-8} \text{ m}^2$, which yields current densities of 1 and 10 A/cm² respectively. For comparison, other heavy fermions have critical currents of tens to thousands of amps per square centimetre[20, 117]. But in the similar material UGe₂, critical currents as low as 0.1 A/cm² have been reported[48].

Even given the small current densities possible, one must come remarkably close to the transition temperature (or field) before the zero resistance state is lost. For a small current, this sample reaches zero resistance at 241 mK, and the transition is quite wide, only reaching 50% of the normal state value at 255 mK. A series of DC resistance measurements close to this transition are shown in figure 4.28. Each data point represents six separate voltage measurements, which alternate between positive and negative excitation current, so reject thermoelectric noise very

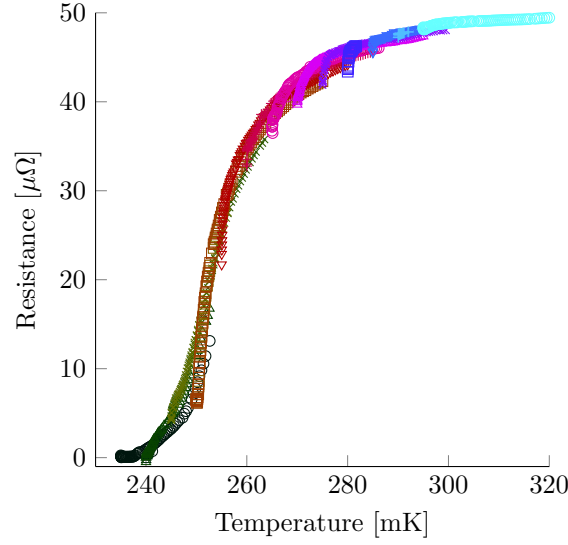


Figure 4.29: The same data as in figure 4.28, but with a simple model of sample heating applied. All the data collapses onto a single curve.

efficiently. If any one of the six measurements is very different from the others, it is omitted, if two are different then the whole point is discarded automatically. The missing points on the graph correspond to periods of excessive environmental noise, which causes flux jumps.

At first glance, it appears that a critical current may be present. This is particularly the case with the colder curves, where there is a zero resistance state up to some current ($60 \mu\text{A}$ in the lowermost curve), then a broad transition towards the normal state resistance. Given the proximity of T_c however, it is prudent to consider the possibility of heating. With a typical contact resistance of $2 \times 50 \text{ m}\Omega$, a current of $200 \mu\text{A}$ dissipates 4 nW in the sample, which must then flow away into the refrigerator. If the thermal link to the refrigerator is assumed to be 160 nW/K , and the sample temperature is calculated as $T_{\text{fridge}} + K \cdot I^2 R$, then the graph in figure 4.29 is obtained.

This heating equates to about 22 mK at $200 \mu\text{A}$, a not unrealistic amount for such a measurement. Usually heating in an AC measurement is somewhat lower, but the special shielding necessary for a SQUID measurement makes good thermalising harder. Overall then, the observations are consistent with ohmic heating of the sample by its contacts, and there is no evidence of a critical current. Similar measurements up to 2 mA were taken, but there heating is very substantial. The simple model used above would predict 2 K , but in reality the thermal link becomes rapidly stronger with increasing temperature. Nevertheless, 2 mA will drive the sample normal even with the fridge at base temperature, and is also sufficient to heat the sample thermometer and even the mixing chamber thermometer. Measurements were also made at various fields below the critical field of the lower pocket, with similar results.

The conclusion therefore is that no critical current has been observed, and the lower limit for

critical current in URhGe can therefore be placed at 1 A/cm^2 . Whilst the SQUID system could probably be modified to provide larger currents, the real limiting factor is heating. The measurement will only become practical with better sample thermalisation, lower resistance sample contacts, or better sample geometries.

An attempt was made to avoid the excessive heating by using pulsed currents. However, the SQUID bridge has a minimum response time of around 100 ms, which is too slow to catch any sign of a critical current before heating. Using the SQUID in open-loop (i.e. without the bridge, just as a null detector) mode allows in theory operation at with a small-signal bandwidth of over 50 kHz, but in practice the controller cannot slew more than one flux quantum fast enough to avoid flux jumps when used with a pulsed current. Even in the superconducting state a large pulse reaches the SQUID through the mutual inductance of the sample voltage and current leads. So the pulsed current measurements did not add new information about the critical current.

Chapter 5

Results on BiPd

5.1 AC Measurements

BiPd has garnered interest recently as it has been identified as a superconductor which lacks inversion symmetry[65]. Whilst this was originally observed in 1957[118], it was not studied in depth at the time, and was mostly forgotten until recently.

The relatively recent re-discovery of the material means that there is only a small amount of published work on it. The first recent paper to note the transition to a $P2_1$ non-centrosymmetric structure (see fig 5.1) appeared in 2011[65], and they also confirmed by resistance, heat capacity and susceptibility measurements the appearance of superconductivity below 3.8 K. Some measurements of resistance at field were also taken, but they do not report any structure to the transition. From these measurements a number of properties are deduced, the specific heat γ at $4 \text{ mJmol}^{-1}\text{K}^{-2}$ indicates generally no heavy fermion physics. The mean free path of over $2 \mu\text{m}$ and good RRRs indicate clean samples. Estimates of coherence length and penetration depth indicate that the material is type II.

Without the complications of heavy fermions, both de Haas-van Alphen and Shubnikov-de Haas measurements have been successful[120]. These agree well with Fermi surfaces calculated by DFT, which are shown in figure 5.1. A mass renormalisation of ~ 2 , presumably due to phonons, is required to make the mass from the temperature reduction factor fit match the calculated ones. The same renormalisation is required to make DFT match the specific heat γ . As discussed for URhGe in section 4.4.1, there are near-degeneracies at the zone boundary. Unlike URhGe, field is not required to break them, the lack of inversion symmetry allows SOI to break the degeneracy at zero field.

Other experiments have also been conducted which show varying amounts of evidence of unconventional superconductivity. NMR and NQR studies[121] indicate a strong s -wave character, whereas point contact measurements[122] suggest two gaps, one of which is anisotropic. Direct

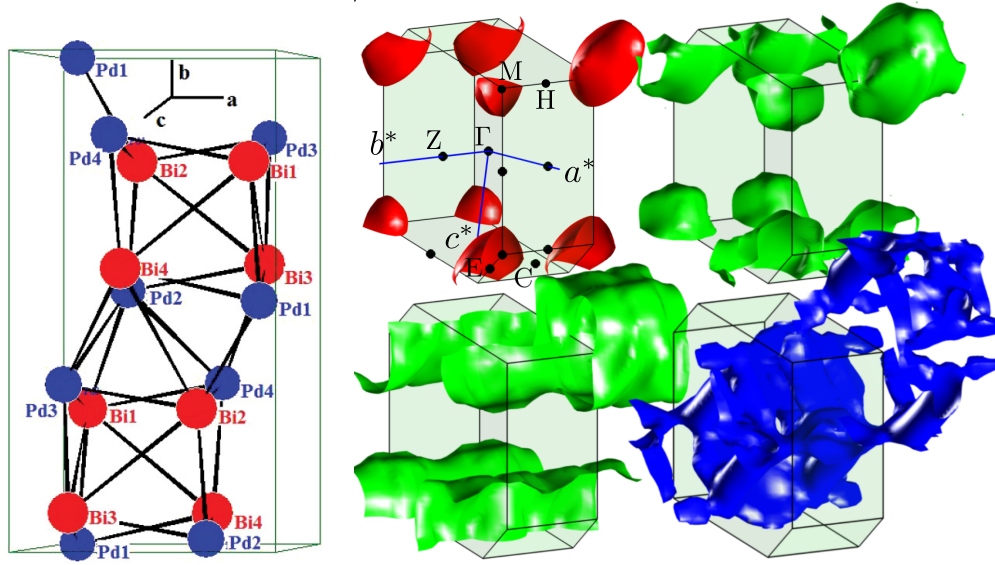


Figure 5.1: **Left:** Structure of BiPd. The space group $P2_1$ is monoclinic and has only two symmetry operations, the identity and a twofold screw along the b axis. There are eight each of Bi and Pd in the unit cell, so four inequivalent sites of each. The lattice parameters are $a = 562.84$ pm, $b = 1066.15$ pm $c = 567.52$ pm, $\alpha = \gamma = 90^\circ$, and $\beta = 101^\circ$. Figure reprinted with permission from the American Physical Society from ref [65], which is available at [dx.doi.org/10.1103/PhysRevB.84.064518](https://doi.org/10.1103/PhysRevB.84.064518). **Right:** Calculated Fermi surfaces for BiPd. Counting spins separately, four of 12 bands are shown, there are four like the top left, two like the top right, two like the bottom left and four like the bottom right. Figure from [119]

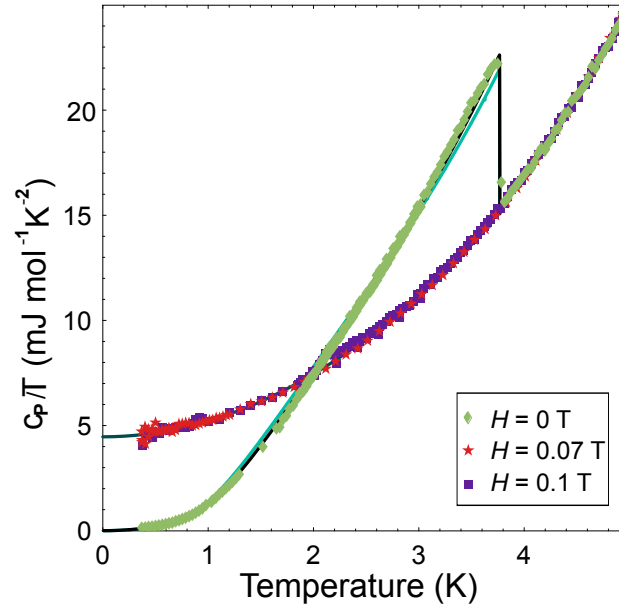


Figure 5.2: Specific heat measurements on a sample of BiPd, adapted from ref[129]. Solid lines are fits to various models, the black line is BCS and the pale blue line is a model using the gap observed in STM measurements. Note that there is no bulk superconductivity above 70 mT.

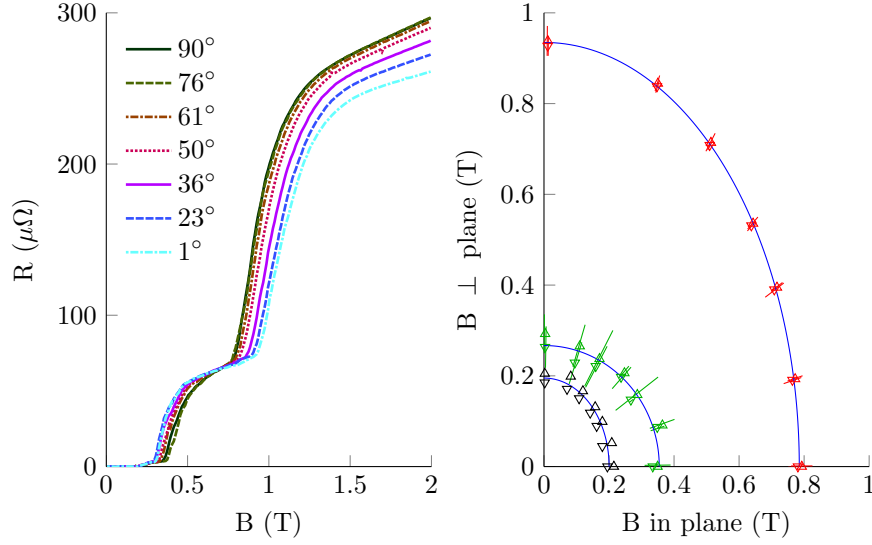


Figure 5.3: Superconducting critical field in BiPd, measured by resistivity on sample BiPd#2. **Left:** Selected resistivity curves. Angles are measured from the b (out of plane) axis. **Right:** Transition points extracted from the curves such as those in the left panel. Triangles indicate direction of field sweep, up or down for increasing or decreasing respectively. Black: Edge of zero resistance state H_{zr} . Green: first kink H_{k1} . Red: second kink H_{k2} . Solid lines are ellipse fits.

measurements of penetration depth[123] also suggest two gaps with different properties. Overall, the details remain rather unclear. Very recently, measurements have also been made with small-angle neutron scattering, and muon spin rotation. These point towards strongly multi-band physics, and also to the loss of bulk superconductivity (as evidenced by a vortex lattice) at fields much smaller than those where the sample reaches the normal resistance[119]. Recent measurements of specific heat at several fields[129], shown in figure 5.2, also show no bulk superconductivity at fields above the first deviation from zero resistance, which occurs at a lower field in that sample.

In order to probe the superconducting properties of the material, a variety of resistivity measurements were made. The blue fridge was used, as it has both a precision rotator and a SQUID resistance bridge (see sections 3.3 and 3.4 respectively), but it is not the ideal system for measuring this material as it has difficulty measuring above 1 K, but the T_c of BiPd is 3.8 K. Nevertheless, some very intriguing results have appeared.

5.1.1 Angular dependence of critical field

Figure 5.3 shows a series of measurements on BiPd#2 using low temperature transformers and on a rotator. Unlike the zero field T_c , the transition is split into several parts. First, at around 0.2 T, the resistance departs from zero by only $5 \mu\Omega$. There are then two similar features consisting of a sharp upwards kink, a steep rise and then a rounding off towards a nearly constant resistance. For reasons which will become apparent in the next section, it is best to discuss the position of

these features according to the initial upwards kink. The lower kink is then close to 0.3 T and the upper one just below 1 T. From here on, the edge of the zero resistance state, the lower and upper kinks will be referred to as H_{zr} , H_{k1} and H_{k2} respectively.

Both of the kinks are field-angle dependent, but in opposite directions. The lower kink is at highest field for $\mathbf{B} \parallel \text{plane}$ and the higher kink is at larger fields for $\mathbf{B} \perp \text{plane}$. The position of these features was extracted and the results are plotted in the right panel of figure 5.3. For the departure from zero resistance the points represent the first resistance significantly above the noise level, at 100 nΩ. For the other two sets of points the kink positions were identified by fitting straight lines over a range of 90 mT or 150 mT (H_{k1} and H_{k2} respectively) each side of the kink and taking their intersection to be the position of the feature. For H_{k2} the field increasing and field reducing sweeps agree well. This is as one would expect from the good signal to noise. Similarly, the H_{zr} line is nicely consistent. Both of these show a small hysteresis, 12 mT wide in the case of H_{k2} , and 20 mT in the case of H_{k1} . All of these field sweeps were conducted at 1.67 mT/s, so these hystereses correspond to a delay of 7–12 seconds. This is longer than one would expect from any electronic effects (such as lock in amplifier time constants, typically 1 s) but within the bounds of possibility for the magnet. It could also be evidence of slow processes within the sample, such as flux line motion with pinning.

The lower kink (green) points have markedly more scatter, and larger uncertainties. Referring back to the raw data, one finds that it is noisier in-between the two kinks. When fitting two lines to extract the kink position, one is in the noisy section, one is not. If the steep line is in the noisy section, it will cause noise in the extracted field, if the near-horizontal line is in the noisy section, it will cause noise in the extracted resistance. Thus the noise only appears in the extracted points for H_{k1} . As this extra noise appears in the same place in all the curves, it is assumed to be intrinsic to the sample. This is further addressed in section 5.2, where the origins are more apparent.

All three transitions are well fitted by ellipses. The parameters of the fits are:

	H_{zr} (T)	H_{k1} (T)	H_{k2} (T)
\mathbf{B} in plane	0.200 ± 0.002	0.354 ± 0.010	0.785 ± 0.001
\mathbf{B} out of plane	0.195 ± 0.003	0.267 ± 0.008	0.935 ± 0.002

note that H_{zr} is circular within the uncertainty. Some anisotropy is to be expected, given the structure of BiPd, and ellipses are the default shape for anisotropic superconductivity. What is interesting is that the two ellipses have different anisotropy, with the lower kink reaching higher fields in the in-plane direction than the out of plane one and the outer kink *vice versa*. This points toward there being two different superfluids present, with different behaviour. Whether they coexist microscopically or macroscopically is not clear from the AC data.

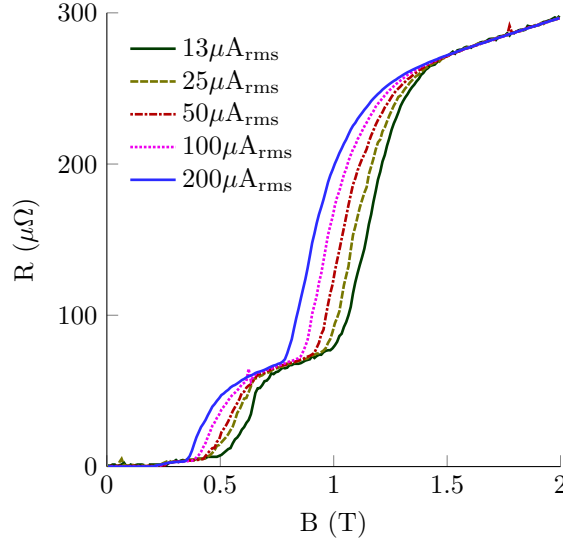


Figure 5.4: Current dependent resistance of BiPd#2 with field in-plane.

5.1.2 Current dependence of critical field

In addition to being angle dependent, the structured transition is very current dependent. Figure 5.4 shows the transition measured with different currents with $\mathbf{B} \parallel \text{plane}$. This figure shows resistance, so any area where the curves do not lie together is evidence of a non-linear IV curve. As always when considering nonlinear IV behaviour, it is prudent to consider the possibility of heating. These measurements were taken at 200 mK, and experience shows that heating of more than ~ 20 mK is rare. Compared to a critical temperature of 3.8 K, this heating should have minimal effect. This conclusion is borne out by further measurements in section 5.2.

Examining the curves in detail, we see that there are several areas in which there is no current dependence. Firstly, in the high field limit. This is the normal state, so the lack of current dependence is expected. Secondly, in the flat section between the transitions the resistance is very nearly current independent. This suggests that the sample is nearly ohmic in this region. Finally, both the zero resistance state and the initial deviation from it show no clear current dependence. In the case of the latter, the feature is sufficiently small that any deviation could be lost in the noise.

Note that although the curves in figure 5.4 are equally spaced, the currents are not. This implies a roughly exponential dependence on current. Drawing any clear conclusions from the current dependence in this figure is difficult though, as the detailed nature of the IV curve is not known. This motivates the DC measurements presented in the next section.

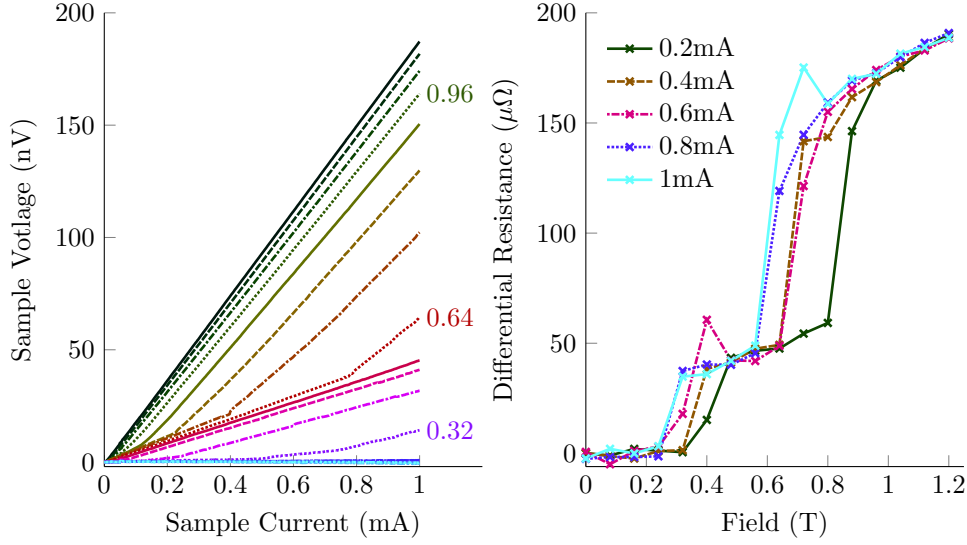


Figure 5.5: **Left:** IV curves measured on BiPd#2 using the SQUID bridge. Curves at 75 mT intervals from zero to 1.125 T. All of the curves below 0.3 T lie together along the x -axis, where the sample is superconducting. **Right:** Gradient dV/dI extracted from curves on the left. Distinct states and the slight magnetoresistance of each state is visible.

5.2 DC Measurements

The same sample of BiPd as measured in the previous section (BiPd#2) was measured using the SQUID resistance bridge. A representative collection of IV curves is shown in figure 5.5. These curves were taken by sweeping the current from 0 to 1 mA at $1 \mu\text{A/s}$. Each measurement was taken for both positive and negative sample current in close succession, to identify any contribution from thermoelectric effects. These were identified to have the usual quadratic form, and to never exceed 1 nV. However, fully symmetrising the curves in this way was not practical as some of the fine detail is not repeatable. In particular, the position and exact shape of the kinks varies from run to run by a few millitesla. So the figure shows only positive current curves, but it should be noted that the minor deviation from zero of the curves with $B < 0.2$ T can be entirely explained by thermoelectric effects due to joule heating of the sample.

Our first task is to reconcile this data with that presented in the previous section. To assist with this, the AC and DC measured resistance for a kinked IV curve are simulated in figure 5.6. The intrinsic IV curve is the one measured by DC, and is shown in green in the left panel of the figure. It has been chosen to have a differential resistance of 1Ω from zero up to a critical current which has been normalised to one. Above this current it has a differential resistance of 2Ω . The AC response is calculated from the DC response numerically with a simple lock-in implemented in software. The right panel shows the resistance one would measure by taking $R = V/I$ from the left panel. Obviously, below a normalised current of one, the system is linear and the AC and DC measurements agree completely and yield a resistance of 1Ω . At high normalised current the apparent resistance asymptotically approaches 2Ω . That it will never reach 2Ω in either the AC

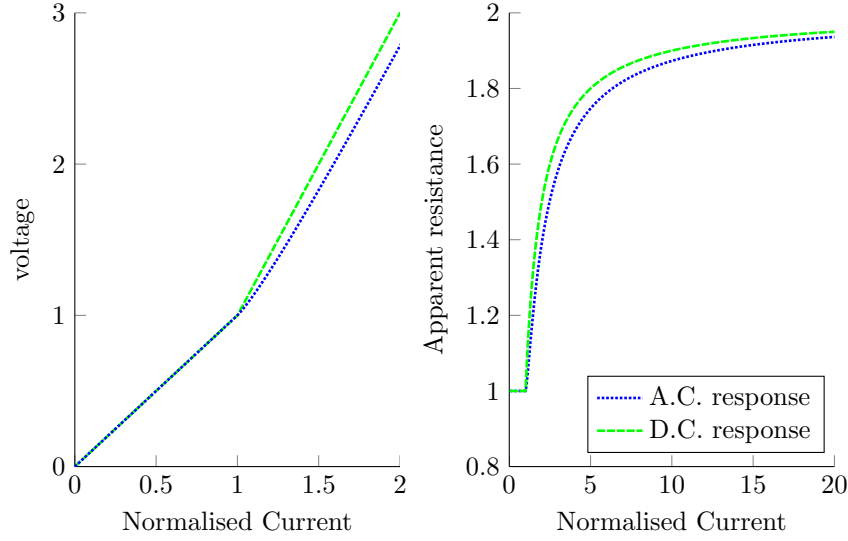


Figure 5.6: Simulated measurements of a kinked IV curve. **Left:** intrinsic IV curve as measured by DC and the one which would be measured by AC using a lock-in. **Right:** Measured resistances calculated as $R = V/I$ from the curves in the left panel.

or DC case directly reflects the fact that the upper section on the IV curve is linear but has a non-zero intercept.

To make direct comparisons between the right panel of figure 5.6 and the measured resistances in figure 5.4 it is necessary to note how field changes the curves in figure 5.5. Firstly, there are two kinks in the IV curves in this figure, one for fields around 0.3 T, the other for fields around 0.6 T. For both of these, the behaviour is the same. Increasing field moves the kink to lower current, which allows us to compare increasing field to increasing current. Secondly, increasing field increases the gradient of the IV curve both above and below the kink. With these points in mind, it is clear that the observed measurements in AC and DC are qualitatively consistent with each other. It is also clear that the point at which the IV curve is kinked is the point at which the AC resistance deviates sharply upwards from its nearly flat state. This justifies the decision in section 5.1 to treat these upwards kinks as the transition points, rather than the perhaps more usual choice of the half height.

As well as qualitatively agreeing in shape, the AC and DC data agree quantitatively in position of the kinks. Figure 5.7 compares in the right panel the AC and DC data. Unfortunately due to the requirement to run both the SQUID bridge and the rotator on the fridge at the same time, and due to the inflexibility of the shielding required on the SQUID bridge, the SQUID bridge samples could not be mounted in the field centre. They were positioned 85 mm above the field centre, and were thus in an area of lower magnetic field. A correction factor of 0.80 was found to match up the data very well. Extrapolating from the magnet specification would yield a correction factor of 0.84, and interpolating from a field measured with a hall sensor at 100 mm above the field centre would yield 0.76. So the figure of 0.80 is considered reliable enough to

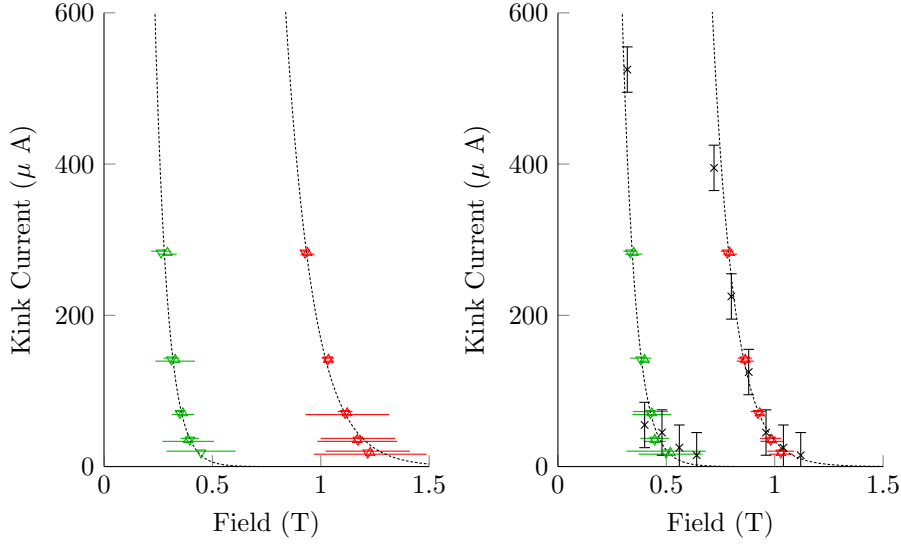


Figure 5.7: Kink current measured on BiPd#2 by AC (triangles) and DC (crosses). AC kink positions are extracted from constant current field sweeps, plotted by peak current (not rms). Upward pointing triangles are measurements made with \mathbf{B} increasing, downwards triangles \mathbf{B} reducing. In cases where there are two data points at the same current, the errorbars are offset slightly from the data points for clarity. DC kink positions from constant field current sweeps. **Left:** $\mathbf{B} \perp$ plane. **Right:** $\mathbf{B} \parallel$ plane. Dotted lines are exponential fits.

say the AC and DC data is in quantitative agreement, though the AC data should be considered superior when quantitatively considering field dependence.

Figure 5.8 shows a large amount of data measured with the SQUID bridge on a different sample, where similar effects are seen. The higher density of data here makes fitting more practical. A fit of the form $Ae^{-\alpha B}$ was found to adequately represent the data. It should be pointed out that a fit of the form $Ae^{-\alpha(B-B_c)}$ could well be more appropriate, but in that case A and B_c are degenerate fit parameters. These fits are shown with data from different samples and different field directions in figures 5.7 and 5.8 as black dotted lines. This exponential decay of a critical current with field has been observed in a variety of materials including niobium alloys[124, 125] and high T_c superconductors[126]. Whilst the origin is still unknown, it is evidence that the observations presented here are critical currents of some form.

When fitting to large currents, it is prudent to consider heating of the sample. The consequences of heating are explained in more detail in section 4.8, but when considering the appearance of a transition or feature such as the kinks, it is enough to recall that the majority of the heating comes from the sample contacts. These are usually quite temperature and current independent, so the main effect is to heat the sample by $\Delta T = K \cdot I^2 R_{cts}$, where K is the thermal resistivity to the bath which generally reduces slowly with temperature. This quadratic form is a poor fit for the data. A thermometer attached to the sample shield indicated a temperature rise of 5 mK from 50 mK at 1000 μ A, dropping to 0.5 mK at 500 μ A exactly as one would expect for a metallic link to the bath. The sample is doubtless hotter than that, but substantial changes on

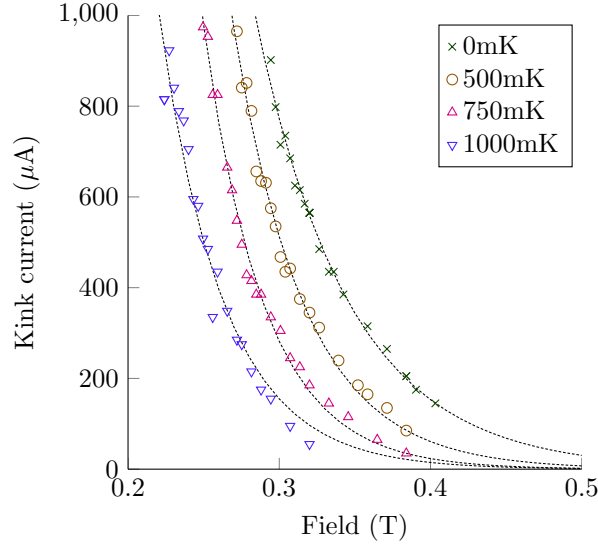


Figure 5.8: Kink positions measured on BiPd#1, using DC, with $\mathbf{B} \perp$ plane, upper kink only. Dotted lines are exponential fits.

the scale seen in figure 5.8 can be ruled out.

It is possible to explain the unusual IV curves as a result of three separate conductivity channels. These channels appear predominantly in series, as one might expect if they arise from inhomogeneity. The first of the channels is the bulk of the material, this is superconducting up to the first observed deviation from zero resistance (at 0.20 T in sample #2). The other two channels consist of small islands, planes or filaments which do not form a complete path through the sample, but do act to short out much of the bulk normal resistance when superconducting. Both of these follow the usual flux-flow behaviour explained in section 1.4.2 and exemplified in figure 1.4. One has a critical current corresponding to the lower kink, the other corresponds to the upper kink. Since these channels occur in series, then for a given current we may simply add the voltages due to each channel. Just below the critical field of one of these, we expect to see a linear (bulk normal) part of the IV curve, plus a part which is zero up to some critical current then linear. The sum of these parts has the same form as the IV curves in figure 5.5. As the field is increased and the critical field passed, the kink moves down to zero current, and the curve becomes the bulk normal resistance again, only steeper as it is no longer partially shorted.

The right panel of figure 5.5 shows how the gradient of the IV curve changes with field. The kinks mark the large steps. If the bulk is normal, then this gradient is simply the resistance of the bulk, with the steps due, effectively, to changing geometrical factor as it is partially shorted out. The slight upward slope with field away from the immediate vicinity of the kinks is then due to magnetoresistance rather than any property of the superconductivity. If we write the total resistance near one kink, neglecting the other for now, as $\rho_{tot} = a\rho_n + (1-a)\rho_{ff}$, then we can separate out ρ_{ff} . If it followed the conventional form, then it would go as $\rho_{ff} \propto B/B_c$, linear in

B. The area around the upper kink is clearly convex, not linear. The lower kink less so, and due to the intrinsic noise at this transition described below extra data does little to clarify the shape. The convexity at the upper kink however can be taken as evidence of a gapped order parameter as observed in UPt_3 [20].

There are a few other features of the DC measurements which are interesting. The first is the repeatability of the measurement at different points in the phase space. Some features are always repeatable: the zero resistance state, the normal state, and the gradient of the IV curve in most of the intermediate states. There are two areas where repeatability is poorer however. The first is in the area below the upper kink, some of this behaviour is visible in figure 5.5 on the 0.32 T curve, which has a small step at $600 \mu\text{A}$. When performing two current sweeps under identical conditions, and within minutes of one another, the position of the lower kink, and the gradient before and after can be different. In rare occasions, the curve can also show sudden jumps or kinks which seem to be a change in the sample properties similar to the difference between sweeps. The sweeps in question are typically 2 to 10 minutes in length, but if it is assumed that sweeps can be different even if they are taken over a few milliseconds, then this explains the increased noise in the AC measurements between the kinks.

If the kinks are to be ascribed to critical currents, then it is possible that these features are due to metastable states of the flux lattice. Given the field and sample size, one would expect 10^6 flux lines between the voltage contacts, so the behaviour of individual flux lines would not normally contribute an effect of this magnitude. In flux flow however, flux lines do often move in clumps of 10^3 – 10^5 [13, 127], so that makes such states possible.

The second main area of poor repeatability is in the exact position of the upper kink. This is usually repeatable between measurements taken soon after one another, but never repeatable if the field has been changed. Whilst the kink is usually well defined in the IV curve, and the gradient above and below remains the same, the position can change. This comes with a change in the IV curve at currents well above the kink: the IV curve is offset. If the kink is understood to be a critical current in the manner of the model described above, is harder to attribute to different arrangements of flux lines. In this case, as this is the upper kink, there should be no pinned flux left once flux flow starts. It seems there is some other source of magnetic hysteresis. If the superconductivity is due to inclusions, it is possible that they might show some magnetism.

Finally, two samples have been measured, BiPd#1 and #2. Both samples show two distinct kinks, with linear IV curves in between. Both samples show poorer repeatability between the two kinks than at either side and both samples show a zero resistance state at low field, with a small deviation from it before the first kink. The temperature dependencies show the same exponential form in both samples. This serves to rule out some form of unusual sample inhomogeneity in a single sample as the source of this behaviour. The major unexplained difference between the samples is in the position of the kinks. The upper kink is reduced from $\sim 1.2\text{ T}$ in the

second sample (figure 5.7, left panel) to only 0.4 T in the first sample (figure 5.8). The origin of this difference is not clear, but it is possible that the superconductivity is confined to e.g. twin boundaries within the sample, and the configuration of these is important in determining the critical field. Very recently, samples grown in a different laboratory have also been measured using AC[128], and show similar features to the two discussed above: two kinks with different anisotropy with field, and a very small deviation from zero resistance at a lower B . In this case the lower kink lies around 100 mT and the upper kink around 400 mT. This is another indicator that the general form is reproducible, but that the exact position of the features varies depending on some as yet unidentified differences between samples.

We can then consider different possible origins for the channels described in the model above. The channels are described conceptually as physical channels, but microscopic coexistence should also be considered. Strong multiband effects are not unexpected in a non-centrosymmetric superconductor, as there will often be a Kramer's degenerate pair of bands which has been split by the SOI. If they are split on an energy scale larger than the superconducting gap, but small compared to other features in the band structure, then they will likely both support superconductivity even without much interband scattering. Since these bands have spin chosen by the momenta, they will both have the mixed parity order parameter described in section 1.4.3, and if the two bands are different then the parity mixing will be different. So a two component order parameter appears. The big problem with this approach to explaining the data presented here is that two microscopically co-existent superfluids must share the same flux-flow critical current. This is simply because they must share the same flux lines, which will be either moving or stationary.

Alternatively, one could posit a model where the sample is divided into several areas, on any length scale over the characteristic lengths of the superconductivity. This could be differing areas of inhomogeneity or inclusions; or bulk, twin boundaries, and the surface. Each of these could have a different critical field, and provided the ones with higher critical field do not provide a continuous path between the voltage contacts, that could result in the behaviour seen. If the origin were simply different areas of quality, one would expect the only difference between them to be the local critical current, which is at odds with the anisotropy observed in section 5.1. These measurements suggest two superfluids with substantially differing properties. This also has implications for the idea that they may be inclusions. For the properties of the inclusions to be anisotropic the induced material would have to either have an anisotropic structure which aligned with the structure of the bulk, or be so small that the surrounding material substantially affects the properties of the superfluid.

On balance then, it is considered most likely that bulk superconductivity is destroyed at the first departure from perfect conductivity. This is observed to be isotropic, and to occur at 0.20 T in sample #2. This is in agreement with the other measurements mentioned at the start of this section. There then remain two different conductivity channels in the material, perhaps surface,

twin boundaries or inclusions, which show different behaviour. Both of these are anisotropic, and both have relatively small critical currents by virtue of limited cross section, but the detailed properties are different.

Chapter 6

Summary and Conclusions

A large part of this work has been the design and development of two new experimental rigs for use on the ‘blue’ dilution refrigerator. The first of these is a mechanical rotator, capable of rotating samples and experiments of up to 40mm inside the magnet bore with a precision of better than 0.01° . This was achieved with a system of bevel and spur gears linking the rotation platform to a drive motor outside the cryostat. The platform angle is measured by modulating the magnetic field, and measuring the modulation with two perpendicular sensing coils. The measurement feeds into a closed loop control program which can reliably and automatically rotate the platform to any given angle without any manual intervention. This was combined with a variety of techniques for making low noise resistivity measurements. Most of these techniques were already available in the laboratory but some, such as the use of balancing transformers, have also been developed further as part of this work.

The second major new experimental rig is the SQUID bridge. This uses a commercially available Model 5000 SQUID and controller as a null-current detector in a simple bridge where the sample is compared to a reference resistor. The sample and reference are each driven by a Keithley 6221 current supply, which are controlled by a PC which also manages the SQUID. The system is designed to work with a high level of automation, detecting issues such as flux jumps and repeating short sections of data as necessary to avoid gaps. This allows direct measurements of the IV curve, and also provides a low-noise resistance measurements. For small currents, and provided good vibrational isolation is in place, a voltage noise as low as $100 \text{ fV}/\sqrt{\text{Hz}}$ (dominated by Johnson noise) is practical. This compares very favourably with even the very best measurements possible with lock-in amplifiers and low temperature transformers.

A broad variety of resistance measurements have been made on URhGe. Unlike previous work on the material, the current direction used for the measurement is carefully controlled on all but the smallest samples, and it is found that both the resistance and magnetoresistance are anisotropic with respect to current. The zero field resistivity is interpreted as a crossover from

metallic to incoherent as a result of two parallel channels, with the crossover temperature rather higher for current along b than either of the other axes. The cusp at T_{Curie} is explained through the Fisher-Langer relation as arising from additional scattering from magnetic fluctuations.

Very large, non-saturating magnetoresistance is observed, and combined with a crossover to negative temperature coefficient of resistance (NCTR), is seen as strong evidence for open orbits in URhGe. Open orbits exist both along k_a and k_c , and most probably these are on the same Fermi surface, implying a nearly flat sheet normal to k_b . To explain the NCTR, a model of coherent to incoherent crossover is advanced, where increasing field causes the localisation of electrons to chains running through the material along the b direction. This model, combined with the observed crossover field and temperature, allows some crude estimations of the properties of the sheets (including $v_F \sim 10^5$ m/s) and from them approximate contributions to the total conductivity and specific heat. These open sheets can account for most of the conductivity, but only a small part of γ .

Careful comparison of samples of different RRR also allows the identification of several other interesting features. There is clearly a peak in ρ_0 at the moment rotation transition, as has been observed before. This is attributed to increased scattering from domain walls which appear as the moment rotates. Also present is a change in anisotropy, the conductivity measured along c increases and along a reduces, with b broadly unaffected. This is interpreted as evidence of some Fermi surface restructuring at the rotation, but not involving any major change to the open sheets. Some restructuring is almost required by the symmetries of the system, and this is discussed in detail in the relevant chapter.

Shubnikov-de Haas measurements were also made. These indicate some small, heavy pockets, as one might expect to find in a heavy fermion material. The limited angle range over which they are visible, and the requirement for high magnetic field facilities to make them visible, means that there is not enough data to obtain the full shape of the Fermi surfaces. There are however some interesting effects tied in with the SdH.

The first unusual observation is giant SdH. This shows a field dependent mass and area, as well as a very unusual field dependent amplitude. Giant SdH can arise when the oscillatory density of states on some part of the Fermi surface enters into the conductivity much more strongly than the usual way, which is by modifying the global τ . If the oscillatory density of states lies on a magnetic breakdown point, between for example an open and a closed orbit, it can move some carriers onto a different orbit type in a manner which oscillates with field. This is most likely evidence that the aforementioned open sheets draw close together somewhere in the zone, and there is a small pocket, this one with mass around $8m_e$, which is separated from the open sheets by only a small energy gap. But once again, there is not quite enough information to say where in the zone this lies, or give any detail about its shape and form.

Other observations build upon SdH measurements which have been reported in our paper,

which is only summarised here[39]. In short, the frequency of the oscillation is changing, which allows a family of possible Fermi surface areas. One of these possible areas reaches zero at the same point that the amplitude of the oscillations goes abruptly to zero. This is taken as evidence of an electronic topological transition, a possibility which is further supported by the measurements of $\rho(T)$ presented in section 4.7. This in turn is seen as providing the method by which the critical field appears to diverge. New measurements further supporting this model is the observation of non-linear IV curves in the region between the two superconducting pockets, which are ascribed to domain-wall superconductivity. Since orbital limiting does not affect 2D domain-wall superconductivity in the way it does the bulk, this persists where the field acting as a tuning parameter exceeds the orbital limiting field for the bulk. It is evidence then that the two pockets of superconductivity are of the same form, and the superconductivity is truly re-entrant. Some other measurements were also made on some intermediate RRR samples with substantial inhomogeneity and partial superconductivity. From these one can conclude that the superconductivity is more robust at high field than low field (against disorder), yet still quite sensitivity to it. This further reinforces the model of an unconventional superconductor with a short coherence length at high field.

Whilst this work gives a lot of insight into the Fermiology of URhGe, there remains a lot which is unknown. Both general magnetoresistance measurements and SdH measurements would benefit greatly from better samples. This could come in two forms, either lower impurity rates, which would bring $\omega_c\tau$ down to lower fields, or better geometries, which would yield better signal to noise. There is no clear way to improve RRRs, so future work could perhaps be on preparing good geometries. Since the high RRR samples from which to begin are typically less than $300\text{ }\mu\text{m}$ these techniques would have to be lithography based. If a sample could be cut which was $30\text{ }\mu\text{m}$ in width and thickness, and $300\text{ }\mu\text{m}$ in length, it would have a resistance of $10\text{ m}\Omega$. Given that the voltage noise on the measurement would remain unchanged and the current, which is limited by joule heating in the sample contacts, could also stay the same then this hundred-fold increase in resistance should translate to a similar increase in signal to noise. One must be somewhat careful with small samples to avoid surface effects, but the smaller of the dimensions above is still almost a thousand times the mean free path, so the measurement should remain reliable. The question of how one might obtain such a sample, and attach wires to it, is not an easy one. One might gain some success by starting with a small crystal mounted and wired in a similar manner to those discussed here, then milling away much of the central section with a focussed ion beam. This would also allow one to know exactly the orientation of the remaining section, and continue the current direction study introduced here to higher qualities.

In addition to URhGe some measurements of BiPd were also taken. These concentrated on probing the nonlinear IV curves and partial superconductivity that is present on the edge of the superconducting pocket. The transition appears to happen in three distinct stages. Firstly a

small deviation from zero resistance at 200 mT in sample #2, or somewhat less in sample #1. This is likely the end of bulk superconductivity, as also observed in very recent STM and specific heat[129] and SANS measurements. Beyond that, the superconductivity is probably confined to surfaces, filaments, twin boundaries, inclusions or similar. As the field is increased, the material goes through two transitions, which can be moved to lower field with current or temperature. At these transitions, the IV curve is kinked, it is linear both above and below the kink, and continuous.

This can be explained by having two channels in addition to the bulk. These separate channels behave as one would expect of a superconductor, but do not form a continuous path through the sample. They have different critical fields and are anisotropic in different directions. One is more robust for fields in-plane, the other for fields out-of-plane. The critical fields also vary somewhat from sample to sample, suggesting that the high RRRs of the samples do not tell the whole story.




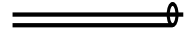




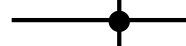
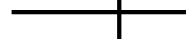
BiPd is a very new material, so there are plenty of opportunities for further work. It might be interesting to do some measurements on samples with different sizes and/or with artificially damaged surfaces to see if these effects are related to the surface or to some features within the material. Metallographic studies might also help identify or rule out inclusions.

Appendix A


Circuit symbols

In addition to the common symbols, I use the following throughout this document.


A.1 Conductors

	Wire , may be used for resistive, copper or superconducting wires, where the resistance is relevant, it will be indicated seperately.
	Twisted pair , unshielded.
	Twisted pair , shielded. Shield may be normal or superconducting, see text.
	Coax , with outer carrying signal.
	Coax , with outer as shield.
	Resistance , parasitic or otherwise not intended.
	Cable or collection of wires with details omitted.
	Enclosure acting as a shield.
	Connection .
	Crossing .


A.2 Components


 **Resistor**, intentional, either a discrete component or a sample.


 **SQUID**.

 **Capacitor**, ceramic unless otherwise noted.

 **Feedthrough capacitor**.

 **Chassis or enclosure ground**.

 **Building (aka mains or line) ground**. Also used when the distinction between building ground and clean ground is not important.

 **Clean Ground**.

Appendix B

Supplementary Information

The supplementary information provided with this thesis contains all the raw data which led to the results presented here, and all the necessary MATLAB scripts to get the results and graphs from that raw data. If you have a print copy of this thesis, the supplementary information should be on a DVD inside the rear cover. Folders are compressed in in ZIP format using the very common DEFLATE algorithm, the important files are mostly ASCII text.

The following files and folders should provide a starting point in finding specific data:

data/: This directory contains all of the data taken on the blue fridge during my PhD (not all of which is my work). It also contains most of the data taken on trips to the high magnetic field laboratory and other data from various places which is used in this Thesis. Data is arranged into directories by when and where it was taken. Each data file has a unique identifier at the start of the filename, consisting of the date in ddmmyy format and an identifier which increments with each file (a,b,c...x,y,z,aa,ab,ac...). The format within the files is plain text comma separated values. More recent files are accompanied by a .dat.key or .desc file which contains additional information about each column, again in plain text format. Each folder should also contain a file called **set_MQinfo** which contains additional information about what sample was wired to each instrument. Each folder also contains *.seq files which are the scripts used to control the refrigerator, and may prove useful in determining what was measured and why. There are also some data analysis scripts, mostly those written to provide an overview of the data as it was coming in.

data/Final Thesis Figures: This folder contains copies of every figure in this thesis and the MATLAB scripts used to create them. These MATLAB scripts should be the starting point in looking for the raw data which led to specific figures.

MLfiles/: This contains a great many MATLAB functions. They are known to work with MATLAB r2014a, and several older versions. Some of them are required to run the scripts mentioned in the previous paragraph, but most are not. Included are all the scripts required to run the refrigerator.

The version of this thesis submitted for examination has the paper [\[39\]](#) attached as an appendix, however it is omitted from this version to avoid infringing the publisher's copyright.

Bibliography

- [1] Ziman J. *Principles of the Theory of Solids*. Cambridge university press, 2nd edition (1972).
- [2] Pippard AB. *Magnetoresistance in metals*, volume 2 of *Cambridge Studies in Low Temperature Physics*. Cambridge University Press (1989).
- [3] Fawcett E. *High-field galvanomagnetic properties of metals*. **Advances in Physics**, **13(50)**:139 (1964). DOI [10.1080/00018736400101021](https://doi.org/10.1080/00018736400101021).
- [4] Shoenberg D. *Magnetic Oscillations in Metals*. Cambridge University Press (1984).
- [5] Blount EI. *Bloch electrons in a magnetic field*. **Physical Review**, **126**:1636 (June 1962). DOI [10.1103/PhysRev.126.1636](https://doi.org/10.1103/PhysRev.126.1636).
- [6] Falicov LM, Pippard AB, and Sievert PR. *Theory of the galvanomagnetic properties of magnesium and zinc*. **Physical Review**, **151**:498 (Nov 1966). DOI [10.1103/PhysRev.151.498](https://doi.org/10.1103/PhysRev.151.498).
- [7] van Ruitenbeek J, Verhoef W, Mattocks P, Dixon A, Vandeursen A, and Devroomen A. *A de Haas-van Alphen study of the field-dependence of the fermi-surface in $ZrZn_2$* . **Journal of Physics F: Metal Physics**, **12(12)**:2919 (1982). DOI [10.1088/0305-4608/12/12/022](https://doi.org/10.1088/0305-4608/12/12/022).
- [8] Julian S, Teunissen P, and Wieggers S. *Fermi-surface of UPt_3 from 3T to 30T - field-induced quasi-particle band polarization and the metamagnetic transition*. **Physical Review B: Condensed Matter and Materials Physics**, **46(15)**:9821 (October 1992). DOI [10.1103/PhysRevB.46.9821](https://doi.org/10.1103/PhysRevB.46.9821).
- [9] Aeppli G, Bucher E, Broholm C, Kjems JK, Baumann J, and Hufnagl J. *Magnetic order and fluctuations in superconducting UPt_3* . **Physical Review Letters**, **60**:615 (February 1988). DOI [10.1103/PhysRevLett.60.615](https://doi.org/10.1103/PhysRevLett.60.615).
- [10] Rourke P, McCollam A, Lapertot G, Knebel G, Flouquet J, and Julian S. *Magnetic-field dependence of the $YbRh_2Si_2$ Fermi surface*. **Physical Review Letters**, **101(23)** (December 2008). DOI [10.1103/PhysRevLett.101.237205](https://doi.org/10.1103/PhysRevLett.101.237205).
- [11] Mercure JF, Rost A, O'Farrell E, Goh S, Perry R, Sutherland M, Grigera S, Borzi R, Gegenwart P, Gibbs A, and Mackenzie A. *Quantum oscillations near the metamagnetic transition in $Sr_3Ru_2O_7$* . **Physical Review B: Condensed Matter and Materials Physics**, **81(23)** (June 2010). DOI [10.1103/PhysRevB.81.235103](https://doi.org/10.1103/PhysRevB.81.235103).
- [12] Mineev V and Samokhin K. *Introduction to Unconventional Superconductivity*. Gordon and Breach (1999).
- [13] Tinkham M. *Introduction to Superconductivity*. McGraw-Hill, 2nd edition (1996).
- [14] Monthoux P, Pines D, and Lonzarich GG. *Superconductivity without phonons*. **Nature**, **450**:1177 (Dec 2007). DOI [10.1038/nature06480](https://doi.org/10.1038/nature06480).
- [15] Monthoux P and Lonzarich GG. *p-wave and d-wave superconductivity in quasi-two-dimensional metals*. **Phys. Rev. B**, **59**:14598 (Jun 1999). DOI [10.1103/PhysRevB.59.14598](https://doi.org/10.1103/PhysRevB.59.14598).

- [16] Fay D and Appel J. *Coexistence of p-state superconductivity and itinerant ferromagnetism*. **Phys. Rev. B**, **22**:3173 (Oct 1980). DOI [10.1103/PhysRevB.22.3173](https://doi.org/10.1103/PhysRevB.22.3173).
- [17] Maeno Y, Hashimoto H, Yoshida K, Nishizaki S, Fujita T, Bednorz J, and Lichtenberg F. *Superconductivity in a layered perovskite without copper*. **Nature**, **372**(6506):532 (December 1994). DOI [10.1038/372532a0](https://doi.org/10.1038/372532a0).
- [18] Rice TM and Sigrist M. *Sr₂RuO₄ : an electronic analogue of ³He?* **Journal of Physics: Condensed Matter**, **7**(47):L643 (1995). DOI [10.1088/0953-8984/7/47/002](https://doi.org/10.1088/0953-8984/7/47/002).
- [19] Kim YB, Hempstead CF, and Strnad AR. *Flux-flow resistance in type-II superconductors*. **Phys. Rev.**, **139**:A1163 (Aug 1965). DOI [10.1103/PhysRev.139.A1163](https://doi.org/10.1103/PhysRev.139.A1163).
- [20] Kambe S, Huxley A, Rodière P, Paulsen C, and Flouquet J. *The critical current and irreversible magnetisation in UPt₃*. **Physica B: Condensed Matter**, **259–261**:670 (1999). DOI [10.1016/S0921-4526\(98\)00989-2](https://doi.org/10.1016/S0921-4526(98)00989-2).
- [21] Bauer E and Sigrist M (editors). *Non-Centrosymmetric Superconductors: Introduction and Overview*, volume 847 of *Lecture Notes in Physics*. Springer (2012). URL www.springer.com/materials/book/978-3-642-24623-4.
- [22] Suhl H, Matthias BT, and Walker LR. *Bardeen-Cooper-Schrieffer theory of superconductivity in the case of overlapping bands*. **Physical Review Letters**, **3**:552 (Dec 1959). DOI [10.1103/PhysRevLett.3.552](https://doi.org/10.1103/PhysRevLett.3.552).
- [23] Tran V, Troc R, and Andre G. *Magnetic ordering in URhSi and URhGe*. **Journal of magnetism and magnetic materials**, **186**(1-2):81 (July 1998). DOI [10.1016/S0304-8853\(98\)00074-2](https://doi.org/10.1016/S0304-8853(98)00074-2).
- [24] de Boer F, Bruck E, Sechovsky V, Havela L, and Buschow K. *UTX compounds in high magnetic-fields*. **Physica B: Condensed Matter**, **163**(1-3):175 (April 1990). DOI [10.1016/0921-4526\(90\)90160-V](https://doi.org/10.1016/0921-4526(90)90160-V).
- [25] Aoki D, Huxley A, Ressouche E, Braithwaite D, Flouquet J, Brison J, Lhotel E, and Paulsen C. *Coexistence of superconductivity and ferromagnetism in URhGe*. **Nature**, **413**(6856):613 (October 2001). DOI [10.1038/35098048](https://doi.org/10.1038/35098048).
- [26] Prokes K, Tahara T, Echizen Y, Takabatake T, Fujita T, Hagmusa I, Klaasse J, Bruck E, de Boer F, Divis M, and Sechovsky V. *Erratum to: Electronic properties of an URhGe single crystal (vol 311, pg 220, 2002)*. **Physica B: condensed matter**, **334**(3-4):272 (July 2003). DOI [10.1016/S0921-4526\(03\)00076-0](https://doi.org/10.1016/S0921-4526(03)00076-0).
- [27] Prokes K, Tahara T, Echizen Y, Takabatake T, Fujita T, Hagmusa I, Klaasse J, Bruck E, de Boer F, Divis M, and Sechovsky V. *Electronic properties of a URhGe single crystal*. **Physica B: condensed matter**, **311**(3-4):220 (February 2002). DOI [10.1016/S0921-4526\(01\)01037-7](https://doi.org/10.1016/S0921-4526(01)01037-7).
- [28] Moriya T and Takahashi Y. *Itinerant electron magnetism*. **Annual Review of Materials Science**, **14**(1):1 (1984). DOI [10.1146/annurev.ms.14.080184.000245](https://doi.org/10.1146/annurev.ms.14.080184.000245).
- [29] Levy F, Sheikin I, Grenier B, and Huxley A. *Magnetic field-induced superconductivity in the ferromagnet URhGe*. **Science**, **309**(5739):1343 (August 2005). DOI [10.1126/science.1115498](https://doi.org/10.1126/science.1115498).
- [30] Levy F, Sheikin I, and Huxley A. *Acute enhancement of the upper critical field for superconductivity approaching a quantum critical point in URhGe*. **Nature physics**, **3**(7):460 (July 2007). DOI [10.1038/nphys608](https://doi.org/10.1038/nphys608).
- [31] Taufour V, Aoki D, Knebel G, and Flouquet J. *Tricritical point and wing structure in the itinerant ferromagnet UGe₂*. **Phys. Rev. Lett.**, **105**:217201 (Nov 2010). DOI [10.1103/PhysRevLett.105.217201](https://doi.org/10.1103/PhysRevLett.105.217201).

- [32] Uhlarz M, Pfeiderer C, and Hayden SM. *Quantum phase transitions in the itinerant ferromagnet ZrZn_2* . **Phys. Rev. Lett.**, **93**:256404 (Dec 2004). DOI [10.1103/PhysRevLett.93.256404](https://doi.org/10.1103/PhysRevLett.93.256404).
- [33] Otero-Leal M, Rivadulla F, García-Hernández M, Piñeiro A, Pardo V, Baldomir D, and Rivas J. *Effect of spin fluctuations on the thermodynamic and transport properties of the itinerant ferromagnet CoS_2* . **Phys. Rev. B**, **78**:180415 (Nov 2008). DOI [10.1103/PhysRevB.78.180415](https://doi.org/10.1103/PhysRevB.78.180415).
- [34] Kirkpatrick TR and Belitz D. *Universal low-temperature tricritical point in metallic ferromagnets and ferrimagnets*. **Physical Review B: Condensed Matter and Materials Physics**, **85**(13) (April 2012). DOI [10.1103/PhysRevB.85.134451](https://doi.org/10.1103/PhysRevB.85.134451).
- [35] Vojta M. *Quantum phase transitions*. **Reports on Progress in Physics**, **66**(12):2069 (2003). DOI [10.1088/0034-4885/66/12/R01](https://doi.org/10.1088/0034-4885/66/12/R01).
- [36] NishiZaki S, Maeno Y, and Mao Z. *Effect of impurities on the specific heat of the spin-triplet superconductor Sr_2RuO_4* . **Journal of Low Temperature Physics**, **117**(5-6):1581 (December 1999). DOI [10.1023/A:1022551313401](https://doi.org/10.1023/A:1022551313401).
- [37] Hardy F and Huxley A. *P-wave superconductivity in the ferromagnetic superconductor URhGe* . **Physical Review Letters**, **94**(24) (June 2005). DOI [10.1103/PhysRevLett.94.247006](https://doi.org/10.1103/PhysRevLett.94.247006).
- [38] Anderson P. *Theory of dirty superconductors*. **Journal of Physics and Chemistry of Solids**, **11**(1-2):26 (1959). DOI [10.1016/0022-3697\(59\)90036-8](https://doi.org/10.1016/0022-3697(59)90036-8).
- [39] Yelland EA, Barraclough JM, Wang W, Kamenev KV, and Huxley AD. *High-field superconductivity at an electronic topological transition in URhGe* . **Nature physics**, **7**(11):890 (November 2011). DOI [10.1038/NPHYS2073](https://doi.org/10.1038/NPHYS2073).
- [40] Miyake A, Aoki D, and Flouquet J. *Field re-entrant superconductivity induced by the enhancement of effective mass in URhGe* . **Journal of the Physical Society of Japan**, **77**(9) (September 2008). DOI [10.1143/JPSJ.77.094709](https://doi.org/10.1143/JPSJ.77.094709).
- [41] Hardy F, Huxley A, Flouquet J, Salce B, Knebel G, Braithwaite D, Aoki D, Uhlarz M, and Pfeiderer C. *(P,T) phase diagram of the ferromagnetic superconductor URhGe* . **Physica B: Condensed Matter**, **359-361**(0):1111 (April 2005). DOI [10.1016/j.physb.2005.01.306](https://doi.org/10.1016/j.physb.2005.01.306).
- [42] Sakarya S, van Dijk N, de Visser A, and Bruck E. *Dilatometry study of the ferromagnetic order in single-crystalline URhGe* . **Physical Review B: Condensed Matter and Materials Physics**, **67**(14) (April 2003). DOI [10.1103/PhysRevB.67.144407](https://doi.org/10.1103/PhysRevB.67.144407).
- [43] Huy N and de Visser A. *Ferromagnetic order in $U(\text{Rh}, \text{Co})\text{Ge}$* . **Solid State Communications**, **149**(1718):703 (2009). DOI [10.1016/j.ssc.2009.02.013](https://doi.org/10.1016/j.ssc.2009.02.013).
- [44] Hassinger E, Aoki D, Knebel G, and Flouquet J. *Pressure-temperature phase diagram of polycrystalline UCoGe studied by resistivity measurement*. **Journal of the Physical Society of Japan**, **77**(7):073703 (2008). DOI [10.1143/JPSJ.77.073703](https://doi.org/10.1143/JPSJ.77.073703).
- [45] Prokeš K, Sechovský V, de Boer FR, and Andreev AV. *The field-induced magnetic structure in UIrGe* . **Journal of Physics: Condensed Matter**, **20**(10):104221 (2008). DOI [10.1088/0953-8984/20/10/104221](https://doi.org/10.1088/0953-8984/20/10/104221).
- [46] Huy NT, Gasparini A, Klaasse JCP, de Visser A, Sakarya S, and van Dijk NH. *Ferromagnetic quantum critical point in URhGe doped with Ru*. **Physical Review B: Condensed Matter and Materials Physics**, **75**:212405 (Jun 2007). DOI [10.1103/PhysRevB.75.212405](https://doi.org/10.1103/PhysRevB.75.212405).

- [47] Boulet P, Daoudi A, Potel M, Noël H, Gross G, André G, and Bourée F. *Crystal and magnetic structure of the uranium digermanide UGe_2* . **Journal of Alloys and Compounds**, **247(1–2)**:104 (January 1997). DOI [10.1016/S0925-8388\(96\)02600-X](https://doi.org/10.1016/S0925-8388(96)02600-X).
- [48] Huxley A, Sheikin I, Ressouche E, Kernavanois N, Braithwaite D, Calemczuk R, and Flouquet J. *UGe_2 : A ferromagnetic spin-triplet superconductor*. **Physical Review B**, **63(14)** (April 2001). DOI [10.1103/PhysRevB.63.144519](https://doi.org/10.1103/PhysRevB.63.144519).
- [49] Nyquist H. *Thermal agitation of electric charge in conductors*. **Physical Review**, **32**:110 (July 1928). DOI [10.1103/PhysRev.32.110](https://doi.org/10.1103/PhysRev.32.110).
- [50] Stanford Research Systems, 1290-D Reamwood Avenue, Sunnyvale, California 94089. *Model SR554 Transformer Preamplifier*, 1.2 edition (July 2004). URL <http://www.thinksrs.com/downloads/PDFs/Manuals/SR554m.pdf>.
- [51] Ekin JW. *Experimental techniques for low temperature measurements*. Oxford University Press (2006).
- [52] Pobell F. *Matter and methods at low temperatures*. Springer, 3rd edition (2007).
- [53] Palm EC and Murphy TP. *Very low friction rotator for use at low temperatures and high magnetic fields*. **Review of Scientific Instruments**, **70(1, 1)**:237 (January 1999). DOI [10.1063/1.1149571](https://doi.org/10.1063/1.1149571).
- [54] Yeoh LA, Srinivasan A, Martin TP, Klochan O, Micolich AP, and Hamilton AR. *Piezoelectric rotator for studying quantum effects in semiconductor nanostructures at high magnetic fields and low temperatures*. **Review of Scientific Instruments**, **81(11)** (November 2010). DOI [10.1063/1.3502645](https://doi.org/10.1063/1.3502645).
- [55] Walker IR. *The observation of resistance oscillations in metals at high magnetic-fields using a SQUID*. **Journal of Low Temperature Physics**, **90(3-4)**:205 (February 1993). DOI [10.1007/BF00682000](https://doi.org/10.1007/BF00682000).
- [56] Ohmichi E, Nagai S, Maeno Y, Ishiguro T, Mizuno H, and Nagamura T. *Piezoelectrically driven rotator for use in high magnetic fields at low temperatures*. **Review of Scientific Instruments**, **72(3)**:1914 (March 2001). DOI [10.1063/1.1347982](https://doi.org/10.1063/1.1347982).
- [57] Lounasmaa OV. *Experimental principles and methods below 1K*. Accademic Press (1974).
- [58] Ehrlich AC. *Oxygen annealing of silver for obtaining low electrical-resistivity – technique and interpretation*. **Journal of materials science**, **9(7)**:1064 (1974). DOI [10.1007/BF00552819](https://doi.org/10.1007/BF00552819).
- [59] Gallop JC. *SQUIDS, the Josephson effects and superconducting electronics*. The Adam Hilger series on measurement science and technology. Bristol : Hilger (1991). ISBN 0750300515.
- [60] Rowlands JA and Woods SB. *High precision 4-terminal resistance bridge utilizing a squid null-detector*. **Review of Scientific Instruments**, **47(7)**:795 (1976). DOI [10.1063/1.1134755](https://doi.org/10.1063/1.1134755).
- [61] Olson JR. *Thermal-conductivity of some common cryostat materials between 0.05 and 2K*. **Cryogenics**, **33(7)**:729 (July 1993). DOI [10.1016/0011-2275\(93\)90027-L](https://doi.org/10.1016/0011-2275(93)90027-L).
- [62] Woodcraft AL, Ventura G, Martelli V, and Holland WS. *Thermal conductance at millikelvin temperatures of woven ribbon cable with phosphor-bronze clad superconducting wires*. **Cryogenics**, **50(8)**:465 (August 2010). DOI [10.1016/j.cryogenics.2010.06.001](https://doi.org/10.1016/j.cryogenics.2010.06.001).
- [63] Connolly A and Mendelssohn K. *Thermal conductivity of tantalum and niobium below 1 degree K*. **Proceedings of the royal society of london: series A-mathematical and physical sciences**, **266(1327)**:429 (1962). DOI [10.1098/rspa.1962.0071](https://doi.org/10.1098/rspa.1962.0071).

- [64] French RA. *Intrinsic type-2 superconductivity in pure niobium*. **Cryogenics**, **8(5)**:301 (1968). DOI [10.1016/S0011-2275\(68\)80007-4](https://doi.org/10.1016/S0011-2275(68)80007-4).
- [65] Joshi B, Thamizhavel A, and Ramakrishnan S. *Superconductivity in noncentrosymmetric BiPd*. **Physical Review B: Condensed Matter and Materials Physics**, **84(6)** (August 2011). DOI [10.1103/PhysRevB.84.064518](https://doi.org/10.1103/PhysRevB.84.064518).
- [66] Whitley W. Personal Communication (August 2011).
- [67] Fisher ME and Langer JS. *Resistive anomalies at magnetic critical points*. **Physical Review Letters**, **20**:665 (March 1968). DOI [10.1103/PhysRevLett.20.665](https://doi.org/10.1103/PhysRevLett.20.665).
- [68] Park S, Jeong Y, Lee K, and Kwon S. *Specific heat and resistivity of a double-exchange ferromagnet $\text{La}_{0.7}\text{Ca}_{0.3}\text{MnO}_3$* . **Physical Review B: Condensed Matter and Materials Physics**, **56(1)**:67 (July 1997). DOI [10.1103/PhysRevB.56.67](https://doi.org/10.1103/PhysRevB.56.67).
- [69] Kim D, Zink B, Hellman F, McCall S, Cao G, and Crow J. *Mean-field behavior with Gaussian fluctuations at the ferromagnetic phase transition of SrRuO_3* . **Physical Review B: Condensed Matter and Materials Physics**, **67(10)** (March 2003). DOI [10.1103/PhysRevB.100406](https://doi.org/10.1103/PhysRevB.100406).
- [70] Hussey N, Mackenzie A, Cooper J, Maeno Y, Nishizaki S, and Fujita T. *Normal-state magnetoresistance of Sr_2RuO_4* . **Physical Review B: Condensed Matter and Materials Physics**, **57(9)**:5505 (March 1998). DOI [10.1103/PhysRevB.57.5505](https://doi.org/10.1103/PhysRevB.57.5505).
- [71] Gunnarsson O, Calandra M, and Han J. *Colloquium: Saturation of electrical resistivity*. **Reviews of Modern Physics**, **75(4)**:1085 (October 2003). DOI [10.1103/RevModPhys.75.1085](https://doi.org/10.1103/RevModPhys.75.1085).
- [72] Wiesmann H, Gurvitch M, Lutz H, Ghosh A, Schwarz B, Strongin M, Allen P, and Halley J. *Simple model for characterizing electrical resistivity in A-15 superconductors*. **Physical Review Letters**, **38(14)**:782 (1977). DOI [10.1103/PhysRevLett.38.782](https://doi.org/10.1103/PhysRevLett.38.782).
- [73] Gurvitch M. *Ioffe-Regel criterion and resistivity of metals*. **Physical Review B: Condensed Matter and Materials Physics**, **24(12)**:7404 (1981). DOI [10.1103/PhysRevB.24.7404](https://doi.org/10.1103/PhysRevB.24.7404).
- [74] Canepa F, Manfrinetti P, Pani M, and Palenzona A. *Structural and transport properties of some UTX compounds where $T = \text{Fe}, \text{Co}, \text{Ni}$ and $X = \text{Si}, \text{Ge}$* . **Journal of Alloys and Compounds**, **234(2)**:225 (1996). DOI [10.1016/0925-8388\(95\)02037-3](https://doi.org/10.1016/0925-8388(95)02037-3).
- [75] Hussey NE, Takenaka K, and Takagi H. *Universality of the Mott-Ioffe-Regel limit in metals*. **Philosophical Magazine**, **84(27)**:2847 (2004). DOI [10.1080/14786430410001716944](https://doi.org/10.1080/14786430410001716944).
- [76] de Visser A, Franse J, and Menovsky A. *Resistivity of single-crystalline UPt_3 and its pressure dependence; interpretation by a spin-fluctuation model*. **Journal of Magnetism and Magnetic Materials**, **43(1)**:43 (1984). DOI [10.1016/0304-8853\(84\)90271-3](https://doi.org/10.1016/0304-8853(84)90271-3).
- [77] Palstra TTM, Menovsky AA, and Mydosh JA. *Anisotropic electrical resistivity of the magnetic heavy-fermion superconductor URu_2Si_2* . **Physical Review B**, **33**:6527 (May 1986). DOI [10.1103/PhysRevB.33.6527](https://doi.org/10.1103/PhysRevB.33.6527).
- [78] Heuer RP. *The effect of iron and oxygen on the electrical conductivity of copper*. **Journal of the American Chemical Society**, **49(11)**:2711 (1927). DOI [10.1021/ja01410a007](https://doi.org/10.1021/ja01410a007).
- [79] Fawcett E and Reed W. *Effects of compensation on galvanomagnetic properties of non-magnetic and ferromagnetic metals*. **Physical Review**, **131(6)**:2463 (1963). DOI [10.1103/PhysRev.131.2463](https://doi.org/10.1103/PhysRev.131.2463).

- [80] Müller W, Tran VH, Oeschler N, and Steglich F. *Electronic properties of URhGe ferromagnet probed by hall effect and thermopower measurements*. In *38. Journées des Actinides together with the 7. School on the Physics and Chemistry of the Actinides* (2008). URL http://inis.iaea.org/search/search.aspx?orig_q=RN:40086441.
- [81] Tran V and Troc R. *Large magnetoresistance of the ferromagnetic intermetallics URhSi and URhGe*. **Physical Review B: Condensed Matter and Materials Physics**, **57(18)**:11592 (May 1998). DOI [10.1103/PhysRevB.57.11592](https://doi.org/10.1103/PhysRevB.57.11592).
- [82] Coleridge PT. *Magnetoresistance and growth of the coherent state in CeCu₆*. **Journal of Physics F: Metal Physics**, **17(5)**:L79 (1987). DOI [10.1088/0305-4608/17/5/002](https://doi.org/10.1088/0305-4608/17/5/002).
- [83] Mahan GD. *Electron green functions in magnetic fields*. **Journal of Physics F: Metal Physics**, **14(4)**:941 (1984). DOI [10.1088/0305-4608/14/4/018](https://doi.org/10.1088/0305-4608/14/4/018).
- [84] Hussey N, Kibune M, Nakagawa H, Miura N, Iye Y, Takagi H, Adachi S, and Tanabe K. *Magnetic field induced dimensional crossover in the normal state of YBa₂Cu₄O₈*. **Physical Review Letters**, **80(13)**:2909 (March 1998). DOI [10.1103/PhysRevLett.80.2909](https://doi.org/10.1103/PhysRevLett.80.2909).
- [85] Wasserman A, Springford M, and Han F. *The de Haas - van Alphen effect in a marginal Fermi liquid*. **Journal of Physics: Condensed Matter**, **3**:5335 (1991). DOI [10.1088/0953-8984/3/28/008](https://doi.org/10.1088/0953-8984/3/28/008).
- [86] Pelzer F. *Amplitude of the de Haas van Alphen oscillations for a marginal Fermi liquid*. **Physical Review B: Condensed Matter and Materials Physics**, **44**:293 (July 1991). DOI [10.1103/PhysRevB.44.293](https://doi.org/10.1103/PhysRevB.44.293).
- [87] Khalid MA, Reinders PHP, and Springford M. *A study of the electron-phonon interaction in the de haas-van alphen effect*. **Journal of Physics F: Metal Physics**, **18(9)**:1949 (1988). DOI [10.1088/0305-4608/18/9/015](https://doi.org/10.1088/0305-4608/18/9/015).
- [88] Lithgow C. Personal Communication (December 2013).
- [89] Hahn T (editor). *International tables for crystallography*, volume A: Space-group symmetry. Published for the International Union of Crystallography by John Wiley & Sons, 5th edition (2002).
- [90] Herring C. *Effect of time-reversal symmetry on energy bands of crystals*. **Physical Review**, **52**:361 (August 1937). DOI [10.1103/PhysRev.52.361](https://doi.org/10.1103/PhysRev.52.361).
- [91] Gold AV. *Solid state physics*, volume 1: Electrons in Metals. Gordon and Breach (1968).
- [92] Ashcroft N and Mermin N. *Solid State Physics*. Holt, Reinehart and Winston (1976).
- [93] Elliott RJ. *Spin-orbit coupling in band theory — character tables for some “double” space groups*. **Physical Review**, **96**:280 (October 1954). DOI [10.1103/PhysRev.96.280](https://doi.org/10.1103/PhysRev.96.280).
- [94] Cohen MH and Falicov LM. *Effect of spin-orbit splitting on the Fermi surfaces of the hexagonal-close-packed metals*. **Physical Review Letters**, **5**:544 (December 1960). DOI [10.1103/PhysRevLett.5.544](https://doi.org/10.1103/PhysRevLett.5.544).
- [95] Joseph AS, Gordon WL, Reitz JR, and Eck TG. *Evidence for spin-orbit splitting in the band structure of zinc and cadmium*. **Physical Review Letters**, **7**:334 (November 1961). DOI [10.1103/PhysRevLett.7.334](https://doi.org/10.1103/PhysRevLett.7.334).
- [96] Cottenier S. *Density Functional Theory and the family of (L)APW-methods: a step-by-step introduction*. Instituut voor Kern en Stralingsfysica, K.U.Leuven, Belgium (2002). URL http://www.wien2k.at/reg_user/textbooks.
- [97] Hohenberg P and Kohn W. *Inhomogeneous electron gas*. **Physical Review**, **136**:B864 (November 1964). DOI [10.1103/PhysRev.136.B864](https://doi.org/10.1103/PhysRev.136.B864).

- [98] Kohn W and Sham LJ. *Self-consistent equations including exchange and correlation effects*. **Physical Review**, **140**:A1133 (November 1965). DOI [10.1103/PhysRev.140.A1133](https://doi.org/10.1103/PhysRev.140.A1133).
- [99] Diviš M, Sandratskii L, Richter M, Mohn P, and Novák P. *Magnetism of URhSi and URhGe: a density functional study*. **Journal of Alloys and Compounds**, **337**:48 (2002). DOI [10.1016/S0925-8388\(01\)01951-X](https://doi.org/10.1016/S0925-8388(01)01951-X).
- [100] Shick A. *Electronic and magnetic structure of URhGe*. **Physical Review B: Condensed Matter and Materials Physics**, **65**(18):180509 (May 2002). DOI [10.1103/PhysRevB.65.180509](https://doi.org/10.1103/PhysRevB.65.180509).
- [101] Fujimori Si, Ohkochi T, Kawasaki I, Yasui A, Takeda Y, Okane T, Saitoh Y, Fujimori A, Yamagami H, Haga Y, Yamamoto E, Tokiwa Y, Ikeda S, Sugai T, Ohkuni H, Kimura N, and Ōnuki Y. *Electronic structure of heavy fermion uranium compounds studied by core-level photoelectron spectroscopy*. **Journal of the Physical Society of Japan**, **81**(1):014703 (2012). DOI [10.1143/JPSJ.81.014703](https://doi.org/10.1143/JPSJ.81.014703).
- [102] Müller W, Tran VH, and Richter M. *Cancellation of spin and orbital moments in URhGe under pressure: A density-functional prediction*. **Physical Review B: Condensed Matter and Materials Physics**, **80**:195108 (November 2009). DOI [10.1103/PhysRevB.80.195108](https://doi.org/10.1103/PhysRevB.80.195108).
- [103] Yelland E. Personal Communication (January 2014).
- [104] Fujimori Si, Kawasaki I, Yasui A, Takeda Y, Okane T, Saitoh Y, Fujimori A, Yamagami H, Haga Y, Yamamoto E, and Ōnuki Y. *Itinerant magnetism in URhGe revealed by angle-resolved photoelectron spectroscopy*. **Physical Review B: Condensed Matter and Materials Physics**, **89**:104518 (March 2014). DOI [10.1103/PhysRevB.89.104518](https://doi.org/10.1103/PhysRevB.89.104518).
- [105] Schofield AJ. *Non-fermi liquids*. **Contemporary Physics**, **40**(2):95 (1999). DOI [10.1080/001075199181602](https://doi.org/10.1080/001075199181602).
- [106] Mathon J. *Magnetic and electrical properties of ferromagnetic alloys near the critical concentration*. **Proceedings of the Royal Society of London. Series A: Mathematical and Physical Sciences**, **306**(1486):355 (1968). DOI [10.1098/rspa.1968.0155](https://doi.org/10.1098/rspa.1968.0155).
- [107] Pfeiderer C, McMullan GJ, Julian SR, and Lonzarich GG. *Magnetic quantum phase transition in MnSi under hydrostatic pressure*. **Physical Review B: Condensed Matter and Materials Physics**, **55**:8330 (April 1997). DOI [10.1103/PhysRevB.55.8330](https://doi.org/10.1103/PhysRevB.55.8330).
- [108] Grosche F, Pfeiderer C, McMullan G, Lonzarich G, and Bernhoeft N. *Critical behaviour of ZrZn₂*. **Physica B: Condensed Matter**, **206207**:20 (1995). DOI [10.1016/0921-4526\(94\)00356-Z](https://doi.org/10.1016/0921-4526(94)00356-Z). Proceedings of the International Conference on Strongly Correlated Electron Systems.
- [109] Ogawa S. *Electrical resistivity of weak itinerant ferromagnet ZrZn₂*. **Journal of the Physical Society of Japan**, **40**(4):1007 (1976). DOI [10.1143/JPSJ.40.1007](https://doi.org/10.1143/JPSJ.40.1007).
- [110] Moriya T and Takimoto T. *Anomalous properties around magnetic instability in heavy electron systems*. **Journal of the Physical Society of Japan**, **64**(3):960 (1995). DOI [10.1143/JPSJ.64.960](https://doi.org/10.1143/JPSJ.64.960).
- [111] Mineev VP. *Interplay between magnetism and superconductivity in URhGe*. **Comptes Rendus Physique**, **7**(1):35 (2006). DOI [10.1016/j.crhy.2005.11.006](https://doi.org/10.1016/j.crhy.2005.11.006).
- [112] Blanter Y, Kaganov M, Pantsulaya A, and Varlamov A. *The theory of electronic topological transitions*. **Physics Reports**, **245**(4):159 (September 1994). DOI [10.1016/0370-1573\(94\)90103-1](https://doi.org/10.1016/0370-1573(94)90103-1).
- [113] Katsnelson M and Trefilov A. *Fermi-liquid theory of electronic topological transitions and screening anomalies in metals*. **Physical Review B: Condensed Matter and Materials Physics**, **61**(3):1643 (January 2000). DOI [10.1103/PhysRevB.61.1643](https://doi.org/10.1103/PhysRevB.61.1643).

- [114] Hackl A and Vojta M. *Zeeman-driven lifshitz transition: a model for the experimentally observed fermi-surface reconstruction in YbRh_2Si_2* . **Physical Review Letters**, **106**(13) (March 2011). DOI [10.1103/PhysRevLett.106.137002](https://doi.org/10.1103/PhysRevLett.106.137002).
- [115] Bruin JAN, Sakai H, Perry RS, and Mackenzie AP. *Similarity of scattering rates in metals showing T -linear resistivity*. **Science**, **339**(6121):804 (2013). DOI [10.1126/science.1227612](https://doi.org/10.1126/science.1227612).
- [116] Miyake A, Aoki D, and Flouquet J. *Pressure evolution of the ferromagnetic and field re-entrant superconductivity in URhGe* . **Journal of the Physical Society of Japan**, **78**(6) (June 2009). DOI [10.1143/JPSJ.78.063703](https://doi.org/10.1143/JPSJ.78.063703).
- [117] Huxley A, van Dijk N, Paul DM, Cubitt R, and Lejay P. *A low field study of the flux line lattice in CeRu_2* . **Physica B: Condensed Matter**, **259–261**:696 (1999). DOI [10.1016/S0921-4526\(98\)01115-6](https://doi.org/10.1016/S0921-4526(98)01115-6).
- [118] Zhuravlev N. *Structure of superconductors. Thermal, microscopic and X-ray investigation of the bismuth palladium system*. **Soviet Physics JETP**, **5**(6) (December 1957).
- [119] Yelland E. Personal Communication (June 2014).
- [120] Yelland EA, Barraclough JM, Thamizhavel A, Joshi B, and Ramakrishnan S. *Spin-orbit splitting of bulk electronic states in noncentrosymmetric superconductor BiPd* . **To be published**.
- [121] Matano K, Maeda S, Sawaoka H, Muro Y, Takabatake T, Joshi B, Ramakrishnan S, Kawashima K, Akimitsu J, and Zheng Gq. *NMR and NQR studies on non-centrosymmetric superconductors Re_7B_3 , LaBiPt , and BiPd* . **Journal of the Physical Society of Japan**, **82**(8) (August 2013). DOI [10.7566/JPSJ.82.084711](https://doi.org/10.7566/JPSJ.82.084711).
- [122] Mondal M, Joshi B, Kumar S, Kamlapure A, Ganguli SC, Thamizhavel A, Mandal SS, Ramakrishnan S, and Raychaudhuri P. *Andreev bound state and multiple energy gaps in the noncentrosymmetric superconductor BiPd* . **Physical Review B: Condensed Matter and Materials Physics**, **86**(9) (September 2012). DOI [10.1103/PhysRevB.86.094520](https://doi.org/10.1103/PhysRevB.86.094520).
- [123] Jiao L, Zhang JL, Chen Y, Weng ZF, Shao YM, Feng JY, Lu X, Joshi B, Thamizhavel A, Ramakrishnan S, and Yuan HQ. *Anisotropic superconductivity in noncentrosymmetric BiPd* . **Physical Review B: Condensed Matter and Materials Physics**, **89**(6) (February 2014). DOI [10.1103/PhysRevB.89.060507](https://doi.org/10.1103/PhysRevB.89.060507).
- [124] Fietz WA, Beasley MR, Silcox J, and Webb WW. *Magnetization of superconducting Nb-25\%Zr wire*. **Physical Review**, **136**:A335 (October 1964). DOI [10.1103/PhysRev.136.A335](https://doi.org/10.1103/PhysRev.136.A335).
- [125] Karasik V, Vasilev N, and Ershov V. *Magnetization of superconducting alloy Ti-22 at\%Nb* . **Soviet Physics JETP-USSR**, **32**(3):433 (1971).
- [126] Farrell DE, Chandrasekhar BS, DeGuire MR, Fang MM, Kogan VG, Clem JR, and Finemore DK. *Superconducting properties of aligned crystalline grains of $\text{Y}_1\text{Ba}_2\text{Cu}_3\text{O}_{7-\delta}$* . **Physical Review B: Condensed Matter and Materials Physics**, **36**:4025 (September 1987). DOI [10.1103/PhysRevB.36.4025](https://doi.org/10.1103/PhysRevB.36.4025).
- [127] Ooijen DV and Gorp GV. *Measurement of noise in the resistive state of type II superconductors*. **Physics Letters**, **17**(3):230 (1965). DOI [10.1016/0031-9163\(65\)90500-7](https://doi.org/10.1016/0031-9163(65)90500-7).
- [128] Lithgow C. Personal Communication (August 2014).
- [129] Sun Z, Enayat M, Maldonado A, Lithgow C, Yelland E, Peets DC, Yaresko A, Schnyder AP, and Wahl P. *Dirac surface states and nature of superconductivity in noncentrosymmetric BiPd* . **ArXiv**, **1407.5667** (July 2014). URL <http://arxiv.org/abs/1407.5667>.